UNIVERSITÀ
DEGLI STUDI
DI PADOVA

Sede Amministrativa: Università degli Studi di Padova

Dipartimento di Scienze Chimiche

CORSO DI DOTTORATO DI RICERCA IN SCIENZA E INGEGNERIA DEI MATERIALI E DELLE NANOSTRUTTURE

CICLO XXXI°

Advanced Ceramics for Sustainable Energy Conversion Processes: from High Functionality Chemical Tailoring to Nanoscale Designed Materials

Tesi redatta con il contributo finanziario di Fondazione Cariparo, nell'ambito del progetto "Materiali nanostrutturati per un'energetica sostenibile"

Coordinatore: Ch.mo Prof. Giovanni Mattei

Supervisore: Prof. Antonella Glisenti

Dottorando: Giovanni Perin

“E noi, per quanto ci troviamo in situazioni inique,
tuttavia serbiamo il nostro invincibile proposito
tanto da non temere la morte stessa”

Abstract

The last decades have been characterized by a constant increase in the need of energy coupled with an increase in the greenhouse gases emissions, since a large amount of the energy is provided by combustion plants burning fossil fuels. The level of CO_2 has reached a negative record and this tendency has to be reversed in favor of a more environmentally sustainable approach. In this scenario different solutions for energy conversion and storage need to be found: the use of fossil fuels has to be reduced and replace with other and more sustainable forms of energy conversion. At the same time the change has to be guided by an improvement in the current technology for energy conversion to facilitate the transition process. For this purpose, the traditional combustion process can be improved using oxy-fuel conditions, where a stream of pure O_2 provided by an oxygen transport membrane is used instead of air and the resulting high concentrated CO_2 flue gas is easier to capture. A cleaner form of energy can be obtained using Solid Oxide Reversible Cells (SORCs), highly efficient electrochemical devices able convert chemicals directly into electrical current without production of pollutants. When operated in electrolysis mode, SORCs allow to store electrical energy in the form of fuels, obtained from CO_2 reduction.

Despite being extremely appealing, both these possibilities are not integrated in large scale energy plants yet, due mainly to their cost and long-term stability issues. These aspects can be improved with materials having a better performance and this can be achieved by an appropriate tailoring of their properties.

This thesis presents the attempt to address these issues by developing novel advanced ceramic materials with high performances in order to fulfill a lower temperature application. In particular, this has been pursued aiming at improving the ionic conductivity of the materials. A GDC/YSZ nanocomposite has been prepared by inkjet printing and characterized as electrolyte, with attention to the interaction between the two phases. Complex perovskites have been designed and optimized to stabilize a high oxygen defective crystal phase displaying mixed ionic and electronic conductivity. These materials have been characterized in their structure, oxygen mobility and conductivity, before being tested as oxygen transport membranes and cathodes for solid oxide fuel cells.

Table of Contents

Chapter 1

Introduction and background

SETTING THE CONTEXT FOR A DISCUSSION ON ENERGY CONVERSION AND HOW TO MAKE IT MORE SUSTAINABLE

In this chapter the context in which the thesis is developed is presented, along with an introduction on main the topics developed in the work. First, a motivation for the pursue of new forms for energy conversion is found analyzing the trends in energy production and greenhouse gases emissions in the recent years, with a glance at projections for the years to come. Successively some possible strategies for overcoming the issues related to the impact of energy conversion processes are listed: a short term action to reduce the emissions of the existing plants, with a focus on CO_2, and a long term objective of developing more efficient methods for energy harvesting. Finally, a method for CO_2 evaluation is considered.

1.1 The environmental impact of energy conversion

In the last decades an increase in the planet temperature due to massive greenhouse gases emission has been observed, driven by the constant increase of population and energy demand. This phenomenon has become critical because of its impact on human health and environment, with effects including environmental cataclysms, glaciers melting and seas tropicalization.[1]

The projections for the Earth overheating foresee that, proceeding at nowadays trends, this process is not going to slow down in the upcoming years.[2] As a consequence of that, all related threatens are expected to get more frequent. Recently, CO_2 level in the atmosphere has broken the record of 400 ppm and is still increasing year after year with an almost linear trend regarded as threatening.[3,4]

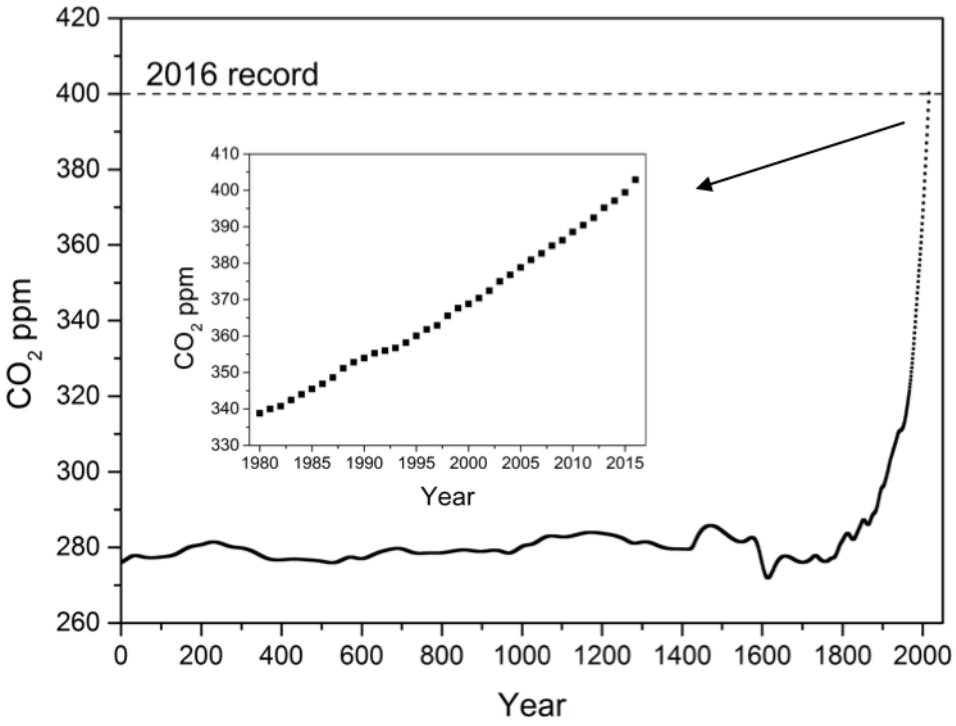

Fig 1.1: Atmospheric CO_2 levels as a function of years. Inset showing the growth of CO_2 level since 1980. Drawn from data taken from [3] and [4].

However, despite being the one produced in largest amount, CO_2 is not even the most harmful greenhouse gas to be released in the atmosphere. Scaling the impact on greenhouse effect with respect of CO_2 (which could be considered as benchmark, with a value of 1), methane (CH_4) has a 28-fold impact with respect to CO_2 and nitrous oxide

(N_2O) impacts is 265 times higher. It is thus fundamental not only to reduce CO_2 emissions, but moreover to limit as much as possible the release of the other gases too, when feasible.[5]

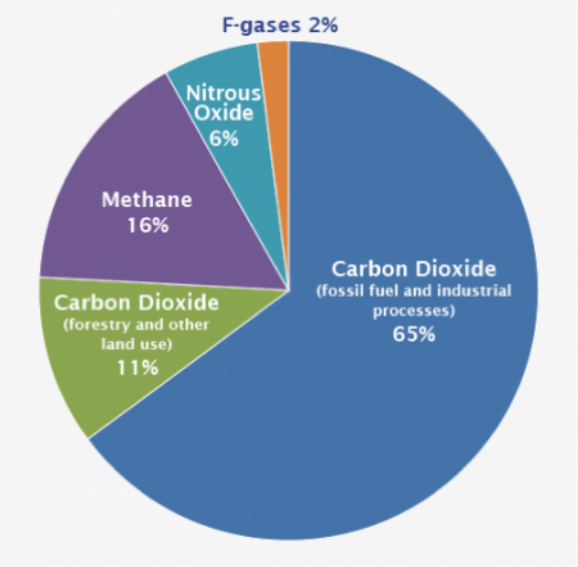

Fig 1.2: Global greenhouse gases emission sorted by gas. Taken from International Panel on Climate Change 2014 meeting [5].

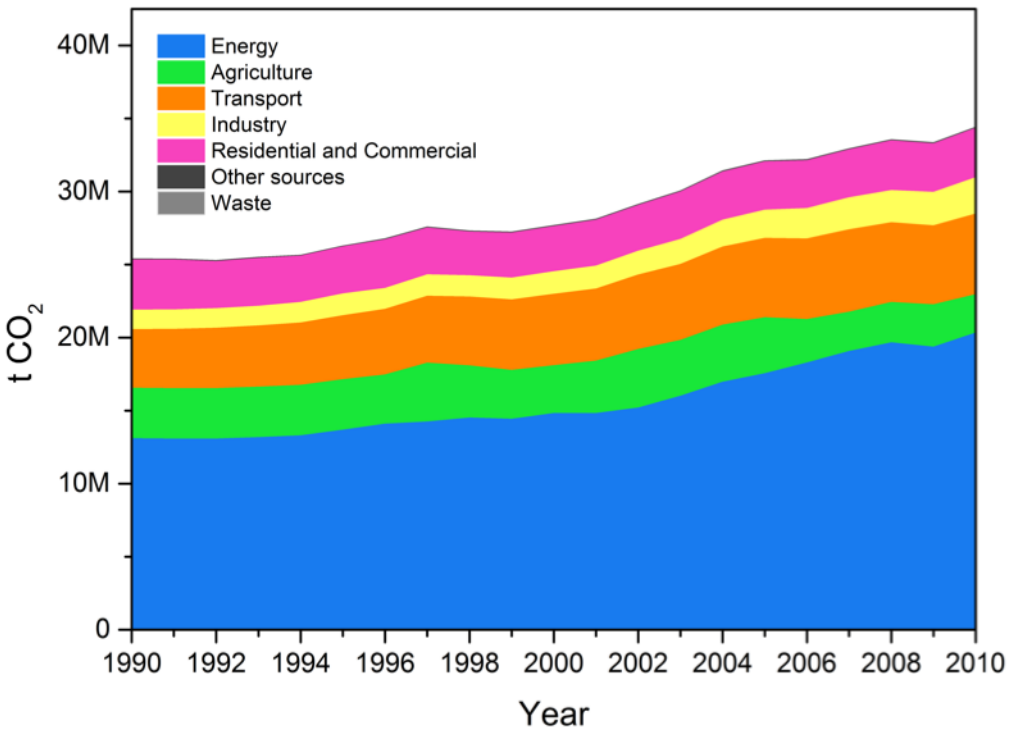

Fig 1.3: CO_2 production (in millions of tons) per year as a function of the sector. Drawn from data taken from [6].

Considering all the greenhouse gases as a function of the sector responsible for their emission, the main sources of anthropogenic pollution are agriculture and energy conversion processes (i.e. combustion), and both of them play a crucial role in human life. Focusing on the latter, figure 1.3 shows that energy conversion accounts for more than half of the CO_2 production.[6] Moreover, this sector is responsible for about half of the methane released in the atmosphere and has a non-negligible role (with an impact which is more than 1000 times higher than transportation) in nitrous oxide emissions. It is thus evident that, while in the case of agriculture emissions are the product of millennia-consolidated biochemical mechanisms, the variety of available possibilities for energy harvesting and the continuous development of new technologies call for an action in this direction. More concretely, with a constantly increasing energetic demand, a more resolute shift to renewable sources is required.

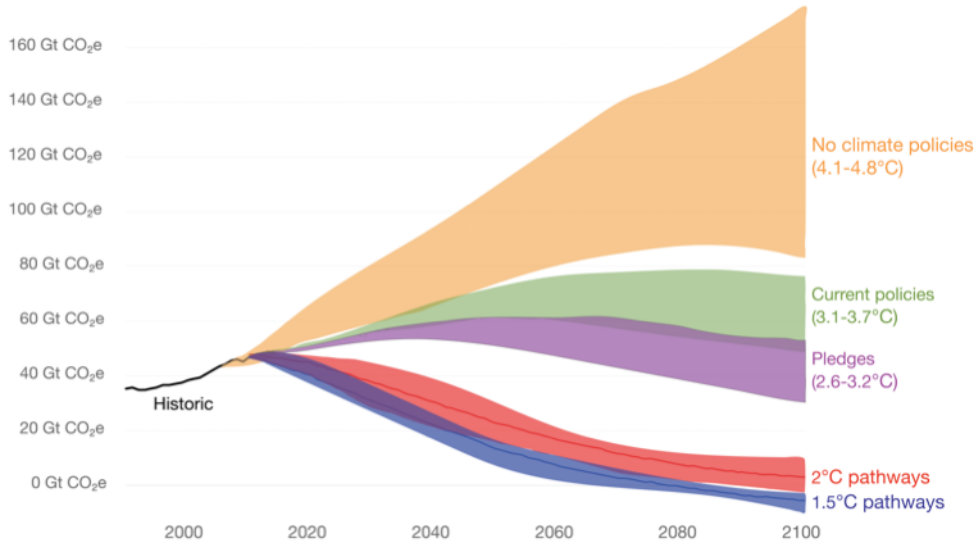

Fig 1.4: Representation of the possible scenarios for temperature increase as a function of years, projected as a function of the amount of CO_2 released per year. The curves are calculated on the base of the temperature increase with respect to the level before industrial revolution. Taken from [7], who elaborated it from [2].

Figure 1.4 pictures the possible scenarios for temperature increase in the upcoming years, as a function of the adopted politics on greenhouse gases emissions.[7] It can be observed that, besides being applied immediately, the effect of the more stringent politics is evident in the long time. This remarks the importance of short term interventions aiming at improving the actual energy conversion processes and reducing as much as possible emissions by the use of closed CO_2 cycles, i.e. avoiding producing new pollutants by consuming new fossil fuels. For this purpose, in the last years many strategies have

emerged concerning Carbon Capture and Storage (CCS) or Carbon Capture and Utilization (CCU).[8,9] These aim at obtaining a concentrated stream of CO_2 from combustion processes in order to store it easily or using it as reactant. In this frame, the concept of CO_2 valorization through conversion represent an interesting perspective, allowing to transform a pollutant and waste byproduct to valuable chemical or fuel.

This approach could impact positively on the carbon balance, in fact if CO_2 is reused for the production of fuels (exploiting energy coming from renewable sources and the electrolysis process, as an example) and subsequently stocked, this could create a close circle with a lower net CO_2 impact on the atmosphere.[10]

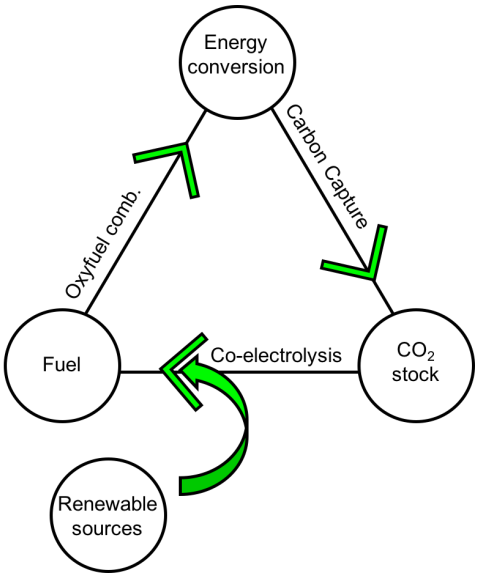

Fig 1.5: Representation of a possible path for the closed CO_2 cycle.

Aiming at a more efficient and sustainable energy production, it becomes evident that combustion related technologies are easy to manage and convenient as long as fossil fuels prices do not run out or become very expensive, but at the price of high CO_2 emissions. In fact, fossil fuel plants are far from being efficient. A first and relevant cut of the energy extracted from combustion is taken away by Carnot's law, which sets an intrinsic limit to this processes before they start. About half of the fuel's energy potential is converted in heat and, besides being recoverable in co-generation cycles, heat is the least efficient form for energy transmission. This means that, besides incomplete fuel utilization, a high amount of fuel is wasted, with the consequence that the production of CO_2 is related to a low value product.

1.2 Fuel cells

An interesting alternative to combustion processes is offered by fuel cells, which are electrochemical devices in which the chemical energy of a fuel is directly converted into electricity without intermediate steps. The working principle of fuel cells resembles the case of batteries, having an anode, electrolyte and cathode with a flow of charges between the two electrodes, but the main difference is that fuel cells are open systems, so they can virtually work for as long as they are fed with reactants.

The origin of fuel cells dates back to 1838-1839 and is due to the joint discoveries of Friederich Schönbein and William Robert Grove, with the former identifying their working principle and the latter observing an electric current between two platinum electrodes immersed in sulphuric acid and separately exposed to hydrogen and oxygen atmospheres.[11]

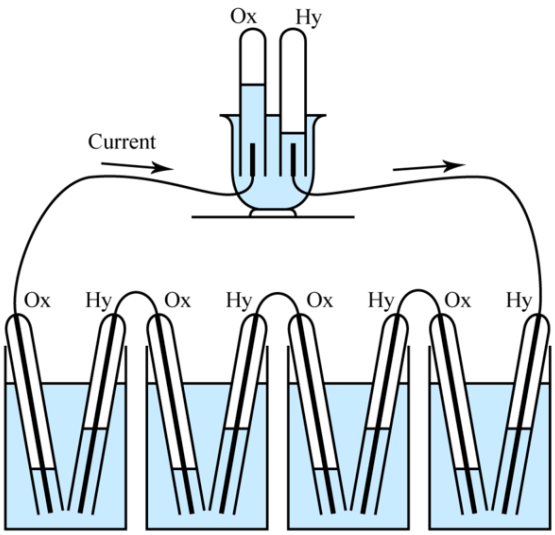

Fig 1.6: Scheme of Grove's cell. Taken from [11]

Despite their discovery dates back to the first half of 1800, the real development of fuel cell's technology did not occur until a century later, with Francis Bacon's alkaline cell running a cell on pure O_2 and H_2 using nickel catalyst. The first solid oxide fuel cell is due to Emil Baur and Hans Preis in 1930, who tested different electrolyte materials, finding the suitability of the so-called "Nernst-Masse" a compound made of 85% ZrO_2, 15% Y_2O_3 discovered in 1899 by Nernst and used at the time as glower in lamps.[12] A consistent

impulse to the development of this technology came also from space programs, making use of polymer electrolyte fuel cells in the beginning and then shifting to the more consolidated alkaline cells for the Apollo missions.[13]

What is notable is that, pushed by the need for addressing the two major issues of these devices, *i.e.* having a good catalytic activity and availability and the problem of handling hydrogen, researchers explored towards different directions, with the result that along the years several technological solution for the use of fuel cells were produced:

- Polymer electrolyte membrane fuel cells (PEM)
- Phosphoric acid fuel cells (PAFC)
- Alkaline fuel cells (AFC)
- Molten carbonate fuel cells (MCFC)
- Solid oxide fuel cells (SOFC)

The classification of FC can be made according to their working principle or to the working temperature: the first three kinds are considered as low-temperature operating fuel cells, the last two are commonly ascribed into the intermediate/high temperature range.

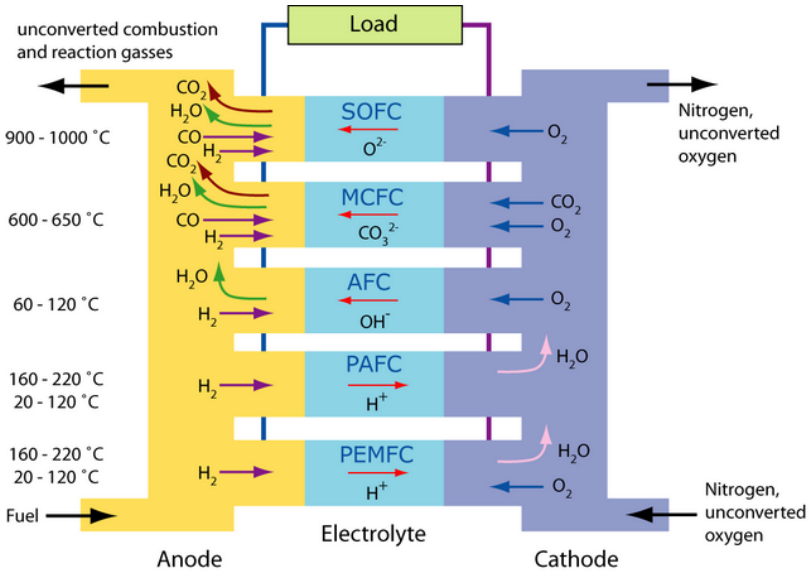

Fig 1.7: Schematic representation of the different kinds of fuel cells, including working temperature range, fuels and transported species through the electrolyte. Taken from [13]

Here their working principles, advantages and disadvantages are briefly described.

1.2.1 Polymer electrolyte membrane fuel cells (PEM, PEMFC)

Polymer electrolyte membrane fuel cells (PEMs) are based on a polymeric membrane carrying protons from the anode to the cathode. The semi-reactions at the electrodes anode and the catode are, respectively:

$$2H_2 \rightarrow 4H^+ + 4e^- \qquad \text{(A)}$$

$$O_2 + 4H^+ + 4e^- \rightarrow 2H_2O \qquad \text{(C)}$$

The protonic conductivity is achieved using a humidified Nafion® membrane (Dupont), a PTFE-derived polymer with sulfonic termination giving protonic conduction properties. Platinum dispersed on carbon black is used as catalyst at both the electrodes.
The main advantage related to this configuration is the short start-up time due to the low temperature of exercise, making them extremely suitable for mobile application and use in vehicles. However, at this temperature platinum is very sensitive to poisoning phenomena (for example from CO), requiring an absolute purity of the fed reactants.
Additionally, the so-called direct methanol fuel cells (DMFCs) also belong to this family. In these configuration methanol is used as fuel, with the advantage of an easier manageability with respect to hydrogen, without requiring for an external reforming stage, for this reason it is called “direct”.[11]

1.2.2 Phosphoric Acid fuel cells (PAFC)

Phosphoric Acid fuel cells (PAFCs) have many aspects in common with PEMs: they both are based on protonic conduction through the electrolyte, for which in this case liquid phosphoric acid is used, and deploy dispersed noble metal catalyst (typically platinum) at the electrodes. The semi-reactions at the electrodes are the same as in the case of PEMs:

$$2H_2 \rightarrow 4H^+ + 4e^- \qquad \text{(A)}$$

$$O_2 + 4H^+ + 4e^- \rightarrow 2H_2O \qquad \text{(C)}$$

In order to have a good protonic conductivity, PAFCs work at 200 °C. This brings the extra benefit that platinum at this temperature is not sensitive to poisoning anymore, simplifying the feeding system. On the other hand the management of the electrolyte, which beside being hazardous requires a constant monitoring of the level of water to avoid dilution, represents the most cumbersome aspect of this technology, which is preferred for stationary application.

1.2.3 Alkaline Fuel Cells (AFC)

Alkaline Fuel Cells (AFCs) have in common the concept of liquid electrolyte with PAFCs, which in AFCs it is dispersed into a porous matrix. Their conduction relies on hydroxides species and an alkaline solution (typically KOH) is used as electrolyte, as the alkaline ambient was found to favor the oxygen reduction reaction. Nickel based catalysts (like Raney metals) are used at the electrodes. The semi-reactions occurring at the electrodes are:

$$2H_2 + 4OH^- \rightarrow 4H_2O + 4e^- \qquad \text{(A)}$$

$$O_2 + 2H_2O + 4e^- \rightarrow 4OH^- \qquad \text{(C)}$$

The advantages of using an alkaline electrolyte are due to the relative low cost of the components and the good efficiency of these cells. However, since the system is irreversibly damaged in presence of CO_2, a separated filtering stage for the purification of air is required. Moreover, as in the case of PAFCs, the management of water in the electrolyte is essential, to avoid dilution phenomena. Often these drawback induce PEMs to be preferred for the easier system manageability.

1.2.4 Molten Carbonate Fuel Cells (MCFC)

In Molten Carbonate Fuel Cells, the electrolyte is made of a mixture of liquid alkaline carbonates (lithium and sodium, or lithium and potassium) retained in a ceramic matrix.

These cells are operated at 600 °C, the temperature at which the carbonates form a highly conductive molten salt. Unlike other kinds of fuel cells CO_2 is not detrimental to the device, but is an essential reactant to be fed at the cathode together with oxygen. Since they perform at high temperature, metallic nickel and nickel oxide can be used at the electrodes. The semi-reaction occurring at the anode and the cathode are respectively:

$$2H_2 + 2CO_3^{2-} \rightarrow 2H_2O + 2CO_2 + 4e^- \qquad \text{(A)}$$

$$2CO_2 + O_2 + 4e^- \rightarrow 2CO_3^{2-} \qquad \text{(C)}$$

A strength point of this configuration is that at the working temperature reforming processes could happen without the requirements of an external stage, allowing a wide variety of fuels to be used. Moreover, in such a scenario the produced CO_2 can be transferred to the cathode and be reused.
MCFCs are typically used in stationary plants for large scale energy production.

1.2.5 Solid Oxide Fuel Cells (SOFC)

Solid Oxide Fuel Cells (SOFCs) are based on a ceramic electrolyte and unlike the other kinds of fuel cell, do not necessitate of any liquid management. They are typically operated at high temperature, in the range between 800 and 1000 °C, to overcome the high energy barrier associated with ionic conduction, as the state of the art material for the electrolyte is Yttrium Stabilized Zirconia (YSZ), which displays a 0.02 $S \cdot cm^{-1}$ conductivity at 800 °C.[14] In these working conditions the use of noble metals-based catalysts is not necessary, therefore a Ni-cermet (made of reduced and connected nickel particles mixed with the electrolyte) is typically used at the anode.[15] Moreover, since the temperature is high enough for internal reforming to occur, SOFCs can run on a variety of different fuels at the anode without the need for a separate reforming stage.[16–18] A perovskitic oxide ($La_{0.8}Sr_{0.2}MnO_3$, LSM) mixed with the electrolyte is used as cathode.
During the operation of the cell, air is fed at the cathode, where oxygen is reduced and incorporated as oxygen ion (O^{2-}) and then is transported through the vacancies of the

electrolyte to the anode, where it can react with the fuel. The two semi-reactions at the cathode and at the anode are, respectively:

$$2H_2 + 2O^{2-} \rightarrow 2H_2O + 4e^- \qquad \text{(A)}$$

$$O_2 + 4e^- \rightarrow 2O^{2-} \qquad \text{(C)}$$

Compared to other fuel cells, SOFCs are the ones displaying the highest efficiency, being typically around 60% for low heat value, with Chinese SOFCMAN reporting values up to 72 %.[19] When these are coupled with co-generation plants, the overall efficiency can easily reach 80-90 %,[20] with lower emission of CO_2 and NO_x than traditional systems.

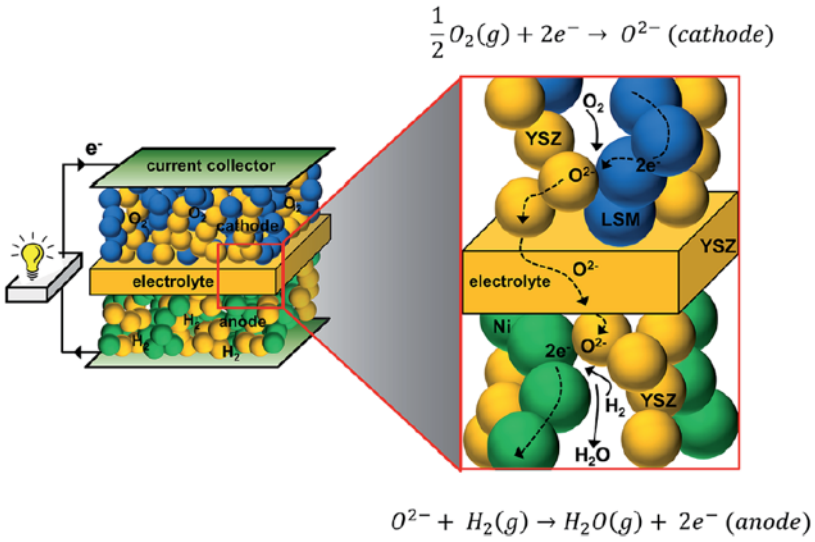

Fig 1.8: Schematic working representation of in a state of the art SOFC fed with hydrogen and air. Taken from [15]

Despite their high efficiency, one of the main issues limiting to the diffusion of SOFCs is the cost and expected lifetime of these devices. Both of them are a direct consequence of the high temperature at which fuel cells operate, limiting the choice of the suitable materials and shortening the lifetime of the components due to interdiffusion, kinetic-demixing and other degradation phenomena.[21,22] Therefore lowering the working temperature would result in the availability of a wider range of materials and minor degradation effects. On the other hand, reducing the working temperature arises a non-negligible drawback, as the conductivity of the electrolyte is expected to decrease and the

kinetics at the electrodes to be slowed down, especially at the cathode.[23–25] For this reason new cathodes with high mixed ionic and electronic conductivity at intermediate temperature have been investigated.

Concerning the electrolyte, in order to keep the same performances and efficiency different strategies can be pursued: finding new suitable materials,[26,27] interfacing nanostructures[28,29] or reducing the thickness of the layer so that the ohmic losses are reduced.[30,31]

The last strategy arises from the fact that a cell's electrolyte is a pure ohmic element and ohmic losses are directly proportional to the thickness. This implied the shift from 1st generation fuel cells (electrolyte supported) to 2nd generation cells (anode supported). Nonetheless, reducing the thickness of the electrolyte is a challenging operation, since the electrolyte is responsible for the gas tightness between the two sides of the cell. For this reason, despite GDC having a higher ionic conductivity which would allow an use at lower temperature, often YSZ is still preferred for its stability. In fact above 600 °C in reducing conditions the formation of Ce^{3+} occurs, leading to two major drawbacks: unit cell volume expansion and electrical losses shorting the cell.[32,33]

A more recent architecture of fuel cells involves the use of a double-layered electrolyte made of YSZ/GDC which ensures a pure ionic conductivity and prevents reaction with the cathode.[34,35]

1.3 Carbon capture, storage and utilization

As observed before, besides the research for smarter strategies for more efficient energy conversion processes, a short term intervention is required in order to reduce CO_2 emissions and counter the climate change.[1]

Despite the huge efforts for achieving large scale production from renewable sources, the market of energy still relies on fossil power plants, which represent a major source for energy conversion and consequently anthropogenic CO_2 production. This highlights the importance of finding a solution for sequestering CO_2 before it is released in the atmosphere. This can be done, for example, by Carbon Capture and Utilization (CCU) or Carbon Capture and Storage (CCS) technologies.[10]

Independently from the final purpose of CO_2, the first step is the same whether CCS or CCU are considered, and it consists in targeting CO_2 before it is released in the atmosphere. Currently, three kind carbon capture technologies are available:

- Pre-combustion capture;
- Post-combustion capture;
- Oxy-fuel combustion capture.

Pre-combustion methods refer to a capture of CO_2 obtained as a byproduct of a fuel conversion process not involving combustion. This is the case of steam reforming or integrated gasification combined cycles, as an example, which aim to obtaining hydrogen as fuel to be burned and need for a removal of carbon dioxide. In this case the capture is typically achieved by the use of physical solvents, like in selexol® (making use of a mixture of dimethyl ethers and polyethylene glycols) and rectisol® (exploiting cold methanol) processes. The advantage of this strategy is that physical solvents can strip a variety of undesired gases (including SO_x) from the combustion flue stream and these can be further separated, nonetheless it's expensive due to the necessary regeneration step.[36]

On the contrary of the aforementioned, post-combustion techniques target the CO_2 that is formed when the combustion process is completed. This can be achieved using different methods, including adsorption in solvent, adsorption by solid sorbents (including porous

organic frameworks), use of membranes, cryogenic separation, pressure and vacuum swing adsorption.

Among them, the use of chemical solvents is the most widespread. These are typically amines, of which monoethanolamine (MEA) is the most commonly used.

A critical issue of post-combustion techniques is the regeneration step, which is even more expensive than in the case of pre-combustion. In fact, chemical solvents need to be heated in order to be regenerated and this operation can impact on the total cost of separation. Moreover, the release of toxic gases coming from the decomposition of amines due to heating should be taken in account.[37]

Oxy-fuel combustion differs substantially from the other two techniques since it aims at avoiding a separation stage for CO_2. This is achieved if a stream of highly concentrated and pure CO_2 is obtained from combustion. Therefore the target of oxy-fuel process is the combustion process itself, and consists in providing a flux of pure oxygen as combustive agent, obtaining as products of combustion only CO_2 and water.[38,39]

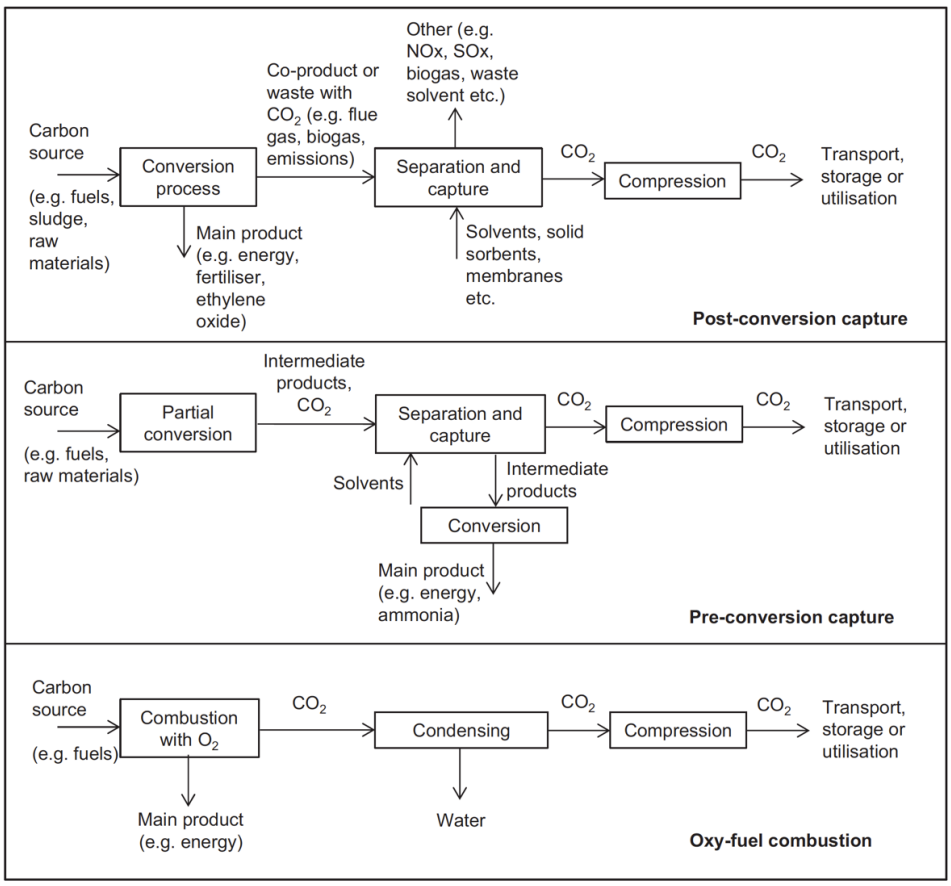

Fig 1.9: Schematic description of the carbon capture processes. Taken from [10]

After capturing CO_2, two possible alternatives exist: storing it (CCS) or making use of it (CCU) as a precursor for the production of new chemicals.

Carbon Capture and Storage (CCS) consists in compressing the captured CO_2 and then shipping it to be stored in the ground, ocean pavement or as mineral carbonate. The former and more widespread option consists into injecting the CO_2 deep into the soil, exploiting depleted gas or oil reservoirs as storing facilities. Carbon dioxide is then trapped under the soil through impermeable rocks (like shales or clays) which prevent the fugue of the gas. Despite being an interesting possibility, that could rely on the vast experience of oil and gas industries about extraction, storage has some major drawbacks. In principle, CO_2 is treated as a problem and no profit is obtained from it. This would discourage investors and limit the development of this kind of technology. But, even more relevant from the environmental point of view is the fact that CO_2 reservoirs in the ground may be subjected to geological phenomena, which may change the conformation of rocks and consequently cause an abrupt release of large amount of CO_2 in the atmosphere.

Last but not least, CCS represents an open cycle, which does not prevent the formation of new CO_2.

As an alternative to storage, Carbon Capture and Utilization (CCU) aims at giving a new life to carbon dioxide through usage in industrial applications or in the production of new chemicals and fuels.[40] This last option is especially interesting, because aims at creating a close circle which does not require the consume of new fuels for energy production and the consequent release of new CO_2 in the atmosphere, but balances the two.[41] CO_2 can not only be used as industrial additive, but even be processed through different techniques in order to obtain valuable products.

1.4 The role of oxygen transport membranes in Carbon Capture and Utilization or Storage

It is evident that one of the critical issues for CO_2 capture-related technologies is obtaining a CO_2-rich flow to be handled without the need for separate filtering stages. This is possible in the case in which pure oxygen is fed for combustion instead of air and the process is known as oxy-fuel combustion. As an additional advantage arising from the removal of nitrogen from the combustion atmosphere, nitrogen oxides are not formed.[42]
A major cost, both from financial and energetic perspective, in oxy-fuel technology is related to the need to supply large quantities of pure oxygen at the combustion stage. Being the only large scale method available for industrial supplies, this typically achieved using oxygen produced by cryogenic distillation of the air. In this method, air separation units (ASUs) cool a stream of air at a temperature at which oxygen liquefies to separate it. Despite producing a stream of pure O_2, this technique is expensive and energy consuming.
An alternative approach allowing to make the production of pure oxygen more sustainable consists in using oxygen transport membranes (OTMs). These are dense and gastight ceramic membranes displaying mixed ionic and electronic conductivity (MIEC) which are capable of transporting oxygen from a high pO_2 side (called feed) to a low pO_2 side (called permeate).
Unlike solid oxide electrolytes, where the driving force for oxygen ions migration is provided by an external electromotive force, in mixed conductivity membranes the driving force for the conduction of oxygen is represented by the oxygen chemical potential gradient between the two sides of the membrane.[43]

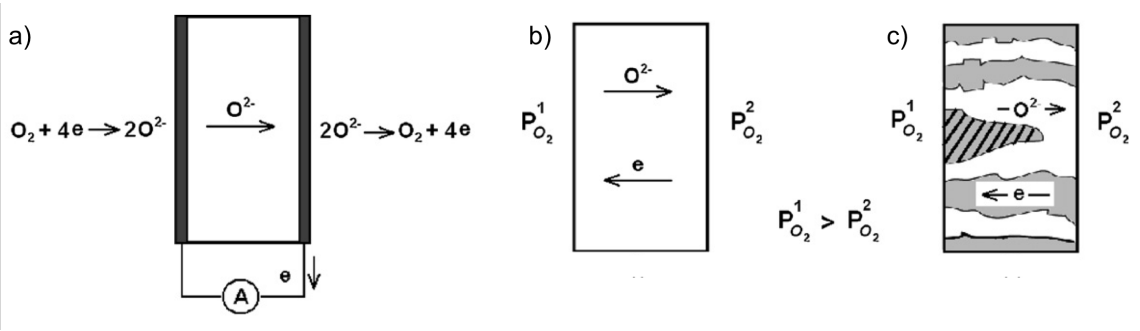

Fig 1.10: Representation of an oxygen permeation membrane driven by electromotive force (a) and pressure gradient in the case of a mixed ionic and electronic conductor (b) and mixed transport obtained by mixing an electronic conductor and an ionic conductor (c). Taken from [43]

In the case of fast surface exchange, the oxygen flux through a permeation membrane is described by Wagner's equation:

$$J_{O_2} = \frac{RT}{16F^2L}\int_{p_{O_2}^{permeate}}^{p_{O_2}^{feed}} \frac{\sigma_{el}\sigma_{ion}}{\sigma_{el}+\sigma_{ion}}\left(p_{O_2}\right) d\ln p_{O_2} \qquad (1)$$

where J_{O_2} is the oxygen permeation flux (mol·m^{-2}·s^{-1}); R and F are the gas and Faraday's constants, respectively; L is the membrane thickness (m); σ_{el} and $\sigma_{ion}$are the electronic and the ionic conductivities (S·m^{-1}), respectively; and $p_{O_2}^{feed}$ and $p_{O_2}^{permeate}$ are the oxygen partial pressures (atm) at the high pressure side and at the low pressure side, respectively.[44] Air or pure oxygen can be used at the feed side, while a variety of sweep gases can be used at the permeate side, like N_2, CO_2, Ar or He.

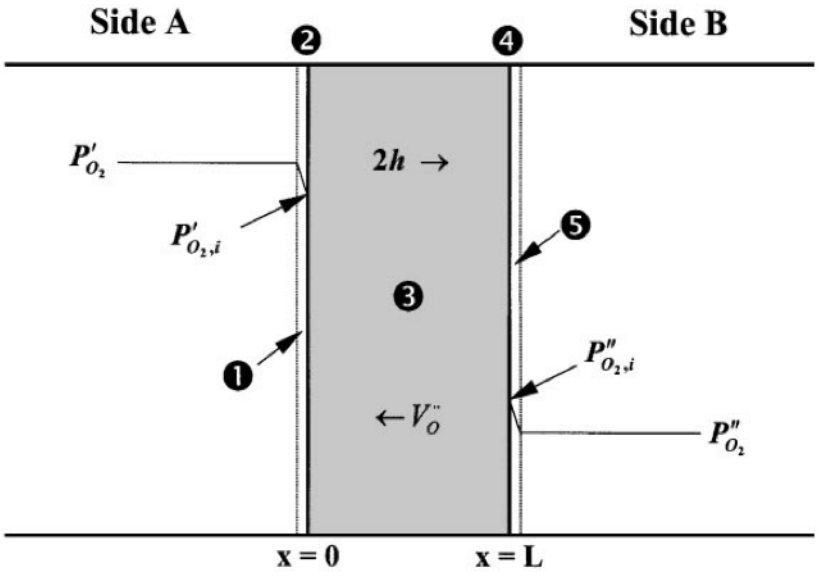

Fig 1.11: Oxygen transport mechanism through a permeation membrane: 1) gas diffusion at high pO_2 side; 2) surface reaction and oxygen incorporation in the membrane; 3) bulk transport; 4) surface reaction at low pO_2 side and oxygen release; 5) gas diffusion and oxygen removal by sweep gas. Taken from [45]

The transport of oxygen through a permeation membrane involves different steps: I) molecular oxygen diffusion from the gas stream to the surface of the membrane II) surface exchange reaction occurring at the high pO_2 surface of the membrane, which includes oxygen adsorption, reduction, dissociation and incorporation in the lattice; III) simultaneous bulk diffusion of oxygen ions and charged species (electrons or holes) into

the dense membrane; IV) Surface exchange reaction occurring at the low pO2 surface of the membrane, including the oxidation and recombination of transported oxygen ions and desorption of molecular oxygen; V) molecular diffusion of oxygen from the membrane surface to the sweep gas stream. Typically in a 1 mm thick membranes the influence of steps I) and V) is so small compared to the other contributions that can be considered negligible.[45]

When the thickness of the membrane is in the range of 300 μm or higher, the oxygen transport is mainly limited by bulk diffusion and the Wagner equation can be rewritten as:

$$J_{O_2} = \frac{RT}{16F^2L}\int_{p_{O_2}^{permeate}}^{p_{O_2}^{feed}} \frac{\sigma_{el}\sigma_{ion}}{\sigma_{el}+\sigma_{ion}}\left(p_{O_2}\right)dlnp_{O_2} \qquad (2)$$

The conductivity expression in () can be rewritten as follows:

$$\sigma_{amb} = \frac{\sigma_{el}\sigma_{ion}}{\sigma_{el}+\sigma_{ion}} = \frac{\sigma_{el}\sigma_{ion}}{\sigma_{total}} = t_{ion}\sigma_{el} = t_{el}\sigma_{ion} \qquad (3)$$

Where σ_{amb} (S·cm^{-1}) is the ambipolar conductivity and t_{ion} and t_{el} represent the transference number for ionic and electronic conduction, respectively. In the case of a mixed ionic and electronic conductor, the electronic conductivity is the dominating contribution to the ambipolar conductivity ($\sigma_{el} \gg \sigma_{ion}$) and the value of the transference number t_{el} is close to unity. The expression for the oxygen flow can thus be rewritten as:

$$J_{O_2} = \frac{RT}{16F^2L}\int_{p_{O_2}^{permeate}}^{p_{O_2}^{feed}} \sigma_{ion}\left(p_{O_2}\right)dlnp_{O_2} \qquad (4)$$

And highlights the importance of finding materials having a high ionic conductivity.

On the contrary, for thin membranes the surface exchange reaction becomes the limiting step in oxygen transport and Wagner equation can be rewritten introducing the critical thickness parameter, firstly defined by Bouwmeester and Burgraaf:[46]

$$J_{O_2} = -\frac{1}{1+\frac{2L_C}{L}}\frac{RT}{16F^2L}\int_{p_{O_2}^{permeate}}^{p_{O_2}^{feed}}\sigma_{ion}\left(p_{O_2}\right)dlnp_{O_2} \qquad (5)$$

Where L_C is:

$$L_C = \frac{D_S}{k_s} \qquad (6)$$

And D_S and k_s are the self-diffusion coefficient and the surface exchange coefficient of oxygen. Both of them can be determined by isotopic exchange measurements.

It worth remarking that L_C should not be considered as an intrinsic property of the material, since it is affected by a wide range of experimental conditions like temperature, pO_2 gradient and surface roughness and porosity.

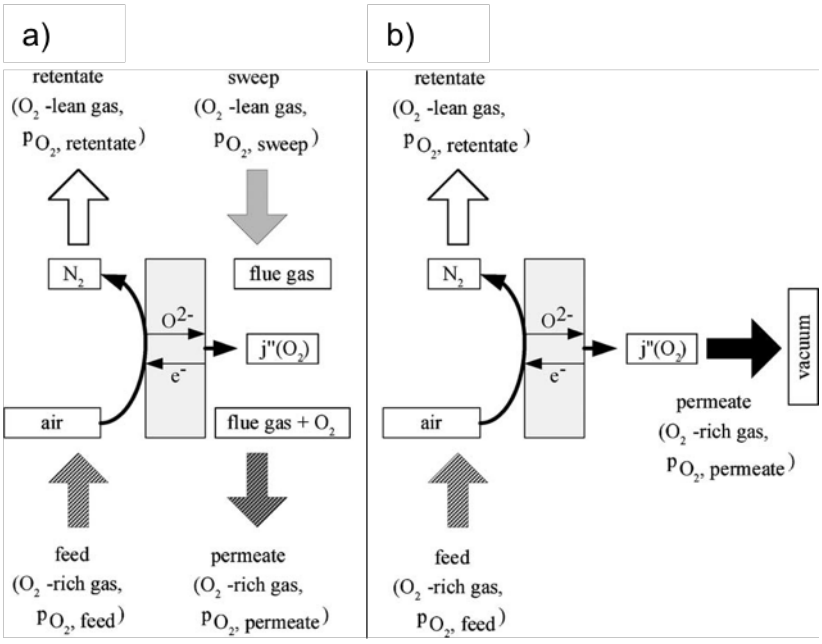

Fig 1.12: Four-end (a) and three-end (b) configuration for the integration of an oxygen permeation membrane in oxy-fuel combustion process. Taken from [47]

Oxygen transport membranes can be integrated in oxyfuel plants following two different approaches, called three-end and four-end, respectively.[47] These configurations can be distinguished according to two criteria: the operation mode (i.e. if the gradient is created by vacuum or using a sweep gas) and their integration (i.e. if they require or not a separate heating stage). The three-end mode is also called indirect configuration, because the

produced oxygen is not directly in contact with the flue gas in the combustion process and thus requires a vacuum stage for removal of oxygen from the membrane. The oxygen is then separately mixed with the flue gases in a second stage. The four end mode is also called direct configuration, because the produced oxygen is directly removed on the permeate side by the flue gases stream, so that no additional pumping stage after permeation is required and oxygen is used immediately in combustion. This implies that the four-end mode is more energetically efficient and could be thermally integrated with the combustion plant, without requiring a separate heating stage.
Despite being more energetically efficient, four-end mode exposes the membrane to more harsh conditions, including a high amount of CO_2, steam and other pollutants like SO_2, which could accelerate degradation phenomena.

At the moment, oxygen transport membranes are not integrated in industrial processes for energy production yet. One of the main challenges to address is obtaining materials coupling high permeability and stability, especially in critical atmospheres. So far, the most stable materials show a modest oxygen flux at high temperature. These oxides display a good tolerance to CO_2 containing environments, but do not have sufficient ionic or electronic conductivity to grant high flux of oxygen. On the contrary, materials like $Ba_{0.5}Sr_{0.5}Co_{0.8}Fe_{0.2}O_{3-\delta}$ (BSCF) or $La_{0.6}Sr_{0.4}Co_{0.2}Fe_{0.8}O_{3-\delta}$ display high mixed conductivity properties and for this reason they have been widely investigated, but long term stability is still problematic. In particular for what concerns the former, extremely high fluxes have been observed, reaching 12.2 $mL_N min^{-1} cm^{-2}$ in air at 1000 °C,[48] but at the price of a low tolerance to CO_2 containing environments.[49]

1.5 The potential of solid oxide electrolysis in CO_2 utilization

As aforementioned, the sequestration of CO_2 should not disregard the utilization of carbon dioxide as precursor for the production of chemicals and fuels. What makes CO_2 utilization more interesting with respect to the storage option is the need for efficiently storing the excess of energy produced by discontinuous renewable sources, and the valuable use of CO_2, which could further drive the development of the technology.[50]

The choice of utilizing energy produced from renewable sources for CO_2 reduction process is the most reasonable, in fact it would produce a positive balance in the whole process, or at least a closed loop. Moreover, this could offer a solution in case of an excess of energy production from discontinuous sources, which could be converted during the harvesting peaks and subsequently consuming the fuel used when is necessary.

For making CO_2 valuable it is necessary to reduce it and this can be achieved through different techniques making use of thermochemical,[51–53] electrochemical[54–56] or photochemical methods;[57,58] biotechnological methods involving algae are also under development.[59]

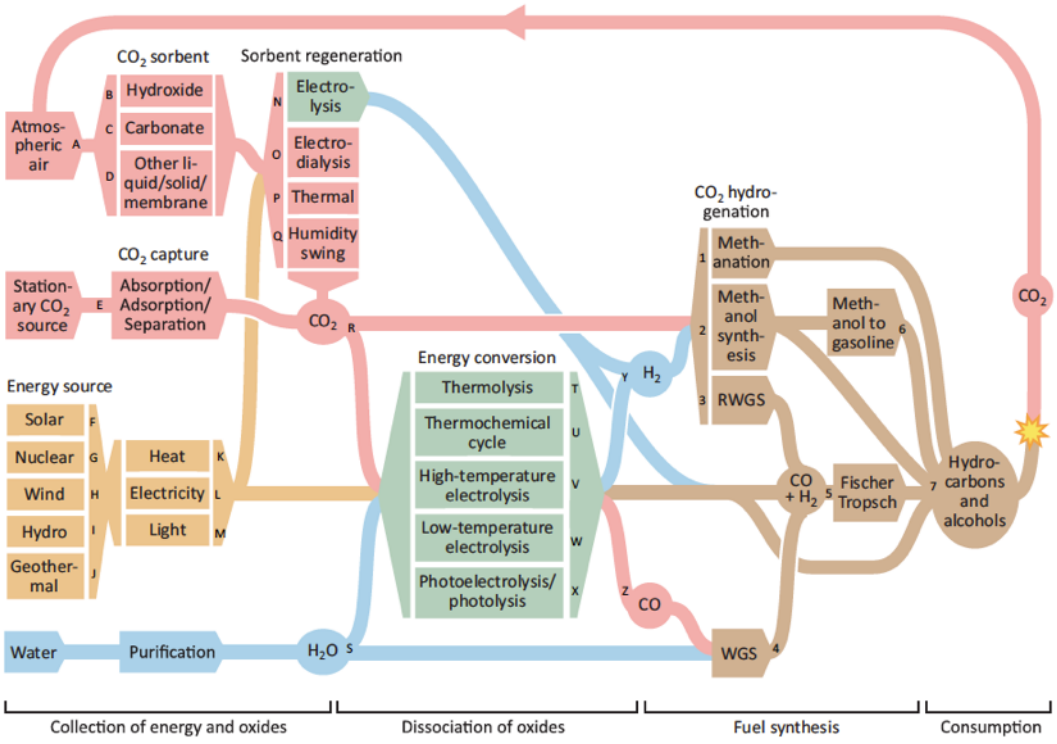

Fig 1.13: A scheme of the possible pathways from CO_2 capture to the production of synthetic fuels. Taken from [41]

Among the available techniques for CO_2 reduction, electrolysis is particularly appealing since no movement of mechanical parts is involved in the reduction process (as for example occurs in thermolysis and thermochemical cycles for capturing the maximum sun's intensity), does not manage liquids and this solution provides a high flexibility, because electrolysis allows to directly tune the rate of reaction by controlling the applied current.

Solid Oxide Electrolysis Cells (SOECs) have been first reported in 1967 by Spacil and Tedmon and water electrolysis was designed for producing oxygen during space travels,[60] in the case of CO_2 the concept of electrolysis for the production of fuels was introduced later by Isenberg in 1981.[61] Though the interest in SOECs has been growing just recently, electrolysis technology has indirectly benefitted of the intensive investigation on fuel cells in the last 40 years, since the working principle behind it is very similar to the case of a fuel cell. Before looking at it is worth saying that since in electrolysis mode the polarity of the electrodes is reversed with respect to a fuel cell, their name is switched too and, to prevent confusion between the two working modes which have opposite nomenclature, often the electrodes are simply called fuel electrode (i.e. the fuel cell anode, electrolyzer cathode) and air electrode (i.e. the fuel cell cathode, electrolyzer anode).[62]

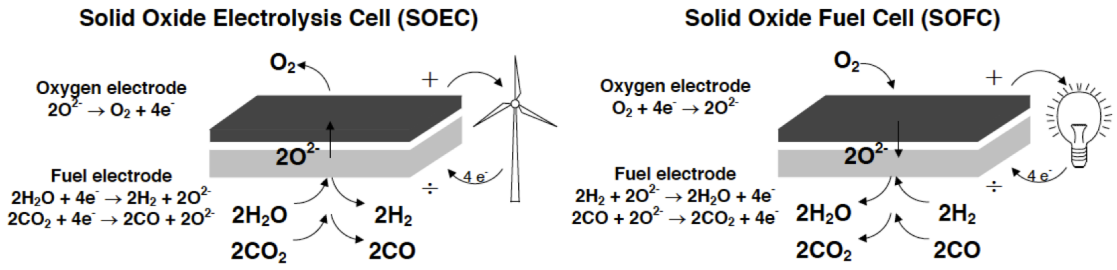

Fig 1.14: Representation of the working mode of a solid oxide electrolysis cell and a solid oxide fuel cell. Taken from [62]

In electrolysis mode, fuels are provided at the fuel electrode, where they are reduced and the produced oxygen ions are carried through the electrolyte reaching the air electrode, where they recombine to molecular oxygen and are released as gas.

The difficulty in the reduction process lies in the high stability of CO_2 (ΔG_f^0= -396 kj/mol) which requires a high energetic input to be performed. This can be reduced when the process is coupled with water in the co-electrolysis process. As an additional benefit, in

presence of water the formation of carbon is hindered, impurities in the feed gas are more easily removed and, above 830 °C, reverse water gas shift reaction can push towards higher CO_2 conversion.[63,64]

The semi-reactions occurring at the electrodes of a SOEC during co-electrolysis are:

$$2O^{2-} \rightarrow O_2 + 4e^- \qquad \text{(A)}$$

$$H_2O + 2e^- \rightarrow H_2 + O^{2-} \qquad \text{(C)}$$

$$CO_2 + 2e^- \rightarrow CO + O^{2-} \qquad \text{(C)}$$

The chemical reactions of reverse water gas shift (above 827 °C) and methanation can also taking part into the processes occurring at the nickel electrode.

Despite being extremely appealing, SOECs are further from commercialization than SOFCs and this is mainly due to harsher degradation phenomena. They are subjected to electrode delamination due to the formation of oxygen bubbles in the electrolyte near the interface, demixing of air electrode materials and migration and coarsening of nickel at the fuel electrolyte in presence of high pO_2, as an example.[65–68]

Recently, the concept of Solid Oxide Reversible Cells (SORCs) has been proposed and consists of using the same device by alternating between fuel cell and electrolysis cell working mode. The cell can thus be operated in either one working mode or the reverse according to the applied potential and the kind of reactants fed at the electrodes. It has been demonstrated that cycling between fuel cell operation and electrolysis operation is an effective strategy for eliminating degradation occurring in electrolysis mode, even working at high currents (1 A).[69]

Bibliography

1 S. Solomon, G.-K. Plattner, R. Knutti and P. Friedlingstein, *Proc. Natl. Acad. Sci.*, 2008, **106(6)**, 1704–1709.

2 Climate Action Tracker Emission Gaps, https://climateactiontracker.org/global/cat-emissions-gaps/, (accessed 28 September 2018).

3 Trends in Atmospheric Carbon Dioxide, https://www.esrl.noaa.gov/gmd/ccgg/trends/, (accessed 28 September 2018).

4 Scripps CO2 program.

5 International Panel on Climate Change, https://www.ipcc.ch/report/ar5/wg3/, (accessed 28 September 2018).

6 F. N. Tubiello, M. Salvatore, R. D. Cóndor Golec, A. Ferrara, S. Rossi, R. Biancalani, S. Federici, H. Jacobs and A. Flammini, *ESS Work. Pap. No.2*, 2014, **2**, 4–89.

7 H. Ritchie and M. Roser, CO2 and other Greenhouse Gas Emission, https://ourworldindata.org/co2-and-other-greenhouse-gas-emissions, (accessed 28 September 2018).

8 R. S. Haszeldine, *Science (80-.).*, 2009, **325**, 1647–1652.

9 A. J. Hunt, E. H. K. Sin, R. Marriott and J. H. Clark, *ChemSusChem*, 2010, **3**, 306–322.

10 R. M. Cuéllar-Franca and A. Azapagic, *J. CO2 Util.*, 2015, **9**, 82–102.

11 J. Larminie and A. Dicks, *Fuel cell systems explained*, 2003.

12 T. Emil and H. Preis, .

13 U. of C. DoITPoMS, Fuel Cells, https://www.doitpoms.ac.uk/tlplib/fuel-cells/printall.php, (accessed 28 September 2018).

14 K. C. Wincewicz and J. S. Cooper, *J. Power Sources*, 2005, **140**, 280–296.

15 W. H. Kan, A. J. Samson and V. Thangadurai, *J. Mater. Chem. A*, 2016, **4**, 17913–17932.

16 Y. Jiang and A. V. Virkar, *J. Electrochem. Soc.*, 2001, **148**, A706.

17 T. Hibino, A. Hashimoto, M. Yano, M. Suzuki, S. Yoshida and M. Sano, *J. Electrochem. Soc.*, 2002, **149**, A133.

18 S. Park, J. M. Vohs and R. J. Gorte, *Nature*, 2000, **404**, 265–267.

19 M. Andersson and B. Sunden, *Technology Review – Solid Oxide Fuel Cell*, 2017.

20 A. Buonomano, F. Calise, M. D. d'Accadia, A. Palombo and M. Vicidomini, *Appl. Energy*, 2015, **156**, 32–85.

21 S. Badwal, *Solid State Ionics*, 2001, **143**, 39–46.

22 H. Yokokawa, H. Tu, B. Iwanschitz and A. Mai, *J. Power Sources*, 2008, **182**, 400–412.

23 E. D. Wachsman and K. T. Lee, *Science (80-.).*, 2011, **334**, 935–939.

24 Z. Gao, L. V. Mogni, E. C. Miller, J. G. Railsback and S. A. Barnett, *Energy Environ. Sci.*, 2016, **9**, 1602–1644.

25 A. Atkinson, S. Barnett, R. J. Gorte, J. T. S. Irvine, A. J. Mcevoy, M. Mogensen, S. C. Singhal and J. Vohs, *Nat. Mater.*, 2004, **3**, 213–223.

26 S. Sanna, V. Esposito, J. W. Andreasen, J. Hjelm, W. Zhang, T. Kasama, S. B. Simonsen, M. Christensen, S. Linderoth and N. Pryds, *Nat. Mater.*, 2015, **14**, 500–504.

27 F. Yang, H. Zhang, L. Li, I. M. Reaney and D. C. Sinclair, *Chem. Mater.*, 2016, **28**, 5269–5273.

28 Q. Su, D. Yoon, A. Chen, F. Khatkhatay, A. Manthiram and H. Wang, *J. Power Sources*, 2013, **242**, 455–463.

29 S. Lee, W. Zhang, F. Khatkhatay, H. Wang, Q. Jia and J. L. Macmanus-Driscoll, *Nano Lett.*, 2015, **15**, 7362–7369.

30 P. C. Su, C. C. Chao, J. H. Shim, R. Fasching and F. B. Prinz, *Nano Lett.*, 2008, **8**, 2289–2292.

31 H. S. Noh, K. J. Yoon, B. K. Kim, H. J. Je, H. W. Lee, J. H. Lee and J.-W. Son, *J. Power Sources*, 2014, **247**, 105–111.

32 H. L. Tuller and A. S. Nowick, *J. Phys. Chem. Solids*, 1977, **38**, 859–867.

33 D. Marrocchelli, S. R. Bishop, H. L. Tuller and B. Yildiz, *Adv. Funct. Mater.*, 2012, **22**, 1958–1965.

34 R. Knibbe, J. Hjelm, M. Menon, N. Pryds, M. Søgaard, H. J. Wang and K. Neufeld, *J. Am. Ceram. Soc.*, 2010, **93**, 2877–2883.

35 E. O. Oh, C. M. Whang, Y. R. Lee, S. Y. Park, D. H. Prasad, K. J. Yoon, B. K. Kim, J.-W. Son, J. H. Lee and H. W. Lee, *Ceram. Int.*, 2014, **40**, 8135–8142.

36 M. Kanniche, R. Gros-Bonnivard, P. Jaud, J. Valle-Marcos, J. M. Amann and C.

Bouallou, *Appl. Therm. Eng.*, 2010, **30**, 53–62.

37 M. Wang, A. Lawal, P. Stephenson, J. Sidders and C. Ramshaw, *Chem. Eng. Res. Des.*, 2011, **89**, 1609–1624.

38 T. Wall, Y. Liu, C. Spero, L. Elliott, S. Khare, R. Rathnam, F. Zeenathal, B. Moghtaderi, B. Buhre, C. Sheng, R. Gupta, T. Yamada, K. Makino and J. Yu, *Chem. Eng. Res. Des.*, 2009, **87**, 1003–1016.

39 G. Scheffknecht, L. Al-Makhadmeh, U. Schnell and J. Maier, *Int. J. Greenh. Gas Control*, 2011, **5**, 16–35.

40 B. Hu, C. Guild and S. L. Suib, *J. CO2 Util.*, 2013, **1**, 18–27.

41 C. Graves, S. D. Ebbesen, M. Mogensen and K. S. Lackner, *Renew. Sustain. Energy Rev.*, 2011, **15**, 1–23.

42 Environmental Protection Agency (EPA), *Nitrogen oxides (NOx), why and how they are controlled*, 1999.

43 J. Sunarso, S. Baumann, J. M. Serra, W. A. Meulenberg, S. Liu, Y. S. Lin and J. C. Diniz da Costa, *J. Memb. Sci.*, 2008, **320**, 13–41.

44 S. M. Hashim, A. R. Mohamed and S. Bhatia, *Adv. Colloid Interface Sci.*, 2010, **160**, 88–100.

45 S. J. Xu and W. J. Thomson, *Chem. Eng. Sci.*, 1999, **54**, 3839–3850.

46 H. J. M. Bouwmeester and A. J. Burggraaf, in *Membrane Science and Technology*, 1996, vol. 4, pp. 435–528.

47 H. Stadler, F. Beggel, M. Habermehl, B. Persigehl, R. Kneer, M. Modigell and P. Jeschke, *Int. J. Greenh. Gas Control*, 2011, **5**, 7–15.

48 S. Baumann, J. M. Serra, M. P. Lobera, S. Escolástico, F. Schulze-Küppers and W. A. Meulenberg, *J. Memb. Sci.*, 2011, **377**, 198–205.

49 S. Engels, T. Markus, M. Modigell and L. Singheiser, *J. Memb. Sci.*, 2011, **370**, 58–69.

50 M. Aresta, A. Dibenedetto and A. Angelini, *Chem. Rev.*, 2014, **114**, 1709–1742.

51 W. C. Chueh, M. Abbott, D. Scipio and S. M. Haile, *Science (80-.).*, 2010, **63**, 2010.

52 P. Furler, J. Scheffe, M. Gorbar, L. Moes, U. Vogt and A. Steinfeld, *Energy and Fuels*, 2012, **26**, 7051–7059.

53 P. Furler, J. R. Scheffe and A. Steinfeld, *Energy Environ. Sci.*, 2012, **5**, 6098–6103.

54 H. Ishida, K. Tanaka and T. Tanaka, *Organometallics*, 1987, **6**, 181–186.

55 S. Zhang, Y. Chen, F. Li, X. Lu, W. Dai and R. Mori, *Catal. Today*, 2006, **115**, 61–69.

56 A. Loiudice, P. Lobaccaro, E. A. Kamali, T. Thao, B. H. Huang, J. W. Ager and R. Buonsanti, *Angew. Chemie Int. Ed.*, 2016, **55**, 5789–5792.

57 B. Kumar, M. Llorente, J. Froehlich, T. Dang, A. Sathrum and C. P. Kubiak, *Annu. Rev. Phys. Chem.*, 2012, **63**, 541–569.

58 J. M. Lehn and R. Ziessel, *Proc. Natl. Acad. Sci. U. S. A.*, 1982, **79**, 701–704.

59 A. Kumar, S. Ergas, X. Yuan, A. Sahu, Q. Zhang, J. Dewulf, F. X. Malcata and H. van Langenhove, *Trends Biotechnol.*, 2010, **28**, 371–380.

60 H. S. Spacil and C. S. Tedmon, *J. Electrochem. Soc.*, 1969, **116**, 1627.

61 A. Isenberg, *Solid State Ionics*, 1981, **3**–**4**, 431–437.

62 S. D. Ebbesen and M. Mogensen, *ECS Trans.*, 2013, **50**, 167–182.

63 S. D. Ebbesen and M. Mogensen, *J. Power Sources*, 2009, **193**, 349–358.

64 P. Kim-Lohsoontorn and J. Bae, *J. Power Sources*, 2011, **196**, 7161–7168.

65 a V Virkar, *Int J Hydrog. Energ*, 2010, **35**, 9527–9543.

66 R. Knibbe, M. L. Traulsen, A. Hauch, S. D. Ebbesen and M. Mogensen, *J. Electrochem. Soc.*, 2010, **157**, B1209–B1217.

67 A. V. Virkar, *J. Power Sources*, 2007, **172**, 713–724.

68 K. Chen and S. P. Jiang, *J. Electrochem. Soc.*, 2016, **163**, F3070–F3083.

69 C. Graves, S. D. Ebbesen, S. H. Jensen, S. B. Simonsen and M. B. Mogensen, *Nat Mater*, 2015, **14**, 239–244.

Chapter 2

Thesis objectives and structure

AN OVERVIEW ON THE OBJECTIVES AND TOPICS DEVELOPED IN THE THESIS

The main objective of this thesis was to identify promising ceramic materials to be applied in the field of energy conversion and storage for a sustainable development.

For the reasons presented in chapter 1, nowadays situation is critical and the direction we will decide to take may have a deep impact on the environment in the years to come. Considering how the energy consumption is increasing year after year and how the access to it affects people's quality of life, a decrease in energy conversion processes is not conceivable, therefore it is necessary to act in order to improve them and reduce their impact on the environment. Typically this process requires time and often years are necessary between the development of a new solution to its actual technological integration and diffusion. For this reason it is necessary to act with a strategy that considers both interventions in the near future, concerning the existing plants and how it is possible to reduce their environmental impact, and interventions in the long term, aiming to replacing the traditional plants for energy conversion with more sustainable and efficient technologies which can in the meanwhile become more mature and consolidated.

In order to fulfill this objective two application fields were identified: oxygen transport membranes and solid oxide fuel cells.

The former is relevant in the context of combustion plants for energy conversion from fossil fuels, where the management of the flue gases can be largely improved by feeding pure oxygen in the combustion. Actually they provide the largest amount of energy.

The latter represent a challenging, yet growing, possibility for the direct conversion of chemicals into electrical energy without the drawbacks of combustion processes, allowing

to obtain higher and cleaner energy from the same fuel used during combustion. As seen in chapter 1, the optimization of fuel cells should necessary pass through the improvement of cathodes and electrolytes performances.

Oxygen transport membranes and fuel cells work at high temperature and make use of ceramic materials which share similar requirements. In fact, both membranes and fuel cells performances are strictly related to the conductivity properties of the constituent materials. This analogy becomes even more relevant for what concerns the cathodes, for which mixed ionic and electronic conductivity is essential, while In the case of the electrolyte pure ionic conductivity is required in order not to lose efficiency during operation.

Therefore it is evident how obtaining ceramics with a high ionic conductivity would result beneficial for the studied fields. This objective was pursued through different strategies: investigating new formulations of the materials, interfacing known materials in high contact environment and working on processing techniques to tailor their properties.

The contents of the thesis are organized in 8 chapters, briefly summarized as follows:

- **Chapter 1** provides a general introduction on the issue of energy production and an overview on the topics of fuel cells and oxygen membranes, highlighting the energy-related context in which they can be used.

- **Chapter 2** describes the objective of the thesis and its content.

- **Chapter 3** gives an insight into the main materials involved into this thesis, their structure, properties and how they have been synthesized.

- **Chapter 4** presents the characterization techniques used in this work, their basic principles and some advantages and disadvantages.

- **Chapter 5** consists of the work on a GDC/YSZ electrolyte deposited in the form of thin film by ink-jet printing to be used for intermediate and low temperature

operation in solid oxide fuel cells. The material is produced through a novel hybrid synthesis route involving pre-formed nanoparticles and a reactive sol-gel matrix. The stability of the resulting nanocomposite with a focus on interdiffusional processes between ceria and zirconia is studied, the rheological properties of the resulting ink are characterized and finally the ionic conductivity of a thin film electrolyte produced by ink-jet printing is tested for low temperature operation.

- **Chapter 6** contains the work done on the evaluation of a doping strategy for stabilizing the cubic phase of $SrCoO_3$ perovskite and the subsequent use of these materials as oxygen permeation membranes. The first part of the chapter focuses on the effect of dopants and investigates their influence on the structural stability of the perovskite. Subsequently, the evolution of oxygen mobility is investigated as a function of temperature and atmosphere and linked to the doping. Finally dense ceramic membranes are prepared and tested in oxygen permeation, with the most promising sample being tested in oxy-fuel relevant conditions.

- **Chapter 7** is closely linked to chapter 6, since the perovskites composition conceived, developed and tested as oxygen permeation membranes are translated into the context of solid oxide fuel cells, where are investigated as cathode materials for intermediate temperature operation. Their conductivity is studied as a function of doping and oxygen mobility. Finally, the electrochemical activity of the materials as cathodes is tested in symmetrical cell configuration and the contributions to the total resistance are identified.

- **Chapter 8** summarizes the obtained results and gives an outlook on the future perspectives of this thesis.

Chapter 3

Investigated materials

AN INTRODUCTION ABOUT THE USED MATERIALS, THEIR STRUCTURE AND PROPERTIES

In this chapter the main materials used in the thesis are presented and their structure and properties are illustrated.

3.1 Yttrium Stabilized Zirconia (YSZ)

Zirconium dioxide (ZrO_2, called zirconia) is a white insulating oxide with refractory properties, which make it suitable for applications requiring high temperature and chemical resistance, like barrier coatings.[1] Other fields of application for zirconium oxide include gas sensing,[2] dental prosthesis[3] and hard ceramics.

Zirconia has three polymorphs, being monoclinic at room temperature up to 1370 °C, tetragonal between 1370 °C and 2320 °C and cubic above 2320 °C.[4]

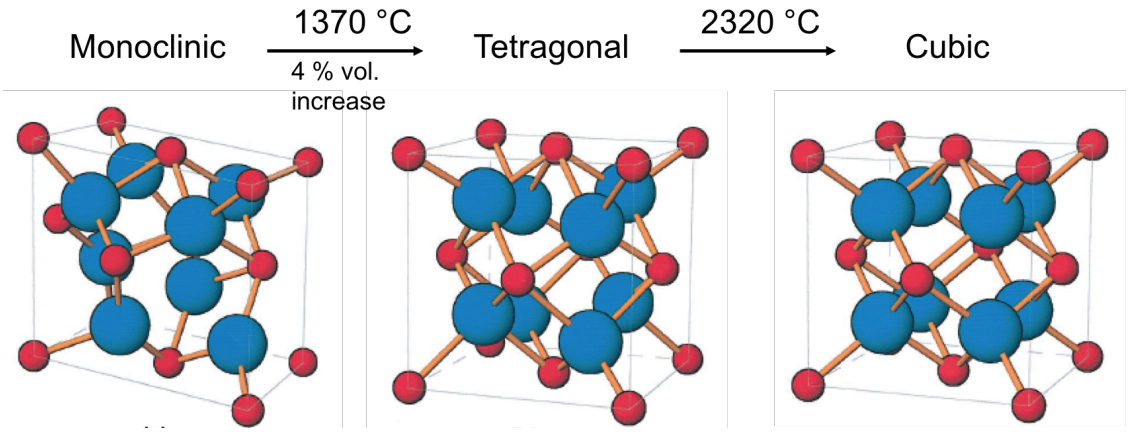

Fig 3.1.: Crystal structure of the three phases of zirconia. Taken from [4]

The phase transition between monoclinic and tetragonal structure causes a 4% volume increase which can result in poor matching with other materials, with consequent cracks and difficult manufacturing of sintered zirconia.[5]

In its natural form, zirconium oxide does not present a significant amount of oxygen vacancies, resulting in a limited ionic conductivity. The substitution of an acceptor element (typically yttrium, Y^{3+}) for zirconium induces the a stabilization of the cubic structure over a wide range of temperatures, with the additional benefit of introducing a larger amount of oxygen vacancies available for ionic conduction.

The substitution mechanism is described by:

$$Y_2O_3 \xrightarrow{ZrO_2} 2\,Y'_{Zr} + 3O_O^X + V_O^{\bullet\bullet} \qquad (1)$$

Where Y'_{Zr} is Y^{3+} replacing a Zr^{4+} atom and $V_O^{\bullet\bullet}$ is an oxygen vacancy.

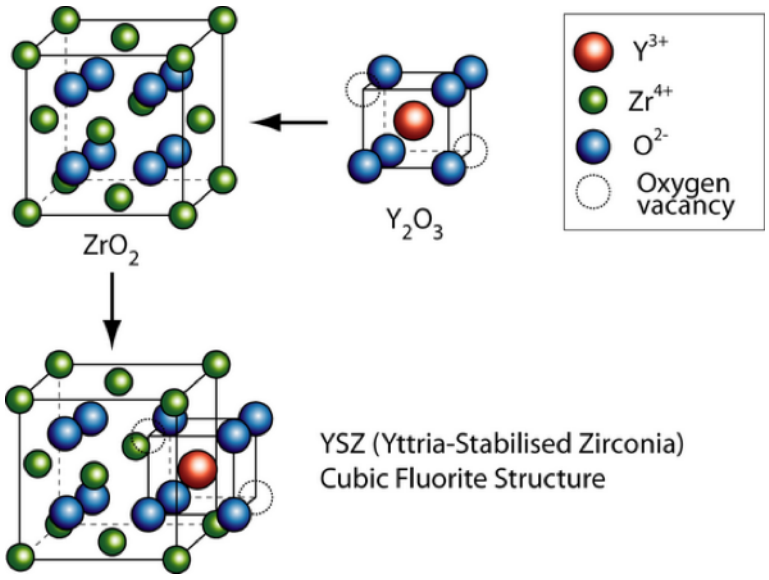

Fig 3.2.: Doping zirconia by yttria and resulting YSZ structure. Taken from [5]

The maximum ionic conductivity is obtained for Sc^{3+} (r_i=0.87 Å in 8-fold coordination) substitution for Zr^{4+} (r_i=0.84 Å in 8-fold coordination), since the ionic radiuses of the two cations are similar. [6,7] Despite that, often Y^{3+} (r_i=1.02 Å in 8-fold coordination) is preferred for the lower cost and better stability.[8]

YSZ has a pure ionic conductivity over a wide range of oxygen partial pressures, making it an ideal candidate for fuel cells electrolytes. In fact, despite other ionic conductors have

been discovered, YSZ is still considered among the state of the art materials. However, high temperature (>800 °C) is required to have conductivity values in the range of 10^{-2} $S \cdot cm^{-1}$.[9]

3.1.2 Gadolinium Doped Ceria (GDC)

Cerium dioxide (CeO_2, called ceria) is a material extensively studied in catalysis,[10] water splitting[11] and recently in giant electrostriction, too.[12]

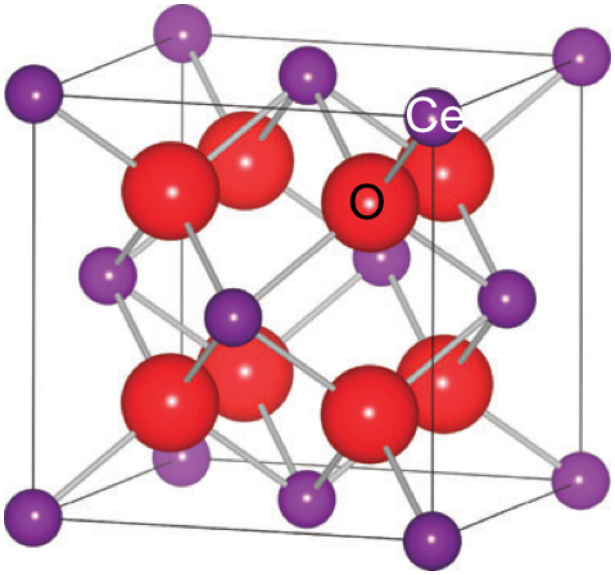

Fig 3.3.: Crystal structure of the three phases of zirconia. Taken from [13]

Differently from zirconia, at room temperature cerium oxide is already stable in fluorite structure, with intrinsic oxygen defects present due to the Ce^{3+}/Ce^{4+} redox couple.[13] Replacing cerium with a trivalent cation induces the formation of more extrinsic defects. The maximum conductivity is measured for samarium (Sm^{3+}, r_i=1.08 Å in 8-fold coordination) replacement (SDC)[14] for cerium (Ce^{4+}, r_i=0.97 Å in 8-fold coordination), however often gadolinium (Gd^{3+}, r_i=1.05 Å in 8-fold coordination) is the typical choice preferred for its lower price.

$$Gd_2O_3 \xrightarrow{CeO_2} 2\,Gd'_{Ce} + 3O_O^X + V_O^{\bullet\bullet} \qquad (2)$$

GDC displays higher ionic conductivity than YSZ, especially in the low temperature range (σ_i=3·10^{-2} S·cm^{-1} at 600 °C)[9] however is not as stable in reducing environments: in fact above 600 °C and in reducing conditions (pO_2<10^{-20} atm),[15] Ce^{3+} is formed and the reduction is coupled with a 2% change in volume which may result detrimental for the mechanical stability.[16] Consequently to the formation of Ce^{3+}, reduced ceria displays a non-negligible n-type electronic conductivity, which turn the material into a mixed conductor. This may result in an internal short circuit of the cell and performances degradation.

A typical strategy for avoiding GDC exposure at reducing atmosphere consists in coupling it with YSZ, obtaining a double layered electrolyte. In this structure ceria acts also as a barrier for zirconium diffusion towards the cathode material (typically perovskites), preventing the formation of the $SrZrO_3$ insulating phase.[17]

3.2 Perovskites

Perovskites are a family of materials represented by the stoichiometric formula ABX_3, where A is a large 12-fold coordinated cation (typically belonging to alkaline, alkaline earths or rare earths group), B is a smaller 6-fold coordinated cation (typically a transition metal) and X can be oxygen, nitrogen or a halide, with oxides being the most used in SOFCs.[18,19]

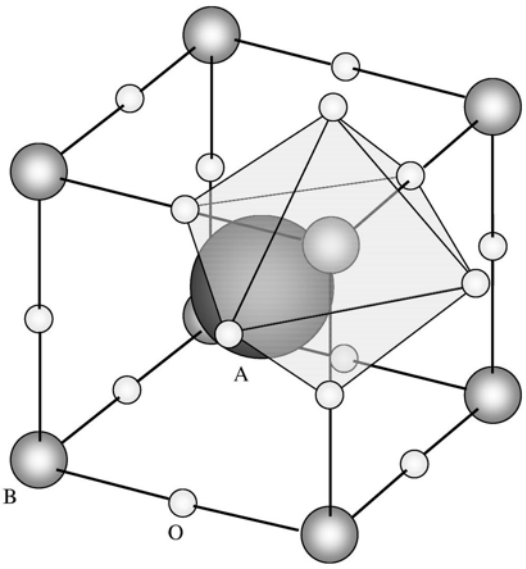

Fig 3.4.: Perovskite crystal structure. Taken from [19]

Since their discovery in 1840, perovskites have been growing in consideration due to the extremely wide range of properties they display: besides being often good oxidation catalysts[20] they can display superconductivity,[21] colossal magnetoresistance,[22] ferroelectricity,[23] or photocatalytic activity.[24]

The archetype structure of perovskite is represented by $CaTiO_3$, having a perfect cubic structure. When another cation is replacing calcium or titanium, this produces a distortion in the structure. To calculate the deviation from the cubic symmetry and obtain an estimation of the extent of distortion, the tolerance factor t was first introduced by Goldschmidt:[25]

$$t = \frac{(r_A + r_O)}{\sqrt{2}(r_B + r_O)} \qquad (3)$$

where r_A, r_B and r_O represent the ionic radiuses of A-cation, B-cation and oxygen ion, respectively.

Cubic structure is observed for 0.9<t<1 values, while for values below 0.9 a distorted structure (orthorhombic, rhombohedral or tetragonal) is detected, down to a limit value of 0.7 below which the perovskite is not stable anymore. For t>1 hexagonal structure is observed.

An interesting feature of perovskite is that, besides tolerating a distortion of the lattice, they can easily accommodate a certain extent of defects without the crystal structure being destabilized. This occurs through charge compensation mechanisms, which can be explained as follows: since the three oxygen atoms from the stoichiometry are bringing a fixed -6 valency, A and B-site cations total valency has to compensate the charge and not always the cations are matched as $A^{(+3)}B^{(+3)}O_3$, $A^{(+2)}B^{(+4)}O_3$ or $A^{(+1)}B^{(+5)}O_3$ between A and B-site. As an example, when the total valence of cations is below +6 and no higher oxidation states are available, charge is compensated by the creation of oxygen defects, which are responsible for ionic conduction. However, the creation of too many oxygen defects results in ordering phenomena which lead to a phase transition from perovskite to brownmillerite structure,[26] which has frozen vacancies. This is not desired, since for ionic conductivity defects mobility is required.

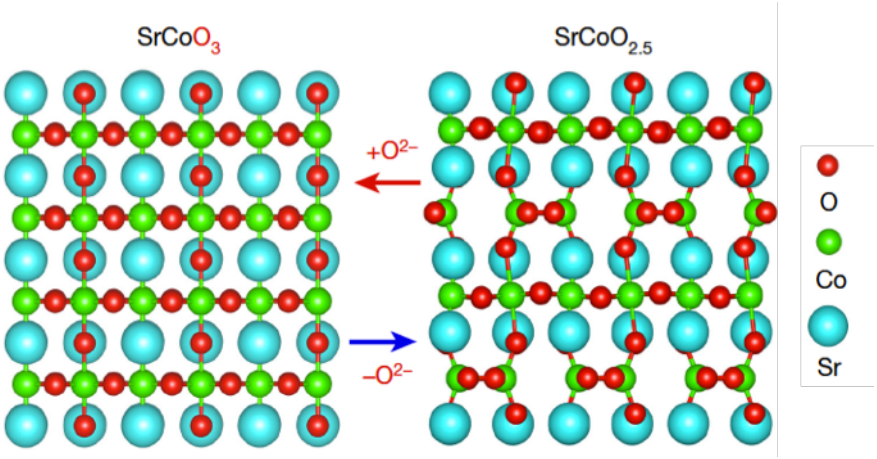

Fig 3.5.: Transition equilibrium between perovskite and brownmillerite structure. Taken from [26]

When B-site cations have more oxidation states available, charge compensation mechanisms can induce the formation of a $B^{n+}/B^{(n+1)+}$ redox couple responsible for electronic conductivity.

Moreover, cations defects can be tolerated too, and this possibility can be exploited to tune the surface composition of a sample through segregation effects.

The possibilities of doping allow even to introduce more dopants in A and B-sites simultaneously, creating a double doped system of the type $A_{1-x}A'_xB_{1-y}B'_yO_3$, where many cations effects are displayed simultaneously, including mixed ionic and electronic conductivity (MIEC).

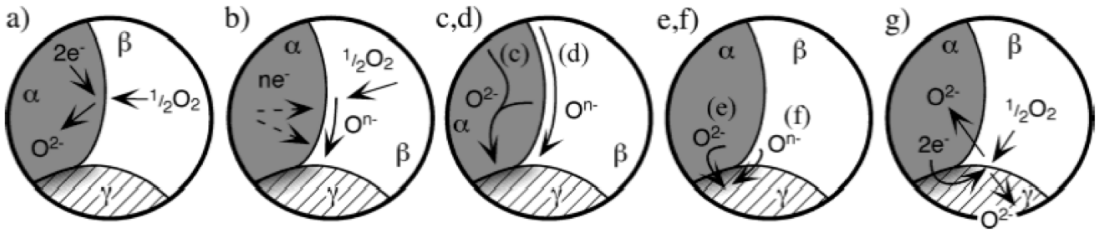

Fig 3.6.: Possible mechanisms for oxygen reaction at the cathode. α,β and γ represent cathode, gas phase and electrolyte respectively. Taken from [33]

Because of their mixed ionic and electronic conductivity, perovskites have been widely investigated as cathodes, supported by their good stability in air at high temperatures. The most studied compositions are based on manganese (LSM),[27,28] cobalt (LSC)[29] iron (LSF, LSGF)[30] or cobalt and iron (LSCF, BSCF)[31,32]. In the case of manganese containing compounds, since they do not display ionic conductivity LSM is commonly mixed with the electrolyte material in order to enhance the amount of sites available for oxygen reduction (called three-phase boundary).[33] The main disadvantage is that in this configuration the surface are of the electrode is not completely exploited, while in the case of a mixed conductor, the whole electrode area can be used for the oxygen reduction reaction.

Oxygen transport membranes based on perovksites have been tested too and a notable interest has been devoted to the La-Sr-Co-Fe system,[34,35] for which the highest permeation fluxes were observed with increasing contents of strontium and cobalt. This phase is expected to have a high amount of oxygen vacancies available for conduction, however $SrCoO_3$ is not stable as cubic perovskite, rearranging to brownmillerite structure.

Bibliography

1 X. Q. Cao, R. Vassen and D. Stoever, *J. Eur. Ceram. Soc.*, 2004, **24**, 1–10.

2 N. Miura, T. Sato, S. A. Anggraini, H. Ikeda and S. Zhuiykov, *Ionics (Kiel).*, 2014, **20**, 901–925.

3 Z. Özkurt and E. Kazazoğlu, *J. Oral Implantol.*, 2011, **37**, 367–376.

4 J. P. Brog, C. L. Chanez, A. Crochet and K. M. Fromm, *RSC Adv.*, 2013, **3**, 16905–16931.

5 R. H. J. Hannink, P. M. Kelly and B. C. Muddle, *J. Am. Ceram. Soc.*, 2004, **83**, 461–487.

6 R. D. Shannon, *Acta Cryst.*, 1976, 751–767.

7 O. Yamamoto, Y. Arachi, H. Sakai, Y. Takeda, N. Imanishi, Y. Mizutani, M. Kawai and Y. Nakamura, *Ionics (Kiel).*, 1998, **4**, 403–408.

8 C. Haering, A. Roosen, H. Schichl and M. Schnöller, *Solid State Ionics*, 2005, **176**, 261–268.

9 K. C. Wincewicz and J. S. Cooper, *J. Power Sources*, 2005, **140**, 280–296.

10 A. Trovarelli, *Catal. Rev.*, 1996, **38**, 439–520.

11 W. C. Chueh, M. Abbott, D. Scipio and S. M. Haile, *Science (80-.).*, 2010, **63**, 2010.

12 R. Korobko, A. Patlolla, A. Kossoy, E. Wachtel, H. L. Tuller, A. I. Frenkel and I. Lubomirsky, *Adv. Mater.*, 2012, **24**, 5857–5861.

13 L. Malavasi, C. A. J. Fisher and M. S. Islam, *Chem. Soc. Rev.*, 2010, **39**, 4370–4387.

14 K. Eguchi, T. Setoguchi, T. Inoue and H. Arai, *Solid State Ionics*, 1992, **52**, 165–172.

15 S. R. Wang, H. Inaba, H. Tagawa, M. Dokiya and T. Hashimoto, *Solid State Ionics*, 1998, **107**, 73–79.

16 D. Marrocchelli, S. R. Bishop, H. L. Tuller and B. Yildiz, *Adv. Funct. Mater.*, 2012, **22**, 1958–1965.

17 E. Mete, R. Shaltaf and Ellialtıoğlu, *Phys. Rev. B - Condens. Matter Mater. Phys.*, 2003, **68**, 3–6.

18 T. Bay, T. Natural, H. Museum and C. Road, 2017, **81**, 411–461.

19 H. Tanaka and M. Misono, *Curr. Opin. Solid State Mater. Sci.*, 2001, **5**, 381–387.

20 M. A. Peña and J. L. G. Fierro, *Chem. Rev.*, 2001, **101**, 1981–2017.

21 C. A. Hancock, J. M. Porras-Vazquez, P. J. Keenan and P. R. Slater, *Dalt. Trans.*,

2015, **44**, 10559–10569.

22 A. P. Ramirez, *J. Phys Condens. Matter*, 1997, 8171–8199.

23 D. D. Fong, G. B. Stephenson, S. K. Streiffer, J. A. Eastman, O. Aucielo, P. H. Fuoss and C. Thompson, *Science (80-.).*, 2004, **304**, 1650–1653.

24 E. Grabowska, *Appl. Catal. B Environ.*, 2016, **186**, 97–126.

25 V. M. Goldschmidt, *Naturwissenschaften*, 1926, **14**, 477–485.

26 N. Lu, P. Zhang, Q. Zhang, R. Qiao, Q. He, H. B. Li, Y. Wang, J. Guo, D. Zhang, Z. Duan, Z. Li, M. Wang, S. Yang, M. Yan, E. Arenholz, S. Zhou, W. Yang, L. Gu, C. W. Nan, J. Wu, Y. Tokura and P. Yu, *Nature*, 2017, **546**, 124–128.

27 J. D. Kim, G. D. Kim, J. W. Moon, Y. il Park, W. H. Lee, K. Kobayashi, M. Nagai and C. E. Kim, *Solid State Ionics*, 2001, **143**, 379–389.

28 J. Nielsen and J. Hjelm, *Electrochim. Acta*, 2014, **115**, 31–45.

29 O. Gwon, S. Yoo, J. Shin and G. Kim, *Int. J. Hydrogen Energy*, 2014, **39**, 20806–20811.

30 S. P. Simner, J. F. Bonnett, N. L. Canfield, K. D. Meinhardt, J. P. Shelton, V. L. Sprenkle and J. W. Stevenson, *J. Power Sources*, 2003, **113**, 1–10.

31 A. Esquirol, N. P. Brandon, J. A. Kilner and M. Mogensen, *J. Electrochem. Soc.*, 2004, **151**, A1847.

32 Z. Chen, R. Ran, W. Zhou, Z. Shao and S. Liu, *Electrochim. Acta*, 2007, **52**, 7343–7351.

33 S. B. Adler, , DOI:10.1021/cr020724o.

34 N. Y. Y. Teraoka, H.M. Zhang, S. Furukawa, *Chem. Lett.*, 1985, 1743–1746.

35 Y. Teraoka, Y. Honbe, J. Ishii, H. Furukawa and I. Moriguchi, *Solid State Ionics*, 2002, **152**–**153**, 681–687.

Chapter 4

Characterization techniques and experimental protocols used for the analysis and testing of the samples

AN OVERVIEW AND DESCRIPTION OF THE CHARACTERIZATION TECHNIQUES AND TESTING PROCEDURES

Besides the synthesis and preparation of a material, characterization of its properties represent a fundamental step before proceeding with the testing, in order to assess the suitability of the sample for the targeted application and the good outcome of the synthesis step.

Crystal structure, microstructure and surface composition are intertwined properties which can influence the final performance of a material. Moreover, it is useful to determine the evolution of the sample in the testing conditions, where solid-gas reaction, oxidation/reduction processes or diffusion phenomena could occur. When complex electrochemical reactions involving transport of charged species occur, they can display effects due to the simultaneous presence of many properties of the sample, like oxygen mobility, ionic and electronic conductivity.

In other cases, like in the context of ink-jet printing, the full characterization of the properties of an ink allow to have a precise estimation of what the printability behavior of the ink could be.

In this chapter are reported the characterization techniques adopted for the investigation of the properties of the prepared samples, the physical principles on which they are based on and their advantages and limitations.

4.1 X-Ray diffraction (XRD)

The characterization of the obtained crystal phase is the first step after the synthesis of a sample. This allows determining the structure of the synthesized material and gives an assessment of the synthesis procedure. For this purpose, X-Ray diffraction (XRD) is used. In fact, XRD is a powerful technique able to provide information about the crystal phases present in a sample.

Since a crystal can be described as a periodical array of atoms, these arrays can be seen as atomic planes which interact with an incident electromagnetic radiation. A geometrical description of this interaction is given by Bragg. [1]

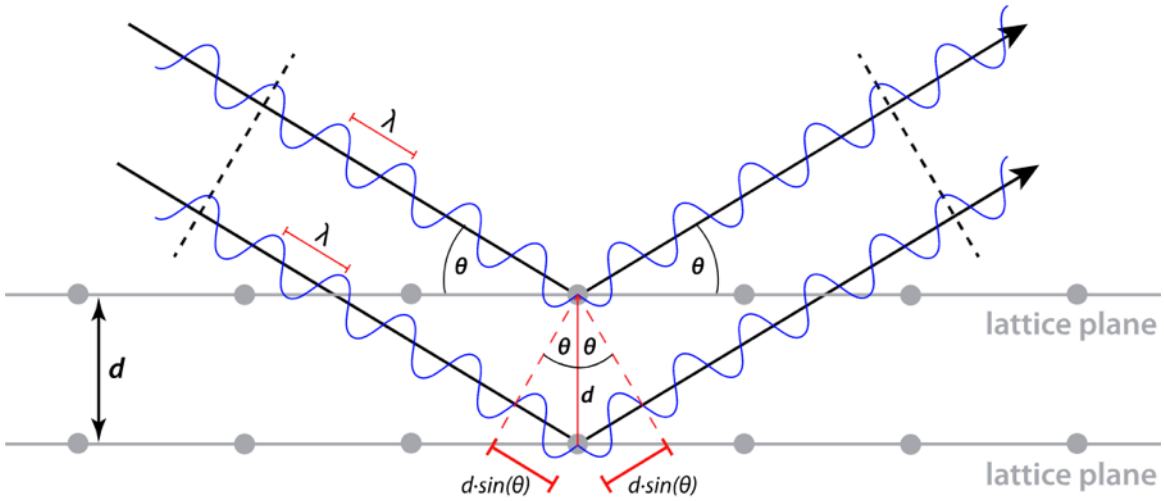

Fig 4.1: Schematized interaction between X-Ray radiation and an array of lattice planes in a crystal. Taken from [1]

Bragg's law defines the condition for constructive interference as when the difference in the optical path of two parallel beams is an integer multiple of the incident radiation's wavelength:

$$n \cdot \lambda = 2d \cdot sin\theta \qquad (1)$$

where n is an integer number, λ is the wavelength of incident radiation (1.5406 Å, for Cu Kα) d is the spacing between the diffracting lattice planes and θ is the incident angle.

Therefore, for each specific crystallographic direction Bragg's condition is fulfilled for a single value of θ. Scanning an angular range allows determining the characteristic diffraction peaks for a certain compound. These are compared with database references

(JCPDS patterns) in order to identify the sample and detect the eventual presence of secondary phases.

The advantages of X-ray diffraction are related to the short time necessary to carry out an analysis and the easy preparation of the sample. Moreover, this is a non-destructive technique allowing to recover completely the analyzed material after the analysis. Despite being simple, the preparation of the sample should be as careful as possible, in order to avoid the production of artefacts in the diffraction pattern.

X-ray diffraction measurements were carried out using a Bruker D8 diffractometer equipped with a Cu Kα source (λ=1.5406 Å) and a solid state detector, working in Bragg Brentano geometry.

4.2 X-Ray Photoelectron Spectroscopy (XPS)

X-ray Photoelectron Spectroscopy (XPS) is a surface-related technique based on the emission of photoelectrons upon the irradiation of a sample with a X-ray source. Since the photoemission occurs from discrete quantized levels, the energies of the emitted electrons are characteristic of the considered element and energy level involved in the transition. Moreover, despite being the penetration length of X-rays approximately 1 μm, the mean free path of photoelectrons is approximately 10 nm, making XPS a technique sensitive to the upmost atomic layers. The characterization depth can be further reduced working with angle resolved XPS.

For all these reason, XPS can provide information about the surface of a sample, revealing which kind of elements are present, their oxidation state and the amount in which they are present.

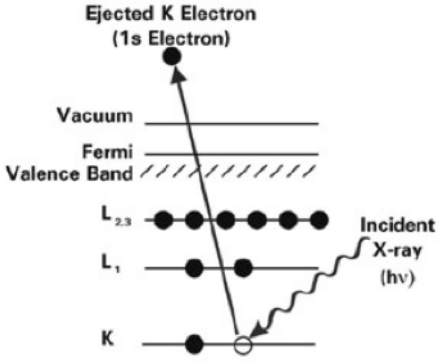

Fig 4.2: Schematized interaction of the photoemission induced by the incidence of X-ray radiation on a sample. Taken from [2]

Figure 4.2 shows the interaction between an incident photon and an electronic level, resulting in an emitted electron.[2] When the photoelectron reaches the spectrometer, their energies are related as follows:

$$E_k = h\upsilon - E_b - \phi \quad (2)$$

Where E_k is the measured kinetic energy of the emitted electrons, $h\upsilon$ is the energy of the incident radiation, E_b is the binding energy and ϕ the work function of the spectrometer. Since E_k is the quantity measurable by the spectrometer and $h\upsilon$ and ϕ are known, it is possible to rearrange (2) obtaining:

$$E_b = h\upsilon - E_k - \phi \quad (3)$$

that allows determining the binding energy for the specific photoemission level of an element.

Besides evaluating the differences in the value of the binding energy, sometimes the identification of an oxidation state in XPS is simplified by the presence of some characteristic peaks called shake-ups. Those are the result of a final configuration interaction when the photoelectron is emitted and represent a peculiar feature of certain oxidation states of an element (Co^{2+}, Ce^{4+}, as an example), thus they can be used as fingerprints for the identification of the spectra.

Another information obtained by XPS is the quantitative analysis of the elemental composition of the surface, which is obtained from the integration of the photoemission peaks. Since the surface of a sample is the place where most of the catalytic reactions occur, where many electrochemical reactions begin and where reacting species are adsorbed, knowing its composition allows understanding the behavior in testing conditions. For example, often the real composition of the surface of a sample is different from the values expected from stoichiometry. Being able to identify segregation phenomena could provide an extremely useful tool for the comprehension of the samples reactivity.

Despite being a very sensitive, XPS is a technique requiring ultra-high vacuum conditions ($p<10^{-8}$ mbar) and some elements may be degraded by X-ray irradiation in vacuum.[3] For this reason, it's recommendable to reduce the sample exposition to X-rays and double check that the sample spectrum is not changed after the measurement.

X-ray photoelectron spectroscopy was carried out with a Perkin Elmer Φ 5600ci Multi Technique System. The spectrometer was calibrated assuming the binding energy (BE) of the Au $4f_{7/2}$ to be 84.0 eV with respect to the Fermi level.[4] An Al Kα standard source working at 250 W was used to collect both extended (survey - 187.85 eV pass energy, 0.5 $eV \cdot step^{-1}$, 0.05 $s \cdot step^{-1}$) and detailed spectra (multiplex - 23.5 eV pass energy, 0.1 $eV \cdot step^{-1}$, 0.1 $s \cdot step^{-1}$). The peak positions were corrected for charging effects by considering the C 1s peak at 285.0 eV and evaluating the BE differences.[5,6] Finally, the atomic surface composition was evaluated after a Shirley-type background subtraction, using PHI sensitivity factors.[7]

4.3 Scanning Electron Microscopy (SEM)/Energy Dispersive X-ray Spectroscopy (EDX)

Scanning Electron Microscopy is a microscopy technique making use of electrons as sensing probes. A focused beam of electrons is used to investigate the structure of a sample on a smaller scale (up to 1 nanometer) compared to the one reached using visible light. Moreover, since the interaction of the electron beam of the probe with a sample produces many effects that display at different depth in the sample, it is possible to obtain complementary information on the material through the coupled analysis of different signals.[8]

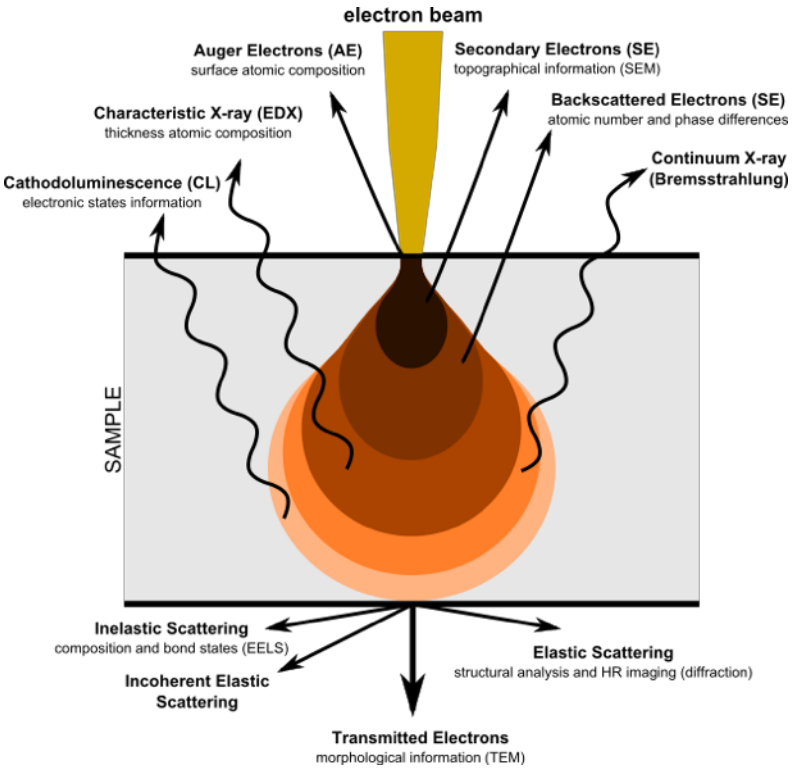

Fig 4.3: Signals produced by the interaction of the electron beam and the sample. Taken from [8]

Figure 4.3 shows the interaction volume of electrons with a sample. Typically in SEM secondary electrons (SE) and backscattered electrons (BSE) are considered. Since only the secondary electrons generated close to the surface have a sufficient mean free path for escaping the sample, they have a higher resolution. For this reason secondary electrons can provide information about the sample topography and are useful to analyze the smaller features.

On the contrary, backscattered electrons are generated from a deeper sampling volume (thus have a smaller resolution) by scattering collisions with the atoms, which is a

phenomenon related to the atomic number. The heavier is an element contained in a sample, the more intense the scattering effect is. Backscattered electrons and can thus give information about the kind and distribution of elements in the sample.

Moreover, the irradiation of the sample with an electron beam produces an interaction between the sample's outer electronic shells, which results in the emission of characteristic X-rays occurring in a larger volume than secondary and backscattered electrons. The measurement of the emitted X-rays is called Energy Dispersive X-ray Spectroscopy (EDX) and allows a determination of the bulk composition. Often this technique is coupled to quantitative analysis from XPS for observing the differences between the bulk and the surface of a sample.

The main disadvantage related to SEM is the need for a conductive sample, which allows the electron to escape from the surface after being irradiated. When the conductivity of the sample is not high enough, charging effects can display, producing artefacts in the images. These can be prevented through the deposition of a thin conductive layer (typically a few nanometers of gold or carbon) on the specimen, that has to be kept in consideration when investigating the nanometric features of a material.

Zeiss Supra and a Zeiss Merlin microscopes were used to characterize the produced samples.

4.4 Iodometric Titration

Determining the amount of oxygen nonstoiochiometry (δ) in a perovskite is crucial for understanding its mixed conductivity properties. In fact, the presence of oxygen vacancies is fundamental for having ionic conduction and it can be associated with the formation of higher oxidation state concerning B-site cations, producing redox couples responsible for electronic conductivity.

A simple, yet effective, method for determining the oxygen nonstoichiometry is iodometric titration. It consists of dissolving the material in a hydrochloric acid solution in presence of iodide ions (typically coming from KI) that can reduce the transition metal species (according to the specific oxidation state of the metal and standard potential) and then the amount of produced iodine is measured by titration with a standard thiosulfate solution.[9]

When a perovskite is dissolved in presence of iodide, the following reactions occur (considering cobalt as an example):

$$Co^{3+} + I^- \rightarrow Co^{2+} + \frac{1}{2}I_2 \qquad (4)$$

$$Co^{4+} + 2I^- \rightarrow Co^{2+} + I_2 \qquad (5)$$

Where I^- is oxidized to I_2. In excess of iodide ions in solution, iodine further reacts forming triiodide, which is chemically equivalent to iodine but stable in solution:

$$I_2 + I^- \rightarrow I_3^- \qquad (6)$$

the amount of produced iodine can be measured by reaction with thiosulfate:

$$\frac{1}{2}I^2 + S_2O_3^{2-} \rightarrow I^- + \frac{1}{2}S_4O_6^{2-} \qquad (7)$$

In presence of high amounts of triiodide, the solution presents a brown color, which turns to pale yellow as the reaction gets closer to the equivalent point. For this reason, in proximity of the equivalent point a starch solution is used as indicator. Starch reacts with triiodide forming a dark blue complex which facilitates the observation of the equivalent point.

It is important that the addition of starch is done just before reaching the equivalent point, since in excess of I_3^- the reaction with starch could sequestrate part of the available triiodide and provide deceiving results.

Despite being easy to perform, iodometric titration requires carefulness: it is important that the reaction is performed in an inert environment, since the oxygen in the atmosphere could react with the iodine subtracting it from the solution.

4.5 Thermogravimetric analysis (TGA)/ Differential thermal analysis (DTA)

Whenever a solid or a liquid is heated in a gas environment, an interaction with the surrounding atmosphere will occur. In the case of a liquid, this can produce an evaporation of the solvent, decomposition and burning of the organic molecules; in solid samples it determines crystallization, sintering or oxygen adsorption/release phenomena. Phase transition could occur during heating and their identification is crucial to detect the formation of undesired crystal phases that could display different activity from the main phase. Moreover, if the sample is heated in a reactive atmosphere similar to the testing environment (CO_2, H_2, etc.) which produces changes on the sample, these modifications can be observed.

Thermal analysis methods are powerful techniques providing a wide range of information about the changes occurring in a sample when it is heated. Two of these techniques are thermogravimetric analysis (TGA) and differential thermal analysis (DTA), which are often coupled and provide complementary information.[10]

Thermogravimetric analysis (TGA) consists in measuring the mass of a sample as the temperature is increased, recording a change in the weight as a function of the reactive atmosphere in which the sample is immersed. The measurement gives information about chemical and physical phenomena occurring in the sample including solid-gas equilibrium reactions (for example the oxygen incorporation or release in oxides), thermal decomposition, adsorption and desorption of gases.

Differential thermal analysis (DTA) is a technique in which the sample and a reference holder are heated in the same atmosphere and the difference in temperature between the two is recorded. When plotted, the changes in temperature appear in the shape of peaks and valleys, which are associated with solvent evaporation, crystallization, melting or glass transition in the sample.

The coupling of the two techniques provides an effective tool for determining which physical or chemical phenomena are occurring in the sample during heating.

Thermogravimetric and differential thermal analysis were performed with a STA 409 PG (Netzsch) and a SDT 2960 TGA/DTA (TA instruments), using alumina crucibles.

4.6 O_2-TPD

Thermal programmed adsorption/desorption is a simple technique for determining the bonding strength of chemical species attached to a sample. These could be both naturally incorporated in the sample structure or previously dosed during a conditioning step.[11]
This characterization consists in a controlled heating of the sample in a stream of gas (called carrier gas) and monitoring the flue gases transported by the stream. A thermal conductivity detector (TCD) records the difference between the conductivity of the stream coming from the sample and a reference stream bypassing the sample. This difference is plotted as a sequence of peaks (desorption) or valleys (adsorption) as a function of temperature, and allows recognizing the presence of sites with different bonding strength. Since the desorption is usually operated with a fast thermal ramp to avoid dilution of the released gases, it is not possible to recognize the nature of the desorbed gases in the case of many species being involved, differently from what is done in gas chromatography. This can be achieved by coupling a mass spectrometer with TPD.
The Thermal Programmed Desorption measurements were carried out with an Autochem II (Micromeritics) equipped with TCD detector and coupled with a mass spectrometer (ESS Evolution) in order to analyze the composition of the gases coming to the detector.
The experimental procedure consisted of three steps: a cleaning step at mild temperature (2h in He flow at 450 °C) for removing surface adsorbed species, a dosing step at high temperature (2h in pure O_2 at 900 °C, descent in pure O_2) and the desorption step, consisting in a thermal ramp where the released gases are monitored.

4.7 Ink characterization

Inks properties are controlled by several parameters, which determine their flowing properties, adhesion to a substrate (wettability) and jettability when printed. An overview of the characterization techniques of the main properties is presented.

4.7.1 Particles size distribution (PSD)

Particle size distribution (PSD) is a technique based on Fraunhofer's diffraction theory. According to this theory, when a coherent light source is irradiated on a sample containing particles, these will produce a scattering of the light and the angle between the scattered beam and the incident beam is inversely proportional to the particles dimension. This means that large particles will produce scattering at small angles, while small particles will scatter at large angles. The integrated intensity of the scattered radiation allows determining the fraction of particles having a certain size, thus a distribution of the particles size is obtained. [12]

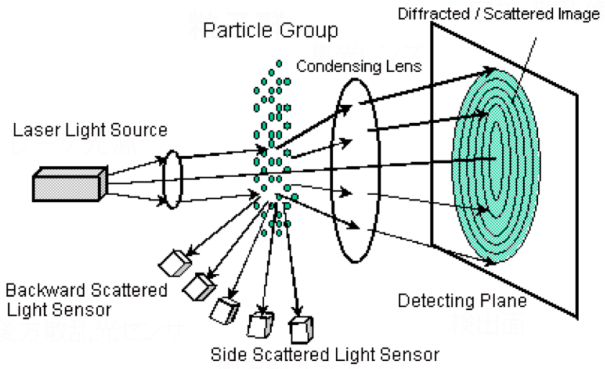

Fig 4.4: Schematized interaction of a laser source with a sample containing particles that give diffraction. Taken from [12]

The disadvantage of this technology is that it a has threshold of detection which is around 0.1 μm, meaning that below this dimension the determination of particle size is less precise. However, considering the printing nozzle's diameter (21.5 μm) and the suggested printing criteria enounced in chapter 2, this range is enough for assessing if the particles dimension is suitable for printing. A Laser Diffraction Particle Size Analyzer LS 13 320 (Beckman Coulter) was used for measuring the particles size, after dispersing them in ethanol.

4.7.2 Surface tension

Surface tension is a crucial parameter concerning printability. Not only it is a member in the definition of printability number Z, but it has a direct influence on the interaction between the ink and the substrate. In fact, if the surface tension of the ink is higher than the substrate surface energy, the printed droplets do not cover uniformly the surface and a discontinuous pattern is produced.

The tensiometer is an instrument allowing to determine the surface tension of a liquid by measuring the internal pressure of a bubble of gas (air, for example) formed in a liquid using a capillary.[13] According to Young-Laplace equation, the internal pressure (Pa) of the bubble is:

$$p = \frac{2\sigma}{r} \qquad (8)$$

Where σ and r are the surface tension ($N \cdot m^{-1}$) and the curvature radius (m), respectively. The bubble produced at the tip of the capillary is evolving with time, having a curvature radius which is increasing up to a maximum value, before decreasing and subsequently being released from the capillary.

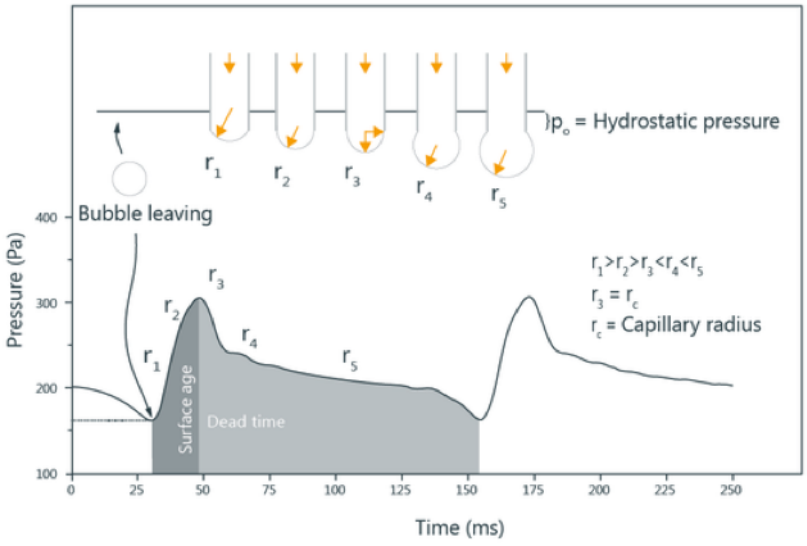

Fig 4.5: Evolution of a bubble's curvature radius and pressure at the tip of the capillary as a function of time. Taken from [13]

The pressure reaches a maximum in correspondence of the maximum curvature radius, which is the value of the capillary radius. In this point the surface tension can be calculated, once the effect of the hydrostatic pressure (related to the density of the liquid and to the depth of immersion of the probe) is subtracted:

$$\sigma = \frac{(p_{max} - p_0) \cdot r}{2} \qquad (9)$$

where σ is surface tension (N·m^{-1}), p_{max} and p_0 are maximum and hydrostatic pressure (Pa), respectively and r is the curvature radius of the capillary (m).
A BP 50 Bubble Pressure Tensiometer (Krüss) was used for measuring the dynamic surface tension.

4.7.3 Density

The density of the ink was evaluated by repeatedly weighting 10 ml of the liquid. Although this method might not seem very accurate, it's worth remarking that density does not affect significantly the final printability, since the most relevant contribution to it is coming from viscosity.

4.7.4 Viscosity

Rheology is the science studying and describing the response of a liquid medium (like an ink, a paste or a slurry) to the application of an external force. According to the kind of response as a function of time, the behavior of liquids can be classified under different categories: viscous, elastic or viscoelastic. As an example, since inks for inkjet printing are usually very diluted, they typically display viscous behavior.
Another criterion used for classification is the medium response as a function of the applied force. This classification is made on the basis of Newton's law:

$$\tau = \eta \cdot \gamma \qquad (10)$$

where τ is the shear stress (Pa), η is the viscosity (mPa·s) and γ is the shear rate (s^{-1}).

The so-called Newtonian fluids exhibit a viscosity which is constant and not depending on the applied force. On the contrary, if viscosity increases with shear rate (shear thickening) or decreases with the shear rate (shear thinning) the fluid displays non-Newtonian behavior.

In the case of suspensions of particles, both Newtonian or non-Newtonian behavior have been observed, according to the concentration and dimension of the suspended particles.

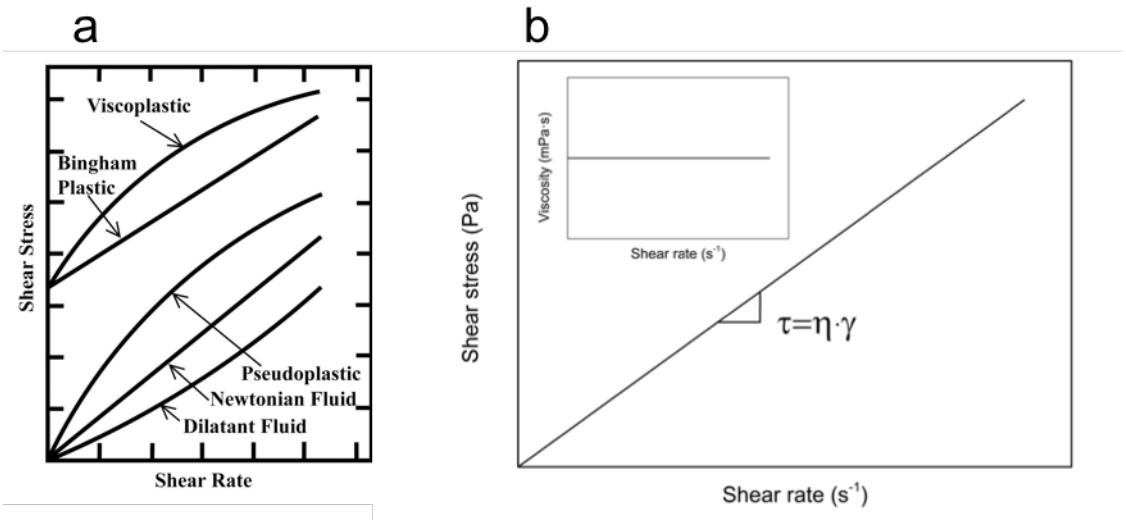

Fig 4.6: Different flow behaviors of Newtonian and non-Newtonian fluids (a); shear stress and viscosity (inset) as a function of shear rate for a Newtonian fluid (b).

In the case of a Newtonian fluid, the viscosity is represented by the slope of shear stress versus shear rate plot, which shows a linear trend.

Since viscosity can span over a wide range of values and it is not under a square root like the other three terms, it is the parameter affecting the most the printability number. Moreover, being very sensitive to sample preparation procedure and external environmental conditions (temperature, humidity), it is thus important that viscosity is measured immediately after the ink preparation and prior to printing, to ensure a good reproducibility.

Viscosity measurements were carried out using an Anton Paar Rheometer (MCR 302), working in rotational mode. A parallel plate measuring system was chosen, using a 50 mm diameter plate and a gap distance of 0.5 mm.

To prevent solvent evaporation, The temperature was constantly kept at 21 °C and a solvent trap was placed over the measurement plate.

Before measuring the viscosity, the inks were pre-treated with a three-steps procedure aiming at removing any effect coming from the loading procedure of the sample. The three steps consisted of: one minute at a shear rate of 1 s^{-1}; one minute in rest conditions at shear rate 0 s^{-1}, one minute at 1 s^{-1}. The measurements were conducted in step mode, using 60 steps with 10 s waiting time between 1 s^{-1} - 1000 s^{-1} shear rate range.

4.7.5 Printability number

Before printing the ink, the printability was assessed through the calculation of the printability number Z from the properties determined from the previous characterization. Z is defined as:

$$Z = \frac{1}{Oh} = \frac{\sqrt{a \cdot \rho \cdot \sigma}}{\eta} \qquad (11)$$

Where a is the characteristic length (μm) represented by the printing nozzle diameter, ρ is density (g/cm^3), σ is surface tension (mN·m^{-1}) and η is the viscosity (mPa·s).

4.8 Oxygen permeation

The oxygen permeation measurements were conducted in an oxygen membrane rig built at DTU Risø, previously described in the works of Samson and Pirou.[14,15]

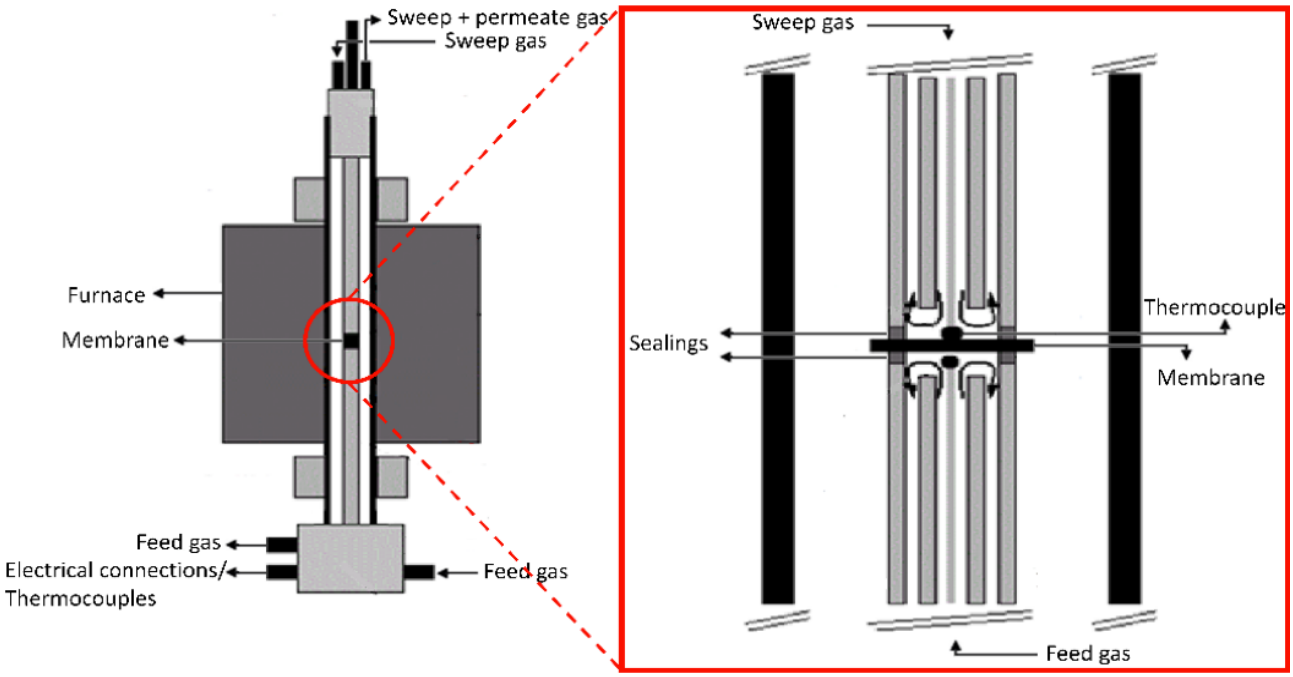

Fig 4.7: Schematic representation of the testing setup used at DTU for oxygen permeation measurements. Taken from [15]

Figure 4.7 shows the scheme of the testing unit used at DTU for the permeation measurements. The sample was placed between two alumina tubes sealing each side of the membrane, creating the chambers. Inside each chamber a tube with thinner diameter was used for introducing the gases into the test house, directly in proximity of the sample. Two thermocouples were placed at the center of the thinner tubes, monitoring the temperature close to the surface of the membrane.

The membrane and the tubes were placed in the middle of a height-adjustable tubular furnace. In order to ensure sealing from the external atmosphere, two rings of tape cast sodium aluminum silicate (NAS, Na_2O 17.8%, Al_2O_3 9.4%, SiO_2 72.8%) [16] with an inner diameter of 9 mm and a 515°C glass transition temperature were placed between the membrane and the alumina tubes. Further sealing was obtained using a NAS paste to coat the side walls and ensure that no oxygen was entering the sweep gas compartment from the outside, so that oxygen was only coming from the permeation membrane. The sealing

was realized after heating up the membrane in air up to 850°C followed by cooling at 750°C. Prior to the testing procedure, the total gas outlet flow was checked at both the sides of the membrane, to exclude the presence of leaks.

During the test air with a flow of 300 $ml_N \cdot min^{-1}$ was fed to the feed side (high pO_2), while various flows of N_2 or CO_2 ranging from 50 to 250 $ml_N min^{-1}$ were fed to the permeate side (low pO_2). The inlet flow of gasses was determined by mass flow controllers (Brooks) while the outlet gas was determined by a mass flow meter (Bronkhorst). An house built zirconia-based pO_2 sensors were used to determine the pO_2 of the inlet (before feeding the membrane) and outlet gas (after sweeping the membrane).

The oxygen permeation flux through the membrane was quantified by the difference between the pO_2 at the inlet and the outlet, as given by:

$$J_{O_2} = \frac{p^{out}_{O_2 permeate} \cdot n^{out} - p^{in}_{O_2 permeate} \cdot n^{in}}{A} \qquad (12)$$

where J_{O_2} is the oxygen permeation flux, $p^{out}_{O_2 permeate}$ and $p^{in}_{O_2 permeate}$ are the oxygen partial pressures of the outlet and the inlet gases, respectively, n^{out} and n^{in} are the molar flow rates of inlet and outlet gases, respectively, and A is the area of the permeate side of the membrane.

The oxygen partial pressure at the two sides was determined by the voltage measured by the sensors and converted through the Nernst equation:

$$V = \frac{RT}{4F} ln \frac{p_{O_2}}{p_{O_2\, ref}} \qquad (13)$$

Where V is the open circuit voltage of the sensor, R, T and F are the gas constant, absolute temperature (K) and Faraday constant, respectively and p_{O_2} and $p_{O_2,ref}$ are the measured pressure (atm) and the oxygen partial pressure at the reference electrode (constantly kept at 0.21 atm), respectively.

4.9 Electrical conductivity measurement

The electrical conductivity (σ) of a sample describes how much the material is capable of conducting charged species like electrons, hole or ions. It is commonly measured in $S \cdot m^{-1}$ and is defined as the reciprocal of the resistivity (ρ):

$$\sigma = \frac{1}{\rho} \qquad (14)$$

Usually resistivity (Ω) is the quantity determined experimentally and conductivity is obtained using (14).

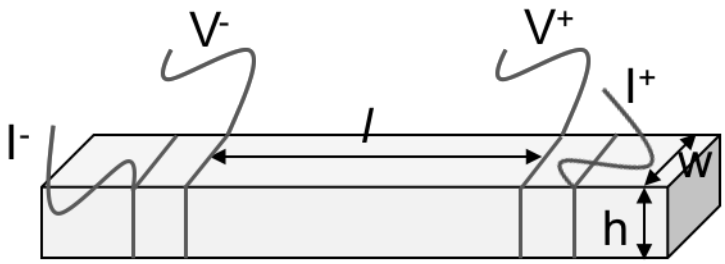

Fig 4.8: Representation of a typical setup used for conductivity measurements: an electric current is flowing between the outer wires and a voltage is measured between the inner wires.

Figure 4.8 shows the most typical setup for conductivity measurement: in this configuration an electric current is applied between the outer wires, and a voltage is measured between the inner wires. The resulting resistance is described by Ohm's law:

$$R = \frac{V}{I} \qquad (15)$$

and the resulting resistivity is:

$$\rho = \frac{w \cdot h}{l} R \qquad (16)$$

where ρ is the resistivity (Ω·m), w and h are the width and the height of the sample (m), respectively, and l is the spacing between the voltage wires (m).

Despite being one of the most widespread geometries, rectangular bars are not necessarily easy to produce and the wiring procedure should be very careful, in order to avoid loose contact or a change in l. Moreover, the resistivity is measured only in the direction of the probes.

Another possible configuration for the measurement of the resistivity exploits cylindrical pellets, in two-dimensional approximation. This condition is fulfilled as long as the pellet radius is much larger than its thickness. Moreover it should be uniform, with no voids present on the surface.

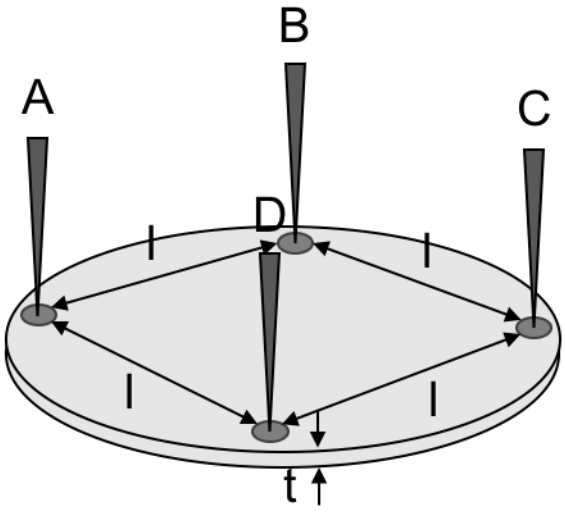

Fig 4.9: Representation of a typical setup used for in-plane conductivity measurements: four probes are symmetrically placed near the edges of the sample and contacted with conductive paste.

In this configuration, called Van der Pauw technique, the conductivity is measured in plane between four probes which are equally spaced and forming a square. As an example, if current flows between probes A and B and a voltage is measured between probes C and D, the resulting resistance is:

$$R_{ABCD} = \frac{V_{CD}}{I_{AB}} \qquad (17)$$

Such a configuration has different advantages: it is geometry independent, allowing to measure the resistance even on samples of irregular shape, but, even more important, through a rotation of the measurement probes, provides a measurement of the average resistance of the sample. In fact, after a rotation of the probes A→B, B→C, C→D, D→A it is possible to measure the resistance (R_{BCDA}) in the perpendicular direction with respect to the starting point. Van der Pauw demonstrated the following relation:[17]

$$e^{-\frac{\pi \cdot d \cdot R_{ABCD}}{\rho}} + e^{-\frac{\pi \cdot d \cdot R_{BCDA}}{\rho}} = 1 \qquad (18)$$

From which, generalizing R_{ABCD} as the horizontal resistance (R_{hor}) and R_{BCDA} as vertical resistance (R_{ver}), the resistivity of the sample can be obtained:

$$\rho = \frac{\pi \cdot d}{ln2} \frac{(R_{hor}+R_{ver})}{2} \cdot f \qquad (19)$$

where ρ is the resistivity (Ω·m), d is the thickness of the sample (m), R_{hor} and R_{ver} are the resistances (Ω) determined in the two perpendicular directions and f is a corrective factor. f is derived from the series expansion of (18) and is taking in account the difference in the values of R_{hor} and R_{ver}. Figure 4.10 shows, that up to 30% difference in the values of R, f could be omitted with an accuracy in the measurement within 99%.[18]

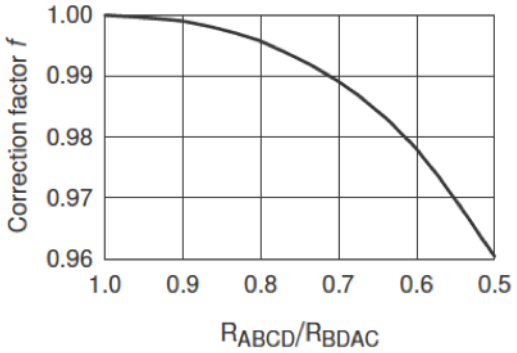

Fig 4.10: Correction factor f as a function of the R_{hor}/R_{ver} ratio. Taken from [18]

4.10 Electrochemical Impedance Spectroscopy

Electrochemical Impedance Spectroscopy (EIS) is a non-destructive measurement technique for the characterization of electrochemical systems. The power of this technique is the possibility of separate analysis of different electrochemical processes happening simultaneously at the electrode through a single frequency scan. This allows to isolate the influence of chemical and physical phenomena at a certain potential.[19]

The EIS measurement consists of applying an alternating potential signal (AC) at a fixed frequency to an electrochemical cell and then reading the current response through the cell, scanning a wide range of frequencies. It is crucial that the amplitude of the signal is small, in order to be sure to obtain a pseudo-linear response from the cell. In that case, the response of the system to a sinusoidal excitation will be a sinusoidal wave at the same frequency, but including a phase shift term. Since the measurement is operated in alternate current, the excitation potential and the response current can be written as:

$$E(t) = E_0 \cdot sin(\omega t) \qquad (20)$$

$$I(t) = I_0 \cdot sin(\omega t + \varphi) \qquad (21)$$

The impedance response Z is calculated using the generalized form of Ohm's law:

$$Z(t) = \frac{E(t)}{I(t)} = \frac{E_0 \cdot sin(\omega t)}{I_0 \cdot sin(\omega t + \varphi)} = Z_0 \frac{sin(\omega t)}{sin(\omega t + \varphi)} \qquad (22)$$

where E_0 and I_0 are the amplitudes of the AC potential and current, Z_0 is the impedance, ω and t are the angular frequency and time, respectively and φ is the phase shift.

Recalling Euler's notation, the potential and current response can be expressed as:

$$E(t) = E_0 \cdot e^{(j\omega t)} \qquad (23)$$

$$I(t) = I_0 \cdot e^{(j\omega t - \varphi)} \qquad (24)$$

And the impedance can be rewritten as:

$$Z(t) = \frac{E(t)}{I(t)} = Z_0 e^{(j\varphi)} = Z_0(cos(\varphi) + i \cdot sin(\varphi)) \quad (25)$$

which has a real and an imaginary component:

$$Re(Z) \equiv Z' \equiv |Z| cos\,(\varphi) \quad (26)$$

$$Im(Z) \equiv Z'' \equiv |Z| sin\,(\varphi) \quad (27)$$

The impedance can be plotted in different ways, for example separating the imaginary and real components in the so called Nyquist plot, or as absolute value as a function of frequency, in the so called Bode plot. These plots visualize different and complementary information about the phenomena occurring in the tested sample.[20]

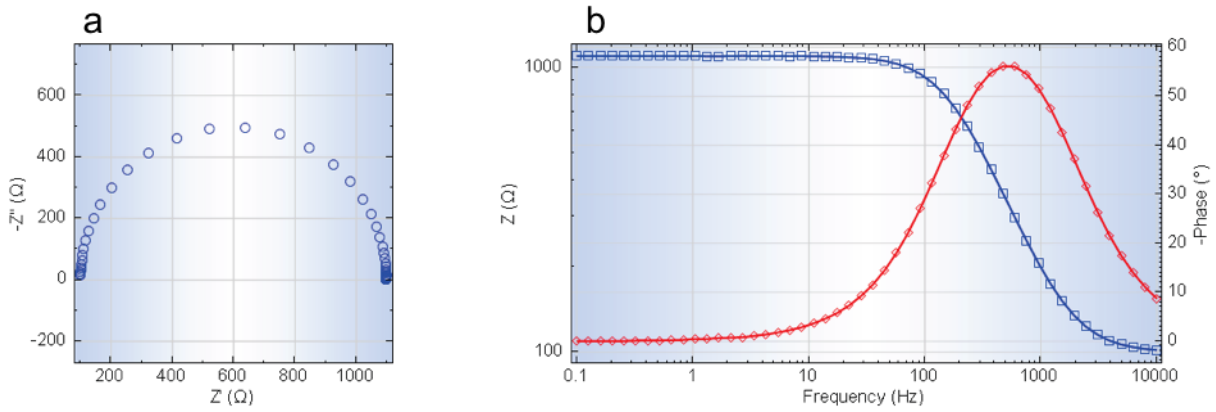

Fig 4.11: Typical Nyquist (a) and Bode (b) plot obtained from EIS measurement. Taken from [20]

In the case of the characterization of a thin film, a two electrode configuration in which the electrodes are deposited on the same surface of the film can be adopted. Such a configuration can be used for measuring the in-plane ionic conductivity of a sample deposited on a dielectric substrate. The dielectric substrate prevents measuring resistance contribution which are not coming from the film.

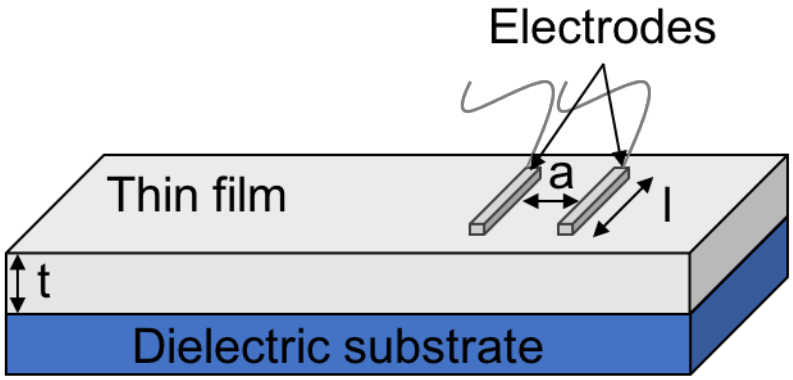

Fig 4.12: Representation of the impedance setup for lateral conductivity measurement carried out on thin films.

Figure 4.12 shows the setup for lateral conductivity measurement on a thin film sample. This is normalized for the geometrical factors of the film:[21,22]

$$\sigma = \frac{l}{R \cdot a \cdot t} \qquad (28)$$

where l is the length of the electrodes (m), R is the resistance (Ω) measured by EIS, a is the distance (m) between the electrodes and t is the thickness of the film (m). The value of R is obtained from the Nyquist plot and is measured as the difference between the intercepts on the real Z axis.

The measurements were carried out using a Solartron 1260 frequency response analyzer and an Autolab PGSTAT204 potentiostat (Metrohm).
All the obtained impedance spectra have been analyzed with ZView software (Scribner associates).

4. 11 Bibliography

1 Condition for the Constructive Interference of Waves from a Crystal Film, http://www.didaktik.physik.uni-muenchen.de/elektronenbahnen/en/elektronenbeugung/einfuehrung/bragg-bedingung.php, (accessed 25 September 2018).

2 What is XPS?, https://xpssimplified.com/whatisxps.php, (accessed 25 September 2018).

3 E. Paparazzo, *Surf. Sci.*, 1990, **234**, L253–L258.

4 D. A. Shirley, *Phys. Rev. B*, 1972, **5**, 4709–4714.

5 D. Briggs and M. P. Seah, 1983, **1**, 397–427.

6 N. S. McIntyre, in *Symposium on Progress in Quantitative Surface Analysis*, ed. ASTM International, 1986, p. 217.

7 G. E. Wanger, C. D.; Riggs, W. M.; Davis, L. E.; Moulder, J. F.; Muilenberg, *Handbook of X-ray Photoelectron Spectroscopy*, Perkin-Elmer Corp., Physical Electronics Division, 1979.

8 Different Types of SEM Imaging – BSE and Secondary Electron Imaging.

9 E. Pomjakushina, , DOI:10.1016/j.materresbull.2004.10.009.

10 B. Wunderlich, in *Encyclopedia of Materials: Science and Technology (Second Edition)*, 2001, pp. 9134–9141.

11 S. Schroeder and M. Gottfried, *Temperature-Programmed Desorption (TPD) Thermal Desorption Spectroscopy (TDS)*, 2002.

12 Particle Size Distribution Calculation Method, https://www.shimadzu.com/an/powder/support/practice/p01/lesson22.html, (accessed 25 September 2018).

13 Bubble Pressure Tensiometer, https://www.kruss-scientific.com/services/education-theory/glossary/bubble-pressure-tensiometer/, (accessed 25 September 2018).

14 A. J. Samson, M. Søgaard and P. Vang Hendriksen, *J. Memb. Sci.*, 2014, **470**, 178–188.

15 S. Pirou, J. M. Bermudez, P. V. Hendriksen, A. Kaiser, T. R. Reina, M. Millan and R. Kiebach, *J. Memb. Sci.*, 2017, **543**, 18–27.

16 K. A. Nielsen, M. Solvang, S. B. L. Nielsen, A. R. Dinesen, D. Beeaff and P. H. Larsen, *J. Eur. Ceram. Soc.*, 2007, **27**, 1817–1822.

17 L. J. Van der Pauw, *Philips Res. Reports*, 1958, **13**, 1–9.

18 N. Bonanos, *Techniques for measurement of the in-plane resistivity*, 2004.

19 C. Gabrielli, 1998, 130.

20 Raw data from FRA measurement, http://www.ecochemie.nl/download/NovaTechNotes/NOVA_technical_note_15_-_Raw_FRA_data_xNOVA_1.10x.pdf, (accessed 25 September 2018).

21 K. Mohan Kant, V. Esposito and N. Pryds, *Appl. Phys. Lett.*, 2012, **100**, 033105-1–3.

22 S. Sanna, V. Esposito, A. Tebano, S. Licoccia, E. Traversa and G. Balestrino, *Small*, 2010, **6**, 1863–1867.

Chapter 4: Characterization techniques and experimental protocols used for the analysis and testing of the samples

Chapter 5

$Gd_{0.2}Ce_{0.8}O_{1.9}/Y_{0.16}Zr_{0.84}O_{1.92}$ nanocomposite thin films for low temperature ionic conductivity

THE DEVELOPMENT OF A NANOSCALE TAILORED, INK-JET PRINTABLE ELECTROLYTE COUPLING CERIA AND ZIRCONIA PROPERTIES FOR SOLID OXIDE FUEL CELLS

In this chapter a novel composite material, coupling the benefits of Gadolinium Doped Ceria (GDC) and Yttrium Stabilized Zirconia (YSZ), is investigated in the form of ink-jet printable sol-gel ink for the realization of a thin film electrolyte for SOFCs.

Ceria is chosen for its superior ionic conductivity already at low temperature (~0.03 $S \cdot cm^{-1}$ at 600 °C), but above 600 °C it is sensitive to reducing environments, which promote the detrimental Ce^{4+}-Ce^{3+} reduction: the presence of a redox couple allows a path for electronic leakage and the reduction is associated with an increase in volume which might compromise the mechanical stability of the electrolyte. On the other side, Zirconia has the advantage of being stable over a wide range of oxygen partial pressures but displays a lower ionic conductivity (~0.0025 $S \cdot cm^{-1}$ at 600 °C) and is reactive towards cathode materials (LSM, LSCF). Typically in a fuel cell the two materials are interfaced in the form of a double layered electrolyte structure, however they have a wide range of reciprocal solubility and the formation of solid solutions could occur at high temperature. The resulting material has a lower ionic conductivity compared to the starting components. Nonetheless, coupling the properties of Ceria and Zirconia allows to exploit their advantages, if the composite is properly tailored.

In order to do that, a novel hybrid route is explored, involving pre-formed GDC nanoparticles (produced via continuous hydrothermal synthesis) and a reactive sol-gel ink as precursor of YSZ. This strategy aims at reducing the temperature necessary for the thermal processing of the materials and offers a good control on the stoichiometry,

allowing to prevent uncontrolled mass diffusion. Using a liquid starting material, this can be suitable to be processed by ink-jet printing for the production of a thin film electrolyte. For this purpose, the properties of the liquid ink relevant for printing (particle size dispersion, surface tension and viscosity) are characterized.

The crystal structure and microstructure of the calcined GDC/YSZ nanocomposite are investigated in order to characterize the solid solution formation mechanism and determine the stability of Ce/Zr interface, aiming to observing if a relevant amount of Ce^{3+} is formed in reducing conditions.

The resulting electrochemical properties of the nanocomposite may represent a good trade-off between stability and high ionic conductivity in a single electrolytic material.

5.1 Introduction

Solid state ionic conductors, *i.e.* solid state ionics, are an important family of materials that can transport electrical current through ions, either positive (e.g. Li^+, H^+, Na^+) or negative (O^{2-}, OH^-). They are the building blocks of energy conversion and storage devices, including batteries, fuel cells and membranes.

Oxygen defective metal oxides are used as O^{2-}-ions electrolytes and electrodes in the form of ceramic layers for applications such as sensors, solid oxide fuel cells, electrolysers and membranes. For the electrolyte, dense layers ensure separation and gas-tightness between two chemical environments of different reactive atmospheres, *e.g.* fuel and air. Electrolytes also require a nearly pure ionic transport, in order to avoid electronic losses and drops of efficiency.[1–3] For the electrodes, mixed ionic-electronic conductivity (MIEC) and chemical reactivity towards gases are typically achieved by mixing electrochemically active materials with ionic conductors, especially with the aim to enhance contact zone suitable for the solid-gas conversion reactions.[4] Mixed electronic-ionic conductivity is also required in membranes for oxygen separation or oxidation of hydrocarbons.[5,6] Among the O^{2-} conductive materials, defective oxides with AO_2 fluorite structure have been intensively investigated for their high ionic conductivity and chemical stability, and yttrium stabilized zirconium oxide (YSZ) and gadolinium doped ceria (GDC) are still the most used materials.[7,8] For zirconia, the most performing cubic phase is stabilized by doping with trivalent cations, *e.g.* Y^{3+}, that introduces extrinsic oxygen vacancies, resulting in a material with wide thermochemical stability and nearly pure ionic conductivity of $\sim 10^{-2}$ $S \cdot cm^{-1}$ at 800 °C under both low and high O_2 gas concentrations.[9] Differently from zirconia, cerium oxide (ceria, CeO_2) is naturally stable in cubic structure with a high concentration of intrinsic oxygen defects. Oxygen vacancy concentration is further enhanced extrinsically via acceptor dopants, *e.g.* by Gd^{3+}, reaching a typical ionic conductivity of $\sim 10^{-2}$ $S \cdot cm^{-1}$ at just 600 °C.[9] Despite being a faster conductor than YSZ, doped-ceria exhibits a non-negligible electronic conduction at low oxygen activity and high temperature ($T > 600$ °C, $pO_2 < 10^{-20}$ atm), due to a small-polarons conduction effects rising from the co-existence of Ce^{4+}/Ce^{3+} oxidation states.[10] Ce^{4+} reduction to Ce^{3+} is also accompanied by a severe increase of the crystalline cell's volume, *i.e.* chemical expansion,

up to 2% of the volume, and even by fast interdiffusive effects at low temperatures.[11,12] The choice for this materials is thus limited by the working conditions under which uncontrolled expansion, interdiffusion and consequent degradation can be accelerated under processing and/or operation.[13–17] Beside conductivity and stability, the performances have to be preserved by nano-scaling the thickness of the layers, *i.e.* in the form of thin films.[18–22] This strategy is widely adopted in miniaturized electrochemical energy devices for low temperatures operation.[23,24] By nano-designing different ionic materials are coupled in multilayers, composites and even in heterostructures, where the role of the interface become dominant over the properties of the constitutive materials.[25–27] As it has already been proved in multi-layered electrolytes, merging the YSZ stability at low pO_2 with the high ionic conduction of GDC is appealing.[22,28,29] However, such a strategy can result cumbersome, especially for traditional ceramic processing routes; GDC and YSZ have the same crystal structure and are reciprocally soluble over a wide range of compositions, forming ceria-zirconia solid solutions during co-sintering,[30,31] which are generally characterized by low ionic conductivity.[32,33] Therefore, consolidation and crystallization of GDC/YSZ composites has to be designed carefully to occur at low temperatures, especially to avoid the formation of the undesired phases, which at the nanoscale with a large interface between the components, can severely affects the overall properties. Moreover, nanostructured materials are characterized by an elevated reactivity and fast diffusion mechanisms that can be easily unleashed by unavoidable thermal-chemical treatments.[34–38]

Among the numerous technologies available for the deposition of thin films, inkjet printing is growing in consideration because of its appealing advantages such as low cost, use in 3D printing platforms, the possibility of continuous and customizable printing, no need of vacuum conditions for the deposition and the large flexibility for printable materials and substrates.[39] For the ink formulations, these are generally either colloidal inks, based on powders, *e.g.* nanoparticles, or reactive metalorganic precursors.[40,41] This allows reducing the temperature for the thermal processing, which is generally used to consolidate particles into continuous ceramic layers.[42]

In this chapter, a novel strategy developed for an ink-jet printable dense nanocomposite which combines the advantages of GDC and YSZ in the form of a single layer is presented. This is achieved through a novel hybrid chemical strategy based on the use of pre-crystallized GDC nanoparticles, synthesized by continuous hydrothermal synthesis, finely dispersed in a reactive YSZ sol-gel solution used as ink. The nanoparticles are adopted to enhance the electrical properties, while the sol-gel is to form a dense YSZ matrix at lower processing temperatures than for the traditional sintering treatments.

Due to the aforementioned criticalities of GDC both in reducing conditions and the formation of detrimental Ce-Zr solid solution, the evolution of crystal structure, composition and microstructure of the nanocomposite is investigated in light of the diffusion mechanisms activated at different thermochemical processing for both reducing and oxidative conditions.

The printing properties of the resulting ink are characterized and a thin film is subsequently printed and its crystal structure and microstructure is characterized. The electrochemical activity of the nanocomposite is finally investigated by impedance spectroscopy, evaluating the stability of performances at conditions of different oxygen activity.

5.2 Experimental

5.2.1 Hybrid $Gd_{0.2}Ce_{0.8}O_{1.9}/Y_{0.16}Zr_{0.84}O_{1.92}$ synthesis

The thin films were synthesized by means of dispersing GDC nanoparticles into a reactive YSZ sol-gel matrix. The colloidal $Gd_{0.2}Ce_{0.8}O_{1.9}$ nanoparticles were synthesized by continuous hydrothermal flow synthesis in the form of water based colloids, as also reported in a previous work[43]. The nanoparticles were subsequently dispersed adding Dispex A40 (Ciba-BASF, UK) to the aqueous solution using an ultrasonic processor (Hielscher UP200St, Germany). The solid loading of the $Gd_{0.2}Ce_{0.8}O_{1.9}$ nanoparticles solution was determined to be 7.1% wt/wt by thermogravimetric analysis (TGA, TG 209 F1 Libra, Netzsch, Germany).

The 8%Y_2O_3-ZrO_2 sol-gel reactive ink was synthesized according to a previously reported method,[41] using N-methyl-diethanolamine (MDEA) as ligand to chelate the zirconium precursor (Zirconium(IV)-propyl solution, 70% wt in 1-propanol, Sigma-Aldrich) to avoid uncontrolled reaction. A complexation ratio (r=[MDEA]/[$Zr(OPr)_4$]) of 12 was chosen, since it previously proved to have a printability index (Z, whose suitability ranges have been defined by Derby[44] and Jang[45]) close to 1 (which was already experienced to give reproducible printability in the case of TiO_2[46]) and stability above 15 days.[41] For the ink, the colloidal $Gd_{0.2}Ce_{0.8}O_{1.9}$ nanoparticles dispersed in aqueous solution were added after the stabilization of the Zr-propoxide with MDEA, in order to prevent hydrolization and gelification of the Zr-complexes. A $Gd_{0.2}Ce_{0.8}O_{1.9}/Y_{0.16}Zr_{0.84}O_{1.92}$ maximum molar ratio of 1/3.3 was fixed, in order to ensure a good printability, prevent cartridge's nozzles clogging[40] and avoid percolation.

Thermogravimetric analysis in air was performed on the as prepared ink (TGA, TG 209 F1 Libra, Netzsch, Germany), using a 5 °C/min ramp.

Several ink-samples were calcined at 280 °C in air (this was the minimum temperature needed to dry the starting material and thus to obtain powder-samples, here reported as "as-synthesized"), from 400 to 1400 °C (every 100 °C), in synthetic air (flow rate 25 sccm) and, finally, from 400 to 1200 °C (every 100 °C), in 5% H_2/N_2 (flow rate 25 sccm) for 1 hour.

5.2.2 Samples characterization

The evolution of the crystallographic phase for each material was investigated by X-ray diffraction (XRD) with a Bruker D8 (Cu-Kα radiation, λ=1.54056 Å) using a solid-state detector and acquiring parameters of 0.01 step size, and 0.5 s·step^{-1} time. Diffraction patterns of powders resulting from the ink calcination at the various temperatures and in the two atmospheres (air, 5% H_2/N_2) were recorded. Both the as-produced particles and the calcined ink were characterized by TEM, using a Jeol JEM 3000F microscope operating at 300 kV.

The SEM characterization of the thermal-treated samples was carried out by a Zeiss MERLIN scanning electron microscope on carbon coated samples.

XPS spectra were carried out with a Perkin Elmer ϕ5600ci Multi Technique System. The spectrometer was calibrated by assuming the binding energy (BE) of the Au $4f_{7/2}$ line to be 84.0 eV with respect to the Fermi level.[47] Both extended spectra (survey −187.85 eV pass energy, 0.5 eV·step^{-1}, 0.05 s·step^{-1}) and detailed spectra (for Ce 3d, Gd 3d, O 1s and C 1s –23.50 eV pass energy, 0.1 eV·step^{-1}, 0.1 s·step^{-1}) were collected with a standard Al Kα source working at 200 W. The standard deviation in the BE values of the XPS line is 0.10 eV. The peak positions were corrected for the charging effects by considering the C 1s peak at 285.0 eV and evaluating the BE differences.[48,49]

5.2.3 Ink characterization and printing of the film

The particle size distribution of the GDC solution and the resulting GDC/YSZ ink was measured by means of a laser particle size analyser (Beckman Coulter LS 13320).

The viscosity of the ink was measured using an Anton Paar Rheometer (MCR 302) operating at a constant temperature of 21 °C in rotational mode, using a 50 mm diameter plate in parallel-plate mode and 0.5 mm gap distance. A solvent trap was used to prevent solvent evaporation. The experiments were performed using a three-steps pre-treatment consisting of one minute at 0.1 s^{-1} shear rate followed by 1 minute rest (0 s^{-1} shear rate) and one minute at 10 s^{-1} shear rate.

The ink surface tension was determined using a bubble pressure tensiometer (BP 50, Krüss).

The resulting printability index Z was assessed considering Derby's definition:[44,50]

$$Z = \frac{1}{Oh} = \frac{\sqrt{a \cdot \rho \cdot \sigma}}{\eta} \qquad (1)$$

Where a is the characteristic length for which the printing nozzle diameter was taken (21.5 μm), ρ is the density (g/cm^3), σ is the surface tension (mN/m) and η is the viscosity (mPa·s).

In order to perform the electrical characterization of the composite material, a thin film was printed with a Pixdro LP50 ink-jet printer. The printer was equipped with DMC disposable piezoelectric printheads from Dimatix that have 16 nozzles with a diameter of 21.5 μm and a nominal droplet volume of 10 pL. Prior to printing, the ink was filtered using a syringe filter with a 450-nm mesh. The thin film was printed on a one-side-polished 1x1 cm square substrate of single crystal (0001) sapphire (Crystal GmbH) using a 400-dpi resolution (corresponding to an estimated printed volume of ca. 0.25 μL/cm^2) and subsequently calcined for 6 hours in air at 750 °C, heating and cooling with 1 °C/min ramps.

The crystal structure of the printed film was determined by grazing incidence X-ray diffraction (ω=0.5 °), with 0.01 step size and 0.5 s·step^{-1} time acquiring parameters.

5.2.4 Electrochemical characterization

Electrochemical impedance spectroscopy (EIS) was performed in a symmetric 2-electrode configuration by using a Solartron 1260 frequency response analyser over the frequency range of 1 Hz-86 kHz, using 200 mV AC voltages for the acquisition. This configuration is suitable to characterize the in-plane ionic conduction in the thin film samples on dielectric substrates, as also reported in previous papers.[15,51,52]

To measure the lateral conductivity of the sample, symmetric silver electrodes with *ca.* 1 mm spacing and 2 mm width were painted on the surface of the thin film. EIS measurements were performed in the temperature range of 400–750 °C in synthetic air flow (flow rate 50 sccm, waiting 30 minutes for sample's equilibration before every data acquisition) and the obtained resistance was normalized by the geometrical factors (the thickness of the film was determined after testing through SEM characterization of cross

section on the cold-fractured sample). Total conductivity measurements were performed in different oxygen activity atmospheres at 600 and 650 °C in stream of synthetic air, nitrogen and 5% H_2/N_2 (flow rate 50 sccm).

5.3 Results and discussion

5.3.1 YSZ formation

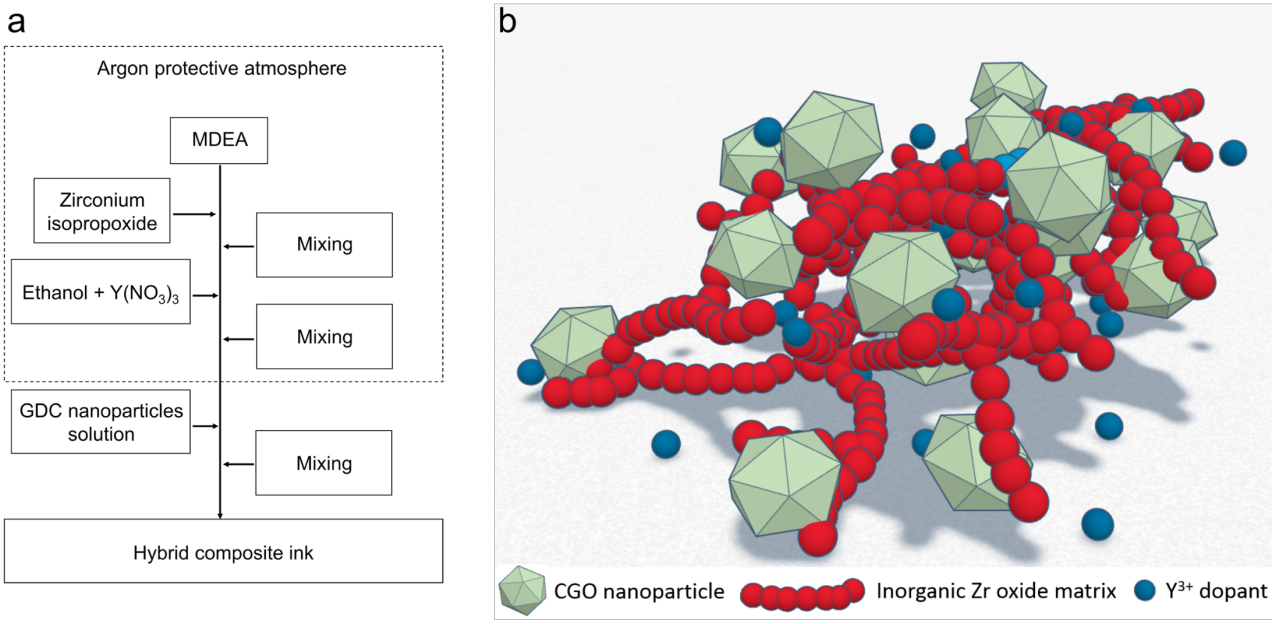

Fig 5.1: Preparation protocol for the ink (a) and concept representation of the hybrid GDC/YSZ electrolyte before the thermal treatment (b).

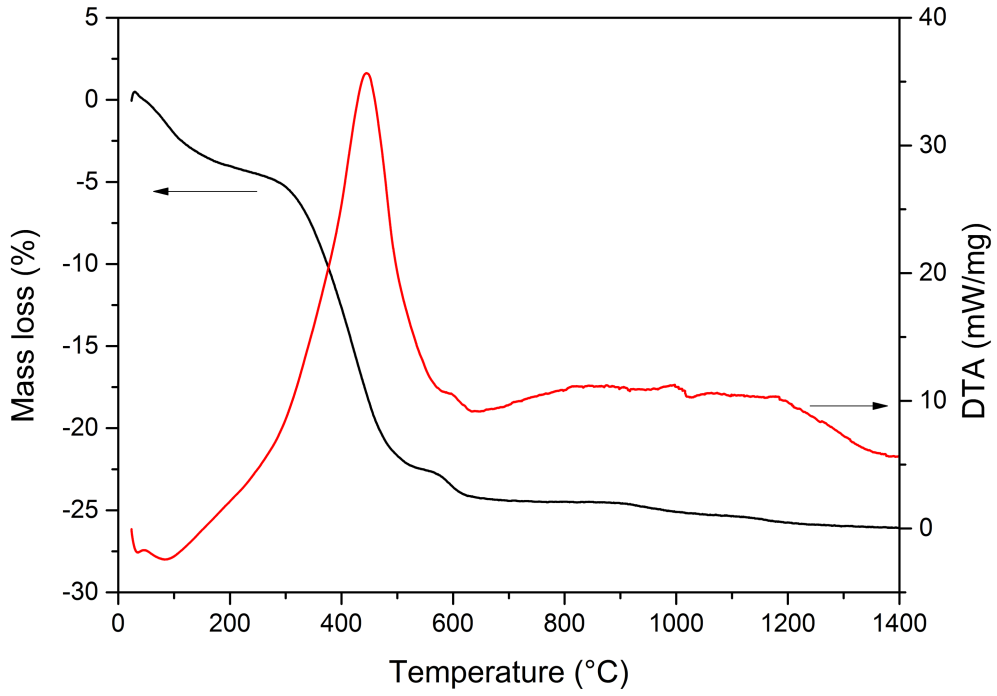

Fig 5.2: Thermogravimetric analysis (TGA) and differential thermal analysis (DTA) of the sol-gel ink in air, measured in the RT-1400 °C range, with 5 °C/min thermal ramp.

Figure 5.1b shows the concept of the hybrid electrolyte material synthesized in the form of sol-gel before the calcination step (solvents and MDEA are not represented). It is possible to observe the GDC nanoparticles surrounded by a matrix of Zr-alcoxide chains that creates a continuous framework in which the yttrium dopant ions are uniformly dispersed. Figure 5.2 shows the results of the TGA/DTA on the sol-gel material in air. From the thermogravimetric analysis it is possible to observe that different weight loss regions are present, which are related to removal of ethanol and water solvents (RT-120 °C), decomposition of the MDEA (120-280 °C) and removal of residual carbon (280-500 °C). The observed regions are consistent with a former study on titania sol-gel inks, where Ti-propoxide precursor was chelated with MDEA.[46] The differential thermal analysis shows the presence of a large peak associated with the removal of carbon at 450 °C, therefore the formation of crystalline zirconia is expected to occur between 280 and 450 °C. In the case of pure YSZ, in a previous study on the printability of a YSZ sol-gel ink, the onset of crystallization was observed at 500 °C.[41] The choice of the temperature for the thermal treatment should consider that nanosized systems are highly reactive and for an use as electrolyte, the formation ceria/zirconia solid solution is not desired, as it has a lower ionic conductivity compared to YSZ and GDC.[32,33]

Therefore, for the synthesis of a nanocomposite of GDC and YSZ it is crucial that the two materials do not undergo interdiffusion phenomena. Ceria and zirconia, however, have the same crystalline structure and a wide range of reciprocal solubility is reported for cerium and zirconium oxide.[30,31,53] Elemental diffusion, and thus mass diffusion, in such defective oxides is a complex effect that is controlled by oxygen defects and cation migration.[54] Moreover, mass diffusion in ceria-zirconia systems can be dramatically changed with the atmosphere. Typically, while in air Zr^{4+} is the predominant ion diffusing into the GDC lattice, in reducing conditions the diffusion process is reversed, becoming Ce^{3+} the predominant diffusing ion. This is due to a higher concentration of vacancies and larger interstitial sites produced by reducing conditions, unleashing Ce^{3+} mass diffusion.[55,56] The diffusion processes do not depend only on the thermochemical conditions, but are also affected by other parameters such as the presence and the amount of dopants, the crystallinity degree of the compounds and even the dimensions of the particles can play a relevant role in facilitating or hindering mass diffusion.[31,57]

5.3.2 XRD

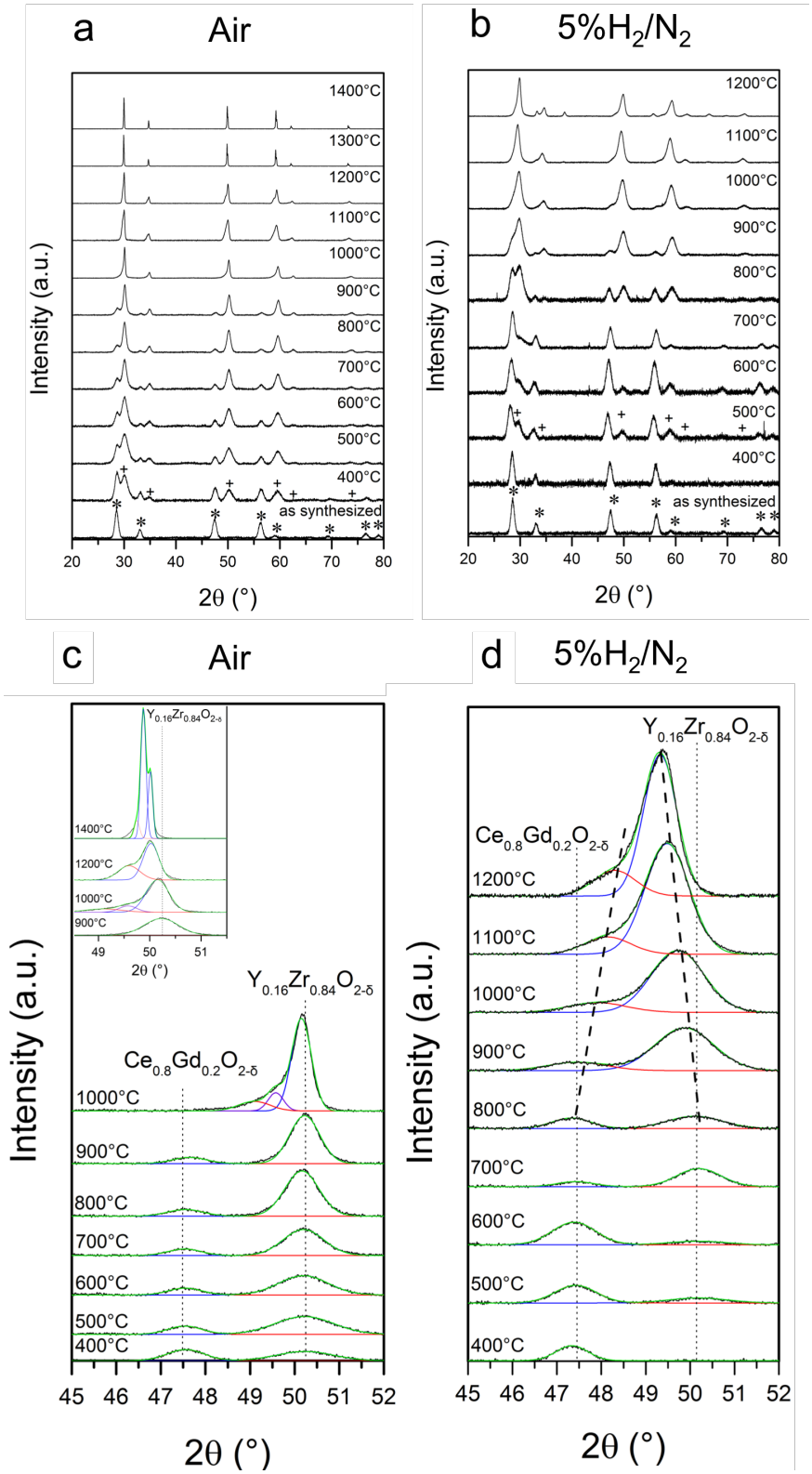

Fig 5.3: Normalized X-ray diffraction patterns of samples calcined in air up to 1400 °C (a), samples calcined in 5% H_2/N_2 atmosphere up to 1200 °C (b); $Gd_{0.2}Ce_{0.8}O_{1.9}$ (*) and $Y_{0.16}Zr_{0.84}O_{1.92}$ (+) references symbols included. Magnification on (220) peak up to 1000 °C of samples calcined in air (c), with inset on high temperature evolution of YSZ peak; magnification on (220) peak up to 1200 °C of samples calcined in 5% H_2/N_2 (d).

When interdiffusion occurs, the migration of cations with different valence, ionic radius or coordination induces a modification of lattice parameter in the host lattice. As a result, the lattice parameter can expand if a larger ion enters the lattice or shrink if it diffuses out from the lattice, *e.g.* if Y^{3+} diffuses out from YSZ this will result in a shrinkage of the lattice parameter, having Y^{3+} a larger ionic radius (r=1.02 Å in cubic 8-fold coordination)[58] than Zr^{4+} (r= 0.84 Å in cubic 8-fold coordination).[58] Since the modification of lattice parameters induces a shift of the diffraction peaks compared to those of the original structure, X-ray diffraction is able to provide useful information about diffusion processes.

Figure 5.3 shows the evolution of the crystal structure with temperature in the different atmosphere conditions, *i.e.* in air (a, c) and in 5% H_2/N_2 (b, d). The as-synthesized samples (Figures 5.3 a and b) display the typical diffraction pattern of cubic GDC but no reflections of the YSZ. These become clearly visible from 400 °C for the samples calcined in air and slightly evident from 500 °C for the samples calcined in 5% H_2/N_2. Compared to our former studies on YSZ thin films produced by reactive sol-gel precursors,[41] it is possible to observe that in the case of intimate contact environment with GDC nanoparticles, YSZ crystallization is observed at 400 °C in air (Fig. 5.3 a), a temperature 100 °C lower than in the case of pure YSZ. It is also possible to notice that the formation of YSZ is affected by the calcination atmosphere.

Assuming that the intensity of GDC diffraction peaks is not modified between 500 and 900 °C, the GDC diffraction peaks can be used as a reference to compare the relative intensities of the YSZ peaks. These are more intense when the removal of the organic framework is performed in air (Figure 5.3 a and c), indicating a rapid crystallization of the YSZ phase. On the contrary, for the samples calcined in 5% H_2/N_2 (Figure 5.3 b and d) the formation of YSZ proceeds at lower rates.

The calcination atmosphere plays a role not only in the crystal growth, but even in the diffusion mechanisms, as it can be noticed from the evolution of the (220) reflections of GDC and YSZ (Figure 6.3 c and d). Interdiffusion is activated at a temperature of *ca.* 100 °C lower (900 °C in air and 800 °C in 5% H_2/N_2, respectively) compared to what observed in the case of sintering a mixture of the powders of 130-nm GDC and 100-nm YSZ.[55] The large interface between the matrix and the nanoparticles can likely enhance the diffusion processes. Despite being both activated at low temperatures, the natures of the two

diffusion behaviors appear different. In air the diffusion process occurs abruptly; conversely, in reducing conditions it evolves slowly. Above 900 °C in air (c), complete disappearance of GDC reflections is observed while an asymmetric signal appears at a lower angle with respect to the peak in correspondence to the YSZ, suggesting the formation of a solid solution between GDC and YSZ. Above 1200 °C in air (inset in Figure 5.3 c), it is observed that YSZ and GDC are not completely mixed to form a solid solution with unique composition, as indicated by the presence of two reflections (c, inset) related to two different cubic phases. These are detected at lower angles than YSZ (220) reflection, at 1400 °C, suggesting that the stabilization effect due to Y^{3+} (r=1.02 Å in cubic 8-fold coordination)[58] doping is in competition with the formation of the solid solution at the observed temperatures, hindering the diffusion of zirconium. Despite the similar ionic radiuses of Ce^{4+} (r=0.97 Å in cubic 8-fold coordination, 5% smaller than Y^{3+})[58] and Gd^{3+} (r= 1.05 Å in cubic 8-fold coordination, 3% bigger than Y^{3+}),[58] this effect can be explained considering that Zr^{4+}, Y^{3+} and Gd^{3+} have different diffusion rates due to either differences in cation size (Zr) and charge (Gd, Y) with respect to the hosting cation Ce^{4+}. [59,60]

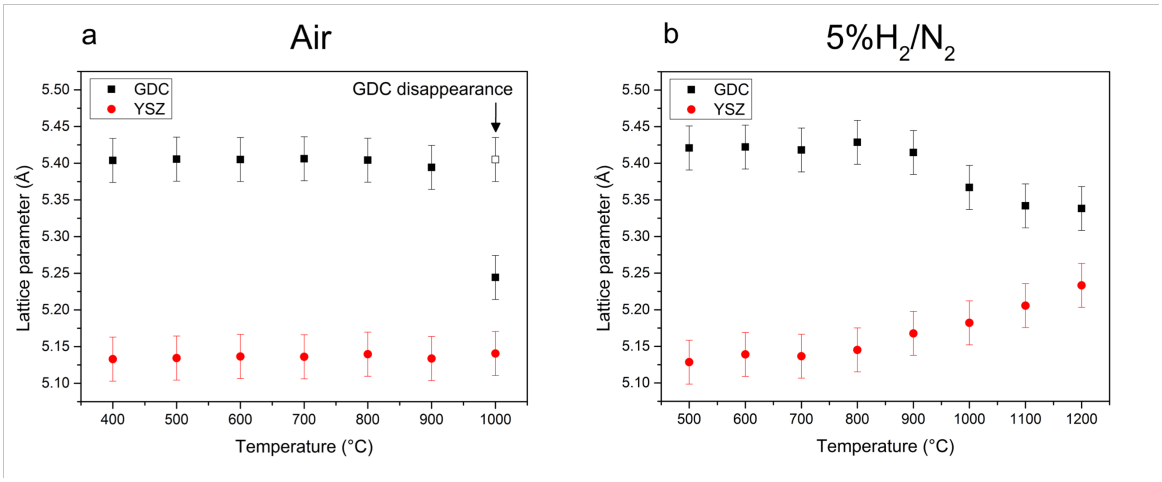

Fig 5.4: Evolution of lattice parameters of GDC and YSZ as a function of temperature, calculated from (220) reflections, for samples calcined in air (a) and in 5% H_2/N_2 (b).

Since a shift of GDC and YSZ lattice parameters is detected at high temperature in reducing conditions, with the former observed to move towards a higher angle and the latter towards a lower angle, the evolution of lattice parameters is investigated. A detailed analysis of the evolution with temperature of lattice parameters, calculated from the XRD (220) reflections, is reported in figure 5.4. This shows that in reducing atmosphere (Figure 5.4 b) the diffusion processes are activated above 800 °C and their evolution is slower

compared to that in air (Figure 5.4 a), where the diffusion is observed above 900 °C. From the calculation of lattice parameters (Figure 5.4 b) it can be noticed that above 800 °C GDC lattice is shrinking, while simultaneously YSZ lattice is expanding. This suggests that a migration of Ce^{3+} (r= 1.14 Å in cubic 8-fold coordination) from GDC to YSZ is occurring, accordingly with literature results. The difference in the rates of the two diffusion processes can be explained considering the different mechanisms involved in the process. Beside the differences in the ionic radius and valence of the cations, grain boundaries can also play a determining role. In air, Zr^{4+} (r= 0.84 Å in cubic 8-fold coordination)[58] diffusion into GDC is favored, having Ce^{4+} a larger radius (r= 0.97 Å in cubic 8-fold coordination which is 15% larger)[58] and the same valence. On the contrary, in reducing conditions the migration of Ce^{3+} (r= 1.14 Å in cubic 8-fold coordination) from the GDC lattice is favored by the presence of a high amount of Ce^{3+} and Gd^{3+} (r= 1.05 Å in cubic 8-fold coordination). However, Ce^{3+} and Gd^{3+} diffusion in YSZ lattice occurs at a slower rate, since it is hindered by both the larger ionic radiuses and the different valence, which have been reported before to give solute drag diffusion effects at the grain boundaries. [61–63]

5.3.3 TEM

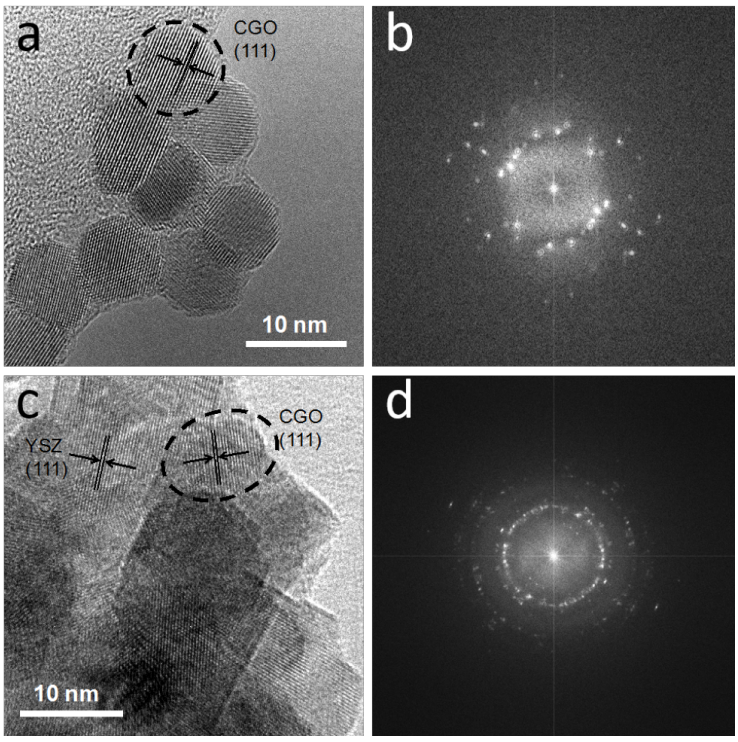

Fig 5.5: TEM images of as-synthesized GDC nanoparticles (a) and relative Fourier transform (b), hybrid $Gd_{0.2}Ce_{0.8}O_{1.9}/Y_{0.16}Zr_{0.84}O_{1.92}$ composite after calcination in air at 800 °C (c) and relative Fourier transform (d).

Figure 5.5 shows the TEM analysis of the as-synthesized GDC nanoparticles with an average diameter below 10 nm. Fourier transform allows measuring the characteristic (111) lattice spacing of 3.1 Å (b). In presence of YSZ matrix calcined at 800 °C in air (Figure 5.5 c) sharp grain boundaries are observed, but it is still possible to distinguish round-shaped GDC particles. Their (111) spacing can still be identified from Fourier transform (d), together with YSZ (111) that has a lattice spacing of 2.9 Å. The values obtained for GDC and YSZ lattice spacing are consistent with the values obtained from the XRD characterization. The evolution of microstructure as function of temperature and calcination atmosphere can be observed by SEM. This technique can provide complementary information about the interaction between the GDC nanoparticles and the YSZ matrix.

5.3.4 SEM

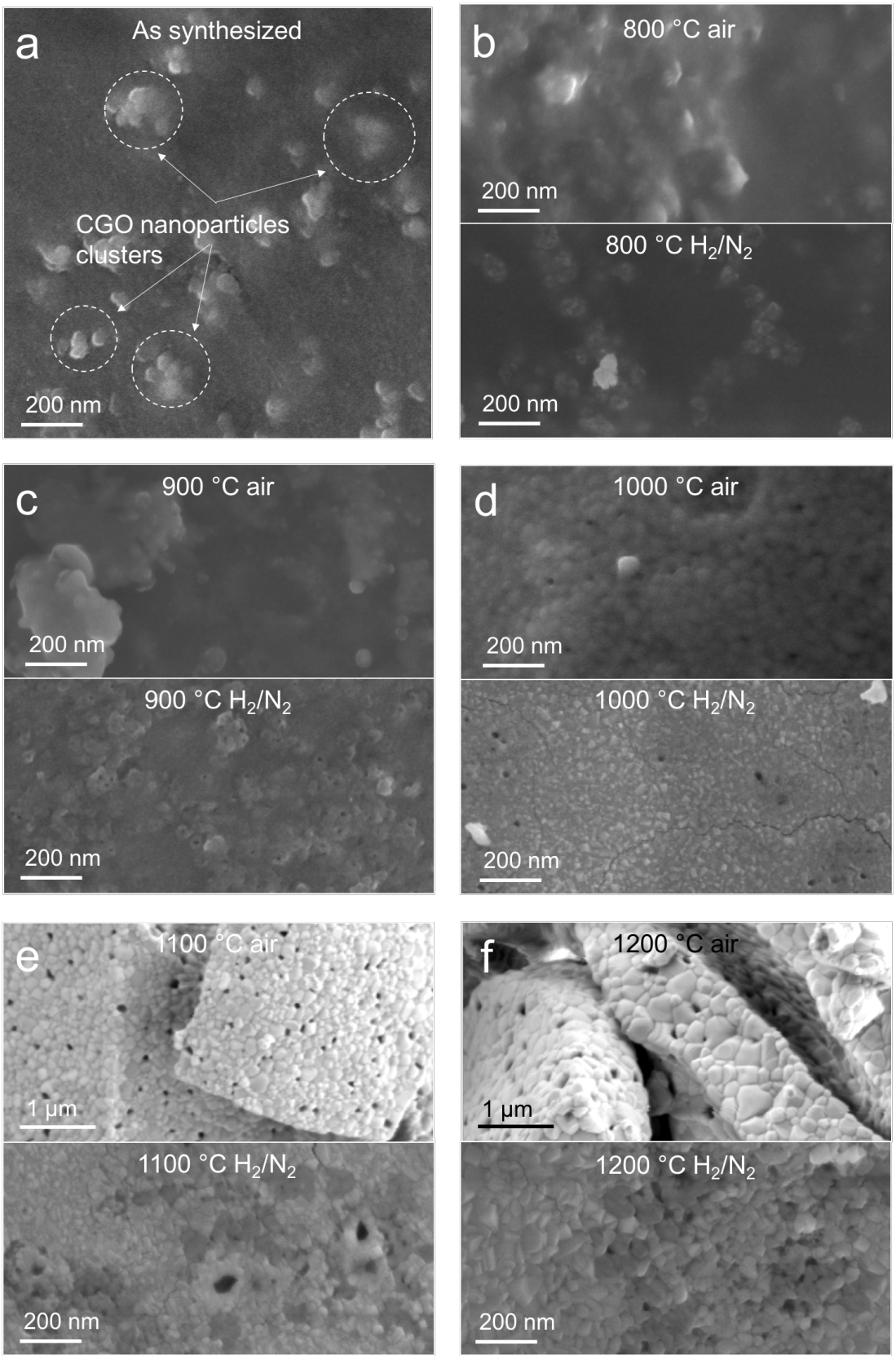

Fig 5.6: Scanning electronic micrographs of the samples: as-synthesized (a) and calcined in air and 5% H_2/N_2 at 800 (b), 900 (c) 1000 (d), 1100 (e) and 1200 °C (f).

Figure 5.6 shows SEM pictures of the microstructure of the samples investigated at different temperatures in air and in 5% H_2/N_2. In the as-synthesized sample (a), small clusters of GDC nanoparticles are immersed in the YSZ matrix and individual particles of each phase could not be detected. As also discussed in figure 5.3 c, d, X-ray diffraction does not show any shift in the crystal structures for the samples calcined in air and in 5% H_2/N_2 at 800 °C. This is also confirmed by the SEM observations, where at 800 °C the nanoparticle clusters and the surrounding matrix features can still be recognized, consistently with what is reported in the TEM analysis of the sample calcined in air at 800 °C (Figure 5.5 b).

A significant change is recorded in both air and reducing atmosphere at 1000 °C (Figure 5.6 d). In agreement with what is observed with XRD, a unique microstructure is detected for samples treated in air, where it is not possible to distinguish the features of GDC nanoparticles. In the samples treated in reducing conditions small crystallites with sharpened grain boundaries are formed, but different features belonging to the two starting materials can still be recognized. The microstructure evolution of the nanocomposites at 1200 °C in figure 5.6 f shows a growth in the crystal grains for both the samples treated in air and in 5% H_2/N_2. The grain dimension of the samples treated in air is in the hundreds of nm range, indicating that a remarkable grain growth occurred because of the thermo-chemical treatment. This is not observed in the case of the samples treated in reducing environment, in which numerous crystallites smaller than 100 nm are detected. This effect can be attributed to the high amount of Ce^{3+} present in reducing conditions above 1000 °C, suppressing zirconia grain boundary migration.

As a summary of such results it is possible to conclude that, despite being activated at a lower temperature by the low oxygen activity (10^{-28} atm< pO_2 <10^{-12} atm between 500 and 1400 °C), the diffusion of Ce^{3+} towards YSZ in reducing environment is severely hindered by the presence of numerous grain boundaries and their structural and chemical properties.

5.3.5 XPS

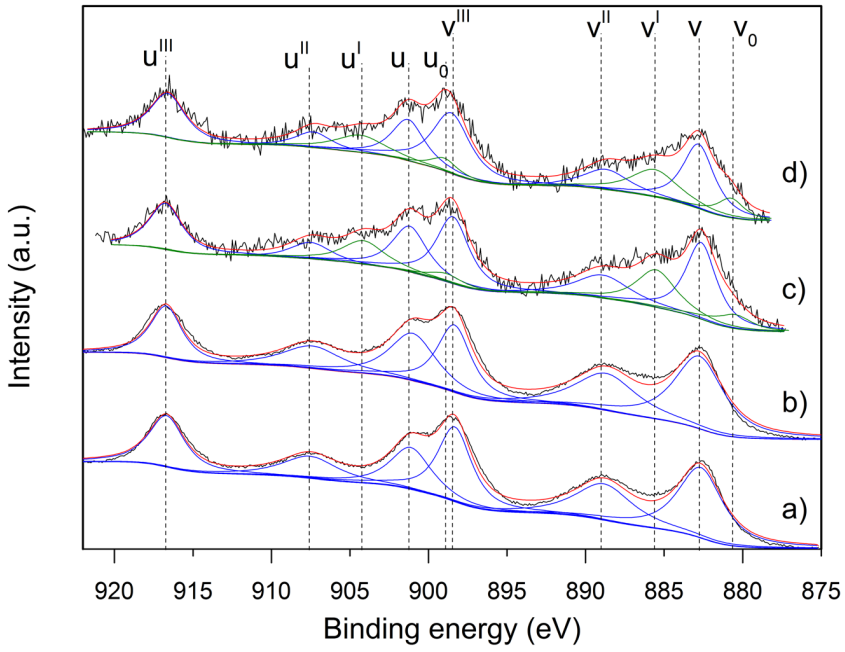

Fig 5.7: Ce 3d photoemission peaks of GDC nanoparticles as-collected (a) and treated at 900 °C in 5%H_2/N_2 (b) and of hybrid GDC/YSZ powders from samples calcined at 900 °C in air (c) and in 5% H_2/N_2 (d).

To clarify the effect of chemical composition on the materials thermochemical evolution, XPS of Ce 3d is carried out. Being aware that the valence state of cerium can be severely affected by the measurement conditions, the analysis of every sample should be carried out separately and the acquisition time should be limited to prevent the cerium reduction artefact.[64]

Figure 5.7 shows the spectrum of cerium with several contributions for each of the 3/2 and 5/2 components. These are marked with *u* and *v* respectively, according to Burroughs' notation,[65] and are due to electron correlation phenomena which affect the final state occupation of Ce *4f* level.[66] This results in six peaks in the case of CeO_2 (*v, v'', v''', u, u'', u'''*) and four peaks for Ce_2O_3 (v_0, *v'*, u_0, *u'*). The two oxidation states have distinct features, so Ce_2O_3 and CeO_2 pure oxides spectra can be used as references for the interpretation of a mixed valence oxide spectrum. However, when both Ce^{3+} and Ce^{4+} are present, the interpretation of the photoemission spectrum can be complicated by the simultaneous presence of ten peaks. Moreover, a simple linear combination of the pure CeO_2 and Ce_2O_3 spectra taken as references can't describe the spectrum accurately, since the ratio between the relative intensities of the peaks is suggested not to change linearly with the

degree of reduction.[67,68] After Shirley's background subtraction, peaks are fitted and the weight of the single oxidation state can be defined as the sum of peaks areas relative to that oxidation state:

$$Ce^{3+} = v_0 + v' + u_0 + u' \qquad (2)$$

$$Ce^{4+} = v + v'' + v''' + u + u'' + u''' \qquad (3)$$

The concentration of Ce^{3+} can be obtained by the ratio:[67,69]

$$Ce^{3+}_{\%} = \frac{Ce^{3+}}{Ce^{3+}+Ce^{4+}} \times 100 \qquad (4)$$

The amount of Ce^{3+} obtained for samples calcined at 900 °C in air (c) and 5% H_2/N_2 (d) is 30% and 34%, respectively. Similar amounts of Ce^{3+} has been observed previously by Mullins. [68]

No Ce^{3+} signals are observed for the as-collected GDC nanoparticles, showing that only Ce^{4+} is present on the surface of the nanoparticles. For a comparison, the spectrum of the bare GDC nanoparticles treated at 900 °C in 5% H_2/N_2 (keeping the gas flow during both the heating and the cooling phase and then exposed to air at room temperature) is reported in figure 5.7 b. No significant modification is observed, suggesting that GDC nanoparticles undergo a fast re-oxidation process. Room-temperature surface oxidation of Ce^{3+} to Ce^{4+} has been observed previously.[70]

This shows that the presence of the YSZ matrix has an influence on the surface of GDC nanoparticles, suggesting a possible interaction between cerium atoms on the surface and the zirconium precursor occurring during the calcination treatment. Possible reaction paths are suggested: 1) The Zr-containing matrix in which the GDC nanoparticles are completely immersed (as observed from SEM in figure 5.6) hinders the interaction of GDC with the surrounding atmosphere during calcination; 2) GDC nanoparticles can take part in the oxidation of the organic framework, losing a part of their oxygen. Cerium oxide is a well-known catalyst for oxidation and is capable of releasing oxygen in a reducing environment and at high temperatures;[71] 3) Once the YSZ matrix is formed around the

GDC nanoparticles, Ce^{3+} originated at the interface is stabilized by the interaction with the doped zirconium oxide.

It is worth noticing that beside the surface interaction between GDC nanoparticles and YSZ matrix, no significant changes in the GDC crystal structures are detected from XRD in air below 1000 °C, whereas in the samples treated in reducing atmosphere a contraction in the lattice parameter of GDC is detected at lower temperatures (800 – 1200 °C). This effect suggests that for samples treated in air, the presence of Ce^{3+} is limited to the interface with YSZ matrix, being on the contrary present in higher amount in samples undergoing a reducing treatment. The formation of Ce^{3+} at the interface between GDC and YSZ has been observed before in samples prepared by PLD.[72]

5.3.6 Rheology

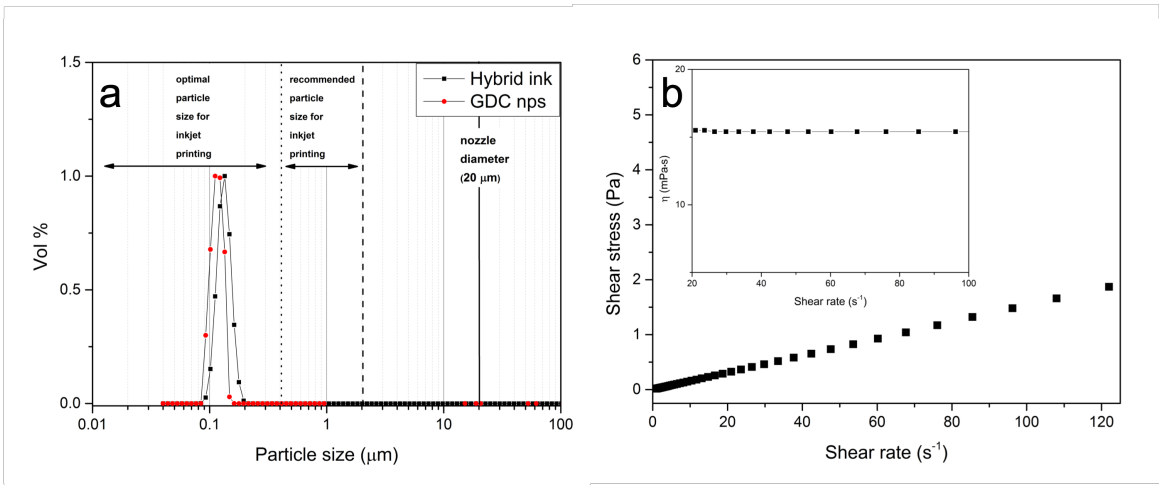

Fig 5.8: Particle size dispersion of the starting GDC solution and the synthesized sol-gel ink (a); shear stress as a function of the shear rate and viscosity as a function of the shear rate (inset) of the sol-gel ink (b).

After the characterization of the interaction between YSZ/GDC and of the diffusion mechanisms occurring in nanocomposite, the properties of the resulting ink are investigated. In order to avoid the nozzle's clogging when printing, the particles size should not exceed a recommended threshold value, which is 10% the nozzles diameter (~2 μm in this case), moreover after adding the nanoparticles solution in the ink formulation, the formation of larger aggregates should be prevented.

Figure 5.8 a shows the results of the particle size dispersion determined for the starting GDC solution and the resulting ink. The particles size has a range between 85 and 150 nm,

with a sharp peak 115 nm, indicating a uniform dispersion of the particles below 2% nozzle diameter (<400 nm, in this case), which represents the optimal recommendation for ink-jet printing. A slight increase in the particles dimension is observed in the sol-gel ink, having a size distribution between 95 and 200 nm with a 135 nm peak, but still included into the optimal region. The size of the aggregates is consistent with what is observed from SEM characterization in figure 5.6 a.

Figure 5.8 b shows the determined viscosity of the ink, which is 15.4 mPa·s and, since the shear stress is increasing linearly with the shear rate, the liquid displays a Newtonian behavior, for which a higher precision in printing is expected.

	η (γ=100 s^{-1}) (mPa·s)	σ ($mN \cdot m^{-1}$)	ρ ($g \cdot cm^3$)	Z
YSZ sol-gel ink	14.9	29.5	1.01	1.64
Hybrid GDC/YSZ ink	15.4	29.5	1.01	1.59

Table 5.1: Viscosity, surface tension, density and resulting printability number for the YSZ sol-gel ink (taken from [41]) and the GDC/YSZ hybrid ink.

The viscosity, surface tension and density of the ink are characterized and compared with the values observed in the case of pure YSZ sol-gel ink. Table 5.1 shows the obtained values: it can be noticed that the addition of GDC nanoparticles is affecting mainly the viscosity of the ink, which increases.

The calculated Z value for the GDC/YSZ ink is 1.59, which is still within the printability range.[44]

5.3.7 Film characterization

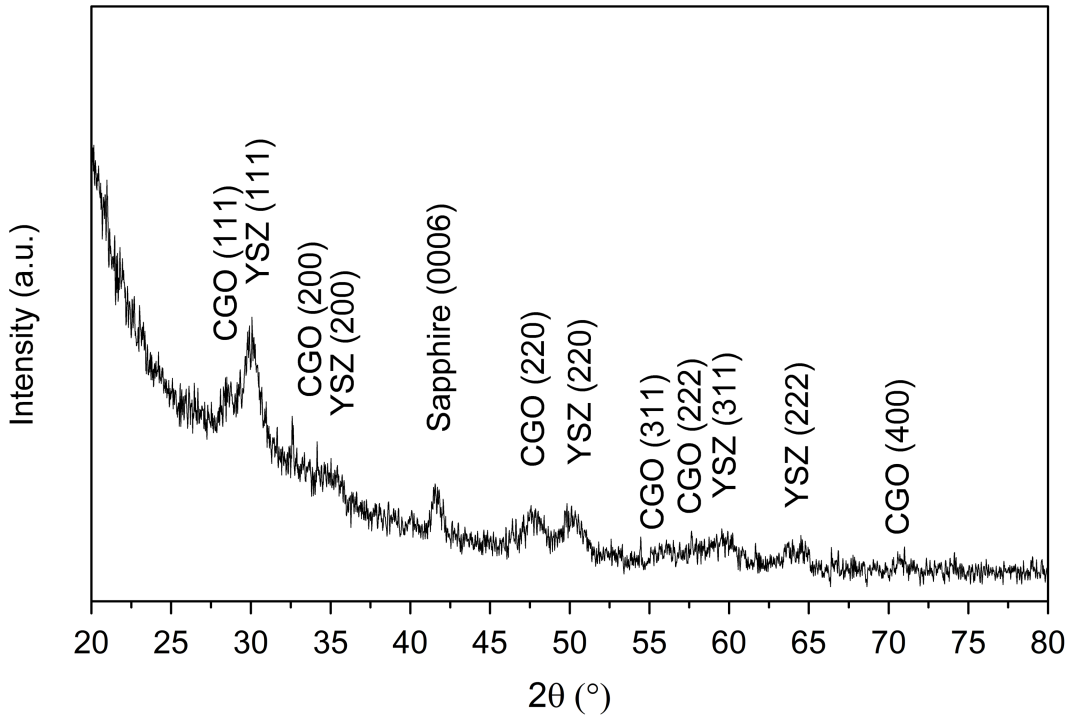

Fig 5.9: grazing incidence (ω= 0.5 °) X-ray diffraction pattern of the GDC/YSZ thin film printed on single crystal sapphire substrate, after 6h calcination at 750 °C in air.

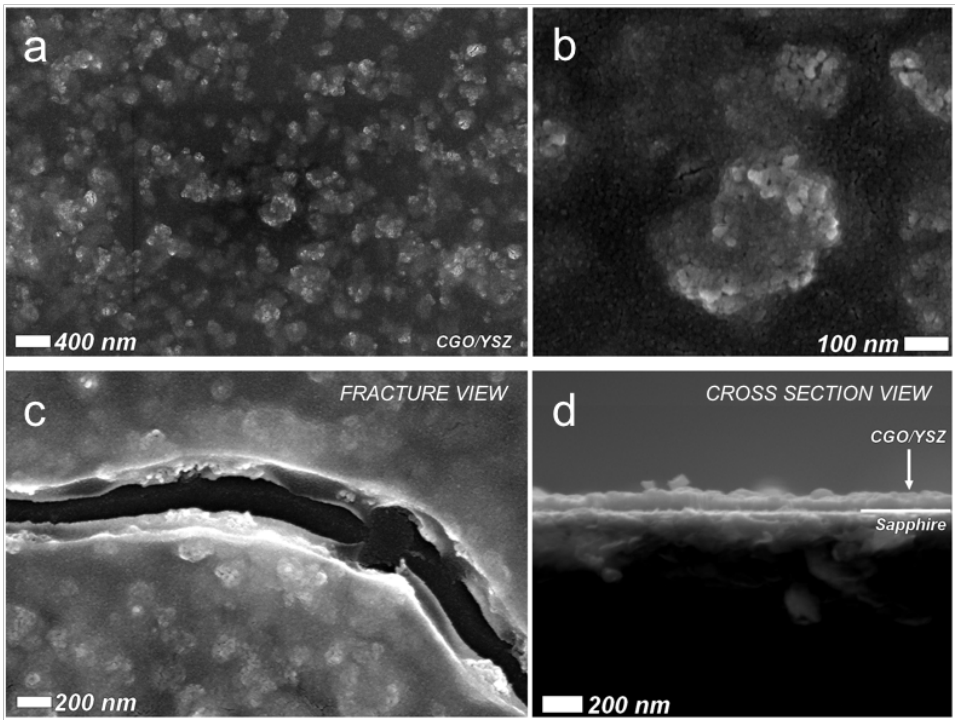

Fig 5.10: SEM images of the thin film printed on sapphire (0001) substrate and calcined at 750 °C in air for 6 hours: top-view pictures showing the dispersed nanoparticles in the matrix forming clusters (a), detail on a cluster of nanoparticles (b), top-view detail on a fracture showing the particles into the YSZ matrix (c); cross section of cold-fractured sample after testing (d).

After printing and calcining the deposited material, the crystal structure of the printed thin film is determined by grazing incidence XRD, and is displayed in figure 5.9: the main reflections of GDC and YSZ can be observed and no secondary phases are detected.
Figure. 5.10 shows SEM observations of the thin film produced by inkjet printing in a single layer deposition on a single crystal (0001) sapphire substrate. The microscopy (Figure 5.10 a) shows a continuous matrix made of YSZ in which a high amount of GDC nanoparticles are dispersed in the form of clusters (shown in detail in figure. 5.10 b). As also observed in the powder-samples (Figure 5.6), also in the thin film the particles are embedded within the YSZ matrix which is surrounding them completely, as can be observed in figure 5.10 c. The cross section of the sample (Figure 5.10 d) shows a continuous uniform layer with a thickness below 100 nm.

5.3.8 EIS

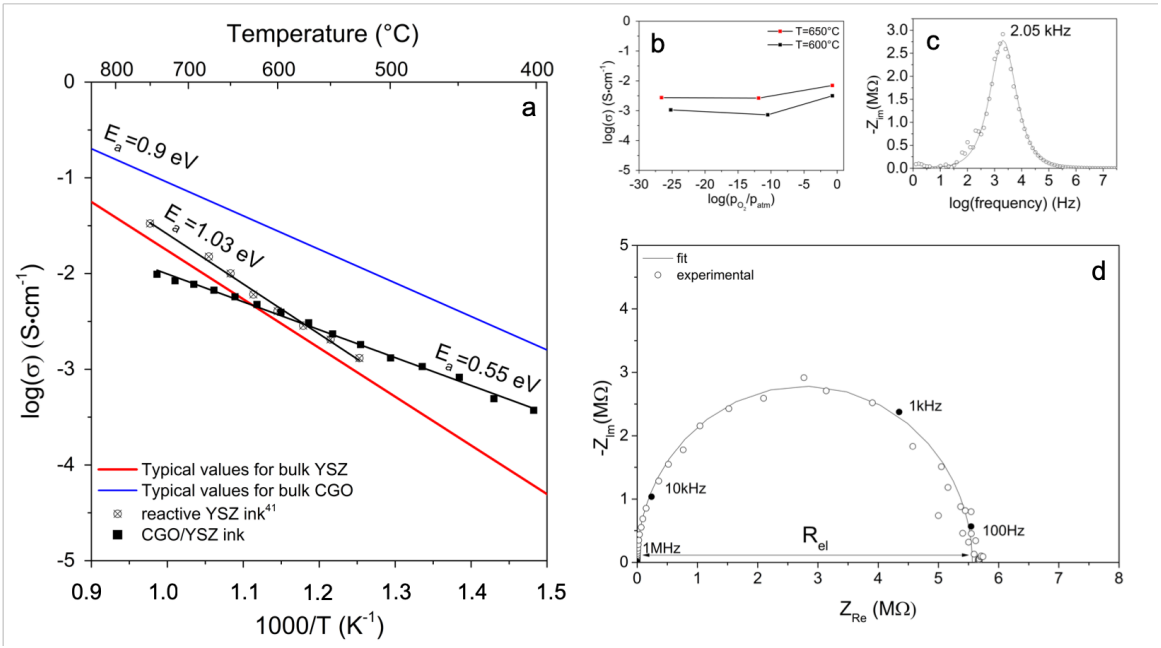

Fig 5.11: Arrhenius plot of in plane conductivity measured on the GDC/YSZ thin film produced by inkjet printing (a), references value for YSZ thin film produced by sol-gel inkjet printing[41] and bulk YSZ[73] and GDC[9] are reported for a comparison. Total conductivity in function of oxygen partial pressure, measured at 600 and 650 °C in air, nitrogen and 5% H_2/N_2 (b); Bode (c) and Nyquist (d) plots for the measurement at 600 °C in air

Focusing on the electrochemical properties, figure 5.11 summarizes the results of the conductivity measurements. The Nyquist plot (d) shows a characteristic single semi-arc in

which the grain boundary is the dominating contribution, and this is modelled with a single R//C Voigt element. This result clearly indicates the activation of ionic conduction with both the activation of ohmic and capacitive effects. The Bode plot of the same data is also included (figure 5.11 c). The overall characterization indicates an ohmic resistance that is measured at the relaxation frequency of 10 Hz, obtaining a value of 5.6 MΩ, and the apex frequency for the capacitive effect at 2 kHz at 600 °C. The resistance values obtained at different temperatures in air are normalized by the geometrical factors and the total conductivity of the sample is plotted as Arrhenius plot in figure 5.11 a. The Arrhenius plot of the conductivity of GDC/YSZ thin film measured in air includes reference values for bulk YSZ [73] and bulk GDC,[9] conductivity values measured for the YSZ thin film produced with sol-gel reactive ink [41] are also included. The conductivity values observed at low temperatures show a beneficial effect of GDC presence in the composite, leading to a conductivity higher than that of the bulk and thin-film YSZ below 600 °C. This can be explained considering the unusual low activation energy obtained (0.55 eV) for the ionic conduction, which suggests the presence of fast contributions likely coming from the grain boundaries and interfaces of the composite.[74] Moreover, these effects highlight the role of GDC and YSZ interface, as what was observed for samples characterized by an inner contact between the two materials where a high oxide ion mobility occurred.[75] A possible reason for that is the presence of Ce^{3+} observed at the interface between the nanoparticles and the matrix, which should be compensated by a higher amount of oxygen vacancies,[72] but the presence of a lattice strain near the interfaces cannot be excluded. A constant capacitance of ca 15 pF is obtained from the fitting of the semicircles, suggesting that the conductivity process is due mainly to the bulk of the grains and may be enhanced by the interface.[76]

The total conductivity is measured at different oxygen partial pressures, (figure 5.11 b), in order to exclude possible electronic conduction contributions coming from GDC. Ceria based electrolytes typically display an abrupt enhancement of conductivity in reducing environments, which is associated with the partial reduction of cerium oxide at low oxygen activities ($pO_2 < 10^{-25}$ atm) and the onset of electronic conductivity. This behavior is well known in ceria-based materials and is due to the formation of Ce^{4+}/Ce^{3+} couple

responsible for electronic conduction, which is promoted in presence of a high amount of dopants.[77]

From the total conductivity measurements (figure 5.11 b), it can be noticed that the total conductivity of the material is not significantly changed in reducing environment. This suggests that the uniform dispersion of GDC nanoparticles does not produce a path of percolation for the electronic conduction, ensuring constant electrolyte performances over a wide range of pO_2.

5.3.9 Printing on NiO/YSZ substrate

The results obtained from the EIS characterization of the GDC/YSZ thin film drove the investigation towards the use of a traditional NiO/YSZ anode. This substrate is produced in house at DTU by tape-casting and allows testing cells with a large area. The deposition of the ink is realized after the thermal processing (debindering and sintering, at 1400 °C) and polishing of the anode, to reduce the impact of surface roughness on the film.

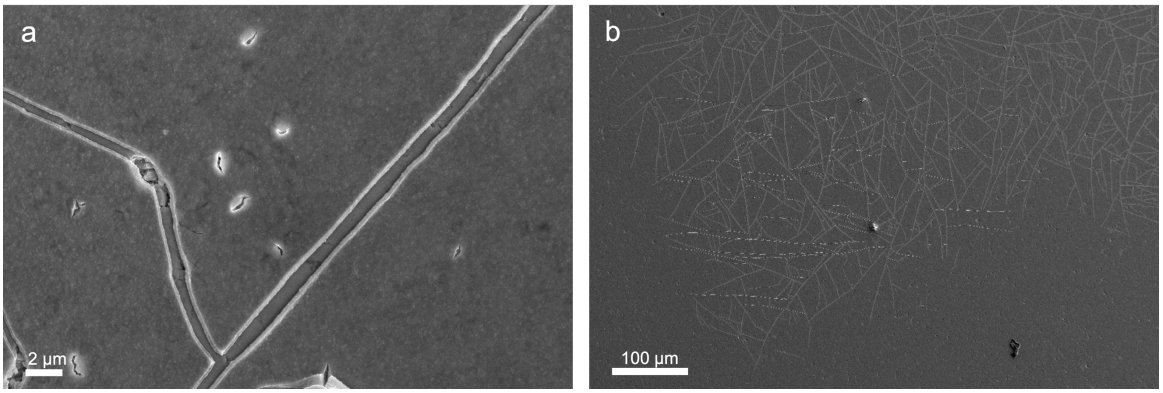

Fig 5.12: SEM images of the layer printed on polished NiO/YSZ substrate at high (a) and low magnification (b)

Figure 5.12 shows the surface of the printed layer, which is characterized by the presence of many cracks of different dimensions that don't allow using the substrate for a cell. These have been observed for different printings and thermal processing conditions. The small ones (length: ~1 µm) are probably due to the porosity of the substrate, which could result in non-uniform thickness of the printed layer due to capillarity effects, while the large ones (length: 10-100 µm) seem to be related to the shrinkage of the film occurring during the removal of the organics. Further efforts to produce a crack-free substrate and test a complete cell are still in progress.

5.4 Conclusion

In this chapter a novel $Gd_{0.2}Ce_{0.8}O_{1.9}/Y_{0.16}Zr_{0.84}O_{1.92}$ nanocomposite has been produced as an ink-jet printable thin-film. This is achieved by a hybrid chemical method including the dispersion of GDC nanoparticles into a YSZ sol-gel reactive matrix. This approach allows obtaining a composite material suitable for low-temperature processing and GDC nanoparticles show a beneficial effect on the formation of crystalline YSZ, which is already detected at 400 °C.

The resulting material does not show presence of interdiffusion phenomena below 900 °C, where the onset of diffusion in reducing environment is detected. The diffusion mechanism is deeply influenced by the thermochemical environment: in air, a sudden disappearance of GDC (probably due to fast diffusion of Zr) is observed at 1000 °C; in reducing conditions the diffusion is sluggish and associated with a migration of Ce^{3+} from GDC to YSZ, resulting hindered by both the large dimension of the cation and the large amount of grain boundaries present in the material.

The formation of a small amount Ce^{3+} at the interface between GDC and YSZ is observed by XPS and seems to be independent from the calcination atmosphere. Compared to reduced bare nanoparticles, which rapidly reoxidize when exposed to air at room temperature, the nanocomposite shows a stabilizing effect of the YSZ matrix on Ce^{3+}.

The particle size dispersion of GDC is analyzed, showing a thin dispersion range centered around 100 nm, which becomes slightly large in the GDC/YSZ hybrid ink. In both cases the size of the particles is within the optimal range for printing. Compared to the case of pure YSZ sol-gel ink, the incorporation of GDC nanoparticles is slightly modifying the printing parameter Z, being still within the range of printability defined by Derby.

The electrochemical performance of the hybrid electrolyte displays a synergic coupling effect of the YSZ matrix thermochemical resistance with an elevated ionic conductivity enhanced by the presence of non-percolating GDC nanoparticles, obtaining 0.005 $S \cdot cm^{-1}$ at 600 °C. This is reflected by the stable conductivity properties at different oxygen partial pressures.

When the layers are printed on a traditional NiO/YSZ anode substrate, the formation of cracks occurs.

5.5 Bibliography

1 V. V Kharton, F. M. B. Marques, J. A. Kilner and A. Atkinson, in *Solid State Electrochemistry I: Fundamentals, Materials and their Applications*, 2009, pp. 301–334.

2 B. C. H. Steele, *Solid State Ionics*, 1992, **3**, 17–28.

3 B. C. H. Steele, *Curr. Opin. Solid State Mater. Sci.*, 1996, **1**, 684–691.

4 V. Dusastre and J. A. Kilner, *Solid State Ionics*, 1999, **126**, 163–174.

5 H. J. M. Bouwmeester and A. J. Burggraaf, in *Membrane Science and Technology*, 1996, vol. 4, pp. 435–528.

6 Z. Shao, G. Xiong, J. Tong, H. Dong and W. Yang, *Sep. Purif. Technol.*, 2001, **25**, 419–429.

7 J. A. Kilner, *Solid State Ionics*, 2000, **129**, 13–23.

8 X. Guo and R. Waser, *Prog. Mater. Sci.*, 2006, **51**, 151–210.

9 K. C. Wincewicz and J. S. Cooper, *J. Power Sources*, 2005, **140**, 280–296.

10 H. L. Tuller and A. S. Nowick, *J. Phys. Chem. Solids*, 1977, **38**, 859–867.

11 D. Marrocchelli, S. R. Bishop, H. L. Tuller and B. Yildiz, *Adv. Funct. Mater.*, 2012, **22**, 1958–1965.

12 D. W. Ni, J. A. Glasscock, A. Pons, W. Zhang, A. Prasad, S. Sanna, N. Pryds and V. Esposito, *J. Electrochem. Soc.*, 2014, **161**, F3072–F3078.

13 E. D. Wachsman and K. T. Lee, *Science (80-.).*, 2011, **334**, 935–939.

14 S. de Souza, S. Visco and L. C. De Jonghe, *Solid State Ionics*, 1997, **98**, 57–61.

15 S. Sanna, V. Esposito, M. Christensen and N. Pryds, *APL Mater.*, 2016, **4**, 121101-1–5.

16 P. Lacorre, Ë. Goutenoire, O. Bohnke, R. Retoux and Y. Laligant, *Nature*, 2000, **404**, 9–11.

17 D. W. Jung, K. L. Duncan and E. D. Wachsman, *Acta Mater.*, 2010, **58**, 355–363.

18 S. Lee, W. Zhang, F. Khatkhatay, H. Wang, Q. Jia and J. L. Macmanus-Driscoll, *Nano Lett.*, 2015, **15**, 7362–7369.

19 L. MacManus-Driscoll, *Fuel Cells Bull.*, 2016, **2016**, 15.

20 C.-C. Chao, C.-M. Hsu, Y. Cui and F. B. Prinz, *ACS Nano*, 2011, **5**, 5692–5696.

21 S. Heiroth, T. Lippert, A. Wokaun, M. Döbeli, J. L. M. Rupp, B. Scherrer and L. J. Gauckler, *J. Eur. Ceram. Soc.*, 2010, **30**, 489–495.

22 H. S. Noh, H. Lee, B. K. Kim, H. W. Lee, J. H. Lee and J.-W. Son, *J. Power Sources*, 2011, **196**, 7169–7174.

23 H.-S. Noh, J.-W. Son, H. Lee, H.-S. Song, H.-W. Lee and J.-H. Lee, *J. Electrochem. Soc.*, 2009, **156**, B1484.

24 T. H. Lee, S. S. Baek, K. Y. Park, Y. Seo, B. Park, H. T. Lim and J.-Y. Park, *J. Alloys Compd.*, 2017, **706**, 330–339.

25 S. Sanna, V. Esposito, J. W. Andreasen, J. Hjelm, W. Zhang, T. Kasama, S. B.

Simonsen, M. Christensen, S. Linderoth and N. Pryds, *Nat. Mater.*, 2015, **14**, 500–504.

26 D. S. Aidhy, Y. Zhang and W. J. Weber, *J. Phys. Chem. C*, 2014, **118**, 4207–4212.

27 D. Montaleone, E. Mercadelli, A. Gondolini, M. Ardit, P. Pinasco and A. Sanson, *J. Eur. Ceram. Soc.*, 2018, 0–1.

28 R. Knibbe, J. Hjelm, M. Menon, N. Pryds, M. Søgaard, H. J. Wang and K. Neufeld, *J. Am. Ceram. Soc.*, 2010, **93**, 2877–2883.

29 D. H. Myung, J. Hong, K. Yoon, B. K. Kim, H. W. Lee, J. H. Lee and J.-W. Son, *J. Power Sources*, 2012, **206**, 91–96.

30 E. Tani, M. Yoshimura and S. Somiya, *J. Am. Ceram. Soc.*, 1983, **66**, 506–510.

31 F. Zhang, C.-H. Chen, J. C. Hanson, R. D. Robinson, I. P. Herman and S.-W. Chan, *J. Am. Ceram. Soc.*, 2006, **89**, 1028–1036.

32 P. Fornasiero, G. Balducci, R. Di Monte, J. Kašpar, V. Sergo, G. Gubitosa, A. Ferrero and M. Graziani, *J. Catal.*, 1996, **164**, 173–183.

33 C. E. Hori, H. Permana, K. Y. S. Ng, A. Brenner, K. More, K. M. Rahmoeller and D. Belton, *Appl. Catal. B-Environmental*, 1998, **16**, 105–117.

34 R. W. Balluffi and J. M. Blakely, *Thin Solid Films*, 1975, **25**, 363–392.

35 R. P. Reolon, S. Sanna, Y. Xu, I. Lee, C. P. Bergmann, N. Pryds and V. Esposito, *J. Mater. Chem. A*, 2018, 7887–7896.

36 G. Constantin, C. Rossignol, P. Briois, A. Billard, L. Dessemond and E. Djurado, *Solid State Ionics*, 2013, **249**–**250**, 98–104.

37 D. W. Ni and V. Esposito, *J. Power Sources*, 2014, **266**, 393–400.

38 F. Teocoli, D. W. Ni, K. Brodersen, S. P. V. Foghmoes, S. Ramousse and V. Esposito, *J. Mater. Sci.*, 2014, **49**, 5324–5333.

39 P. Calvert, *Chem. Mater.*, 2001, **13**, 3299–3305.

40 M. Rosa, P. N. Gooden, S. Butterworth, P. Zielke, R. Kiebach, Y. Xu, C. Gadea and V. Esposito, *J. Eur. Ceram. Soc.*, , DOI:10.1016/j.jeurceramsoc.2017.11.035.

41 C. Gadea, Q. Hanniet, A. Lesch, D. Marani, S. H. Jensen and V. Esposito, *J. Mater. Chem. C*, 2017, **5**, 6021–6029.

42 V. Esposito, C. Gadea, J. Hjelm, D. Marani, Q. Hu, K. Agersted, S. Ramousse and S. H. Jensen, *J. Power Sources*, 2015, **273**, 89–95.

43 Y. Xu, N. Farandos, M. Rosa, P. Zielke, V. Esposito, P. Vang Hendriksen, S. H. Jensen, T. Li, G. Kelsall and R. Kiebach, *Int. J. Appl. Ceram. Technol.*, 2018, **15**, 315–327.

44 B. Derby, *Annu. Rev. Mater. Res.*, 2010, **40**, 395–414.

45 D. Jang, D. Kim, J. Moon, D. Jang, D. Kim and J. Moon, *Langmuir*, 2009, **25**, 2629–2635.

46 C. Gadea, D. Marani and V. Esposito, *J. Phys. Chem. Solids*, 2017, **101**, 10–17.

47 D. A. Shirley, *Phys. Rev. B*, 1972, **5**, 4709–4714.

48 D. Briggs and M. P. Seah, 1983, **1**, 397–427.

49 N. S. McIntyre, in *Symposium on Progress in Quantitative Surface Analysis*, ed.

ASTM International, 1986, p. 217.
50 N. Reis and B. Derby, *Mater. Res.*, 2000, **625**, 117–122.
51 K. Mohan Kant, V. Esposito and N. Pryds, *Appl. Phys. Lett.*, 2012, **100**, 033105-1–3.
52 S. Sanna, V. Esposito, A. Tebano, S. Licoccia, E. Traversa and G. Balestrino, *Small*, 2010, **6**, 1863–1867.
53 F. Zhang, C. Chen, J. C. Hanson, R. D. Robinson, I. P. Herman and S. Chan, *J. Am. Ceram. Soc.*, 2006, **89**, 1028–1036.
54 S. W. Kim, S. G. Kim, J. Il Jung, S. J. L. Kang and I. W. Chen, *J. Am. Ceram. Soc.*, 2011, **94**, 4231–4238.
55 V. Esposito, D. W. Ni, D. Marani, F. Teocoli, K. T. S. Thydén, D. Zanetti de Florio and F. C. Fonseca, *J. Mater. Chem. A*, 2016, 16871–16878.
56 D. W. Ni, D. Z. de Florio, D. Marani, A. Kaiser, V. B. Tinti and V. Esposito, *J. Mater. Chem. A*, 2015, **3**, 18835–18838.
57 S.-L. Hwang and I. W. Chen, *J. Am. Ceram. Soc.*, 1990, **73**, 3269–3277.
58 R. D. Shannon, *Acta Cryst.*, 1976, 751–767.
59 P.-L. Chen and I.-W. Chen, *J. Am. Ceram. Soc.*, 1996, **79**, 1801–1809.
60 K. Eguchi, N. Akasaka, H. Mitsuyasu and Y. Nonaka, *Solid State Ionics*, 2000, **135**, 589–594.
61 P. -L Chen and I. -W Chen, *J. Am. Ceram. Soc.*, 1994, **77**, 2289–2297.
62 I.-W. Chen, *Interface Sci.*, 2000, **8**, 147–156.
63 P. L. Chen and I. W. Chen, *J. Am. Ceram. Soc.*, 1996, 79, 1793–1800.
64 E. Paparazzo, G. M. Ingo and N. Zacchetti, *J. Vac. Sci. Technol. A Vacuum, Surfaces, Film.*, 1991, **9**, 1416–1420.
65 B. P. Burroughs, A. Hamnett, A. F. Orchard and G. Thornton, *J.C.S Dalt.*, 1976, 1686–1698.
66 A. Kotani, T. Jo and J. C. Parlebas, *Many-body effects in core-level spectroscopy of rare-earth compounds*, 1987, vol. 37.
67 M. Romeo, K. Bak, J. El Fallah, F. Le Normand and L. Hilaire, *Surf. Interface Anal.*, 1993, **20**, 508–512.
68 D. R. Mullins, S. H. Overbury and D. R. Huntley, *Surf. Sci.*, 1998, **409**, 307–319.
69 E. J. Preisler, O. J. Marsh, R. A. Beach and T. C. McGill, *J. Vac. Sci. Technol. B Microelectron. Nanom. Struct.*, 2001, **19**, 1611.
70 G. Praline, B. E. Koel, R. L. Hance, H.-I. Lee and J. M. White, *J. Electron Spectros. Relat. Phenomena*, 1980, **21**, 17–30.
71 A. Trovarelli, *Catal. Rev.*, 1996, **38**, 439–520.
72 K. Song, H. Schmid, V. Srot, E. Gilardi, G. Gregori, K. Du, J. Maier and P. A. Van Aken, *Microsc. Microanal.*, 2014, **20**, 420–421.
73 J. Jiang and J. L. Hertz, *J. Electroceramics*, 2014, **32**, 37–46.
74 I. Kosacki, T. Suzuki, V. Petrovsky and H. U. Anderson, *Solid State Ionics*, 2000, **136–137**, 1225–1233.
75 Q. Su, D. Yoon, A. Chen, F. Khatkhatay, A. Manthiram and H. Wang, *J. Power*

Sources, 2013, **242**, 455–463.

76 J. T. S. Irvine, D. C. Sinclair and A. R. West, *Adv. Mater.*, 1990, **2**, 132–138.

77 B. Steele, *Solid State Ionics*, 2000, **129**, 95–110.

Chapter 6

Improving the performances of $SrCoO_{3-\delta}$ membranes for oxygen separation through Fe, Nb-doping induced phase stabilization

AN INVESTIGATION ON THE DOPING STRATEGY TO ENHANCE THE STABILITY OF THE STATE OF THE ART STRONTIUM COBALTATE MATERIAL TO BE APPLIED AS OXYGEN PERMEATION MEMBRANE

In this chapter a doping strategy for the stabilization of the cubic phase of $SrCoO_{3-\delta}$ is investigated, in order to obtain materials to test for oxygen permeability. The cubic phase of $SrCoO_{3-\delta}$ displays one of the highest oxygen permeation fluxes observed so far in literature, but is not stable over a wide range of temperature therefore should be stabilized by the insertion of dopants in the lattice.

After evaluating the effect of several donor dopants on the crystal structure, iron substitution is investigated: $SrCo_{0.95}Nb_{0.05}O_{3-\delta}$ (SCN), $SrCo_{0.85}Fe_{0.1}Nb_{0.05}O_{3-\delta}$ (SCNF1), $SrCo_{0.75}Fe_{0.2}Nb_{0.05}O_{3-\delta}$ (SCNF2) and $SrCo_{0.65}Fe_{0.3}Nb_{0.05}O_{3-\delta}$ (SCNF3) are synthesized. Niobium provides a charge balancing contribution decreasing the amount of oxygen vacancies, iron can enhance the stability because undergoes more easily charge compensation phenomena, moreover has a lower basicity than cobalt and enhances the tolerance to CO_2. The samples are characterized in their oxygen nonstoiochiometry and mobility properties at room temperature and as a function of temperature in both air and nitrogen atmosphere.

Dense pellets are sintered and their total conductivity and surface composition as a function of iron doping is investigated. Finally their oxygen permeation capability is tested and the most stable sample is tested using CO_2 as sweep gas, simulating the atmosphere of oxyfuel plants.

Besides being a technologically relevant field, oxygen permeability provides a good screening of materials with mixed ionic and electronic conductivity (MIEC), which might be used as cathodes in solid oxide reversible cells. In fact, both ionic and electronic conductivities are required to have oxygen permeation, as a flow of electrons is balancing the flow of oxygen ions in the opposite direction.

The resulting permeation fluxes are proportional to the mixed conductivity of the materials and provide a good technique for estimating the ambipolar conductivity, which generally in MIECs is well approximated with ionic conductivity.

6.1 Introduction

The constantly increasing demand for energy requires to pursue smart strategies in order to reduce CO_2 emissions and counter the climate change.[1] Despite the huge efforts for achieving large scale production from renewable sources, fossil power plants still represent a major source of energy and anthropogenic CO_2 production, highlighting the importance of sequestering CO_2 before it is released in atmosphere. This can be done, for example, by Carbon Capture and Utilization (CCU) or Carbon capture and storage (CCS) technologies, which provide a strategy for tackling the growing emissions responsible for dangerous environmental threatening, that are not just limited to global warming.

A possible method for CCS is represented by oxy-fuel combustion, which consists of feeding a gas stream of oxygen instead of air in the combustion process, avoiding the formation of nitrogen oxides. The result is a CO_2-enriched flue gas (up to 90-95 % of CO_2 content) which can be compressed and stored.[2,3] The challenge in this strategy is represented by the fact that large scale oxygen production is still achieved by cryogenic separation technology which has an elevate energy demand, especially when is considered in relation to small and medium plants. This energy demand could be significantly lowered considering the use of ceramic oxygen transport membranes (OTMs), which could be integrated in the combustion plant without the need for a separate heating stage.[4,5]

A typical OTM is consisting of a dense and gastight ceramic which has mixed ionic and electronic conduction (MIEC) allowing the transport of oxygen ions through the vacancies in the crystal lattice and a flow of electrons in the opposite direction. This is achieved with a driving force represented by the oxygen chemical potential gradient through the membrane, which is due to the different oxygen atmospheres at the sides of the membrane. In the case of fast surface exchange, the oxygen flux through the permeation membrane is described by Wagner's equation:

$$J_{O_2} = \frac{RT}{16F^2L}\int_{p_{O_2}^{permeate}}^{p_{O_2}^{feed}} \frac{\sigma_{el}\sigma_{ion}}{\sigma_{el}+\sigma_{ion}}\left(p_{O_2}\right) dlnp_{O_2} \qquad (1)$$

where J_{O_2} is the oxygen permeation flux (mol·m^{-2}·s^{-1}); R and F are the gas and Faraday's constants, respectively; L is the membrane thickness; σ_{el} and σ_{ion} are the electronic and the ionic conductivities, respectively; and $p_{O_2}^{feed}$ and $p_{O_2}^{permeate}$ are the oxygen partial pressures at the high pressure side and at the low pressure side, respectively.[6]

It is evident from equation (1) that the permeation flux can be significantly enhanced when the thickness of the membrane is reduced[7] and that, once a certain thickness is fixed, the mixed ionic and electronic conductivity of the material can play an important role in defining the O_2-permeation performances.

For this reason, a great attention has been devoted to the research of mixed ionic and electronic materials and perovskites have been considered promising since 1980.[8] Perovskites are a family of compounds represented by the formula ABO_3, in which A represents a large 12-fold coordinated cation (typically an alkaline, alkaline earth or rare-earth element), B a smaller 6-fold coordinated cation (typically an element belonging to the transition metals). In the case of oxygen permeation, oxygen vacancies are the sites for ionic transport and thus the defective $ABO_{3-\delta}$ are considered, but the anionic site could be occupied by P, N, or halides.[9] What makes perovskites extremely appealing and interesting for many application fields is the possibility of tailoring their properties with doping, since most of the periodic table's elements are suitable for insertion in a perovskite cell and the crystal structure has an elevate tolerance to the presence of defects and nonstoichiometry.[10] The perovskite archetype is represented by $SrTiO_3$ and has a perfect cubic structure. When other ions are introduced or replaced in the lattice, they can cause a distortion of the cubic structure which extent can be calculated by Goldschimdt's tolerance factor:[11]

$$t = \frac{(r_A + r_O)}{\sqrt{2}(r_B + r_O)} \qquad (2)$$

where r_A, r_B and r_O represent the ionic radiuses of A-cation, B-cation and oxygen ion, respectively.

A cubic structure has been reported for perovskites having 0.9<t<1 values, for values below 0.9 a distorted structure (orthorhombic, rhombohedral or tetragonal) is observed and hexagonal structure is associated to values above 1. The importance of Goldschimdt's

tolerance factor should not be underestimated: in fact, even though it represents a rule of thumb for determining the lattice distortion based on geometrical parameters, it has been outlined a strict correlation between crystal structure and conductivity properties. The highest ionic conduction is observed for cubic structures, where an isotropic motion of lattice vacancies is possible and it has been that observed that in a cubic lattice an improvement of the superposition of orbitals due to the 180° B-O-B angle is, resulting in a higher electronic conduction compared to structures with tilted angles.[12] Beside geometry, in perovskites another constraint exists and is due to the charge balancing between the cations in the A and B sites. This can be achieved through the following combinations: $A^{(+3)}B^{(+3)}O_3$, $A^{(+2)}B^{(+4)}O_3$ or $A^{(+1)}B^{(+5)}O_3$ between A and B-site cations valence. In rare cases the tolerance to defects can reach extreme values, with ReO_3 being reported as having a perovskitic structure with 100% A-site defects.[13] As a result of doping and charge compensation, when the total valence of cations is below +6 it is compensated with the creation of oxygen defects, which are responsible for ionic conduction; on the contrary when it is above +6 the oxygen excess can be stored in the material. The latter case is well known in $LaMnO_{3+\delta}$ -based compounds and exploited for oxygen storage capacity (OSC) purposes. Considering the former case, the tolerance to nonstoichiometry of oxygen has a threshold value, which in the case of oxygen defects is an oxygen coefficient of 2.5: below this value oxygen defects rearrange in an ordered structure which is freezing vacancies motion, consequently hindering ionic conduction. This stoichiometry is typically associated with the orthorhombic brownmillerite or hexagonal structure.

After finding high permeation fluxes in the $LaFeO_3$-$LaCoO_3$-$SrCoO_3$-$SrFeO_3$ family, Teraoka *et al*[14] encouraged the investigation of perovskite-based compounds towards this group of compounds, for which an increase in oxygen permeation has been observed with increasing Co and Sr content. The increase in oxygen permeability is coupled with a decrease in stability: due to the high amount of defects, undoped $SrCoO_{3-\delta}$ is reported to have hexagonal or brownmillerite structure (depending on synthesis condition)[15] and undergoes a phase transition to cubic perovskite at high temperature. Beside the lower performances of brownmillerite and hexagonal phase, it's worth to remark that a phase transition can induce mechanical stresses since it is usually characterized by an abrupt

change in volume. This can cause the mechanical failure of the membrane due to excessive stresses. For this reason, the stabilization of a unique crystal phase over a wide range of temperatures is preferred and many efforts have been devoted at finding a doping strategy allowing to stabilize the cubic structure of $SrCoO_{3-\delta}$ at room temperature. Among the most consolidated techniques there is the use of iron as dopant, obtaining $SrCo_{0.8}Fe_{0.2}O_{3-\delta}$, or the substitution of strontium for barium that has been reported as an effective strategy for enhancing the stability of $SrCoO_{3-\delta}$. After Shao first reported on $Ba_{0.5}Sr_{0.5}Co_{0.8}Fe_{0.2}O_{3-\delta}$ (BSCF),[16] many efforts have been devoted to investigate the properties of BSCF as cathode or OTM, with Baumann reporting the highest O_2-permeation flux (12.2 ml·min^{-1}·cm^{-2} at 1000 °C, under air/argon) so far.[7] However, barium has a lower tolerance to CO_2 than strontium and a decrease in electronic conductivity is generally reported as barium content increases. [17] Iron doping is not effective below a certain amount, since the formation of brownmillerite phase occurs. [18]

Another strategy for enhancing the stability of SC phase consists in using aliovalent doping through a fixed valency donor element: this can reduce the nonstoichiometry and stabilize the disordered vacancy phase over a wide range of temperatures. Nagai *et al* investigated the use of several dopants on $SrCo_{0.9}M_{0.1}O_{3-\delta}$ and highlighted the beneficial effect of La, Ti, Cr and Nb in stabilizing the cubic phase of the perovskite and the resulting improvement of the oxygen permeation.[18] On the other hand, it has been observed that oxygen permeation flux decreases as the dopant amount increases.[19] To preserve the best activity of $SrCoO_{3-\delta}$, the dopant should be used in the minimum amount necessary to stabilize the crystal structure.

In this chapter different doping strategies are investigated in order to stabilize the cubic phase of $SrCoO_{3-\delta}$: starting from fixed valency elements (Zr, Nb, Mo) the best candidate is identified and then the effect of iron on the structural stability, conductivity and oxygen mobility properties is studied. The resulting $SrCo_{0.95}Nb_{0.05}O_{3-\delta}$ (SCN), $SrCo_{0.85}Fe_{0.1}Nb_{0.05}O_{3-\delta}$ (SCNF1), $SrCo_{0.75}Fe_{0.2}Nb_{0.05}O_{3-\delta}$ (SCNF2) and $SrCo_{0.65}Fe_{0.3}Nb_{0.05}O_{3-\delta}$ (SCNF3) perovskites are investigated as possible oxygen permeation membranes. The samples are prepared by means of citrate route and characterized by means of X-ray diffraction (XRD), iodometric titration (IT), thermogravimetric analysis (TGA), X-ray photoelectron

spectroscopy (XPS) and thermal programmed desorption of oxygen (O_2-TPD). Dense pellets are sintered to measure the conductivity of the samples with 4-probes van der Pauw technique and finally oxygen permeation is tested at different temperatures. The more performing sample is tested in oxyfuel conditions. The microstructure of the membranes has been investigated before and after the test, in order to determine the influence of sintering and operative conditions on the final permeation performances.

6.2 Experimental

6.2.1 Samples synthesis

$SrCoO_{3-\delta}$ (SC), $SrCo_{0.95}Zr_{0.05}O_{3-\delta}$ (SCZ), $SrCo_{0.95}Nb_{0.05}O_{3-\delta}$ (SCN) $SrCo_{0.95}Mo_{0.05}O_{3-\delta}$ (SCM), $SrCo_{0.85}Fe_{0.1}Nb_{0.05}O_{3-\delta}$ (SCNF1), $SrCo_{0.75}Fe_{0.2}Nb_{0.05}O_{3-\delta}$ (SCNF2), $SrCo_{0.65}Fe_{0.3}Nb_{0.05}O_{3-\delta}$ (SCNF3) powders were synthesized by means of citrate route followed by combustion, using $Sr(NO_3)_2$ (ACS reagent, >99%, Sigma Aldrich), $Co(NO_3)_2{\cdot}6H_2O$ (ACS reagent, >98%, Sigma Aldrich), ZrO_2 (99%, Sigma Aldrich), Nb_2O_5 (325 mesh, 99.9%, Sigma Aldrich), $(NH_4)_2MoO_4$ (99.98, Aldrich) and Fe (metal chips, 99.98%, Aldrich) as precursors. These were dissolved separately in deionized water or nitric acid (puriss p.a. ≥65%, Sigma Aldrich) and then mixed. A controlled amount of nitric acid (10 ml per gram of final perovskite product) was added to solution in order to obtain an homogeneous combustion. Citric acid monohydrate (ACS reagent, >99%, Sigma Aldrich) was then added in the ratio 1.9 with respect to the total amount of cations and the pH was adjusted with ammonium hydroxide (ACS reagent, 28-30% NH_3 basis, Sigma Aldrich) until a value of 7 was reached, monitoring it with a calibrated pH-meter. The obtained solution was heated at 90°C to remove water and the pH was monitored and kept at a constant value of 7 through the addition of ammonia, until a dense gel was formed. The gel was then dried at 200°C, which induced the release of gases forming a sponge-like structure that was finally burnt at 400°C in order to remove the organic framework. The resulting powder was finely ground in an agate mortar and then calcined at 1000°C for 6 hours, followed by grinding and a second thermal treatment at 1200°C for 12 hours in order to obtain the desired perovskitic structure.

6.2.2 Samples characterization

The crystal structure of the synthesized samples was determined by X-ray diffraction using a Bruker D8 with Cu Kα radiation (λ = 1.5418 Å), collecting diffraction patterns at room temperature in a Bragg-Brentano geometry over a 2θ range of 20-80°, with a step size of 0.015° and 1s step time.

The oxygen nonstoichiometry (δ) and average oxidation state of B-site cations at room temperature was determined by iodometric titration. In brief, 50 mg of powder were

dissolved in a 6mol L^{-1} HCl solution in presence of excess KI (ACS grade, Millipore Sigma), the procedure was performed under nitrogen atmosphere to prevent the oxidation of I^- ions (from KI) by atmospheric air. This was followed by titration with a standard thiosulfate solution ($S_2O_3^{2-}$, 0.01 N, Titolchimica). A few droplets of homemade starch solution were added in proximity of equivalence point. Each measurement was performed four times and averaged to obtain the resulting nonstoichiometry. The evolution of oxygen nonstoichiometry with temperature was investigated with thermogravimetrical analysis performed with a SDT 2960 TGA/DTA (TA instruments). Ramps of 10 °C/min under air or nitrogen flow were used. The resulting nonstoichiometry was determined with the following equation:

$$\delta = \frac{MM \times m_0 - (MM - 15.9994 \times \delta_0) \times m}{15.9994 \times m_0} \qquad (3)$$

where m_0 and m are the original weight and the weight at a certain temperature, MM is the molar mass of the sample (expressed as $SrCo_{0.95-x}Fe_xNb_{0.05}O_3$) and δ_0 is the oxygen nonstoichiometry determined at room temperature. From the same expression it is possible to determine the average valence of B-site cations.

O_2-Temperature programmed desorption was performed with a Autochem 2920 II equipped with TCD detector and associated with an ESS Evolution mass spectrometer in order to analyze the composition of the gases coming to the detector. 100 mg of sample were placed in a quartz U-tube by means of a small piece of quartz wool, to ensure homogeneous diffusion of gas through the sample. The experimental procedure consists of three phases: a 2h cleaning step in He flow (flow 50 sccm) at 450°C, followed by cooling and then a temperature ramp (10°C/min) in pure oxygen (flow 50 sccm) to 900°C with a 2h dwell. The sample is cooled in pure O_2 and then desorption phase is run using He (flow 50 sccm) as sweep gas up to 1000°C (ramp 10°C/min).

X-ray photoelectron spectroscopy was carried out with a Perkin Elmer Φ5600ci Multi Technique System. Calibration of the spectrometer was made assuming the binding energy (BE) of the Au $4f_{7/2}$ to be 84.0 eV with respect to the Fermi level.[20] An Al Kα standard source working at 250 W was used to collect both extended (survey - 187.85 eV pass energy, 0.5 eV·$step^{-1}$, 0.05 s·$step^{-1}$) and detailed spectra (multiplex - 23.5 eV pass energy, 0.1 eV·$step^{-1}$, 0.1 s·$step^{-1}$, for Co 2p, Fe 2p, Nb 3d, Sr 3d, O 1s, C 1s). The standard

deviation in the BE values of the XPS lines is 0.10 eV. The peak positions were corrected for charging effects by considering the C 1s peak at 285.0 eV and evaluating the BE differences.[21,22] Finally, the atomic percentage was evaluated after a Shirley-type background subtraction and PHI sensitivity factor were used.[23]

In order to measure electrical conductivity and oxygen permeation, dense pellets were prepared by uniaxial pressing followed by isostatic pressing (p=65 tons, t=30 s) and sintering at 1250°C for 12 hours. For electrical conductivity, four small dots of platinum paint (SPI supplies) were applied at the corners of the resulting pellets (16mm diameter, 2mm thickness, >90% density) and dried (1 hour at 1000 °C, using 1°C/min heating and cooling ramps) to ensure good electrical contact. A Keithley 2400 SourceMeter was used for DC-electrical conductivity measurements performed in air (flow 50 sccm) between room temperature and 950°C at a 25°C interval, using a 1°C/min heating ramp.

Scanning electron microscopy was performed on both the as synthesized and tested membranes, using a Zeiss Supra 40VP, with 20kV acceleration voltage.

6.2.3 Oxygen permeation test

Oxygen permeation measurements were conducted in an oxygen membrane rig built at DTU Risø, previously described by Samson and Pirou.[24,25] The membrane was placed between two alumina tubes which seal the membrane from the top and the bottom, and the gases were introduced into the test house with thinner alumina tubes placed inside the tubes described above, reaching the sample proximity.

The membrane and the tubes were placed in the middle of a height-adjustable tubular furnace. In order to ensure sealing from the external atmosphere, two rings of tape cast sodium aluminum silicate (NAS, Na_2O 17.8%, Al_2O_3 9.4%, SiO_2 72.8%) [26] with an inner diameter of 9 mm and a 515°C glass transition temperature were placed between the membrane and the alumina tube. A NAS paste was used to coat the side walls and ensure that no oxygen was entering the sweep gas compartment from the outside, so that oxygen was only coming from the permeation membrane. The sealing was realized after heating up the membrane in air up to 850°C followed by cooling at 750°C. Prior testing, the total gas outlet flow was checked in both the sides of the membrane, to exclude the presence of leaks.

During the test air with a flow of 300 $ml_N min^{-1}$ was fed to the feed side, while various flows of N_2 or CO_2 ranging from 50 to 250 $ml_N min^{-1}$ were fed to the permeate side. The inlet flow of gasses was determined by mass flow controllers (Brooks) while the outlet gas was determined by a mass flow meter (Bronkhorst). In house built zirconia-based pO_2 sensors were used to determine the pO_2 of the inlet (before feeding the membrane) and outlet gas (after sweeping the membrane).

The oxygen permeation was quantified by the difference between the pO_2 at the inlet and the outlet, as given by:

$$J_{O_2} = \frac{p_{O_2 permeate}^{out} \cdot n^{out} - p_{O_2 permeate}^{in} \cdot n^{in}}{A} \qquad (4)$$

where J_{O_2} is the oxygen permeation flux, $p_{O_2 permeate}^{out}$ and $p_{O_2 permeate}^{in}$ are the oxygen partial pressures of the outlet and the inlet gases, respectively, n^{out} and n^{in} are the molar flow rates of inlet and outlet gases, respectively, and A is the area of the permeate side of the membrane.

The oxygen partial pressure at the two sides is determined by the voltage measured by the sensors and converted through the Nernst equation:

$$V = \frac{RT}{4F} ln \frac{p_{O_2}}{p_{O_2\, ref}} \qquad (5)$$

Where V is the open circuit voltage of the sensor, R, T and F are the gas constant, absolute temperature and Faraday constant, respectively and p_{O_2} and $p_{O_2,ref}$ are the measured pressure and the oxygen partial pressure at the reference electrode (0.21 atm), respectively.

6.3 Results and discussion

6.3.1 Phase Stabilization

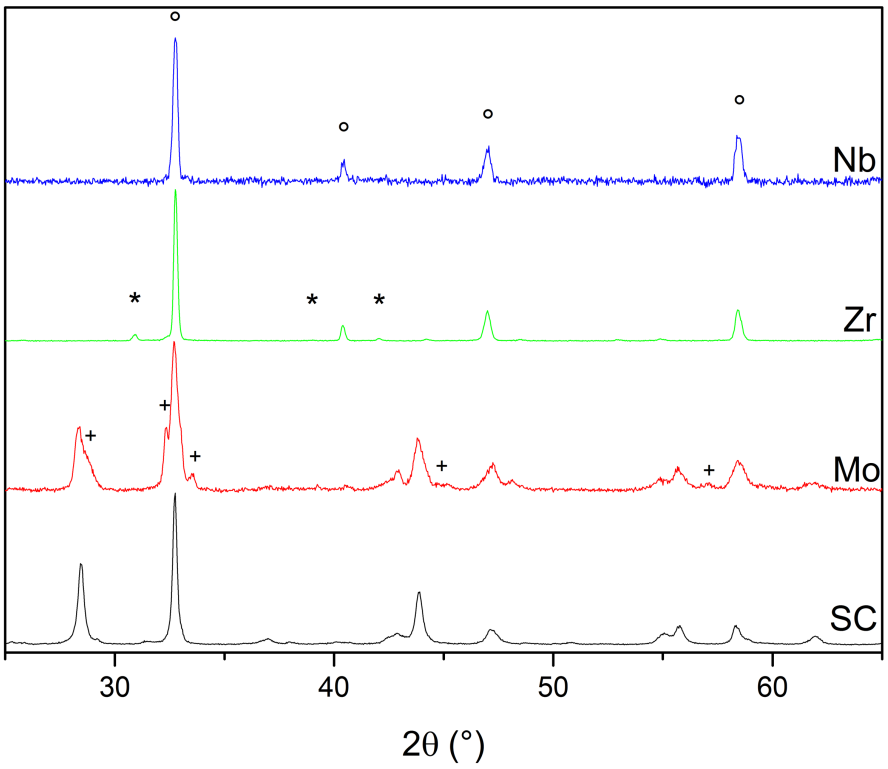

Fig 6.1: XRD patterns of undoped $SrCoO_{3-\delta}$ and molybdenum, zirconium and niobium doped samples. +: $SrMoO_4$; *$SrZrO_3$; °: cubic $SrCo_{0.95}M_{0.05}O_{3-\delta}$ (M=Zr, Nb). All samples were calcined 12h at 1200°C.

Sample	Detected phase	Estimated O coefficient	t-factor
SC (no Co^{4+})		2.5	0.9991
SC (10% Co^{4+})	Hex	2.55	1.003
SC (100% Co^{4+})		3	1.040
SCZ	P+imp.	2.525	0.9963
SCN	P	2.55	0.9983
SCM	H+imp	2.575	0.9986

Table 6.1: Observed crystal phase, estimated oxygen coefficient and calculated tolerance factor for undoped $SrCoO_{3-\delta}$ (SC) and $SrCo_{0.95}M_{0.05}O_{3-\delta}$ (M=Zr, Nb, Mo). In the case of the undoped sample different Co^{4+} contents (0, 10 and 100%) were considered for calculations in order to show the effect of Co^{4+} presence on the tolerance factor.

In order to preserve the conduction properties of $SrCoO_{3-\delta}$, the choice of the doping elements should consider that the best doping effect is realized when the dopants have a ionic radius close to the one of cobalt (Co^{2+}: r_i=0.745 Å ; Co^{3+}: r_i=0.64 Å; Co^{4+}: r_i= 0.59 Å, all 6-fold coordinated and considered in high spin configuration in the case of Co^{2+} and Co^{3+}).[27] It has been reported for other ionic conductors with cubic structure that the maximum of conductivity is obtained when the host and the guest element have similar ionic radiuses.[28,29] For this reason, zirconium (r_i=0.72 Å, 6-fold coordinated), niobium (r_i=0.64 Å, 6-fold coordinated) and molybdenum (r_i=0.59 Å, 6-fold coordinated) have been chosen, aiming to investigating the different charge balance effects.[27]

To evaluate the stabilization effect of doping on the structure of $SrCoO_{3-\delta}$, X-ray diffraction has been performed. Figure 6.1 shows that the undoped sample has a pure hexagonal $BaNiO_3$-type structure and that the choice of the dopant can tune the formation of different crystal structures.

Surprisingly, Mo does not induce significant improvement in the stabilization of the cubic phase, conversely to what has been reported elsewhere,[30] as the reflections of the hexagonal phase and weak signals belonging to $SrMoO_4$ are detected. It is possible that the incorporation of Mo in the lattice of $SrCoO_{3-\delta}$ may require a more severe thermochemical treatment. On the contrary, Zr is found to be very effective in stabilizing the desired cubic structure, but small impurities belonging to the $SrZrO_3$ insulating phase are detected. From that it is evident that a lower amount of Zr could be sufficient to induce the formation of the cubic $SrCoO_{3-\delta}$, but the formation of a larger amount of $SrZrO_3$ during high temperature operation cannot be excluded. This phenomenon is undesired due to the poor conductivity properties of this phase.[31,32] Yang *et al* did not observe the segregation of $SrZrO_3$ up to 10% content of Zr in presence of high iron content ($SrCo_{0.4}Fe_{0.6-x}Zr_xO_{3-\delta}$), however the solubility region for zirconium seems to be very narrow.[33] The use of 5% Nb doping is effective in stabilizing the cubic phase and no impurities are detected, similar results has been observed before in the works Nagai *et al*,[18] Wang *et al*[34] and Usiskin *et al*[35] in the case of 10% niobium doping.

A possible explanation of the different effect of dopants comes from the analysis of the tolerance factors and charge compensation mechanisms for the different compounds. In the case of undoped $SrCoO_{3-\delta}$ three different scenarios are evaluated: 1) no Co^{4+} presence;

2) presence of a small amount of Co^{4+} ; 3) cobalt content totally present as Co^{4+}. It is known from thermodynamics that Co^{4+} isn't the most stable valence for cobalt at room temperature,[36,37] therefore the third case (100% Co^{4+}) can be ruled out, nevertheless it is interesting to notice that in that scenario the tolerance factor would be above 1 (t=1.04), meaning an instability of the cubic phase and formation of the hexagonal phase. In the case of cobalt present as only Co^{3+}, it is evident that a large amount of oxygen vacancies would be produced, meaning a rearrangement of the structure towards a more stable brownmillerite geometry in which vacancies are ordered along a direction thus highly limiting their mobility. Since the brownmillerite $SrCoO_{2.5}$ is reported to have an orthorhombic structure,[15] this hypothesis is not consistent with the observed diffraction pattern.[37] Focusing on the hypothesis of 10% Co^{4+} presence, a value of 1.003 is found, suggesting a slight distortion towards hexagonal phase. The calculated t-factors for the doped $SrCo_{0.95}M_{0.05}O_{3-\delta}$ compounds are 0.9963, 0.9983, 0.9986 for zirconium, niobium and molybdenum, respectively, and in all cases suggest that the formation of the cubic phase should be favored. However, dopant solubility and insertion in the lattice play a role in determining the final structure. Moreover, it is worth having an insight into the charge compensation effect due to the introduction of a donor dopant in the lattice considering the case of niobium, as no secondary phases are detected from the XRD characterization.

Since the undoped compound has an hexagonal structure which is consistent with the presence of Co^{4+}, this can be used as a base for the defect analysis for Nb (considered having a fixed 5+ valence) [35] effect when replacing Co in the structure of $SrCoO_{3-\delta}$. The possible mechanisms are:

$$Nb_2O_5 + 4Co_{Co}^{\bullet} \rightarrow 2Nb_{Co}^{\bullet\bullet} + 2Co_{Co}^{X} + Co_2O_3 + O_2(g) \qquad (6)$$

and

$$Nb_2O_5 + 2Co_{Co}^{X} + 2V^{\bullet\bullet} \rightarrow 2Nb_{Co}^{\bullet\bullet} + 2O_O^{X} + Co_2O_3 \qquad (7)$$

where $Co_{Co}^{\bullet}$ and Co_{Co}^{X} represent Co^{4+} and Co^{3+}, respectively, $Nb_{Co}^{\bullet\bullet}$ is the positively charged dopant and $V^{\bullet\bullet}$ is an oxygen vacancy. Reaction (6) represents a decrease in the oxidation state of cobalt from Co^{4+} to Co^{3+} and (7) is a reduction in the number of oxygen vacancies.

It should be noted that, despite these two mechanisms are competitive, both of them could occur at the same time.

6.3.2 Crystal structure

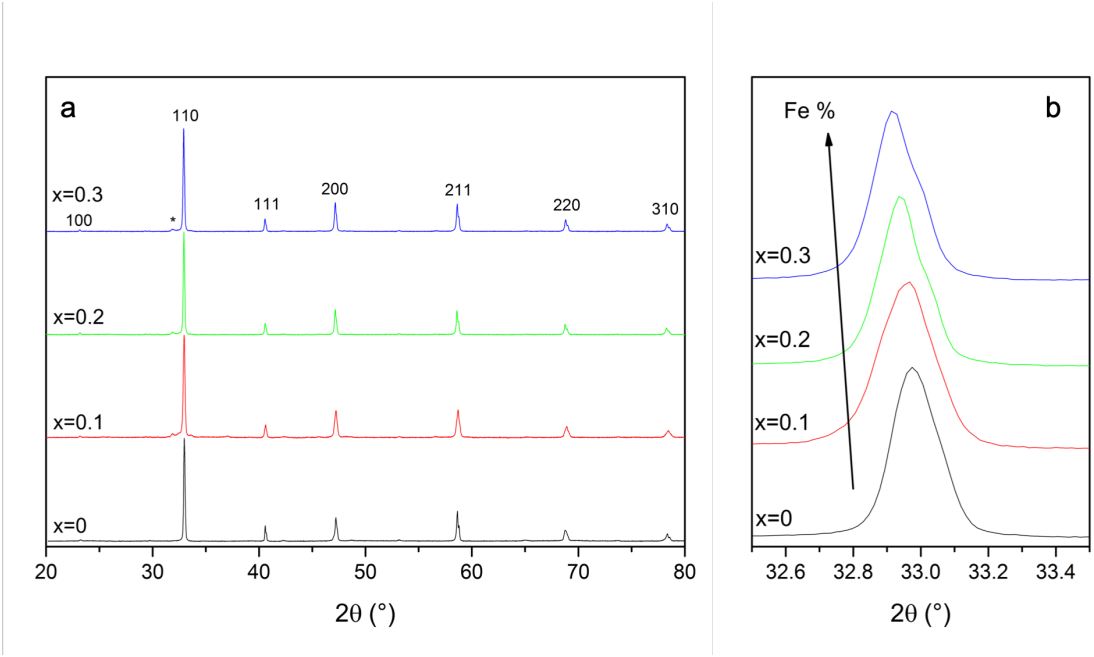

Fig 6.2: XRD patterns of $SrCo_{0.95-x}Fe_xNb_{0.05}O_{3-\delta}$ (x=0; 0.1; 0.2; 0.3) samples; (a) and detailed view of 110 reflection (b). All samples were calcined 12h at 1200°C. *: orthorhombic $Sr_2Co_2O_5$

After identifying niobium as promising candidate for stabilizing of the cubic phase of $SrCoO_{3-\delta}$, the role of iron doping has been investigated. Since iron oxide is less basic than cobalt oxide[38] and has already proved to be an effective stabilizer in $SrCo_{0.8}Fe_{0.2}O_{3-\delta}$ membranes, it is interesting to investigate if the simultaneous doping with Nb and Fe could increase the material robustness without lowering the performances. Teraoka *et al* investigated the influence of B-site cations on oxygen permeation for several transition metals and found that iron is, among the elements with available +3 valence, the one with the closest performances to cobalt.[39]

Figure 6.2 shows the crystal structure detected for all samples as a function of iron dopant content. A cubic perovskitic structure is detected for all samples and the shift observed in the diffraction signals (Figure 6.2 b) suggests a modification in the crystal lattice parameter due to iron incorporation. Considering cobalt and iron ionic radiuses in six-fold coordination, it can be noticed that Fe^{2+} (r_i=0.78 Å, high spin), Fe^{3+} (r_i= 0.645 Å, high spin) and Fe^{4+} (r_i= 0.585 Å) ionic radius is always larger than in the case of the same oxidation

state for cobalt: Co^{2+} (r_i=0.745 Å, high spin), Co^{3+} (r_i=0.61 Å, high spin) and Co^{4+} (r_i=0.53 Å). The replacement of iron for cobalt is inducing an increase in the lattice parameter, which is consistent with the shift of the diffraction peaks to lower angles. This shows that iron has been successfully inserted into the structure.

Sample	a_0 (Å)	t-factor	δ	Oxygen coefficient	n
SCN (x=0)	3.8392	0.9983	0.3233	2.6767	3.10
SCFN1 (x=0.1)	3.8451	0.9966	0.3158	2.6842	3.12
SCFN2 (x=0.2)	3.8495	0.9948	0.2250	2.7750	3.30
SCFN3 (x=0.3)	3.8525	0.9931	0.2933	2.7067	3.16

Table 6.2: Lattice parameter, calculated tolerance factor, oxygen nonstoichiometry (δ) and average Co/Fe valence state at room temperature (n) of $SrCo_{0.95}Nb_{0.05}O_{3-\delta}$ (SCN), $SrCo_{0.85}Fe_{0.1}Nb_{0.05}O_{3-\delta}$ (SCNF1), $SrCo_{0.75}Fe_{0.2}Nb_{0.05}O_{3-\delta}$ (SCNF2), $SrCo_{0.65}Fe_{0.3}Nb_{0.05}O_{3-\delta}$ (SCNF3).

Table 6.2 presents the calculated lattice parameters and tolerance factor, and the measured oxygen nonstoichiometry, oxygen coefficient and average valence of B-site cations determined from iodometric titration. Since niobium is not involved in the titration reaction, it is not included in the calculation of n, that is representative of the average oxidation state of iron and cobalt, which are undistinguished in the iodometric titration procedure. It is possible to notice that iron doping results in a decrease of the t-factor and oxygen nonstoichiometry, with a consequent higher oxidation state for B-site cations. Both the increase in the average oxidation state (n) and the reduction in the amount of vacancies (δ) become more evident as iron content is increasing, suggesting that the charge compensation mechanism of iron from Fe^{3+} to Fe^{4+} is favored with respect to cobalt.[40,41] This effect is more pronounced in SCFN2, having an average oxidation state of 3.3 for B-site cations.

Since small impurities (I/I_{perov}< 4%) of the orthorhombic brownmillerite phase ($Sr_2Co_2O_5$) are detected in Fe-doped samples and this is not observed in absence of iron, a set of samples has been calcined at 1000°C for 6h aiming to freeze the diffusion phenomena in the system before the insertion of the dopants in the lattice is complete, to investigate the effect of dopants on the final structure. Figure 6.3 shows the diffraction patterns for the so obtained samples and it possible to observe that phase impurities are present in larger amount compared to the samples calcined at 1200°C (Figure 6.2).

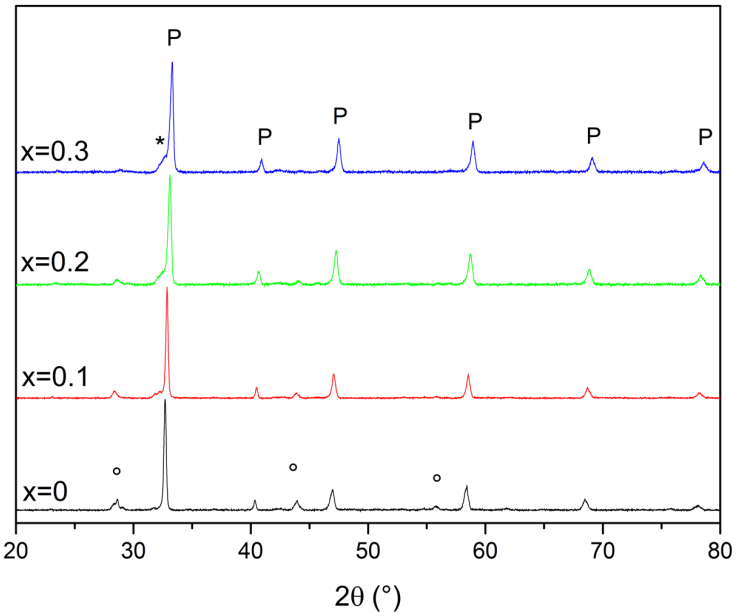

Fig 6.3: XRD patterns of $SrCo_{0.95-x}Fe_xNb_{0.05}O_{3-\delta}$ (x=0; 0.1; 0.2; 0.3) samples calcined for 6h at 1000°C. P: perovskite °: hexagonal $SrCoO_{3-\delta}$ * orthorhombic $Sr_2Co_2O_5$

Beside suggesting that the thermal treatment at 1000°C is not sufficient to observe complete formation of cubic $SrCo_{0.95-x}Fe_xNb_{0.05}O_{3-\delta}$ (x=0; 0.1; 0.2; 0.3), the diffraction patterns show that as the iron content is increasing the formation of the hexagonal phase becomes less favored, while the formation of the orthorhombic brownmillerite is more favored. This is suggesting that the formation of the brownmillerite is favored in presence of Fe,[42] but Nb diffusion in the lattice may not be complete. The formation of a brownmillerite should be avoided, since it has a lower conductivity, but it has been reported that an increasing doping with iron can be beneficial, causing a shift to higher temperature of cobalt's oxygen loss.[40] The addition of niobium and the calcination treatment at 1200°C (Fig. 6.2) seem to be effective in enhancing the stability of the cubic perovskite and suppressing the formation of the brownmillerite phase.

6.3.3 TGA

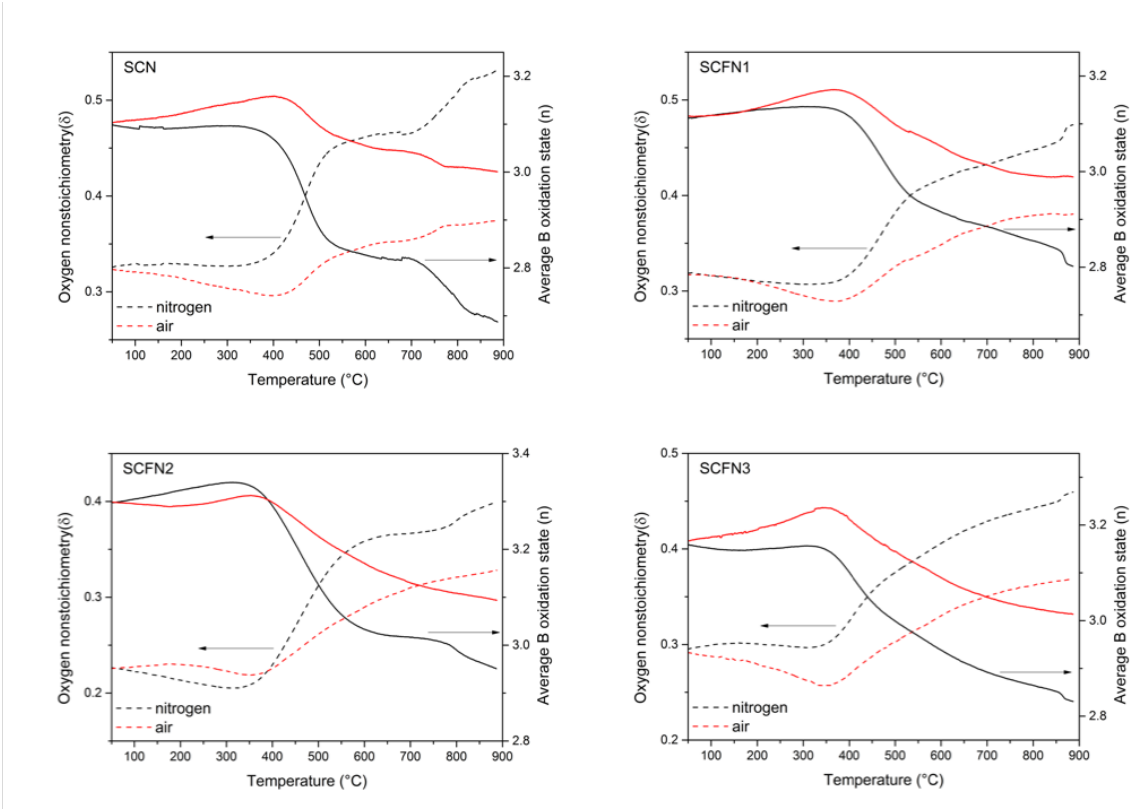

Fig 6.4: Oxygen nonstoichiometry and average oxidation state of B-cations between 50 and 900°C in air and nitrogen atmosphere of $SrCo_{0.95}Nb_{0.05}O_{3-\delta}$ (SCN), $SrCo_{0.85}Fe_{0.1}Nb_{0.05}O_{3-\delta}$ (SCNF1), $SrCo_{0.75}Fe_{0.2}Nb_{0.05}O_{3-\delta}$ (SCNF2), $SrCo_{0.65}Fe_{0.3}Nb_{0.05}O_{3-\delta}$ (SCNF3). Data obtained by thermogravimetric analysis, initial oxygen nonstoichiometry determined by iodometric titration.

After determining the oxygen nonstoichiometry (δ) and average oxidation state of B-cations (n), their evolution with temperature has been investigated by thermogravimetric analysis, in air and N_2 atmosphere. Figure 6.4 shows the evolution of $SrCo_{0.95}Nb_{0.05}O_{3-\delta}$ (SCN), $SrCo_{0.85}Fe_{0.1}Nb_{0.05}O_{3-\delta}$ (SCNF1), $SrCo_{0.75}Fe_{0.2}Nb_{0.05}O_{3-\delta}$ (SCNF2) and $SrCo_{0.65}Fe_{0.3}Nb_{0.05}O_{3-\delta}$ (SCNF3) nonstoichiometry and n with temperature.

Considering the chemical equilibrium of cobalt with surrounding atmosphere, represented by:

$$\frac{1}{2}\,O_2(g) + 2Co_{Co}^{X} + V_l^{X} \leftrightarrow O_l' + 2Co_{Co}^{\bullet} \qquad (8)$$

in which O_l' is produced by the adsorption of gaseous oxygen in the vacant oxygen sites oxidizing Co_{Co}^{X} (Co^{3+}) to $Co_{Co}^{\bullet}$ (Co^{4+}). The same mechanism is valid for iron, with the

formation of Fe^{4+}.[17] According to the atmosphere and the temperature, the perovskite can incorporate oxygen:

$$2Co_{Co}^{X} + V_{O}^{\bullet\bullet} + \frac{1}{2}O_2 \rightarrow O_{O}^{X} + 2Co_{Co}^{\bullet} \qquad (9)$$

or the equilibrium can be reversed and oxygen is released, with a consequent weight loss:

$$O_{O}^{X} + 2Co_{Co}^{\bullet} \rightarrow 2Co_{Co}^{X} + V_{O}^{\bullet\bullet} + \frac{1}{2}O_2 \qquad (10)$$

Considering the case of air two windows can be identified: below 400 °C, a weight increase is observed, the mechanism is described by (9) and leads to the formation of Co^{4+} and Fe^{4+}, which are p-type carriers and have been reported to be responsible for an increase in conduction.[41,43] The average oxidation state (n) observed in the maximum grows with iron doping, being 3.15 (SCN), 3.17 (SCFN1), 3.31 (SCFN2) and 3.23 (SCFN3). This is in agreement with the more favorable formation of higher oxidation states in presence of iron.[40,41] Interestingly, despite the value of n is always the highest in correspondence to the maximum (around 350 °C), in SCFN2 the oxygen incorporation is less pronounced that in the other samples. This can be explained considering the high value of n measured by iodometric titration (3.30): since SCFN2 is already more oxidized than the other samples, a minor amount of oxygen is incorporated. Above 400 °C in air, a constant release of oxygen is observed and a value of 3.00 is detected for all samples except SCFN2, for which the value of n is 3.09.

The oxygen loss in the region above 400°C is more marked when the samples are heated in nitrogen: SCN shows a first steep increase in the nonstoichiometry before 600°C, and a second one above 700°C, leading to a value of cobalt average valence below 2.7. This suggests that the sample is undergoing a fast reduction before 800°C. Considering the possible reactions occurring, at high temperature the decomposition reaction of cobalt oxide is no more negligible:

$$2O_{O}^{X} + 2Co_{Co}^{X} \rightarrow 2Co_{Co}^{\prime} + 2V_{O}^{\bullet\bullet} + O_2 \qquad (11)$$

where Co_{Co}^{X}, $Co_{Co}^{\prime}$ are Co^{3+} and Co^{2+}, respectively. This reaction, could responsible of the reduction of cobalt species to Co^{2+}, with the consequent structure instability.

In the iron doped samples the release of oxygen appears to be less abrupt, proceeding with a continuous mechanism. Doping with iron seems to be even more effective in reducing the release of oxygen in the high temperature region, where the intensity of oxygen release decreases. This might indicate a stabilizing effect of iron over cobalt oxide decomposition.

Sample	Nitrogen			Air	
	δ_0	$\delta_{900\,°C}$	$\Delta\delta$	$\delta_{900\,°C}$	$\Delta\delta$
SCN	0.3233	0.5315	0.2082	0.3746	0.0513
SCFN1	0.3158	0.4741	0.1587	0.3807	0.0649
SCFN2	0.2250	0.3995	0.1745	0.3280	0.1030
SCFN3	0.2933	0.4596	0.1663	0.3682	0.0749

Table 6.3: Initial oxygen nonstoichiometry (δ_0), oxygen nonstoichiometry at 900 °C ($\delta_{900\,°C}$) and their difference ($\Delta\delta$) obtained from TGA measurements in nitrogen and air atmosphere, respectively, for $SrCo_{0.95}Nb_{0.05}O_{3-\delta}$ (SCN), $SrCo_{0.85}Fe_{0.1}Nb_{0.05}O_{3-\delta}$ (SCNF1), $SrCo_{0.75}Fe_{0.2}Nb_{0.05}O_{3-\delta}$ (SCNF2), $SrCo_{0.65}Fe_{0.3}Nb_{0.05}O_{3-\delta}$ (SCNF3).

Table 6.3 shows the resulting oxygen nonstoichiometries obtained from TGA measurements for the samples. It is interesting to notice that the incorporation of iron in the lattice is producing a different effect on the oxygen release properties as a function of the atmosphere. In fact, the difference in the values of δ ($\Delta\delta$) shows an opposite trend whether it is measured in nitrogen or air, respectively.
In nitrogen atmosphere, the values of $\Delta\delta$ decrease with the introduction of iron in the lattice, indicating that oxygen release is hampered, probably due to a more difficult reducibility of iron with respect of cobalt. In air atmosphere the opposite trend is recorded: a slightly higher release of oxygen is observed for all iron containing samples, suggesting that in presence of iron the lattice could accommodate a higher amount of defects. This proves that iron introduction can be beneficial in both atmospheres, granting a lower difference in nonstoichiometry between the two sides of the membrane and a more uniform conduction.

6.3.4 O_2-TPD

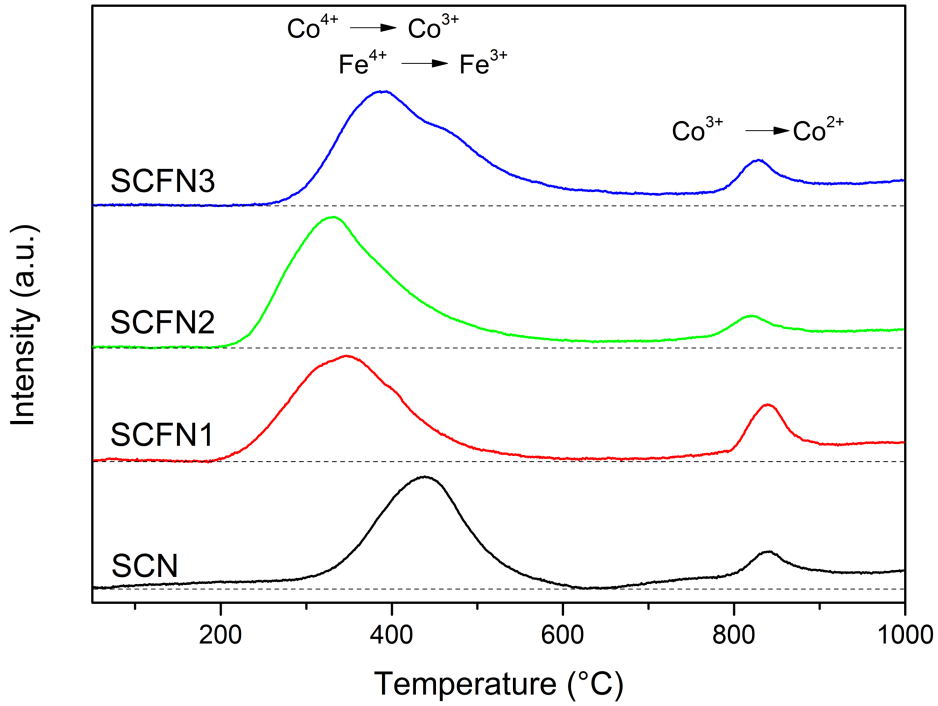

Fig 6.5: O_2-TPD in nitrogen between 50 and 1000 °C of $SrCo_{0.95}Nb_{0.05}O_{3-\delta}$ (SCN), $SrCo_{0.85}Fe_{0.1}Nb_{0.05}O_{3-\delta}$ (SCNF1), $SrCo_{0.75}Fe_{0.2}Nb_{0.05}O_{3-\delta}$ (SCNF2), $SrCo_{0.65}Fe_{0.3}Nb_{0.05}O_{3-\delta}$ (SCNF3). The samples were previously conditioned in pure O_2 for 1h at 900 °C, followed by cooling in pure O_2 atmosphere.

In order to evaluate the effect of doping on the oxygen mobility of the samples, O_2-TPD was performed. This technique consists of a mild pre-conditioning phase to clean the sample's surface to have all the sites for oxygen adsorption available, a second step in which pure oxygen is dosed on the sample at high temperature and a final desorption step in which the bound oxygen is released. Figure 6.5 shows the results for the desorption stage, in which two peaks can be identified: a low temperature large peak in the 200-600 °C interval and a smaller signal centered between 800 and 900 °C. The former is typically labeled as α-oxygen and is due to loosely bound oxygen, the latter is labeled as β-oxygen and arises from tightly bound oxygen species which are typically ascribed to oxygen released from the lattice.[33,44]

A third contribution can be observed, being a broadened signal due to a continuous release of oxygen above 600°C (the dashed line in figure 6.5 is provided as reference), which suggests that at this temperature the lattice mobility of oxygen is already sufficient

for displaying ionic conductivity.[45] Apparently this effect is more pronounced for samples with higher Fe content.

Similar desorption profiles have been observed by McIntosh *et al* and Zhang *et al*,[46,47] with the latter reporting that the substitution of Nb in small amount is effective in reducing the oxygen release at high temperature due to the phase transition from unstable perovskite to brownmillerite.

Focusing on the first peak, α-oxygen species are related to the presence of vacancies, which are saturated during the conditioning step. As a result of this process, the reaction can be described again by the equilibrium of cobalt and iron with surrounding atmosphere:

$$2Co_{Co}^{X} + V_{O}^{\bullet\bullet} + \frac{1}{2}O_2 \rightarrow O_{O}^{X} + 2Co_{Co}^{\bullet} \qquad (9)$$

$$2Fe_{Fe}^{X} + V_{O}^{\bullet\bullet} + \frac{1}{2}O_2 \leftrightarrow O_{O}^{X} + 2Fe_{Fe}^{\bullet} \qquad (12)$$

Where Co_{Co}^{X} , $Co_{Co}^{\bullet}$, Fe_{Fe}^{X} , $Fe_{Fe}^{\bullet}$ and $V_{O}^{\bullet\bullet}$ represent Co^{3+}, Co^{4+}, Fe^{3+}, Fe^{4+} and oxygen vacancy, respectively. In the conditioning step, reaction (9) and (12) represent the saturation of oxygen vacancies and creation of Co^{4+} and Fe^{4+} species which are responsible for p-type conduction. In this context, the temperature programmed desorption represents a sensitive probe able to distinguish the different desorption sites, which may be due to the presence of different species (Fe^{4+}, for example, is expected to be thermodinamically more stable than Co^{4+})[36] or different adsorption sites in the case of cations occupying non-equivalent positions in the lattice.[48,49] Moreover, the onset temperature for desorption of α-oxygen is correlated with both the B-O-B bonding energy and the lattice parameter a_0. The influence of these two parameters can be competitive: in fact, as the lattice parameter is increasing, the average bonding energy for B-O-B is reported to decrease due to a longer bonding distance between the crystal planes.[47] Nonetheless considering B-site cations individually, Fe-O bond energy is larger compared to Co-O.[50,51] This means that for large Fe substitution a competition between the effect of lattice parameter and Fe-O bond energy is expected.[52]

Sample	$T_{peak\ \alpha}$ (°C)	Area α-O2	$T_{peak\ \beta}$ (°C)	Area β-O2	Tot
SCN	435	9.92	839	0.88	10.8
SCFN1	315, 349, 399	11.45	840	1.53	12.98
SCFN2	327, 368	13.52	821	0.73	14.25
SCFN3	389, 461	11.94	828	0.95	12.89

Table 6.4: Peak temperature and normalized peak areas (expressed in $mlO_2 \cdot g_{perov}^{-1}$) for α and β oxygen signals obtained from TPD measurement on $SrCo_{0.95}Nb_{0.05}O_{3-\delta}$ (SCN), $SrCo_{0.85}Fe_{0.1}Nb_{0.05}O_{3-\delta}$ (SCNF1), $SrCo_{0.75}Fe_{0.2}Nb_{0.05}O_{3-\delta}$ (SCNF2), $SrCo_{0.65}Fe_{0.3}Nb_{0.05}O_{3-\delta}$ (SCNF3) performed in the 50-1000 °C interval.

Table 6.4 shows the results obtained for the TPD measurements for SCN, SCFN1, SCFN2 and SCFN3 samples. Comparing the low temperature signals in figure 6.5 it is possible to notice that, while SCN sample has a single peak centered at 435 °C, iron doping seems to induce the formation of a second peak at lower temperature. In all the Fe-doped samples at least two signals are detected and a shift towards lower temperature is observed. This agrees with the presence, beside Co^{4+}, of Fe^{4+}, as suggested before. The onset temperature of the α-oxygen signal increases in the order: SCFN1< SCFN2< SCFN3< SCN. This suggests that the introduction of iron in the lattice is decreasing the B-O bonding energy due to an increase in the lattice parameter, as observed from the XRD measurements, but the larger is the amount of iron, the higher energy is required to desorb oxygen. Moreover, the presence of iron is associated with a larger release of α-oxygen, which gets more pronounced in the samples with a higher content of iron.

Concerning the β-oxygen signal at high temperature, this has been attributed to the release of oxygen due to a partial Co^{3+}- Co^{2+} reduction, since Fe^{3+} is reported to be stable at this temperature.[46] Differently from what was observed for α species, iron doping seems not to affect significantly the onset of β-oxygen peak, probably due to the high temperature, and the amount of oxygen released does not suggest any trend occurring with iron doping.

6.3.5 Electrical conductivity

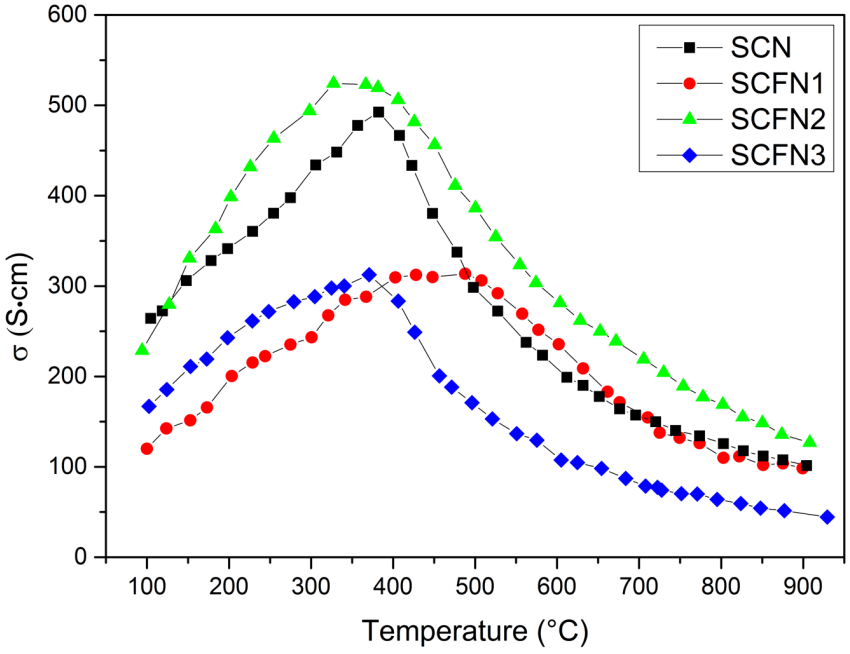

Fig 6.6: Conductivity measured in air between 100 and 900 °C of $SrCo_{0.95}Nb_{0.05}O_{3-\delta}$ (SCN), $SrCo_{0.85}Fe_{0.1}Nb_{0.05}O_{3-\delta}$ (SCNF1), $SrCo_{0.75}Fe_{0.2}Nb_{0.05}O_{3-\delta}$ (SCNF2), $SrCo_{0.65}Fe_{0.3}Nb_{0.05}O_{3-\delta}$ (SCNF3).

As aforementioned, electronic conductivity is an essential requirement for a material in order to have oxygen permeability; for this reason, the conductivity of the samples is tested in air.

Figure 6.6 shows the total conductivities obtained from the four probes measurement: all the samples display a good conductivity in the considered interval, reaching maximum values 490, 315, 525 and 310 $S \cdot cm^{-1}$ for SCN, SCFN1, SCFN2 and SCFN3, respectively.

In their work, Tai *et al* elucidated that the conduction in LSCF occurs *via* polaron hopping mechanism, where p-type carriers are responsible for conduction: when heating the material, after an initial increase in conductivity due to incorporation of oxygen and formation of Co^{4+} and Fe^{4+} (p-type carriers responsible for conduction). After displaying a maximum, a decreases in the conductivity is observed as oxygen is released by the material and cobalt and iron are reduced. The observed trend of conductivity in SCN, SCFN1, SCFN2 and SCFN3 is similar to that reported by Tai *et al*[41] and the results agree with what was observed in the TGA and O_2-TPD measurements: after an initial increase

due to the incorporation of oxygen, the conductivity values have a maximum at 400 °C (except in the case of SCFN1, for which the maximum is shifted at 500 °C) and then decrease. The observed values are consistent with what has been reported before and Wang *et al*, that investigated $SrCo_{1-x}Fe_xO_{3-\delta}$ compounds and observed 520 $S \cdot cm^{-1}$ for 20% iron substitution.[53]

It is worth noticing that at 900°C the electronic conductivity is still remarkable: 101, 98, 229 and 44 $S \cdot cm^{-1}$ are observed for SCN, SCFN1, SCFN2 and SCFN3, respectively. This results confirm that the samples display electronic conduction in the desired operation temperature range (700-950 °C) and, coupling these results with the oxygen nonstoichiometry at high temperature observed from TGA measurements, ensures that the chosen materials have the MIEC properties necessary for oxygen permeation.

6.3.6 XPS

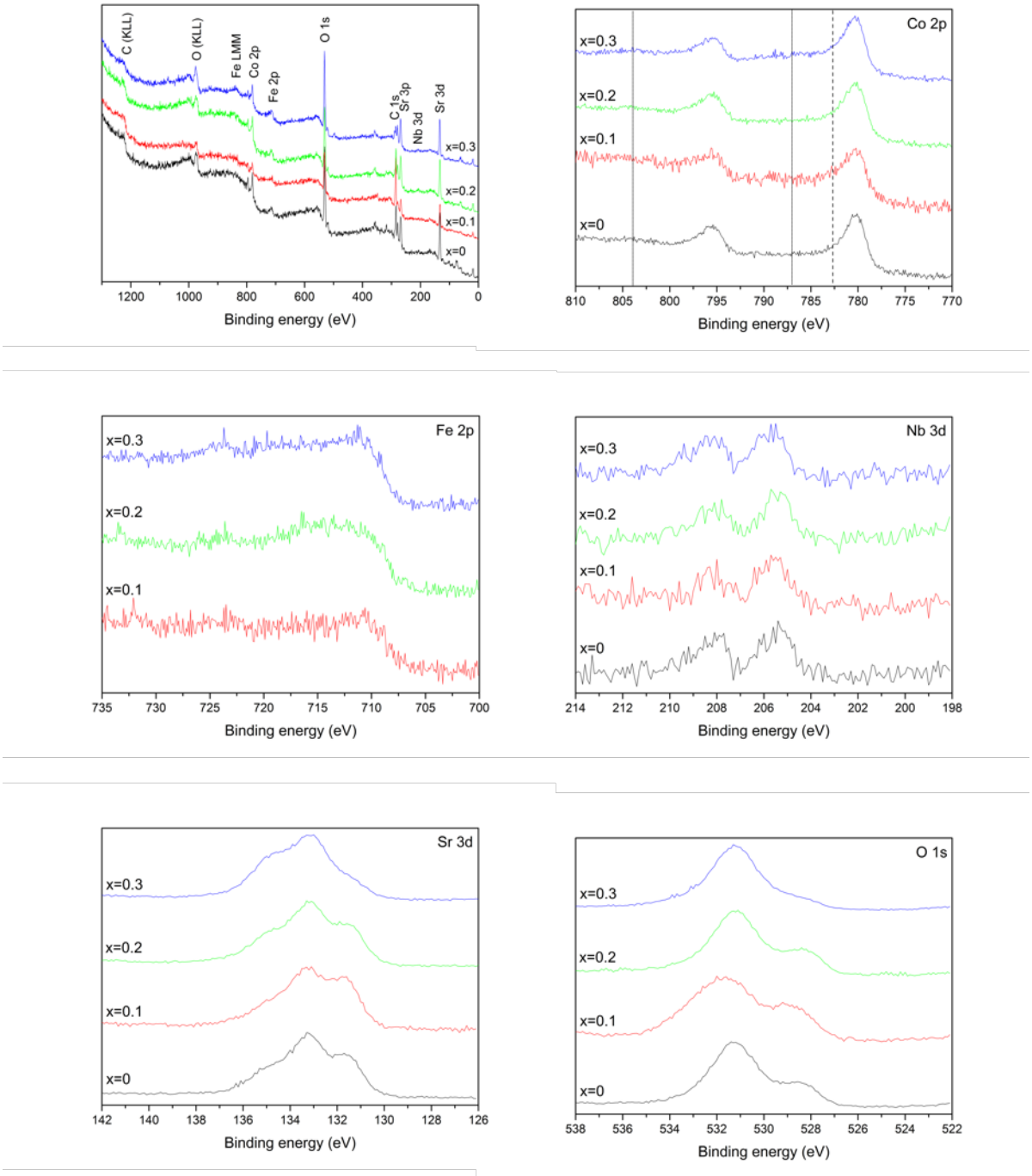

Fig 6.7: XPS spectra of $SrCo_{0.95-x}Fe_xNb_{0.05}O_{3-\delta}$ (x=0; 0.1; 0.2; 0.3) samples: survey scan (top left) and multiplex for the Co 2p, Fe 2p, Nb 3d, Sr 3d and O 1s peaks.

Sample	Sr			Co			Fe			Nb			O		
	XPS	EDX	NOM	XPS	EDX	NOM	XPS	EDX	NOM	XPS	EDX	NOM	XPS	EDX	NOM
SCN	18.4	19.9	20.0	8.6	20.4	19.0	/	/	/	0.6	0.7	1.0	72.4	59	60.0
	XPS	EDX	NOM	XPS	EDX	NOM	XPS	EDX	NOM	XPS	EDX	NOM	XPS	EDX	NOM
SCFN1	13.7	18.7	20.0	5.5	15.9	17.0	3.3	2.0	2.0	0.6	1.1	1.0	76.9	60.1	60.0
	XPS	EDX	NOM	XPS	EDX	NOM	XPS	EDX	NOM	XPS	EDX	NOM	XPS	EDX	NOM
SCFN2	17.9	19.6	20.0	9.0	13.4	15.0	5.2	4.5	4.0	0.6	1.2	1.0	67.3	60.5	60.0
	XPS	EDX	NOM	XPS	EDX	NOM	XPS	EDX	NOM	XPS	EDX	NOM	XPS	EDX	NOM
SCFN3	15.0	18.3	20.0	8.2	10.5	13.0	6.5	5.6	6.0	0.6	1.0	1.0	69.7	63.1	60.0

Table 6.5: Atomic compositions of surface (XPS), bulk (EDX) and nominal values derived from stoichiometry of $SrCo_{0.95}Nb_{0.05}O_{3-\delta}$ (SCN), $SrCo_{0.85}Fe_{0.1}Nb_{0.05}O_{3-\delta}$ (SCNF1), $SrCo_{0.75}Fe_{0.2}Nb_{0.05}O_{3-\delta}$ (SCNF2), $SrCo_{0.65}Fe_{0.3}Nb_{0.05}O_{3-\delta}$ (SCNF3) pellets after sintering.

Sample	Sr			Co			Fe			Nb			B/A (%)			Co/Fe		
	XPS	EDX	NOM	XPS	EDX	NOM	XPS	EDX	NOM	XPS	EDX	NOM	XPS	EDX	NOM	XPS	EDX	NOM
SCN	66.7	48.5	50.0	31.1	49.8	47.5	/	/	/	2.3	1.6	2.5	0.49	1.04	1.00	/	/	/
	XPS	EDX	NOM	XPS	EDX	NOM	XPS	EDX	NOM	XPS	EDX	NOM	XPS	EDX	NOM	XPS	EDX	NOM
SCFN1	59.3	49.6	50.0	23.7	42.1	42.5	14.4	5.3	5.0	2.6	3.0	2.5	0.68	1.11	1.00	1.64	8.19	8.50
	XPS	EDX	NOM	XPS	EDX	NOM	XPS	EDX	NOM	XPS	EDX	NOM	XPS	EDX	NOM	XPS	EDX	NOM
SCFN2	54.8	50.6	50.0	27.5	34.7	37.5	15.9	11.6	10.0	1.8	3.0	2.5	0.83	0.97	1.00	1.72	3.00	3.75
	XPS	EDX	NOM	XPS	EDX	NOM	XPS	EDX	NOM	XPS	EDX	NOM	XPS	EDX	NOM	XPS	EDX	NOM
SCFN3	49.4	51.7	50.0	27.2	29.5	32.5	21.3	15.9	15.0	2.1	2.9	2.5	1.02	0.86	1.00	1.27	1.86	2.17

Table 6.6: Atomic cations compositions of surface (XPS), bulk (EDX) and nominal values derived from stoichiometry; B/A ratios and Co/Fe ratios of $SrCo_{0.95}Nb_{0.05}O_{3-\delta}$ (SCN), $SrCo_{0.85}Fe_{0.1}Nb_{0.05}O_{3-\delta}$ (SCNF1), $SrCo_{0.75}Fe_{0.2}Nb_{0.05}O_{3-\delta}$ (SCNF2), $SrCo_{0.65}Fe_{0.3}Nb_{0.05}O_{3-\delta}$ (SCNF3) pellets after sintering.

The insertion of a dopant in a lattice does not only have an influence on the crystal structure, oxygen stoichiometry and transport properties, but can play a determining role in tuning the surface composition of the sample itself. X-ray photoelectron spectroscopy allows investigating the atomic layers on the surface of a material, which are the active sites for every surface-mediated reaction. In OTMs in particular, the surface represents the site where molecular oxygen adsorbs on vacancies and is dissociated before being transported across the membrane as O^{2-} ion. Therefore, pellets identical to the final membranes are prepared, sintered and their surface is investigated by XPS.

Figure 6.7 shows the collected spectra for the samples, displayed in relation to the iron content, all the investigated elements are present in the survey spectra and no impurity is detected.

In the case of Co spectrum, it is possible to recognize the $2p_{3/2}$ and $2p_{1/2}$ peaks centered at 780.2 and 795.4 eV, respectively, and is worth noticing the absence of shake-up signals. These are characteristic fingerprint of Co^{2+} oxidation state and they should be centered at 786.5 and 803.6 eV (dotted lines are drawn in the Co2p spectra as guidelines for the eye).[54] The absence of shake-up signals is consistent with the presence of cobalt in a higher oxidation state, as it is expected from the stoichiometry and observed in other Co-containing perovskites.[55,56] In the samples with a higher iron content a small peak at 782.5 eV (dashed line is drawn as guideline) is detected. In their work, Chen *et al* suggest that this signal could be due to the presence of Co^{2+}, even though no shake-up is observed.[57] Egorova *et al* found that in the a high amount of Co^{2+} is observed when high amount (20%) of niobium is present as dopant in $Ba_{0.5}Sr_{0.5}(Co_{0.8}Fe_{0.2})_{1-x}Nb_xO_{3-\delta}$,[58] which is not surprising considering the charge compensation mechanisms described before. The higher binding energy and the absence of shake-up peaks suggest that the peak could be due to the presence of a small amount of Co^{4+}.[59] Nevertheless, it should be remarked that the observation of high oxidation state species at XPS is often controversial and a matter of debate. Since the high BE shoulder of $Co2p_{3/2}$ signal is more pronounced in higher Fe-doped samples and is not detectable for SCN, this suggests that iron doping might be effective in stabilizing a higher oxidation state for cobalt. Concerning Fe 2p spectrum, two peaks centered at 710.9 and 723.6 eV are observed, which are consistent with the presence of Fe^{3+}, the low intensity does not allow a detailed analysis of this element.

Zhang *et al* observed the simultaneous presence of Fe^{2+}, Fe^{3+} and Fe^{4+} in $SrFe_{0.8}M_{0.2}O_{3-\delta}$ (M=Ti, Nb, Cr), with Fe^{4+} signal becoming more intense as charge compensation mechanism is less effective due to the lower valence of the dopant ion.[60] Therefore, a possible presence of Fe^{4+} cannot be ruled out. The spectrum of Nb 3d shows two broad signals at 205.6 and 208.1 eV. Compared to the case of pure Nb_2O_5, which has two peaks at 207.4 and 210.1 eV,[61] the spectrum of Nb 3d in perovskites is often found to be centered at a lower binding energy (206.1 and 209.0 eV).[62] Opris *et al* observed that for $Co@Nb_2O_5@Fe_3O_4$ composites a surface reaction between the involved species happens after the deposition of cobalt and thermal treatment, producing a partial reduction of Nb(V) to Nb(IV), which has two peaks at 204.6 and 207.7 eV.[63] This suggests that the presence of Nb(IV) on the surface of the pellets is probably due to the sintering treatment. Focusing on Sr 3d spectrum, it is possible to notice that it has at least three components, at 131.7, 133.2 and 134.8 eV, respectively. These arise from the superposition of two doublets belonging to oxidic strontium in perovskites and strontium carbonate, that have peaks center at 131.7 and 133.2 eV (perovskitic Sr) and 133.5 and 135.6 eV (carbonatic Sr), respectively. [56,64] It is possible to notice that the perovskitic doublet is more intense in the samples with a lower iron amount, while the carbonatic component becomes predominant in the sample with the highest iron doping (SCFN3). Since the signal of $SrCO_3$ is expected to be present on the surface of every strontium contanining perovskites,[36] two explanations are possible for this trend: 1) as iron content increases, the formation of $SrCO_3$ is more likely to happen, which would be the opposite than the observed trends of increased CO_2 tolerance for other Fe-doped cobaltates; 2) as iron content increases, the presence of strontium on the outmost layer (due to segregation phenomena) is reduced. This would imply that the surface termination layers of the material would have a spectrum presenting a high intensity for the signal due to the carbonatic termination, but a lower amount of perovskitic oxygen. Quantitative analysis of atomic ratios could provide an insight into this unexpected trend. The spectrum of oxygen is characterized by the presence of two peaks at 528.6 and 531.3 eV, respectively. The former is characteristic of perovskitic oxygen, the latter is typically due to the presence of hydroxides and carbonates surface contaminants.[55,64] In all samples the signal belonging to surface contaminants is more intense than the perovskitic one. Nonetheless, it is interesting to

notice that, while SCFN3 has a higher amount of carbonatic oxygen similarly to what is observed for strontium signal, in the other iron containing compounds the perovskitic component is slightly more intense than in the undoped sample (SCN).

The analysis of surface composition allows to observe how the effect of doping tunes the atomic ratios on the surface of the pellets. In fact, it is possible to observe that the difference between the surface composition obtained by XPS and the nominal ratios is more pronounced than in the case of the bulk composition obtained by EDX, which is consistent with the expected values within the error range of the technique. A general surface segregation of strontium is observed, which in the SCN sample is present in a double amount with respect to cobalt. The segregation of alkaline and alkaline earths elements is critical issue in many perovskites and has two major drawbacks on the performance of the materials: 1) the amount of B-site cations, which are usually the responsible for the activity, is reduced, with a consequent lower activity; 2) strontium can react with CO_2 to form carbonates. Even though the mechanism has not been completely elucidated, it is suggested that oxygen vacancies can provide an attack site for CO_2 to interact with Sr and could explain the very low tolerance of BSCF to CO_2, which besides Ba higher affinity for carbonates has a larger oxygen nonstoichiometry.[46,60] This means that after occupying a vacancy, if CO_2 reacts with Sr to form carbonates, a vacancy site is permanently filled and not regenerated, with the a consequent reduction in the material's activity. Finally, it should not be underestimated that the formation of carbonates implies a sequestration of Sr from the perovskite, damaging the crystal structure and inducing instability. In the case of OTMs, a lower stability implies difficulties in obtaining gas tightness between the two chambers and a lower mechanical strength of the ceramic membrane.

Interestingly, the quantitative analysis for cations (reported in table 7.6) shows that 10% Fe doping is already effective in reducing the segregation of Sr and this is coupled with an excess of iron being present on the surface. Since iron is known to have a lower basicity compared to cobalt, it is possible that the surface segregation of Fe provides a lower interaction of Sr with CO_2. This seems to agree with the second hypothesis aforementioned when discussing Sr 3d spectrum. In all cases, the amount of cobalt present on the surface is always lower than the nominal value. This is not a new trend,

since it has been reported that Co has a lower tendency to diffuse towards the surface compared to A-site cations and other elements like Cu and Fe.[55] Consequently, the observed Co/Fe ratio is always lower than expected, being 81, 55 and 42% lower than the nominal value for SCFN1, SCFN2 and SCFN3, respectively.

Before testing the oxygen permeation performances of the samples, SEM microscopy is performed, in order to observe the microstructure of the membranes. Figure 7.9 shows the cross section of pellets after the sintering process. All the materials show a compact and dense structure with continuous grains and small isolated porosity, which is not connected. In the case of SCFN3 some larger voids are observed along the grain boundaries, suggesting a less compact structure. This may be due to the higher amount of iron in the sample, requiring a specific thermal treatment in order to improve the densification process. However, during the study of the densification treatments a melting temperature around 1300°C was observed and the protocol for sintering has been optimized to obtain the best compromise between densification and avoiding at the same uncontrolled mass diffusion due to melting.

6.3.7 SEM

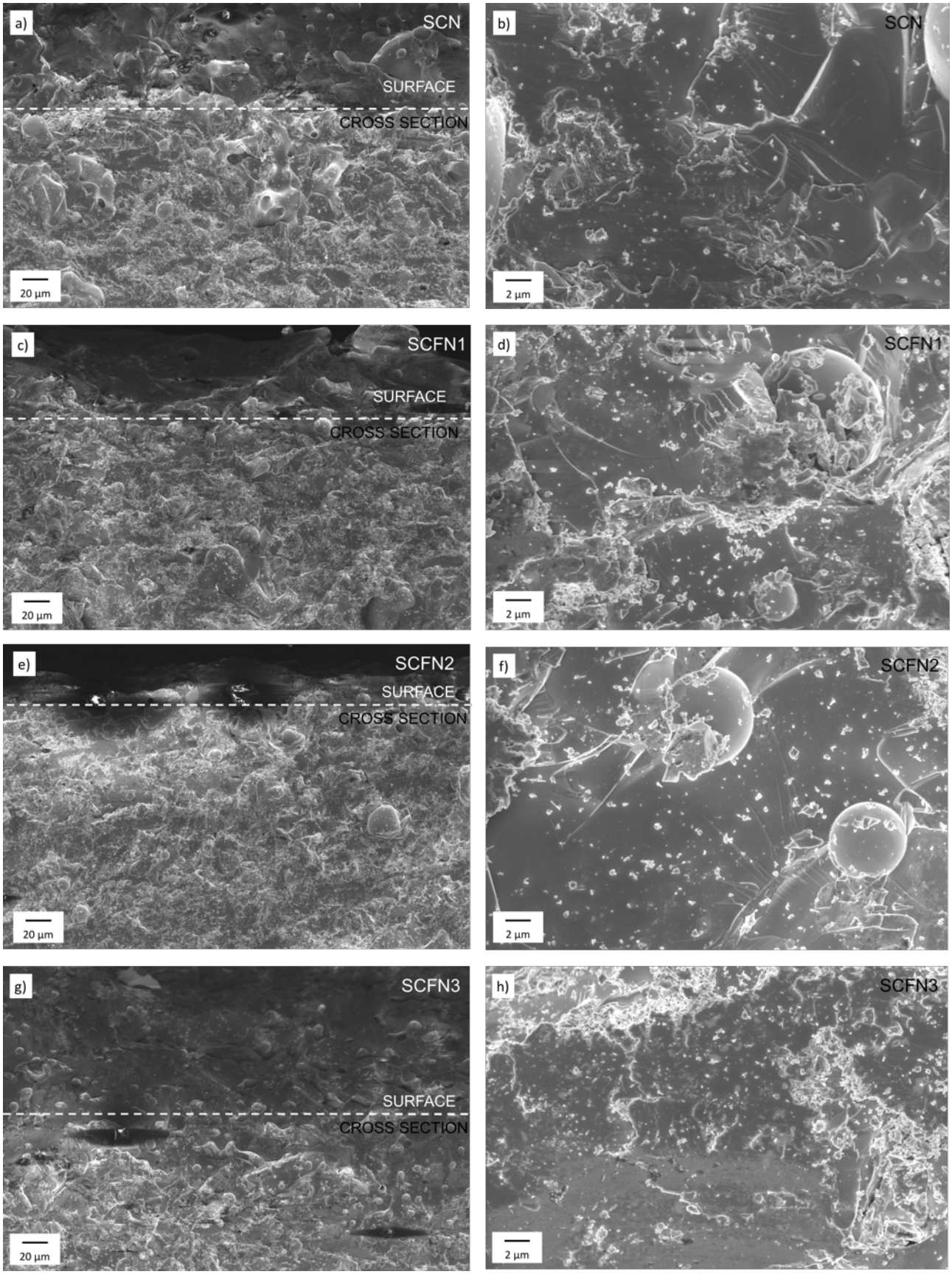

Fig 6.8: Scanning electron micrographs of as synthesized SCN (a, b), SCFN1 (c, d), SCFN2 (e, f) and SCFN3 (g, h) membranes.

6.3.8 Oxygen permeation

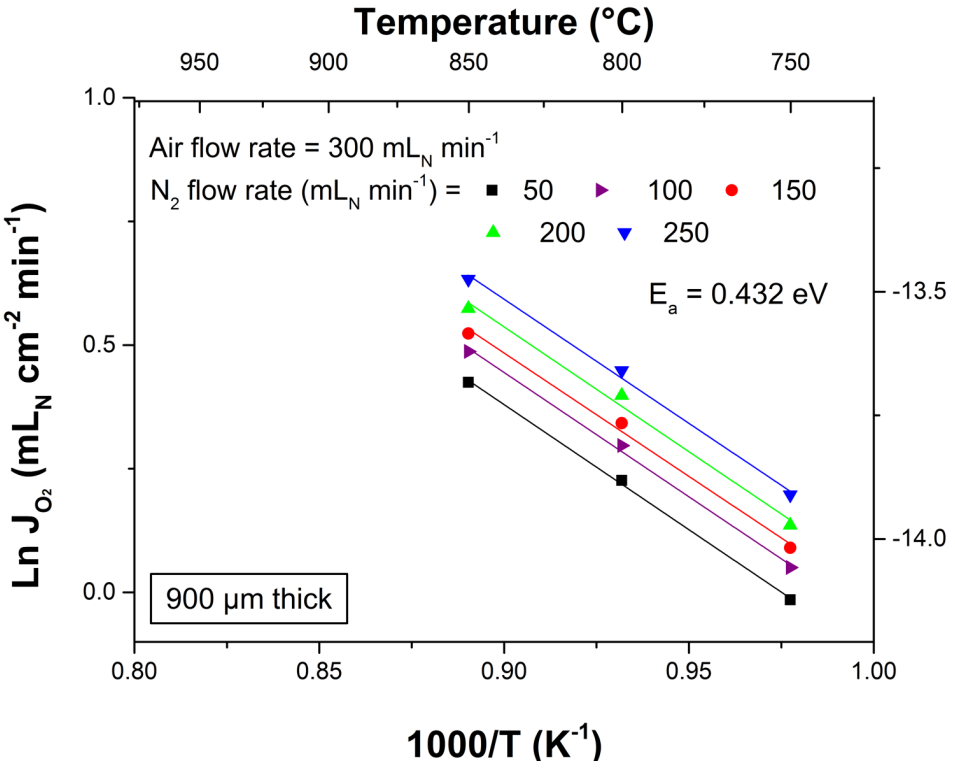

Fig 6.9: Temperature dependence of the oxygen permeation flux through the 900 µm thick SCFN1 pellet. 300mL$_N$min^{-1} of air and 50-250 mL$_N$min^{-1} of N_2 were used as feed and sweep gases, respectively.

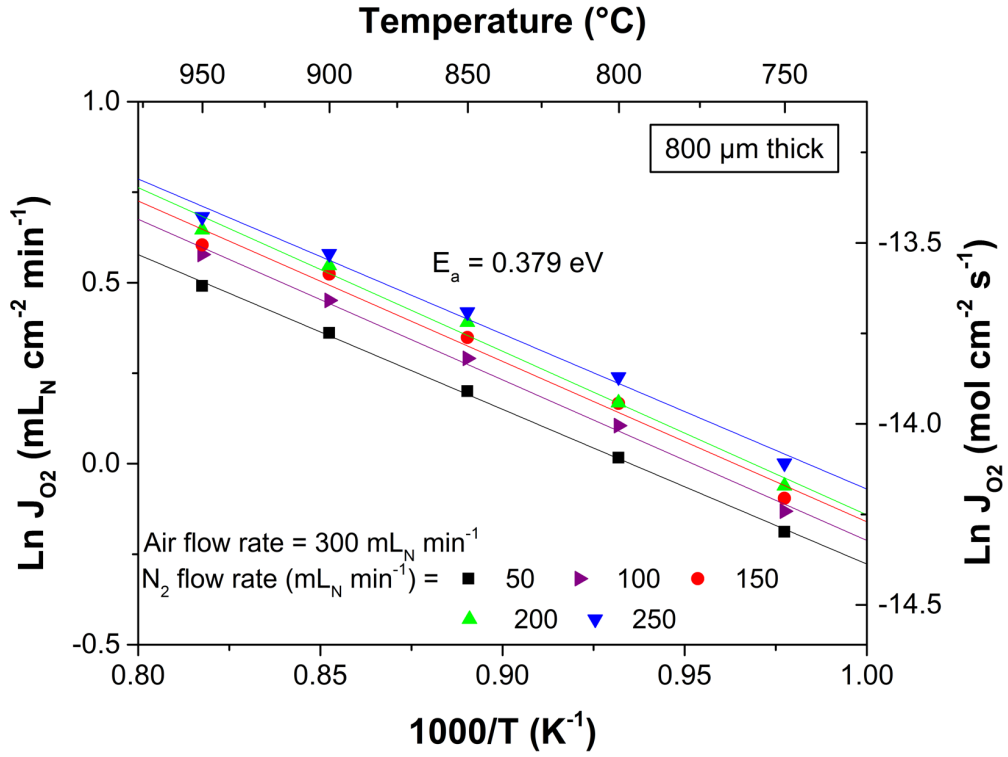

Fig 6.10: Temperature dependence of the oxygen permeation flux through the 800 µm thick SCFN2 pellet. 300mL$_N$min^{-1} of air and 50-250 mL$_N$min^{-1} of N_2 were used as feed and sweep gases, respectively.

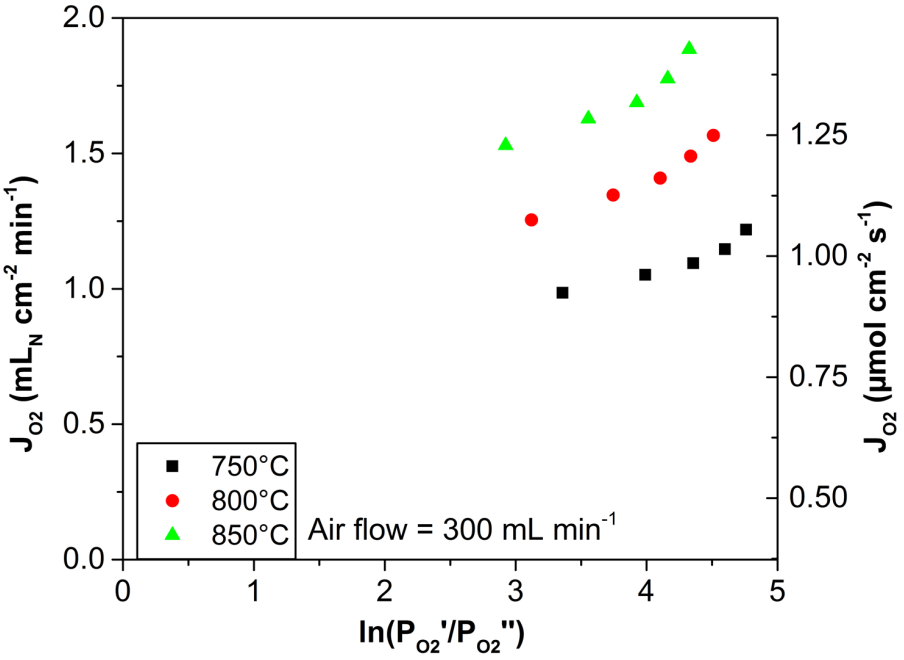

Fig 6.11: Oxygen permeation flux of SCFN1 membrane as a function of the natural logarithm ratio between the oxygen partial pressures at the feed and at the permeate side using N2 as sweep gas and air as feed gas.

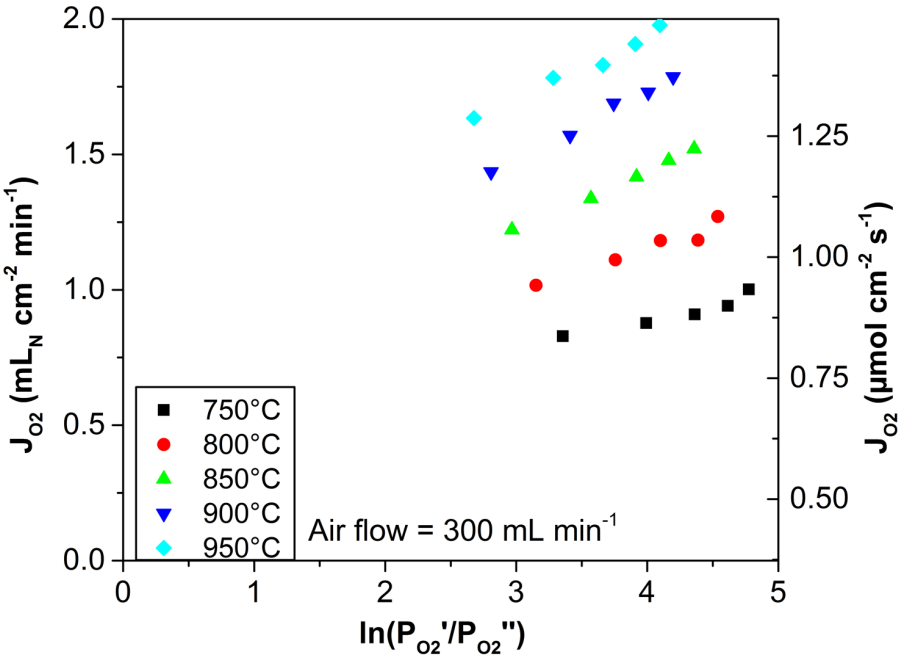

Fig 6.12: Oxygen permeation flux of SCFN1 membrane as a function of the natural logarithm ratio between the oxygen partial pressures at the feed and at the permeate side using N2 as sweep gas and air as feed gas.

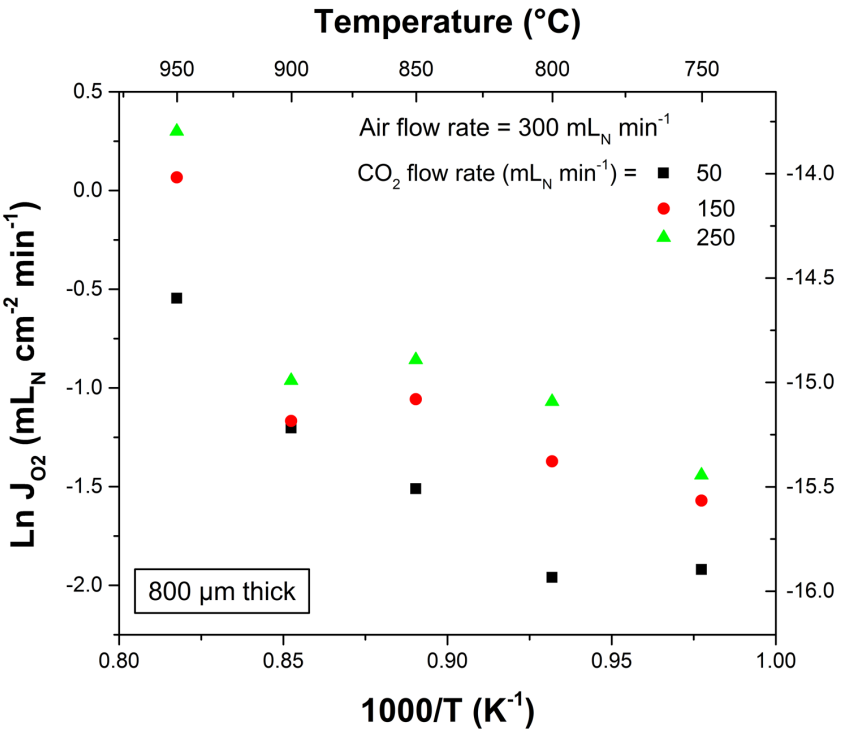

Fig 6.13: Temperature dependence of the oxygen permeation flux through the 800 µm thick SCFN2 pellet. 300mL$_N$min^{-1} of air and 50-250 mL$_N$min^{-1} of CO_2 were used as feed and sweep gases, respectively.

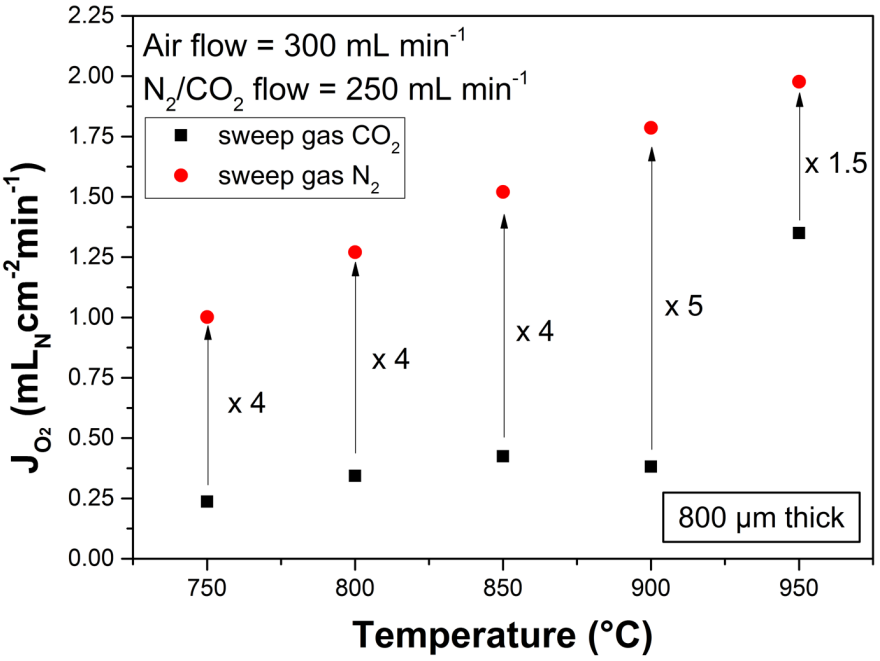

Fig 6.14: Temperature dependence of the oxygen permeation fluxes through the 800 µm thick SCFN2 pellet as a function of the sweep gas. 300mL$_N$min^{-1} of air and 50-250 mL$_N$min^{-1} of N_2 or CO_2 were used as feed and sweep gases, respectively.

Before discussing the O_2-permeation results, it is worth to remark that the membranes have been tested under atmospheric air (including presence of CO_2 and moisture) and no catalyst layer was applied on the surfaces of the membrane. It has been reported that surface modification of cobalt-based OTMs with a catalyst layer can be beneficial both for increasing the permeation flux and enhancing long term stability.[44,65,66] The permeation flux of a coated membrane can be several times higher than in the case of uncoated sample, at the price of increasing the system's complexity.

The oxygen permeation results seem to be influenced by the amount of iron in the chemical composition. Both the sample without iron (SCN) and the sample containing 30% of iron (SCFN3) results are not reported, since they repeatedly displayed an insufficient gas tightness for the results to be considered reliable. This could be due to different reasons: in the case of SCN a shift in the permeation curve is observed at 900°C, showing higher permeation flux above that temperature. This seems to suggest that an order/disorder phase transition is occurring, as the higher flux is indicating.[42] It can't be ruled out that the stabilizing effect of 5% niobium doping in may not be sufficient without the presence of iron to prevent a phase transition to a less conductive phase at high temperatures and reducing conditions. In the same extent, an interaction with the sealing glass paste can't be ruled out, but is expected to affect all the samples in a similar extent. Finally, being SCN the sample with the highest cobalt content, it is expected to have the larger expansion coefficient, which may result in a higher amount of undesired stresses occurring during the sealing procedure.

In the case of SCFN3 pellets, no shifts in the permeation flux were detected, but the samples showed visible cracks on the surface and appeared to be more fragile. Nagai *et al* reported that, among the set of 10% doped SC samples, $SrCo_{0.9}Fe_{0.1}O_{3-\delta}$ seemed to have the largest leaks despite displaying a high relative density. [18] It is thus possible that the ratio Fe/Nb ratio plays a role in the densification rate and final structure of the ceramics, suggesting that a higher Fe content may require a different sintering procedure in order to achieve a higher density of the sample.

SCFN1 and SCFN2 were successfully tested and their permeation fluxes are reported as a function of temperature (Figures 6.9, 6.10) and driving force (Figures 6.11, 6.12). In all cases an increase in the permeation flux as the temperature and the driving force increase

is observed. The oxygen fluxes at 750 °C for SCFN1 and SCFN2 are 1.21 and 1 $mL_N \cdot cm^{-2} \cdot min^{-1}$, respectively (with O_2 flow: 300 sccm; N_2 flow: 250 sccm) and can be considered promising even for a low temperature application. A value of 1.88 $mL_N \cdot cm^{-2} \cdot min^{-1}$ is detected for SCFN1 at 850 °C (O_2 flow: 300 sccm; N_2 flow: 250 sccm). This is the limit temperature at which stable performances of SCFN1 are detected. Despite a lower permeation flux, no instability is observed for SCFN2, for which a 1.95 $mL_N \cdot cm^{-2} \cdot min^{-1}$ flow is measured at 950 °C (O_2 flow: 300 sccm; N_2 flow: 250 sccm).

The calculated activation energy for oxygen permeation is 0.432 and 0.379 eV for SCFN1 and SCFN2 respectively. These values are closer to the 0.42 eV activation energy observed by Shao *et al* for $Ba_{0.5}Sr_{0.5}Co_{0.8}Fe_{0.2}O_{3-\delta}$, [16] than to the activation energy of 0.90 eV for $SrCo_{0.95}Nb_{0.05}O_{3-\delta}$ reported by Zhang *et al*, [19] or to the activation energy of 0.58 eV for $SrCo_{0.9}Nb_{0.1}O_{3-\delta}$ calculated by Yoo *et al*. [67] This suggests that iron doping gives a higher contribution to the activation energy for oxygen permeation compared to niobium.

After observing the stable performances of SCFN2, the same membrane has been tested using CO_2 as sweep gas too, in order to evaluate the applicability of the material in oxyfuel conditions. Figure 6.13 shows the temperature dependence of the logarithm of flow and it is possible to observe that the permeation flux is less stable when CO_2 is used as sweep gas, suggesting that an interaction between the gas and the membrane is occurring. This phenomenon could be due to a possible adsorption of CO_2 on the surface of the membrane to react with strontium. However, compared to the effect of CO_2 flow on BSCF observed by Engels *et al*, the loss in performance of SCFN2 is less abrupt. [68] Figure 6.14 shows that as the temperature increases, the detrimental effect of CO_2 becomes more relevant, suggesting a higher interaction of CO_2 with the membrane. The increase in permeation observed at 950°C suggests that at this temperature a desorption of the previously adsorbed CO_2 might occur and the detrimental effect of CO_2 sweep gas is decreased. This is consistent with the temperature peak for CO_2 desorption observed by Zhang et al for BSCF. [69]

Table 6.7 summarizes the effect of the different sweep gases on SCFN2 performances as a function of temperature. It can be noticed that as the sweep gas is switched to CO_2, the permeation fluxes decrease of about four times and this trend gets more pronounced as

the temperature rises, indicating an interaction of the CO_2 with the surface of the membrane.

	Air/N_2		**Air/CO_2**	
Temperature (°C)	O_2 permeation flux ($mL_N \cdot cm^{-2} \cdot min^{-1}$)	$\ln(pO^{2feed}/pO_2^{permeate})$	O_2 permeation flux ($mL_N \cdot cm^{-2} \cdot min^{-1}$)	$\ln(pO^{2feed}/pO_2^{permeate})$
750	1.00	4.77	0.23	6.19
800	1.27	4.53	0.34	5.12
850	1.52	4.35	0.42	5.61
900	1.78	4.19	0.38	5.72
950	1.95	4.09	1.34	4.47

Table 6.7:Oxygen permeation fluxes and driving force values for SCFN2 membrane as a function of temperature and testing atmosphere. Flows used for the feeding: 300 ml_N air and sweep gas: 250 ml_N N_2 and CO_2 are reported, respectively.

6.3.9 Ionic conductivity

From the obtained oxygen permeation results it is possible to estimate the ionic conductivity values for the tested samples. In fact, in the case of oxygen permeation limited only by bulk diffusion, oxygen flow is described by Wagner's equation:

$$J_{O_2} = \frac{RT}{16F^2L}\int_{p_{O_2}^{permeate}}^{p_{O_2}^{feed}} \frac{\sigma_{el}\sigma_{ion}}{\sigma_{el}+\sigma_{ion}}\left(p_{O_2}\right) dlnp_{O_2} \qquad (1)$$

In principle, this condition is always fulfilled as long as the membrane is thick enough and the diffusion of oxygen along the grain boundaries is negligible.[70,71] The conductivity expression in (1) can be rewritten as follows:

$$\sigma_{amb} = \frac{\sigma_{el}\sigma_{ion}}{\sigma_{el}+\sigma_{ion}} = \frac{\sigma_{el}\sigma_{ion}}{\sigma_{total}} = t_{ion}\sigma_{el} = t_{el}\sigma_{ion} \qquad (13)$$

Where σ_{amb} is the ambipolar conductivity and t_{ion} and t_{el} represent the transference number for ionic and electronic conduction, respectively. In the case of a mixed ionic and electronic conductor, the electronic conductivity is the dominating contribution to the ambipolar conductivity ($\sigma_{el} \gg \sigma_{ion}$) and the value of the transference number t_{el} is close to unity. The expression for the oxygen flow can thus be rewritten as:

$$J_{O_2} = \frac{RT}{16F^2L}\int_{p_{O_2}^{permeate}}^{p_{O_2}^{feed}} \sigma_{ion}\left(p_{O_2}\right) dlnp_{O_2} \qquad (14)$$

Which allows to obtain the expression for the calculation of the ionic conductivity from oxygen permeation flow:[72]

$$\sigma_{ion} = \frac{J_{O_2}\cdot L\cdot 16F^2}{RT}\left(\ln \frac{p_{O_2}^{feed}}{p_{O_2}^{permeate}}\right)^{-1} \qquad (15)$$

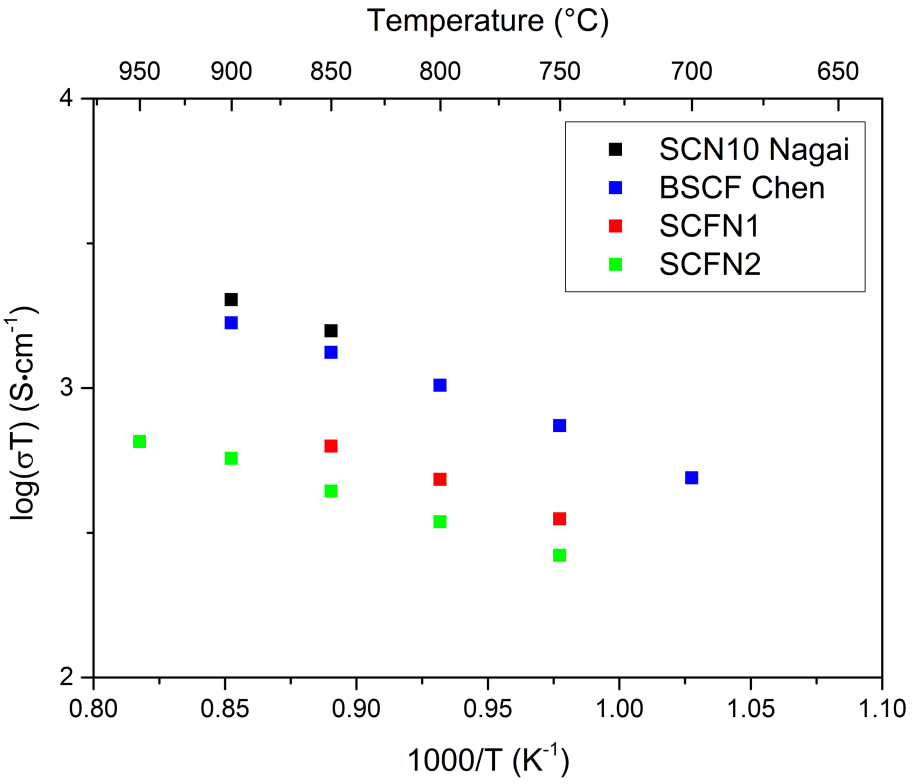

Fig 6.15: Temperature dependence of the ionic conductivities of SCFN1 and SCFN2, calculated from the oxygen permeation measurements. Reference values for $SrCo_{0.9}Nb_{0.1}O_{3-\delta}$ (SCN10) from Nagai *et al* and $Ba_{0.5}Sr_{0.5}Co_{0.8}Fe_{0.2}O_{3-\delta}$ (BSCF) from Chen *et al.*

Figure 6.15 shows the resulting ionic conductivities obtained from oxygen permeation measurements for SCFN1 and SCFN2. The values obtained by Chen *et al* for $Ba_{0.5}Sr_{0.5}Co_{0.8}Fe_{0.2}O_{3-\delta}$ (BSCF) and calculated for $SrCo_{0.9}Nb_{0.1}O_{3-\delta}$ (SCN10) from the results reported in Nagai *et al* work are also displayed.[18,73]

Sample	σ_{ion} (S·cm^{-1}) T=750°C	σ_{ion} (S·cm^{-1}) T=850°C
SCN10	/	1.40
BSCF	0.72	1.18
SCFN1	0.34	0.56
SCFN2	0.26	0.39

Table 6.8: Obtained ionic conductivities for $SrCo_{0.9}Nb_{0.1}O_{3-\delta}$ (SCN10) (calculated from the work of Nagai et al) , $Ba_{0.5}Sr_{0.5}Co_{0.8}Fe_{0.2}O_{3-\delta}$ (BSCF) (taken from the work of Chen et al) and calculated for SCFN1 and SCFN2 samples.

The obtained values for ionic conductivity confirm that the $\sigma_{el} \gg \sigma_{ion}$ hypothesis is a reasonable assumption, since the observed electronic conduction for SCFN1 and SCFN2 at 900°C is above 100 S·cm^{-1}. The ionic conductivities observed are among the highest reported in literature for MIEC materials and are even higher than the values observed for GDC (σ_{ion} =1.5·10^{-1} S·cm^{-1} at 800 °C) and YSZ (σ_{ion} =2·10^{-2} S·cm^{-1} at 800 °C) electrolytes.[74] Nevertheless, additional characterization of the ionic conductivity by dc-conductivity in blocking electrode configuration and determination of oxygen surface exchange and bulk diffusion coefficient by conductivity relaxation technique could provide more information about the ionic conduction mechanism.

Not surprisingly, the highest ionic conductivity is found for SCN10 sample, which is not doped with iron, for which a maximum value of 1.72 S·cm^{-1} is obtained at 900 °C. The introduction of more iron in the lattice induces a decrease in the ionic conductivity, which can be explained considering the oxygen nonstoichiometry at high temperature observed from thermogravimetric analysis (reported in table 6.3). As the iron substitution increases, the resulting nonstoichiometry at high temperature decreases and the charge compensation increases, suggesting that a smaller amount of oxygen vacancies are present in the material. Since these are directly responsible for ionic conduction, the lower values found for SCFN1 and SCFN2 compared to SCN10 could be due to the lower amount of vacancies present in the material.

In the case of BSCF, the higher ionic conductivity observed (0.75 S·cm^{-1} at 750 °C) could be due to the lack of niobium and the presence of barium. As reported by Shao *et al*,[75] a small amount of barium doping in the $Ba_xSr_{1-x}Co_{0.8}Fe_{0.2}O_{3-\delta}$ system enhances the oxygen permeation performances of the samples and a higher nonstoichiometry has been reported for Ba-doped sample with respect to $SrCo_{0.8}Fe_{0.2}O_{3-\delta}$.[46] This suggests that, having barium a larger ionic radius than strontium, it is effective in stabilizing the perovskite even

in presence of a higher amount of oxygen vacancies. Since it has been observed that $Ba_xSr_{1-x}Co_{0.8}Fe_{0.2}O_{3-\delta}$ total electric conductivity is decreasing as Ba content increases,[17] a possible explanation for the higher values for oxygen permeation could be the higher ionic conductivity in Ba-containing materials, due to the presence of a higher amount of vacancies.

6.3.10 After test SEM

In order to elucidate the difficulties observed for SCN and SCFN3 tests, after test SEM microscopy is performed on the tested membranes, aiming at identifying the presence of cracks or pinholes which might have formed during the test and could explain the observed leaks.

Figure 6.16 shows the cross sections of the membranes after the oxygen permeation test. As reported before, the detected leaks in SCN and SCFN3 samples are not negligible compared to the expected fluxes, therefore the results for the permeation of these samples are not reported. Nevertheless, the microstructural analysis can provide an insight into the mechanisms responsible for the failing of the test.

Considering the SCFN2 sample, it can be noticed that despite the exposure to reducing conditions on the sweep side and subsequently to CO_2 in the oxyfuel conditions, the cross section of the sample (Fig 6.16 f) does not show any pinholes or cracks, confirming the material stability in the experimental conditions. On the contrary, for the other samples voids and cracks can be noticed in the microstructure, which can explain the prominent leaks in the case of SCN and SCFN3 and the membrane breakage in the case of SCFN1. Looking at the shape of the holes detected in SCN, it can be noticed that 1-2 μm large pinholes are spread along the whole cross-section of the sample, suggesting the formation of a connected network which may be responsible for the lack in gas-tightness. A possible explanation for this phenomenon is the lower stability of SCN observed from TGA measurements in N_2 for SCN, where a large weight loss was observed above 700°C suggesting a partial reduction of cobalt. The morphology is different in the case of SCFN3, in which 10-20 μm large voids are observed. These point out that the densification of the sample might require a higher temperature sintering treatment in order to be achieved.

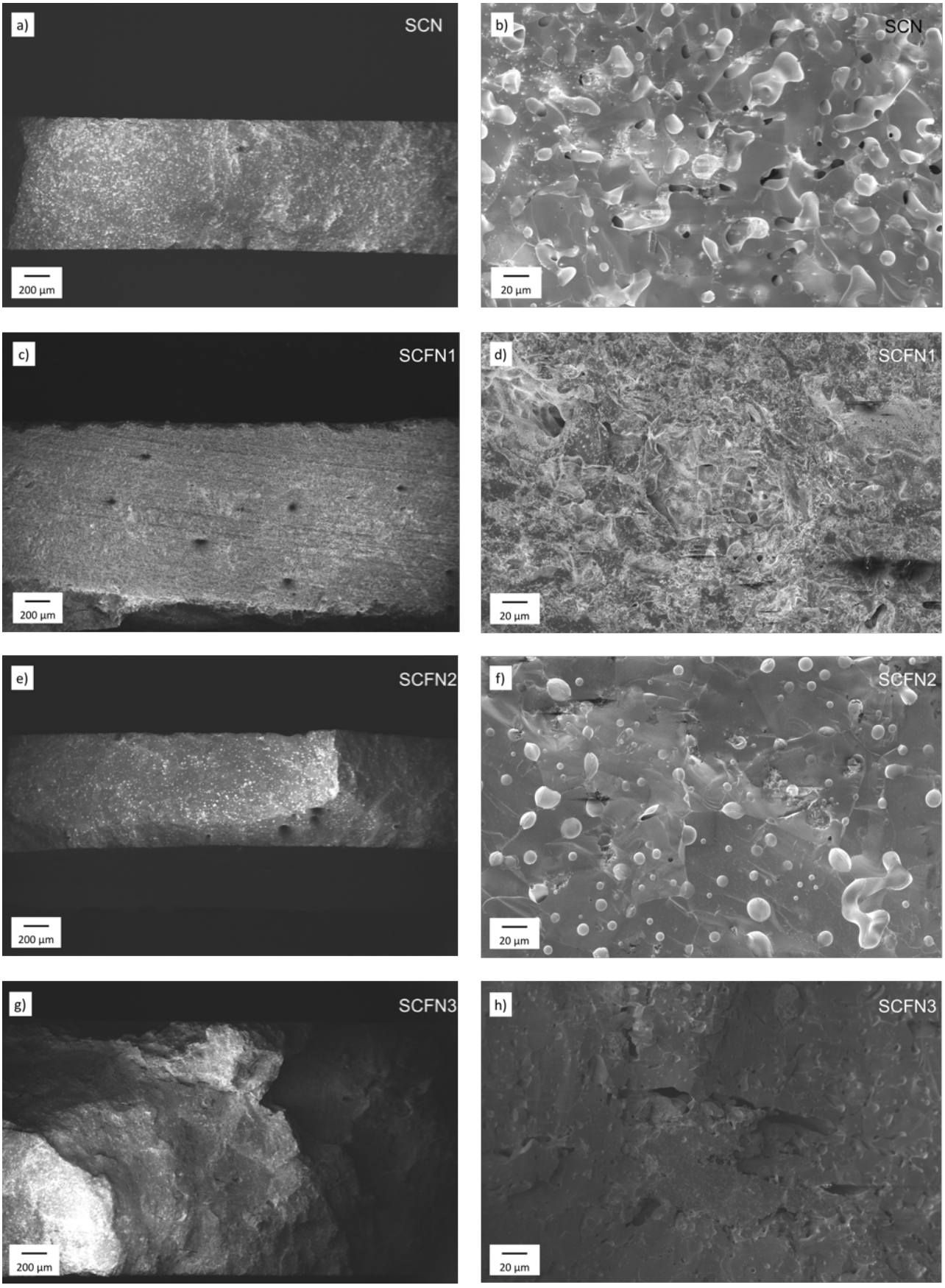

Fig 6.16: Scanning electron micrographs of SCN (a, b), SCFN1 (c, d), SCFN2 (e, f) and SCFN3 (g, h) membranes after oxygen permeation test.

6.4 Conclusion

In this chapter the effect of zirconium, niobium and molybdenum doping on the stabilization of cubic $SrCo_{0.95}M_{0.05}O_{3-\delta}$ perovskite has been investigated and, since niobium proved to be the best candidate, the four $SrCo_{0.95}Nb_{0.05}O_{3-\delta}$ (SCN), $SrCo_{0.85}Fe_{0.1}Nb_{0.05}O_{3-\delta}$ (SCNF1), $SrCo_{0.75}Fe_{0.2}Nb_{0.05}O_{3-\delta}$ (SCNF2), $SrCo_{0.65}Fe_{0.3}Nb_{0.05}O_{3-\delta}$ (SCNF3) samples were formulated, aiming to investigate the effect of iron doping on the stability and transport properties of the materials. These were successfully synthesized by means of citrate route and cubic perovskitic structure was observed in all the samples, highlighting the stabilizing role of niobium and iron doping on the cubic $SrCoO_{3-\delta}$ structure.

Iodometric titration allowed to determine the oxygen nonstoichiometry (δ) at room temperature, that decreased with iron content, while the average B-site cations valency (n) showed the opposite trend, consistently with the formation of a higher amount of Fe^{4+} and Co^{4+} in doped samples. The evolution of δ and n with temperature in air was investigated with thermogravimetric analysis (TGA) in air and nitrogen atmosphere and two different trends with iron doping were observed: while in N_2 the oxygen release at high temperature decreased with iron doping, in air the presence iron seemed to slightly facilitate the release of oxygen at high temperature.

Dense pellets were prepared from the powders and their conductivity and surface composition was investigated. The two temperature windows observed from TGA measurements in air are consistent with the dc-conductivity values observed in four probes measurements: after an increase in conductivity in the low temperature region (T<400 °C) due to the formation of Co^{4+} and Fe^{4+} p-type carriers a maximum is observed around 400°C, being above 500 $S \cdot cm^{-1}$ in SCN and SCFN2. After the maximum, the conductivity decreased, leading to 101.3, 98.5, 228.8 and 44.4 $S \cdot cm^{-1}$ for SCN, SCFN1, SCFN2 and SCFN3, respectively, at 900°C, indicating that the samples are electronic conductors at the testing temperature for of oxygen permeation. The XPS measurements on the surface of the pellets revealed that all the elements are present in the expected oxidation state and iron doping is effective in reducing the segregation of strontium. The Co/Fe ratio was found to be always lower than nominal values, as cobalt showed the tendency to diffuse towards the bulk rather than to the surface of the pellets.

Microstructural analysis revealed a compact, dense and crack-free cross section for all samples with absence of connected porosity.

Oxygen permeation tests were run on the pellets and SCFN1 and SCFN2 were the only samples for which a reliable performance was observed, since SCN and SCFN3 repeatedly presented leaking phenomena. After test analysis by SEM detected the formation of micrometric pinholes in SCN, probably due to reduction of the material, and larger cracks in SCFN3, which suggest that a higher temperature sintering treatment is required for samples containing a larger amount of iron.

The observed permeation fluxes at 750 °C were 1.21 and 1 $mL_N \cdot cm^{-2} \cdot min^{-1}$ for SCFN1 and SCFN2, respectively. SCFN1 reached 1.88 $mL_N \cdot cm^{-2} \cdot min^{-1}$ at 850 °C, but at higher temperature the membrane was not stable. SCFN2 showed stable performances along the whole temperature range, reaching 1.95 $mL_N \cdot cm^{-2} \cdot min^{-1}$ at 950 °C, and was subsequently tested using CO_2 as sweep gas. The observed flows decreased in presence of CO_2, suggesting possible interaction with the surface of the membrane. At 950 °C the oxygen flow is restored, probably due to a desorption of the previously adsorbed CO_2, and a value of 1.34 $mL_N \cdot cm^{-2} \cdot min^{-1}$ is observed using CO_2 sweep gas.

The calculated activation energy for oxygen permeation was 0.432 and 0.379 eV for SCFN1 and SCFN2, respectively, showing closer values to $Ba_{0.5}Sr_{0.5}Co_{0.8}Fe_{0.2}O_{3-\delta}$ (E_a=0.42 eV) than $SrCo_{0.95}Nb_{0.05}O_{3-\delta}$ (E_a=0.90 eV). Fe seems to have a major influence on the activation energy compared to niobium. In the approximation of bulk limited diffusion, the obtained values from oxygen permeation allowed to calculate the ionic conductivity, which was 0.34 and 0.26 $S \cdot cm^{-1}$ at 750 °C for SCFN1 and SCFN2, respectively, higher than in the case of GDC.

6.5 Bibliography

1 S. Solomon, G.-K. Plattner, R. Knutti and P. Friedlingstein, *Proc. Natl. Acad. Sci.*, 2008, **106(6)**, 1704–1709.

2 T. Wall, Y. Liu, C. Spero, L. Elliott, S. Khare, R. Rathnam, F. Zeenathal, B. Moghtaderi, B. Buhre, C. Sheng, R. Gupta, T. Yamada, K. Makino and J. Yu, *Chem. Eng. Res. Des.*, 2009, **87**, 1003–1016.

3 G. Scheffknecht, L. Al-Makhadmeh, U. Schnell and J. Maier, *Int. J. Greenh. Gas Control*, 2011, **5**, 16–35.

4 H. Stadler, F. Beggel, M. Habermehl, B. Persigehl, R. Kneer, M. Modigell and P. Jeschke, *Int. J. Greenh. Gas Control*, 2011, **5**, 7–15.

5 S. S. Hashim, A. R. Mohamed and S. Bhatia, *Renew. Sustain. Energy Rev.*, 2011, **15**, 1284–1293.

6 S. M. Hashim, A. R. Mohamed and S. Bhatia, *Adv. Colloid Interface Sci.*, 2010, **160**, 88–100.

7 S. Baumann, J. M. Serra, M. P. Lobera, S. Escolástico, F. Schulze-Küppers and W. A. Meulenberg, *J. Memb. Sci.*, 2011, **377**, 198–205.

8 J. Sunarso, S. S. Hashim, N. Zhu and W. Zhou, *Prog. Energy Combust. Sci.*, 2017, **61**, 57–77.

9 R. H. Mitchell, *Perovskites: ancient and modern*, 2002.

10 M. A. Peña and J. L. G. Fierro, *Chem. Rev.*, 2001, **101**, 1981–2017.

11 V. M. Goldschmidt, *Naturwissenschaften*, 1926, **14**, 477–485.

12 J. Yi, S. Feng, Q. Zeng and C. Chen, *Chinese J. Chem. Phys.*, 2015, **28**, 189–192.

13 T.-S. Chang and P. Trucano, *J. Appl. Cryst.*, 1978, **11**, 286–287.

14 N. Y. Y. Teraoka, H.M. Zhang, S. Furukawa, *Chem. Lett.*, 1985, 1743–1746.

15 Y. Takeda, R. Kanno, T. Takada and O. Yamamoto, *Z. anorg. allg. Chem.*, 1986, **541**, 259–270.

16 Z. Shao, W. Yang, Y. Cong, H. Dong, J. Tong and G. Xiong, *J. Memb. Sci.*, 2000, **172**, 177–188.

17 Z. Yáng, A. S. Harvey, A. Infortuna, J. Schoonman and L. J. Gauckler, *J. Solid State Electrochem.*, 2011, **15**, 277–284.

18 T. Nagai, W. Ito and T. Sakon, *Solid State Ionics*, 2007, **177**, 3433–3444.

19 K. Zhang, R. Ran, L. Ge, Z. Shao, W. Jin and N. Xu, *J. Memb. Sci.*, 2008, **323**, 436–443.

20 D. A. Shirley, *Phys. Rev. B*, 1972, **5**, 4709–4714.

21 D. Briggs and M. P. Seah, 1983, **1**, 397–427.

22 N. S. McIntyre, in *Symposium on Progress in Quantitative Surface Analysis*, ed. ASTM International, 1986, p. 217.

23 G. E. Wanger, C. D.; Riggs, W. M.; Davis, L. E.; Moulder, J. F.; Muilenberg, *Handbook of X-ray Photoelectron Spectroscopy*, Perkin-Elmer Corp., Physical Electronics Division, 1979.

24 A. J. Samson, M. Søgaard and P. Vang Hendriksen, *J. Memb. Sci.*, 2014, **470**, 178–188.

25 S. Pirou, J. Gurauskis, V. Gil, M. Søgaard, P. V. Hendriksen, A. Kaiser, S. Ovtar and R. Kiebach, *Fuel Process. Technol.*, 2016, **152**, 192–199.

26 K. A. Nielsen, M. Solvang, S. B. L. Nielsen, A. R. Dinesen, D. Beeaff and P. H. Larsen, *J. Eur. Ceram. Soc.*, 2007, **27**, 1817–1822.

27 R. D. Shannon, *Acta Cryst.*, 1976, 751–767.

28 O. Yamamoto, Y. Arachi, H. Sakai, Y. Takeda, N. Imanishi, Y. Mizutani, M. Kawai and Y. Nakamura, *Ionics (Kiel).*, 1998, **4**, 403–408.

29 M. Mogensen, N. M. Sammes and G. A. Tompsett, *Solid State Ionics*, 2000, **129**, 63–94.

30 A. Aguadero, D. Pérez-Coll, J. A. Alonso, S. J. Skinner and J. Kilner, *Chem. Mater.*, 2012, **24**, 2655–2663.

31 J. A. Labrincha, F. M. B. Marques and J. R. Frade, *J. Mater. Sci.*, 1995, **30**, 2785–2792.

32 E. Mete, R. Shaltaf and Ellialtıoğlu, *Phys. Rev. B - Condens. Matter Mater. Phys.*, 2003, **68**, 3–6.

33 L. Yang, L. Tan, X. Gu, W. Jin, L. Zhang and N. Xu, *Ind. Eng. Chem. Res.*, 2003, 2299–2305.

34 J. Wang, X. Jin and K. Huang, *J. Solid State Chem.*, 2017, **246**, 97–106.

35 R. E. Usiskin, T. C. Davenport, R. Y. Wang, W. Guan and S. M. Haile, *Chem. Mater.*, 2016, **28**, 2599–2608.

36 N. N. Greenwood and A. Earnshaw, *Chemistry of Elements II Edition*, 1997.

37 K. S. Ryu, S. J. Lee and C. H. Yo, *Bull. Korean Chem. Soc.*, 1994, 15, 256–260.

38 H. H. Kung, *Transition Metal Oxides: Surface Chemistry and Catalysis*, Elsevier B.V, 1989.

39 Y. Teraoka, T. Nobunaga and N. Yamazoe, *Chem. Lett.*, 1988, 503–506.

40 Z. Chen, R. Ran, W. Zhou, Z. Shao and S. Liu, *Electrochim. Acta*, 2007, **52**, 7343–7351.

41 L. W. Tai, M. M. Nasrallah, H. U. Anderson, D. M. Sparlin and S. R. Sehlin, *Solid State Ionics*, 1995, **76**, 259–271.

42 H. Kruidhof, H. J. M. Bouwmeester, R. H. E. v. Doorn and A. J. Burggraaf, *Solid State Ionics*, 1993, **63**–**65**, 816–822.

43 L. W. Tai, M. M. Nasrallah, H. U. Anderson, D. M. Sparlin and S. R. Sehlin, *Solid State Ionics*, 1995, **76**, 273–283.

44 Y. Teraoka, Y. Honbe, J. Ishii, H. Furukawa and I. Moriguchi, *Solid State Ionics*, 2002, **152**–**153**, 681–687.

45 P. A. Zink, K. J. Yoon, U. B. Pal and S. Gopalan, *Electrochem. Solid-State Lett.*, 2009, **12**, B141.

46 S. McIntosh, J. F. Vente, W. G. Haije, D. H. A. Blank and H. J. M. Bouwmeester, *Solid State Ionics*, 2006, **177**, 1737–1742.

47 G. Zhang, Z. Liu, N. Zhu, W. Jiang, X. Dong and W. Jin, *J. Memb. Sci.*, 2012, **405**–**406**, 300–309.

48 V. Cascos, R. Martínez-Coronado and J. A. Alonso, *Int. J. Hydrogen Energy*, 2014, **39**, 14349–14354.

49 Y. Teraoka, M. Yoshimatsu, N. Yamazoe and T. Seiyama, *Chem. Lett.*, 1984, **13**, 893–896.

50 P. B. Armentrout, L. F. Halle and J. L. Beauchamp, *J. Am. Chem. Soc.*, 1981, **103**, 6501–6502.

51 Y. Zhu, J. Sunarso, W. Zhou and Z. Shao, *Appl. Catal. B Environ.*, 2015, **172**–**173**, 52–57.

52 Y. Teraoka, H.-M. Zhang and N. Yamazoe, *Chem. Lett.*, 1985, 1367–1370.

53 Z. Wang, H. Zhao, N. Xu, Y. Shen, W. Ding, X. Lu and F. Li, *J. Phys. Chem. Solids*, 2011, **72**, 50–55.

54 M. C. Biesinger, B. P. Payne, A. P. Grosvenor, L. W. M. Lau, A. R. Gerson and R. S. C. Smart, *Appl. Surf. Sci.*, 2011, **257**, 2717–2730.

55 A. Glisenti, M. Pacella, M. Guiotto, M. M. Natile and P. Canu, *Appl. Catal. B Environ.*, 2016, **180**, 94–105.

56 M. M. Natile, F. Poletto, A. Galenda, A. Glisenti, T. Montini, L. De Rogatis, P. Fornasiero, S. Chimiche, V. Instm-pado, V. Uni and V. F. Marzolo, *Chem. Mater.*, 2008, 2314–2327.

57 D. Chen, C. Chen, Z. Zhang, Z. M. Baiyee, F. Ciucci and Z. Shao, *ACS Appl. Mater. Interfaces*, 2015, **7**, 8562–8571.

58 Y. V. Egorova, T. Scherb, G. Schumacher, H. J. M. Bouwmeester and E. O. Filatova, *J. Alloys Compd.*, 2015, **650**, 848–852.

59 S. Lü, B. Yu, X. Meng, X. Zhao, Y. Ji, C. Fu, Y. Zhang, L. Yang, H. Fan and J. Yang, *J. Power Sources*, 2015, **273**, 244–254.

60 Z. Zhang, D. Chen, F. Dong, X. Xu, Y. Hao and Z. Shao, *J. Memb. Sci.*, 2016, **519**, 11–21.

61 M. Schmal and H. J. Freund, *An. Acad. Bras. Cienc.*, 2009, **81**, 297–318.

62 C. M. Gore, J. O. White, E. D. Wachsman and V. Thangadurai, *J. Mater. Chem. A*, 2014, **2**, 2363.

63 C. Opris, B. Cojocaru, N. Gheorghe, M. Tudorache, S. M. Coman, V. I. Parvulescu, B. Duraki, F. Krumeich and J. A. Van Bokhoven, *J. Catal.*, 2016, **339**, 209–227.

64 S. Diodati, L. Nodari, M. M. Natile, U. Russo, E. Tondello, L. Lutterotti and S. Gross, *Dalt. Trans.*, 2012, **41**, 5517–5525.

65 B. He, D. Ding, Y. Ling, J. Xu and L. Zhao, *J. Memb. Sci.*, 2015, **477**, 7–13.

66 V. V. Kharton, A. V. Kovalevsky, A. A. Yaremchenko, F. M. Figueiredo, E. N. Naumovich, A. L. Shaulo and F. M. B. Marques, *J. Memb. Sci.*, 2002, **195**, 277–287.

67 C.-Y. Yoo, J. H. Park, D. S. Yun, Y. A. Lee, K. S. Yun, J. H. Lee, H. Yoon, J. H. Joo and J. H. Yu, *J. Phys. Chem. C*, 2016, **120**, 22248–22256.

68 S. Engels, T. Markus, M. Modigell and L. Singheiser, *J. Memb. Sci.*, 2011, **370**, 58–

69.

69 Z. Zhang, D. Chen, Y. Chen, Y. Hao, M. O. Tade and Z. Shao, *J. Memb. Sci.*, 2014, **472**, 10–18.

70 S. Baumann, F. Schulze-Küppers, S. Roitsch, M. Betz, M. Zwick, E. M. Pfaff, W. A. Meulenberg, J. Mayer and D. Stöver, *J. Memb. Sci.*, 2010, **359**, 102–109.

71 W. K. Hong and G. M. Choi, *J. Memb. Sci.*, 2010, **346**, 353–360.

72 C. H. Chen, H. Kruidhof, H. J. M. Bouwmeester and a J. Burggraaf, *J. Appl. Electrochem.*, 1997, **27**, 71–75.

73 Z. Chen, Z. Shao, R. Ran, W. Zhou, P. Zeng and S. Liu, *J. Memb. Sci.*, 2007, **300**, 182–190.

74 K. C. Wincewicz and J. S. Cooper, *J. Power Sources*, 2005, **140**, 280–296.

75 Z. Shao, G. Xiong, J. Tong, H. Dong and W. Yang, *Sep. Purif. Technol.*, 2001, **25**, 419–429.

Chapter 7

Development of Fe and Nb-doped $SrCoO_{3-\delta}$ perovskites as high performing cathodes for IT-SOFCs

PURSUING THE RESEARCH FOR RARE EARTH-FREE MIXED IONIC AND ELECTRONIC CONDUCTORS TO BE APPLIED AS AIR ELECTRODES IN INTERMEDIATE TEMPERATURE REVERSIBLE SOLID OXIDE CELLS

In this chapter $SrCo_{0.95}Nb_{0.05}O_{3-\delta}$ (SCN), $SrCo_{0.85}Fe_{0.1}Nb_{0.05}O_{3-\delta}$ (SCNF1), $SrCo_{0.75}Fe_{0.2}Nb_{0.05}O_{3-\delta}$ (SCNF2) and $SrCo_{0.65}Fe_{0.3}Nb_{0.05}O_{3-\delta}$ (SCNF3), are investigated as SOFC's cathodes, aiming to obtain good performances in the range of intermediate temperatures.

The same materials were previously characterized and tested as oxygen permeation membranes in chapter 6, after an accurate investigation on the possible strategies for stabilizing the cubic phase of $SrCoO_{3-\delta}$ which involved the analysis of several dopants and synthesis conditions.

It is evident that when materials are suitable for oxygen permeation, they fulfill at the same time the requirements for being used as cathode electrodes, with the advantage that it is not necessary to obtain a full dense ceramic for testing, the target temperatures are in the intermediate range (500-750 °C) and the materials are exposed to less harmful conditions, as cathodes are commonly immersed in air atmosphere which has a lower CO_2 content than in the case of flue gases stream.

The oxygen permeation test on SCFN1 and SCFN2 showed an interesting activity concerning oxygen separation and suggested that cobalt replacement for iron may be useful to enhance the stability of these materials. Since iron has a more acidic character compared to cobalt, Fe introduction may be useful to reduce the effect of CO_2 poisoning and has already proved to be effective in tuning the surface composition reducing strontium segregation (as observed with XPS in chapter 6). Moreover, the demonstrated oxygen permeation activity is shedding an encouraging light

on these materials in the perspective of using them as air electrodes in a reversible cell. In fact, one of the most common reasons for reversible cells degradation is the air electrode inability to remove the oxygen ions driven by the electrolyte, which can result in the formation of high pressure bubbles resulting in the delamination of the air electrode and consequent failure of the device.

The high oxygen permeation capability of $SrCo_{0.95-x}Fe_xNb_{0.05}O_{3-\delta}$ family is promising in this perspective and, if coupled with a good electrocatalytic activity, may represent a possible way to address this issue.

7.1 Introduction

Solid oxide fuel cells (SOFCs) are electrochemical devices able to convert chemical energy into electricity with high efficiency, allowing the use of different fuels.[1–3]

Unfortunately, the high temperatures typically required for the cell operation (up to 1000°C) can induce interdiffusion between the cell's components, kinetic demixing of some materials and particle coarsening in porous electrodes, dramatically shortening the device lifetime.[4–8]

These drawbacks, jointly to the elevated costs, limit the diffusion of solid oxide fuel cell, despite many efforts spent to improve this technology in the last 40 years.

A commonly adopted strategy to reduce the degradation of the cell is lowering the operating temperature in the range of intermediate temperatures (500-750°C), however, this results in a decreased activity of the cell components.[9,10] In particular, high temperature is required to activate ionic conduction and reduce the ohmic losses at the electrolyte[11] and to have fast kinetics at the electrodes.[12,13] This is particularly relevant for what concerns cathode, which often has a high activation energy (~1.5eV) for the oxygen reduction reaction.[14,15] In fact, while in the case of the anode Ni-cermets in which negligible polarization resistance has been produced[16,17] thanks to a controlled microstructure and in the case of the electrolyte for which it is possible to improve the performances by reducing thickness,[18,19] the improvements in cathode technology are proceeding at a slower rate. This is due to the intrinsic difficulty of oxygen reduction reaction (ORR), which is challenging, and to the simultaneous need of good ionic and electronic conductivity and long-time stability.[13,20]

For these reasons, traditional cathodes such as $La_{1-x}Sr_xMnO_3$ (LSM) are challenged in their low ionic conductivity. In order to overcome that, a common strategy is to mix the electrolyte and the electrode powders to obtain a composite electrode and enhance the contact area between electron conducting LSM and ionic conductor electrolyte.[21–24] However, this approach's benefits are still limited to a restricted area of the electrode called triple phase boundary, which is represented by spots (as outlined in chapter 2). The development of a mixed ionic and electronic conductor (MIEC), extending the active area available, can greatly contribute to increasing efficiency.

The key feature of perovskites is the possibility of tailoring their chemical and physical properties (catalytic activity, ionic and electronic conductivity) through the chemical composition, and the modification of the crystal structure (going from simple perovskites to double or layered perovskite, to Ruddlesden Popper phases). Perovskites have a chemical formula ABO_3, where A is a 12-fold coordinated metal belonging to alkaline, alkaline earth or rare earth group, and B is typically a 6-fold coordinated transition metal. The incredible flexibility of this family is due to a high tolerance to the presence of defects and the fact that almost 90% of periodic table elements are stable in a perovskitic structure.[26]

In the case of perovskitic oxides, defects of relevance for ionic conductivity are represented by oxygen vacancies whose formation can be enhanced by aliovalent doping; however, aliovalent doping can also induce the formation of a redox couple in the B-site which is associated with electronic conduction.

As a consequence of their mixed conduction properties, Mn-based, Ni-based, Fe-based and Co-based families have been extensively studied as suitable cathodes for IT-SOFCs and mixed metal compositions like $La(Ni,Fe)O_{3-\delta}$, $Sr(Co, Fe)O_{3-\delta}$ have been tested too. [22,25,35,36,27–34] $SrCoO_{3-\delta}$ derived family is in particular interesting because of the elevated permeation flux demonstrated by Teraoka *et al*,[37] who investigated the relationship between La/Sr and Co/Fe compositional ratios and oxygen permeation flux in the $La_{1-x}Sr_xCo_{1-y}Fe_yO_{3-\delta}$ family for the application in oxygen permeation membranes, demonstrating the highest oxygen flux for a cubic phase with the lowest content of La and Fe. However, the $SrCoO_{3-\delta}$ composition is not stable in a cubic phase below 900°C and undergoes a phase transition to hexagonal or brownmillerite phase upon cooling, depending on the conditions. [38] Moreover, it has been demonstrated that the highest electronic and ionic conduction properties, as well as oxygen permeation rate (which is closely related to ionic and electronic conductivity) are due to the cubic perovskite structure and are not of the same extent in the brownmillerite or hexagonal crystal structure. [37–39] This is mainly due to oxygen vacancies ordering phenomena blocking vacancies mobility and to tilted angles between CoO_6 octahedra, which reduce the orbitals superposition and thus electronic conductivity.[40]

Many efforts have been addressed to stabilize the cubic $SrCoO_{3-\delta}$ structure over a wide range of temperatures adopting different doping strategies: on A-site $Sm_{0.5}Sr_{0.5}CoO_{3-\delta}$ (SSC); [41] B-site doping $SrSc_{0.2}Co_{0.8}O_{3-\delta}$ (SSC), [42] $SrCo_{0.8}Fe_{0.2}O_{3-\delta}$ (SCF) [43] or on both A and B-sites. $La_{0.6}Sr_{0.4}Co_{0.2}Fe_{0.8}O_{3-\delta}$ (LSCF) [44] and $Ba_{0.5}Sr_{0.5}Co_{0.8}Fe_{0.2}O_{3-\delta}$ (BSCF) have been widely investigated and have shown very promising electrochemical performances at intermediate temperatures. [45] Another possible strategy for cubic phase stabilization is to use a fixed high valence transition metal. While most of the doping effects have still to be investigated in detail, the effect of doping with a high valence metal results in a decrease of the oxygen vacancies amount with consequent decrease of vacancies order phenomena. Moreover, often fixed valence cations are not easy to reduce below 900°C and can provide an additional stabilization effect in challenging testing conditions (low pO_2, high T, presence of CO_2).

Nagai *et al* have investigated several different dopants and their stabilizing effect on $SrCoO_{3-\delta}$ and their influence on oxygen permeation properties of the samples, highlighting the beneficial role of La, Nb and Ti among the fixed valence elements. [46] This evidence has pushed towards the investigation of other dopants such as Sb, Ta, Sn, Mo and less common oxyanionic dopants as B, Si and P, too. Many of them have proved to be effective in stabilizing the cubic phase and showed promising electrochemical performances; on the other side a general trend is typically observed: a decrease in the conduction properties and electrochemical performance in excess of dopant. [47–53]

Although the effect of doping has been widely investigated for $SrCoO_{3-\delta}$ compounds, double doping has not been studied in deep and not all dopants have the same effect.

In this chapter $SrCo_{0.95}Nb_{0.05}O_{3-\delta}$ (SCN), $SrCo_{0.85}Fe_{0.1}Nb_{0.05}O_{3-\delta}$ (SCNF1), $SrCo_{0.75}Fe_{0.2}Nb_{0.05}O_{3-\delta}$ (SCNF2) and $SrCo_{0.65}Fe_{0.3}Nb_{0.05}O_{3-\delta}$ (SCNF3) perovskites are investigated as possible cathode materials for intermediate temperature solid oxide cells. In this compounds the stabilization effect is reached by doping with Nb and not with expensive rare earths. The samples are prepared by means of citrate route synthesis followed by combustion and the resulting materials are characterized by means of X-ray diffraction (XRD), iodometric titration (IT), thermogravimetric analysis (TGA), scanning electron microscopy (SEM). The conductivity of the pelletized samples is investigated with

4-probes van der Pauw technique and finally symmetric cells on GDC electrolyte are prepared and electrochemically tested under air atmosphere with electrochemical impedance spectroscopy (EIS). The microstructure of tested cells has been investigated, in order to determine the electrode morphology influence on the final electrochemical properties.

7.2 Experimental

7.2.1 Samples synthesis

$SrCo_{0.95}Nb_{0.05}O_{3-\delta}$ (SCN), $SrCo_{0.85}Fe_{0.1}Nb_{0.05}O_{3-\delta}$ (SCNF1), $SrCo_{0.75}Fe_{0.2}Nb_{0.05}O_{3-\delta}$ (SCNF2), $SrCo_{0.65}Fe_{0.3}Nb_{0.05}O_{3-\delta}$ (SCNF3) powders were synthesized by means of citrate route followed by combustion, using $Sr(NO_3)_2$ (ACS reagent, >99%, Sigma Aldrich), $Co(NO_3)_2{\cdot}6H_2O$ (ACS reagent, >98%, Sigma Aldrich), Fe (metal chips, 99.98%, Aldrich) and Nb_2O_5 (325 mesh, 99.9%, Sigma Aldrich) as precursors. These were dissolved separately in deionized water or nitric acid (p.a. ≥65%, Sigma Aldrich) and then mixed. A controlled amount of nitric acid (10 ml per gram of final perovskite product) was added to solution in order to obtain a homogeneous combustion. Citric acid monohydrate (ACS reagent, >99%, Sigma Aldrich) was then added in the ratio 1.9 with respect to the total amount of cations and the pH was adjusted with ammonium hydroxide (ACS reagent, 28-30% NH_3 basis, Sigma Aldrich) until a value of 7 was reached, monitoring it with a calibrated pH-meter. The obtained solution was heated at 90°C to remove water and the pH was monitored and kept at a constant value of 7 through the addition of ammonia, until a dense gel was formed. The gel was then dried at 200°C, which induced the release of gases forming a sponge-like structure that was finally burnt at 400°C in order to remove the organic framework. The resulting powder was finely ground in an agate mortar and then calcined at 1000°C for 6 hours, followed by grinding and a second thermal treatment at 1200°C for 12 hours in order to obtain the desired perovskitic structure.

7.2.2 Samples characterization

The crystal structure of the synthesized samples was determined by X-ray diffraction using a Bruker D8 with Cu Kα radiation (λ = 1.5418 Å), collecting diffraction patterns at room temperature in a Bragg-Brentano geometry over a 2θ range of 20-80°, with a step size of 0.015° and 1s step time.

The oxygen nonstoichiometry (δ) and average oxidation state of B-site cations at room temperature was determined by iodometric titration. In brief, 50 mg of powder were dissolved in a 6mol L^{-1} HCl solution in presence of excess KI (ACS grade, Millipore Sigma),

the procedure was performed under nitrogen atmosphere to prevent the oxidation of I-ions (from KI) by atmospheric air. This was followed by titration with a standard thiosulfate solution ($S_2O_3^{2-}$, 0.01 N, Titolchimica). A few droplets of a homemade starch solution were used in proximity of equivalence point. Each measurement was performed four times and averaged to obtain the resulting nonstoichiometry. The evolution of oxygen nonstoichiometry with temperature was investigated with thermogravimetrical analysis performed with a SDT 2960 TGA/DTA (TA instruments). Ramps of 10 °C/min under air flow were used. The resulting nonstoichiometry was determined with the following equation:

$$\delta = \frac{MM \times m_0 - (MM - 15.9994 \times \delta_0) \times m}{15.9994 \times m_0}$$

where m_0 and m are the original weight and the weight at a certain temperature, MM is the molar mass of the sample (expressed as $SrCo_{0.95-x}Fe_xNb_{0.05}O_3$) and δ_0 is the oxygen nonstoichiometry determined at room temperature. From the same expression it is possible to obtain an average valence of B-site cations.

In order to measure electrical conductivity with van der Pauw method, dense pellets were prepared by uniaxial pressing followed by isostatic pressing (p=60 MPa, t=30 s) and sintering at 1250°C for 12 hours. Four small dots of platinum paint (SPI supplies) were applied at the corners of the resulting pellets (16mm diameter, 2mm thickness, >90% density) and heated (1 hour at 1000 °C, using 1°C/min ramps) to ensure good electrical contact. A Keithley 2400 SourceMeter was used for DC-electrical conductivity measurements performed in air (flow 50 sccm) between room temperature and 950°C at a 25°C interval, using a 1°C/min heating ramp.

Scanning electron microscopy was performed on both the as synthesized powders and cross section of the symmetric cells after testing, using a Zeiss Supra 40VP, using 20kV acceleration voltage.

7.2.3 Symmetric cell realization and electrochemical characterization

Symmetrical electrode cells were realized tape-casting an electrode ink on a GDC ceramic electrolyte. The electrolyte was produced by dry pressing a commercial powder (GDC10, Fuel Cell Materials) and consequent calcination at 1500°C for 6 hours (heating and cooling rate 3°C/min). The resulting electrolytes had a diameter of 20 mm diameter and thickness of 1 mm. Electrode inks were prepared by dispersing the perovskites powders in a vehicle (Vehicle 400, ESL) and the viscosity of the resulting paste was reduced with a thinner (Thinner 404, ESL). A small amount (5% final weight of the ink) of Carbon black (Printex-U, Degussa) was added as pore former. The resulting paste was ground for 10 minutes in an agate mortar in order to reduce particles size and obtain an homogeneous slurry, which was deposited on both sides of the electrolyte, dried for 30 minutes at 100°C and subsequently calcined at 1100°C (heating and cooling rate 3°C/min) for 6 hours. A thin layer of gold paste (Heraeus C5729) was deposited to enhance the electrical contact and subsequently calcined for 30 minutes at 800°C (heating and cooling rate, 1°C/min). The total area of the resulting symmetrical cell was 0,785 cm^2. Electrochemical Impedance Spectroscopy was performed with an Autolab PGSTAT204 potentiostat (Metrohm) in the 550-800°C temperature range in synthetic air atmosphere. During the test a 50mV AC amplitude voltage was applied under open circuit conditions, scanning 0.01 Hz-1MHz frequency range. The resulting impedance spectra were analyzed and fitted with Z-View software (Scribner Associates).

7.3 Results and discussion

7.3.1 XRD

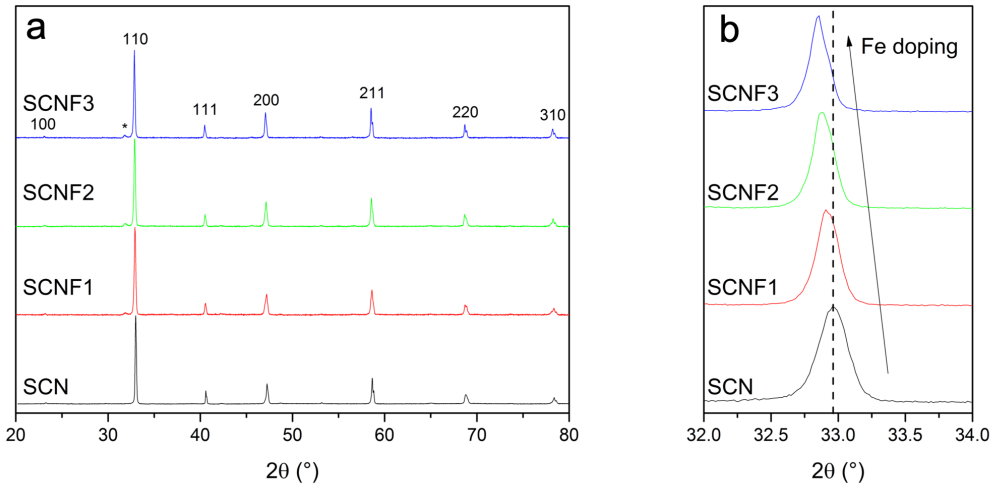

Fig 7.1: XRD patterns of $SrCo_{0.95}Nb_{0.05}O_{3-\delta}$ (SCN), $SrCo_{0.85}Fe_{0.1}Nb_{0.05}O_{3-\delta}$ (SCNF1), $SrCo_{0.75}Fe_{0.2}Nb_{0.05}O_{3-\delta}$ (SCNF2), $SrCo_{0.65}Fe_{0.3}Nb_{0.05}O_{3-\delta}$ (SCNF3) calcined at 1200 °C; * orthorombic $Sr_2Co_2O_5$ (a) and detailed view of 110 reflection (b).

X-ray diffraction patterns show the presence of cubic perovskitic (space group Pm-3m) structure for all samples. The low intensity of (100) reflection and the doublet splitting detected for (211) reflection suggest the possible presence of a tetragonal superlattice ordering, characterized by a long range ordering along the c-direction of the perovskitic. This phenomenon has been observed for 10% Nb and 10% Sb doped $SrCoO_3$ and is associated with the stabilizing effect of fixed high valence dopants, which allows the formation of highly ordered channels for vacancies migration. Further investigation by neutron diffraction could give an insight into the crystal structure. [54,55] The effect of iron doping seems to induce the segregation of a small impurity of orthorhombic $Sr_2Co_2O_5$ (I_{Max_orth}/I_{Max_cub}< 4%), which may be associated with iron doping, not only due to the smaller t-factor (reported in table 7.1). In fact, Nagai *et al.* observed than 10% iron doping is not enough to stabilize the cubic phase in absence of niobium, [46] while Yi *et al*. observed similar results for 10% Fe, but recorded a pure cubic phase in the case of 20% Fe doping and absence of Nb. [40]

The effect of iron incorporation into the perovskitic lattice can be noticed by the shift induced into the diffraction peaks (Figure 1b) and an increase in the lattice parameter (table 7.1). In fact, as iron doping is increasing, a shift towards lower diffraction angles is observed, suggesting that the cell parameter is expanding as a consequence of the insertion of a larger cation into the lattice. This can be explained considering the ionic radii of iron and cobalt: divalent (r_i=0.78 Å, for Fe^{2+} in 6-fold coordination, high spin), trivalent (r_i= 0.645 Å, for Fe^{3+} in 6-fold coordination, high spin) and tetravalent (r_i= 0.585 Å, for Fe^{4+} in 6-fold coordination) iron radii are larger than divalent (r_i=0.745 Å, for Co^{2+} in 6-fold coordination, high spin), trivalent (r_i=0.61 Å, for Co^{3+} in 6-fold coordination, high spin) and tetravalent (r_i=0.53 Å, for Co^{4+} in 6-fold coordination) cobalt radiuses. [56]

7.3.2 Iodometric Titration

Since oxygen vacancies are the reaction sites for the dissociative adsorption of oxygen at the cathode, it is useful to determine the amount of vacancies present in the materials and how these evolve with temperature under reaction atmosphere. In order to do that iodometric titration is employed: in fact this technique gives information about room temperature oxygen stoichiometry (δ) and average oxidation state of Co/Fe cations.
When the $SrCo_{0.95}Nb_{0.05}O_{3-\delta}$ perovskite is dissolved into the hydrochloric acid solution in presence of KI, the following reactions occur: [57,58]

$$Co^{3+} + I^- \rightarrow Co^{2+} + \frac{1}{2}I_2 \qquad (1)$$

$$Co^{4+} + 2I^- \rightarrow Co^{2+} + I_2 \qquad (2)$$

the amount of produced iodine can be measured by reaction with thiosulfate:

$$\frac{1}{2}I^2 + S_2O_3^{2-} \rightarrow I^- + \frac{1}{2}S_4O_6^{2-} \qquad (3)$$

Niobium is not affected by KI. In presence of iron (in $SrCo_{0.85}Fe_{0.1}Nb_{0.05}O_{3-\delta}$, $SrCo_{0.75}Fe_{0.2}Nb_{0.05}O_{3-\delta}$ and $SrCo_{0.65}Fe_{0.3}Nb_{0.05}O_{3-\delta}$ samples), the equilibrium with KI includes the following reactions:

$$Fe^{3+} + I^{-} \rightarrow Fe^{2+} + \frac{1}{2}I_2 \qquad (4)$$

$$Fe^{4+} + 2I^{-} \rightarrow Fe^{2+} + I_2 \qquad (5)$$

for this reason, $SrCo_{0.95}Nb_{0.05}O_{3-\delta}$ is the only sample for which the average oxidation state of cobalt is determined, in all the Fe-doped compounds an average valence state of the B-site cations (n) is determined. Niobium, which has a fixed 5+ valence (as was observed from XPS in chapter 6), is excluded from the calculation of n.

Sample	a_0 (Å)	t-factor	δ	Oxygen coefficient	n
SCN	3.8392	0.9983	0.323	2.677	3.10
SCFN1	3.8451	0.9966	0.315	2.685	3.12
SCFN2	3.8495	0.9948	0.225	2.775	3.30
SCFN3	3.8525	0.9931	0.293	2.707	3.16

Table 7.1: Calculated tolerance factor, oxygen nonstoichiometry (δ) and average Co and Fe valence state at room temperature of $SrCo_{0.95}Nb_{0.05}O_{3-\delta}$ (SCN), $SrCo_{0.85}Fe_{0.1}Nb_{0.05}O_{3-\delta}$ (SCNF1), $SrCo_{0.75}Fe_{0.2}Nb_{0.05}O_{3-\delta}$ (SCNF2), $SrCo_{0.65}Fe_{0.3}Nb_{0.05}O_{3-\delta}$ (SCNF3).

Table 7.1 shows the unit cell parameter (a_0), the resulting t-factor, oxygen nonstoichiometry (δ) and average valence of B-site cations (n) determined for all samples. Interestingly, niobium doping is stabilizing the cubic perovskite structure slightly above the limit observed by Takeda *et al.* in their work, which found the 2.67 value for oxygen as the lowest oxygen coefficient value at which a pure perovskite structure is observed. Below this value a solid solution of perovskite and brownmillerite structure was observed.[38]

It is worth to notice that in all the iron doped samples, Fe introduction in the lattice is effective in reducing oxygen nonstoichiometry and increasing the average oxidation state of B-site cations. A similar trend was observed in the $LnBaCo_{2-x}Fe_xO_{5+\delta}$ system. [59] This is probably due to the fact that iron is more likely to be present in a higher oxidation state, as observed by Tai *et al*. [60,61] This suggests that, beside slightly lowering the t-factor, Fe doping may play a role in preventing the destabilization of the perovskitic structure. In fact, as already mentioned, when vacancies are present in a very high amount, they can undergo ordering phenomena, which are causing the transition from perovskite to a

brownmillerite structure, in which both electronic and ionic conduction properties are reduced with respect to a perovskite structure.[38]

As a matter of fact, oxygen nonstoichiometry at room temperature allows measuring the amount of oxygen vacancies and B-site average oxidation state in the samples, but these are subject to an equilibrium with the surrounding atmosphere and their evolution with temperature can be described in Kröger-Vink's notation (considering SCN sample for simplicity):

$$2Co_{Co}^{X} + V_{O}^{\bullet\bullet} + \frac{1}{2}O_2 \leftrightarrow O_{O}^{X} + 2Co_{Co}^{\bullet} \qquad (6)$$

Where Co_{Co}^{X}, $Co_{Co}^{\bullet}$ and $V_{O}^{\bullet\bullet}$ represent Co^{3+}, Co^{4+} and oxygen vacancy, respectively. It is evident that the formation of oxygen vacancies and the formation of holes (represented by Co^{4+}) are two opposite mechanisms and their equilibrium may change with temperature.

7.3.3 TGA

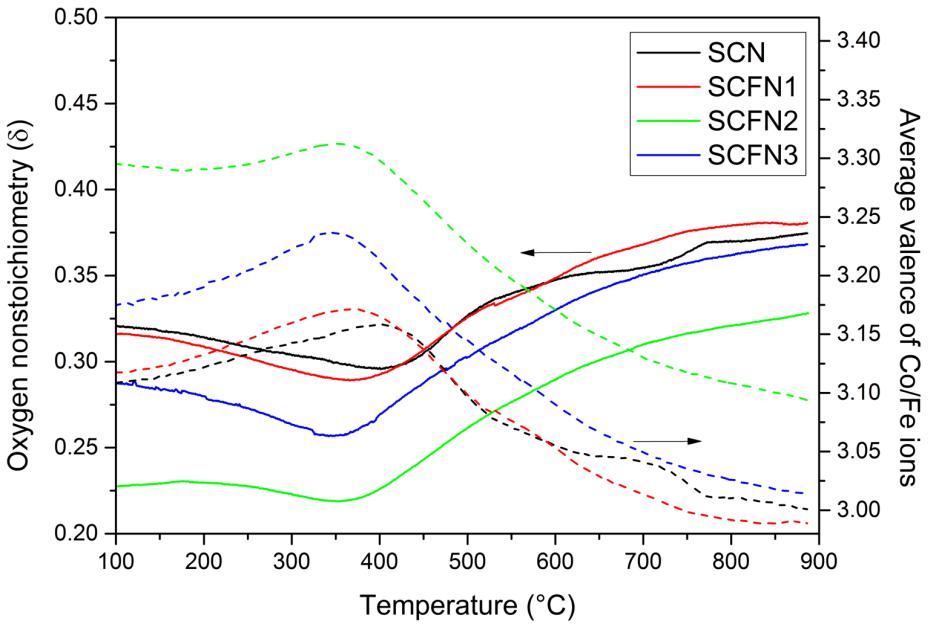

Fig 7.2: Oxygen nonstoichiometry (δ) and average Co and Fe valence state between 400 and 800 °C of $SrCo_{0.95}Nb_{0.05}O_{3-\delta}$ (SCN), $SrCo_{0.85}Fe_{0.1}Nb_{0.05}O_{3-\delta}$ (SCNF1), $SrCo_{0.75}Fe_{0.2}Nb_{0.05}O_{3-\delta}$ (SCNF2), $SrCo_{0.65}Fe_{0.3}Nb_{0.05}O_{3-\delta}$ (SCNF3).

Thermogravimetric analysis (TGA) provides an insight into their evolution with temperature under reaction conditions. The average oxidation state of B-site cations (n), associated with defects analysis is giving information about the electronic conductivity of the sample, which, as it was outlined in chapter 2, is a fundamental requirement for a good performing cathode. This should be coupled with a good ionic conductivity, which has been determined for some of the samples from oxygen permeability measurements in chapter 6.

Figure 7.2 shows the evolution of oxygen nonstoichiometry in the 100-900 °C range in air. It is possible to notice a similar trend in all the samples, for which two different temperature intervals exist: a first one from room temperature up to 350-400 °C the samples are characterized by an increase in weight, which is followed by a larger region at high temperature in which a weight decrease is observed. These observations suggest that at low temperature an oxygen incorporation is occurring up to a maximum value which is expected to be related to a conductivity maximum. In this region the equilibrium in (6) is shifted towards the formation of Co^{4+} (and Fe^{4+} in the case of iron doped samples) through incorporation of oxygen:

$$2Co_{Co}^{X} + V_{O}^{\bullet\bullet} + \frac{1}{2}O_2 \rightarrow O_{O}^{X} + 2Co_{Co}^{\bullet} \qquad (7)$$

At temperature above 400 °C the equilibrium is reversed and a weight loss is observed:

$$O_{O}^{X} + 2Co_{Co}^{\bullet} \rightarrow 2Co_{Co}^{X} + V_{O}^{\bullet\bullet} + \frac{1}{2}O_2 \qquad (8)$$

In this case the weight decrease is due to a loss of oxygen and consequent formation of vacancies.

It is worth to notice that the weight increase in SCFN2 is less pronounced than in the other samples, which is consistent with the observed nonstoichiometry coefficient determined by iodometric titration, from which was found a higher amount of Co^{4+}/Fe^{4+} species already present in the sample at room temperature. Tai *et al* elucidated that the presence of Co^{4+} and Fe^{4+} is associated with p-type conductivity, where electron holes are transported *via* polaron hopping mechanism. [60,61]

The decrease in oxygen content is associated with a reduction of cobalt and iron to lower oxidation state (Fe^{3+} and Co^{3+}) and thus a lower electronic conductivity is expected.

7.3.4 Electrical conductivity

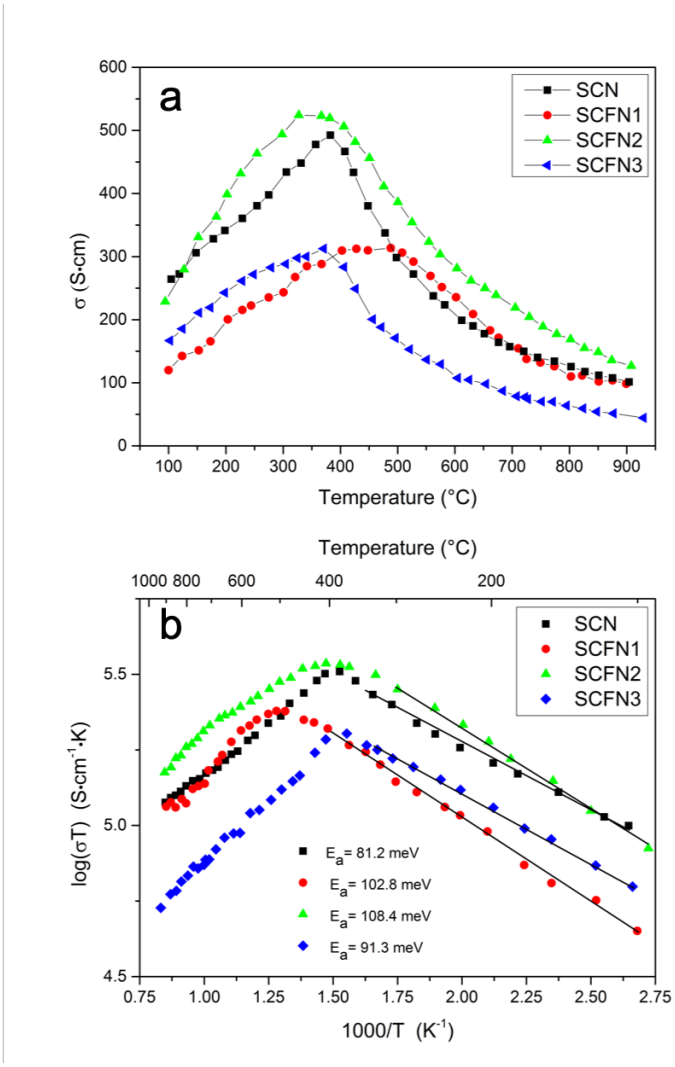

Fig 7.3: Conductivity measured in air between 100 and 900 °C (a) and Arrhenius plot of log(σT) (b) of $SrCo_{0.95}Nb_{0.05}O_{3-\delta}$ (SCN), $SrCo_{0.85}Fe_{0.1}Nb_{0.05}O_{3-\delta}$ (SCNF1), $SrCo_{0.75}Fe_{0.2}Nb_{0.05}O_{3-\delta}$ (SCNF2), $SrCo_{0.65}Fe_{0.3}Nb_{0.05}O_{3-\delta}$ (SCNF3).

Figure 7.3 shows the DC-conductivity and Arrhenius plot value for the four samples: since in mixed ionic and electronic materials, electronic contribution is orders of magnitude larger than ionic conductivity, the curves can be considered as representative of the electronic conductivity of the samples.

It can be observed that electrical conductivity increases with temperature to a maximum value and then decreases. In the case of small polarons conduction in semiconductors, electrical conductivity can be expressed as:

$$\sigma = \frac{A}{T} e^{-\frac{Ea}{kT}} \quad (9)$$

Where A is a constant typical of the material and E_a is the activation energy for small polarons hopping. According to (7), two different regimes can be separated: if kT<Ea the electrical conductivity is dominated by the exponential term and increasing with temperature; if kT>Ea the pre-exponential factor becomes dominant and the total conductivity decreases with temperature. The polarons hopping activation energy (E_a) can be obtained from the low temperature region of ln(σT) plot, as is shown in figure 7.3 b.

For all samples, the two different regions observed in conductivity measurements are consistent with a semiconductor to metal-like transition after the maximum conductivity. This is in agreement with the weight changes observed in TGA measurements: after an initial increase of oxygen content which is responsible for the formation of more p-type carriers (Co^{4+}, Fe^{4+}) at low temperature, the decrease in conductivity above 400 °C is related to the oxygen loss observed, causing a reduction of cobalt and iron and consequently of p-type carriers.

It is possible to notice that iron doping has an influence on the electronic conduction: in all Fe-doped samples a higher activation energy than in the case of undoped SCN is observed, suggesting a lower conductivity. However, despite the replacement of cobalt for iron increases the activation energy, the conductivity of SCFN2 is slightly higher than in the case of undoped SCN. This can be explained considering the average oxidation state of B-site cations observed from TGA characterization: having a higher average oxidation state, the number of holes available for conduction in SCFN2 is higher than in the other compounds in the whole temperature range.

The effect of doping on the transition temperature and value of maximum conductivity is not linear with the amount of iron introduced. This suggests that evaluating the effect of Fe-doping should consider the simultaneous presence of niobium and a possible interaction between the dopants. Yi *et al* investigated electrical and oxygen transport

properties of Fe-doped $SrCoO_{3-\delta}$ ($0 \leq Fe \leq 0.2$), observing an enhancement of conductivity and decrease of the transition temperature with increasing iron doping; this behaviour is due to a better stabilization of the perovskitic structure with a higher iron content. [40] The detrimental role of iron on conductivity was observed by Wang *et al*, which found an increase in the activation energy with iron content, observing a maximum conductivity of 520 $S \cdot cm^{-1}$ in the case of $SrCo_{0.8}Fe_{0.2}O_{3-\delta}$ which is very close to the 525 $S \cdot cm^{-1}$ observed for SCFN2.[36]

An ideal SOFC cathode should be highly conductive, for this purpose it is commonly required that the material displays a total conductivity above 100 $S \cdot cm^{-1}$ at the desired operation temperature. [47,62,63] SCN, SCFN1, SCFN2 and SCFN3 show 490, 315, 525 and 310 $S \cdot cm^{-1}$ in the conductivity maximum, respectively. Compared to $La_{0.8}Sr_{0.2}Co_{1-x}Fe_xO_{3-\delta}$ conductivity values observed by Tai *et al* ($1600 > \sigma > 750$ $S \cdot cm^{-1}$, $0 \leq x \leq 0.3$) these are promising values, considering that the system does not include lanthanum or other rare earths.

All the samples display a conductivity higher than 100 $S \cdot cm^{-1}$ up to 900°C except SCFN3, for which a lower conductivity is observed in the whole temperature interval, probably due to the higher amount of iron which is creating trapping sites for the holes.

It is interesting to notice that for SCFN1 sample, the maximum conductivity temperature is shifted at 500°C, about 100°C higher than in the case of the other samples, where a 300 $S \cdot cm^{-1}$ value is observed. This is the ideal target temperature for low temperature operation in fuel cells and, if the conduction maximum is coupled with good electrochemical properties, SCFN1 may represent a very promising electrode material.

7.3.5 SEM

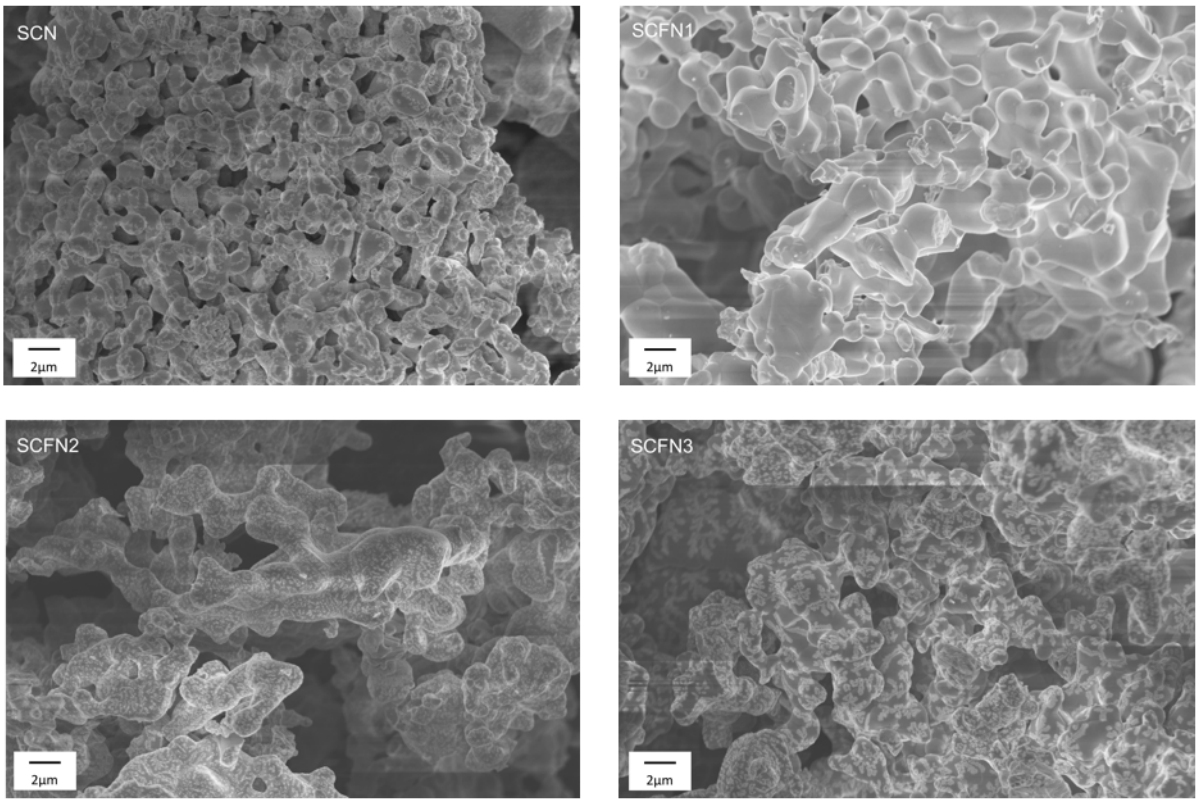

Fig 7.4: Scanning electron micrographs of the powders of $SrCo_{0.95}Nb_{0.05}O_{3-\delta}$ (SCN), $SrCo_{0.85}Fe_{0.1}Nb_{0.05}O_{3-\delta}$ (SCNF1), $SrCo_{0.75}Fe_{0.2}Nb_{0.05}O_{3-\delta}$ (SCNF2), $SrCo_{0.65}Fe_{0.3}Nb_{0.05}O_{3-\delta}$ (SCNF3) before the preparation of the inks for the electrode deposition.

Figure 7.4 shows the microstructure of the $SrCo_{0.95}Nb_{0.05}O_{3-\delta}$ (SCN), $SrCo_{0.85}Fe_{0.1}Nb_{0.05}O_{3-\delta}$ (SCNF1), $SrCo_{0.75}Fe_{0.2}Nb_{0.05}O_{3-\delta}$ (SCNF2) and $SrCo_{0.65}Fe_{0.3}Nb_{0.05}O_{3-\delta}$ (SCNF3) powders before the preparation of the inks for the electrode deposition on GDC for the preparation of the symmetric cell.

It is possible to notice that all the materials have small particles of a 0.5-2 micrometers dimensions in a connected microstructure. All the samples have a small size porosity of a few micrometers between particles and a larger porosity between particles cluster with a wider porosity of 5-10 micrometers that seems to be more pronounced as the iron content increases.

7.3.6 EIS

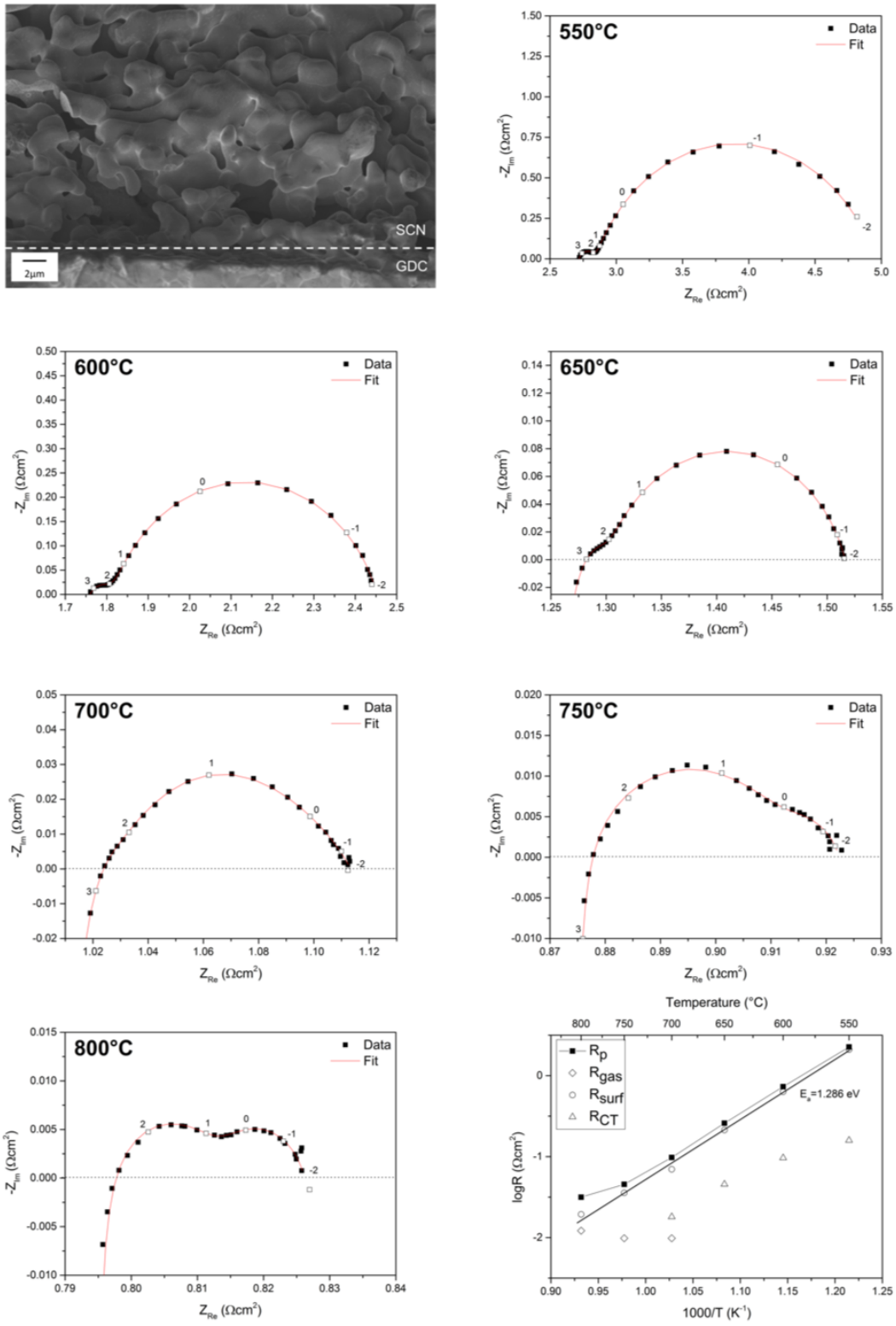

Fig 7.5: Impedance data and fit in the temperature range 550°-800°C for symmetric cell with SCN electrodes on GDC electrolyte, treated at 1100°C. SEM cross section of the cell after test and Arrhenius plot of total polarization resistance and resistances specific for each process are also included.

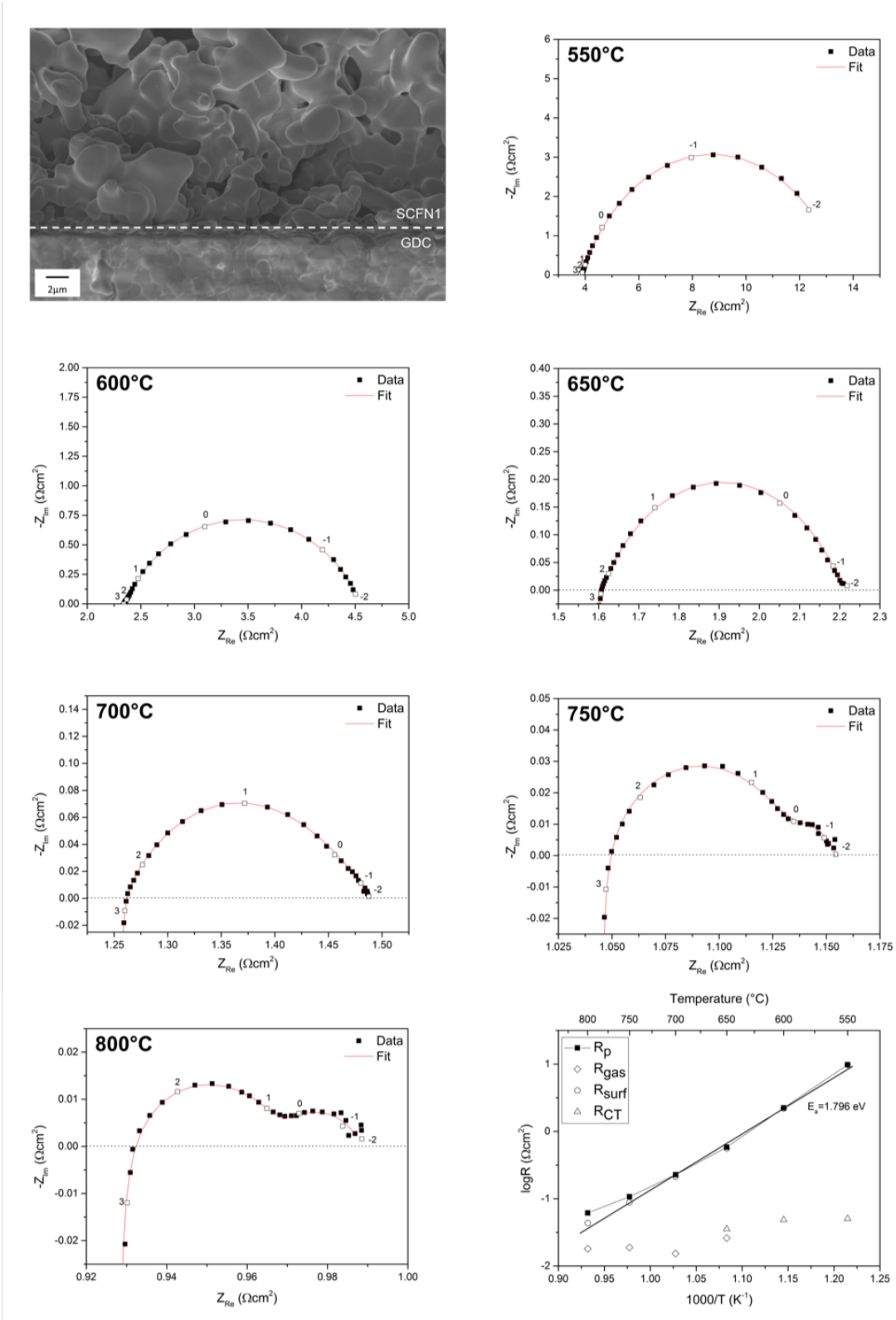

Fig 7.6: Impedance data and fit in the temperature range 550°-800°C for symmetric cell with SCNF1 electrodes on GDC electrolyte, treated at 1100°C. SEM cross section of the cell after test and Arrhenius plot of total polarization resistance and resistances specific for each process are also included.

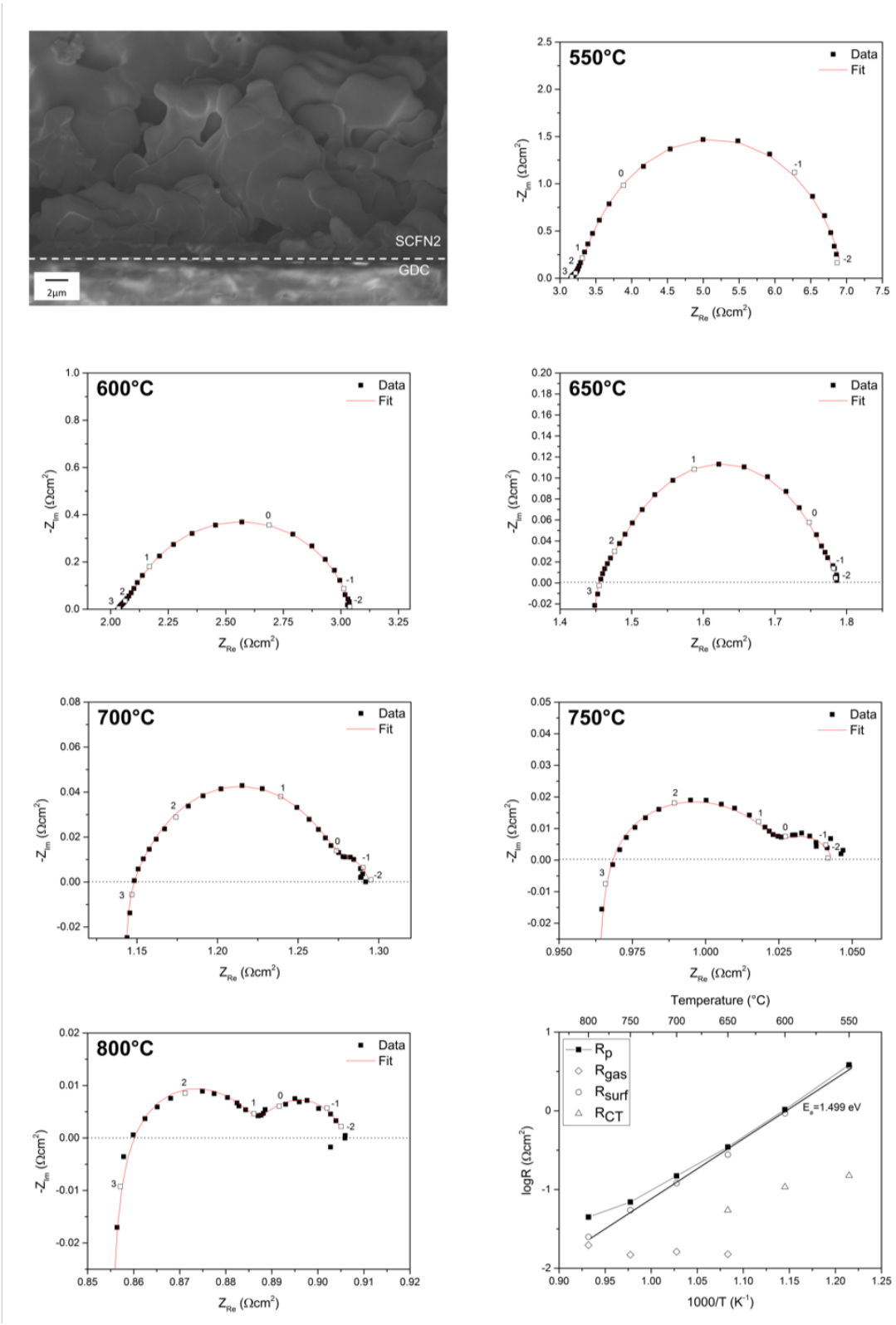

Fig 7.7: Impedance data and fit in the temperature range 550°-800°C for symmetric cell with SCNF2 electrodes on GDC electrolyte, treated at 1100°C. SEM cross section of the cell after test and Arrhenius plot of total polarization resistance and resistances specific for each process are also included.

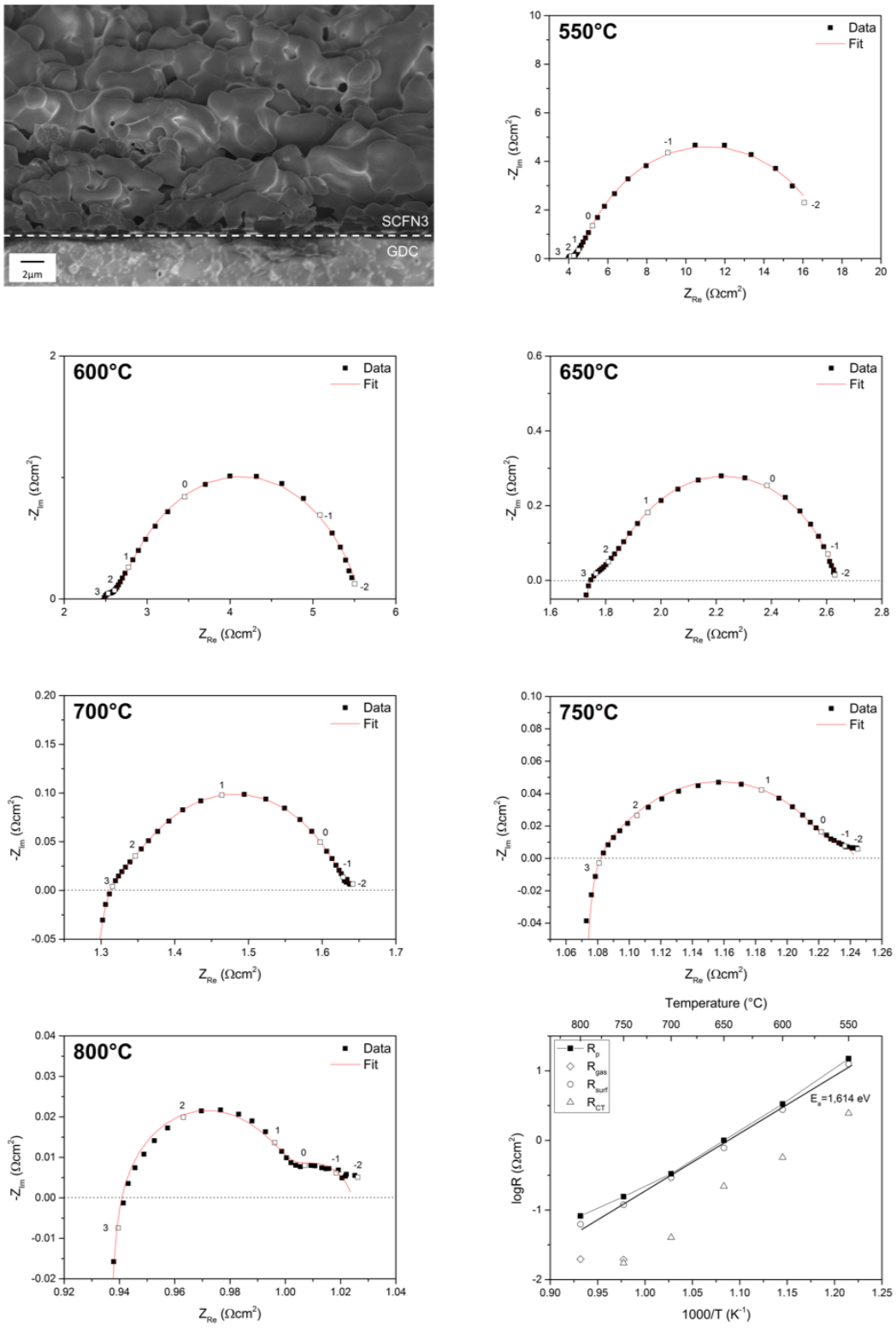

Figure 7.8: Impedance data and fit in the temperature range 550°-800°C for symmetric cell with SCFN3 electrodes on GDC electrolyte, treated at 1100°C. SEM cross section of the cell after test and Arrhenius plot of total polarization resistance and resistances specific for each process are also included.

Figures 7.5-7.8 show the electrochemical impedance spectra recorded in air in the 550-800 °C temperature range for each sample. These include different contributions which are taken in account in the fitting procedure: the inductance coming from the wires (L_1, which is more relevant at high temperature), the resistance due to the electrolyte (R_s) and the contribution due to the cathode. Three different regions were considered for the fitting of the electrode. At high temperature (750-850°C) two contributions can be noticed and these were fitted with an equivalent circuit made of two R//CPE elements, which consider the surface reduction of oxygen and a gas diffusion limit. The latter contribution can be identified by the fact that it is neither frequency dependent nor thermally activated, but is related to gas diffusion limitations of the electrode, for this reason it is associated with a constant resistance (0.01-0.025 $\Omega \cdot cm^2$) and a large (2-7 $F \cdot cm^2$) capacitance. This contribution is not negligible at high temperature, when the kinetics of ORR is fast, but is incorporated and impossible to separate at lower temperatures, when the impedance associated with ORR has a larger resistance. In the low temperature regime two semicircles were recognized: one at high frequency which is related to charge transfer processes and one at intermediate frequency due to ORR. These two contributions were fitted with two R//CPE elements.

For each sample an intermediate region in which the three contributions are simultaneously present was considered, including the three R//CPE elements in figure 7.9.

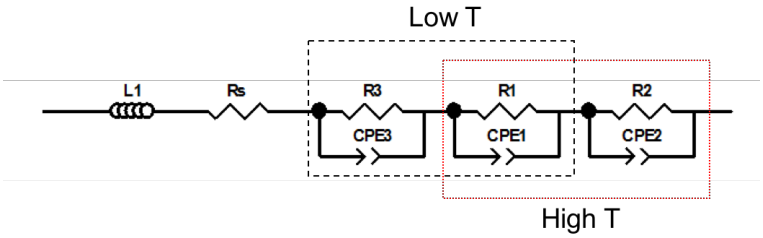

Figure 7.9: Equivalent circuit used for the fitting of impedance spectra, including and inductance contribution, the electrolyte resistance (Rs) and a total of three R//CPE, which represent respectively charge transfer processes (R3), surface exchange processes (R2) and gas diffusion limitations (R2).

The Arrhenius plot for the resistances obtained for every sample shows the different contributions to the total ASR (measured as the difference between the low frequency

and high frequency intercept with Z_{Re} axis) coming from the specific resistances obtained by the fitting procedure.

The obtained ASR values at 600 °C, are 0.73, 2.23, 1.04 and 3.33 $\Omega \cdot cm^2$ for SCN, SCFN1, SCFN2 and SCFN3, respectively. As a general trend, the effect of iron doping seems to increase the resistance values, but this effect is less evident for SCFN2 sample. Considering the ionic conductivities (calculated in chapter 6) and the electronic conductivity values observed from the four probes measurements, this suggests that at low temperature a major contribution comes from electronic conductivity, and the obtained ASR values follow the trend observed for σ_{el}.

As a general trend in can be seen that in all samples a major contribution is coming from the surface exchange reaction (i.e. surface diffusion, incorporation and bulk diffusion of oxygen) while the charge transfer gives a minor contribution to the total resistance of the electrode, suggesting that charge transfer is not the limiting process at the electrode. This is not unexpected, since the samples were developed with the aim of obtaining high mixed ionic and electronic conduction. Due to the larger uncertainty in the fitting of the high frequency semicircle (charge transfer) compared to the one associated with the intermediate frequency one (surface exchange), the activation energy and capacitance for charge transfer are not reported except in table 7.3.

The ASR values obtained at 800°C, are 0.031, 0.061, 0.044, 0.082 $\Omega \cdot cm^2$ for SCN, SCFN1, SCFN2 and SCFN3, respectively. High temperature spectra show two semicircles: beside one at intermediate frequency, there's a contribution from gas diffusion at low frequencies which is not temperature dependent: this can be noticed from the Arrhenius plot of logR for every sample, in which the different contributions to the total resistance of the electrode are separated. In the high temperatures regime, the gas diffusion limitation becomes comparable with the oxygen reduction resistance and a slope change is observed in the Arrhenius plot of the total ASR. [64,65] This effect is even more evident for SCN and SCFN2 samples, which show a better ORR performance.

Due to gas diffusion limitation, at high temperature the difference in ASR is apparently less marked, but the values obtained for R_{surf} show that iron doping is increasing the resistance to surface exchange. This can be noticed looking at the activation energies for the process (presented in table 7.2): Fe introduction can raise E_a up to 0.5eV in the case

of SCFN1. Despite having higher ASR values, similar activation energy values were observed by Wang *et al* for BSCF. [66] Baumann *et al* observed an increase in activation energy from 1.3 eV up to 1.8 eV in the LSC-LSCF-LSFC-LSF series with increasing iron content, which is consistent with the obtained values. [15]

	ASR ($\Omega \cdot cm^2$)			$E_{a\,(surf)}$ (eV)
Sample	@600 °C	@700 °C	@800 °C	
SCN	0.73	0.097	0.031	1.286
SCFN1	2.23	0.227	0.061	1.796
SCFN2	1.04	0.148	0.044	1.499
SCFN3	3.33	0.331	0.082	1.614

Table 7.2: Area specific resistances (ASR) and activation energy for surface exchange process determined from EIS fitting for $SrCo_{0.95}Nb_{0.05}O_{3-\delta}$ (SCN), $SrCo_{0.85}Fe_{0.1}Nb_{0.05}O_{3-\delta}$ (SCNF1), $SrCo_{0.75}Fe_{0.2}Nb_{0.05}O_{3-\delta}$ (SCNF2), $SrCo_{0.65}Fe_{0.3}Nb_{0.05}O_{3-\delta}$ (SCNF3).

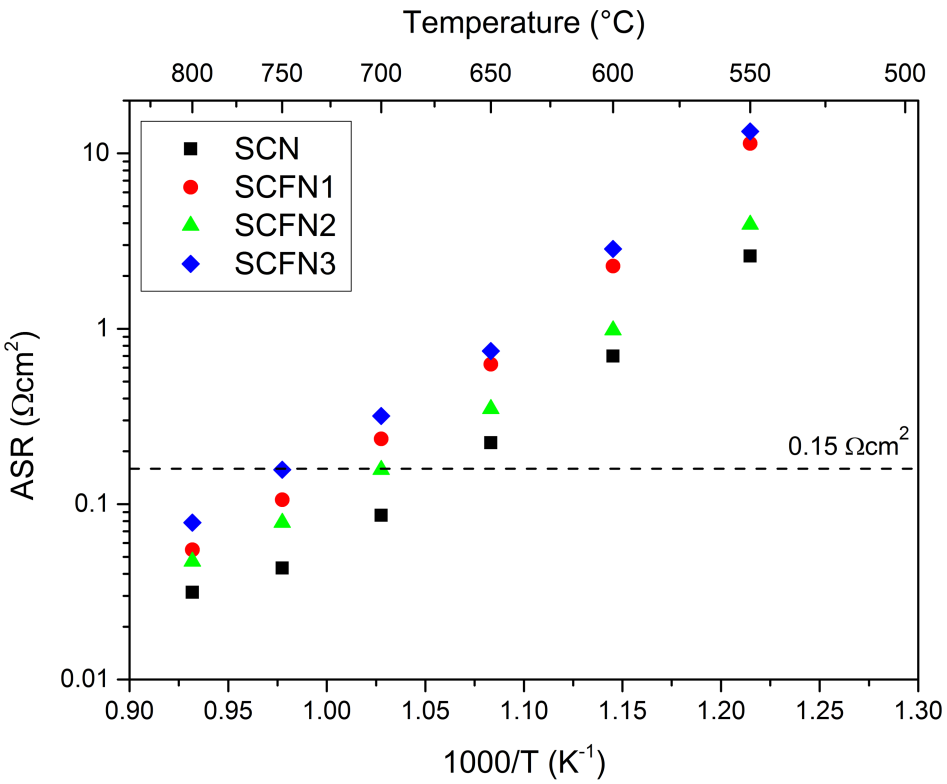

Fig 7.10: Area specific resistance (ASR) in the temperature range 550°-800°C of $SrCo_{0.95}Nb_{0.05}O_{3-\delta}$ (SCN), $SrCo_{0.85}Fe_{0.1}Nb_{0.05}O_{3-\delta}$ (SCNF1), $SrCo_{0.75}Fe_{0.2}Nb_{0.05}O_{3-\delta}$ (SCNF2), $SrCo_{0.65}Fe_{0.3}Nb_{0.05}O_{3-\delta}$ (SCNF3).

Figure 7.10 shows the ASR values obtained for all samples. A reference target ASR value of 0.15 $\Omega \cdot cm^2$ is marked, as identified by Steele. [67] Compared to the target value, it can be noticed that SCN and SCFN2 are the only samples within the desired ASR value at 700°C. However, all the obtained ASR values are larger than the ones typically observed in other doped $SrCoO_{3-\delta}$ samples. As an example, in scandium or samarium doped samples 0.044 and 0.098 $\Omega \cdot cm^2$ ASR was reported at 650 °C, respectively. [41,42] This suggests that the presence of a fixed valence rare earth can definitely enhance the performance of the material. The fitting parameters obtained for R//CPE element allow to calculate the value of the real capacitance associated with every process, through the equation:

$$C = \frac{(Q_0 \cdot R)^{\frac{1}{n}}}{R} \quad (10)$$

where Q_0 and n represent the CPE-T and CPE-P values in the Z-view software, respectively. As already mentioned, since charge transfer semicircle showed larger uncertainty

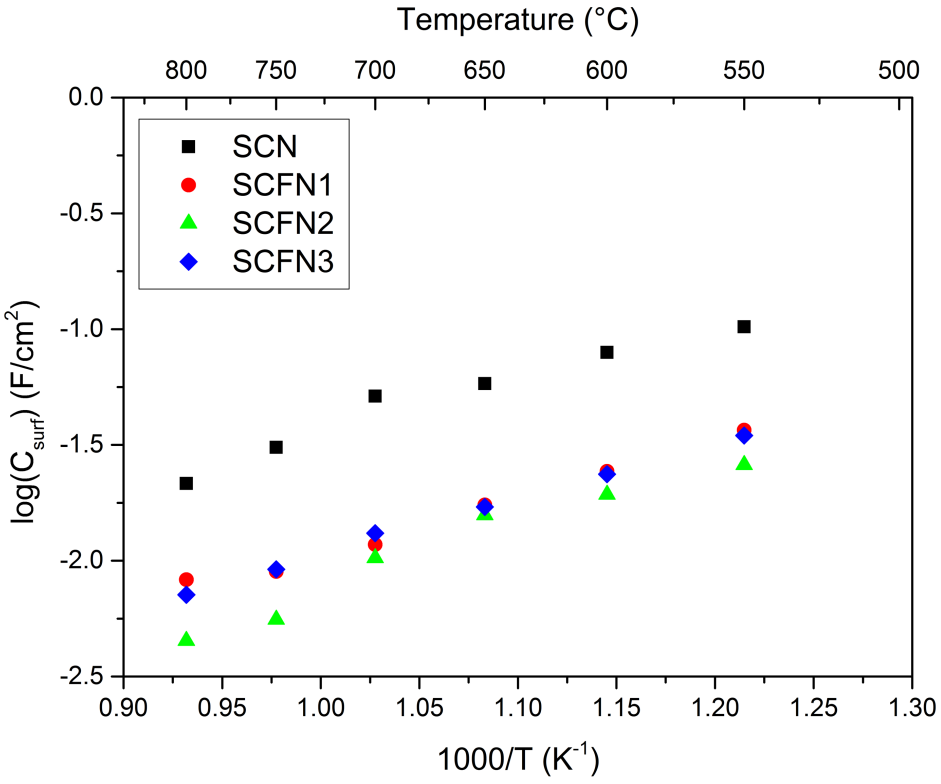

Fig 7.11: Area specific pseudo-capacitance associated with the surface process in the temperature range 550°-800°C of $SrCo_{0.95}Nb_{0.05}O_{3-\delta}$ (SCN), $SrCo_{0.85}Fe_{0.1}Nb_{0.05}O_{3-\delta}$ (SCNF1), $SrCo_{0.75}Fe_{0.2}Nb_{0.05}O_{3-\delta}$ (SCNF2), $SrCo_{0.65}Fe_{0.3}Nb_{0.05}O_{3-\delta}$ (SCNF3).

associated with the fitting, the capacitance values were calculated in order to confirm the identified process and are reported in table 7.3.

Figure 7.11 shows the calculated capacitances for surface exchange process for the four samples. Capacitances decrease with temperature for all samples, but it can be noticed that iron doping is reducing the capacitance in all samples, in particular in SCFN2. Even though a similar trend has been observed in BSCF samples and is consistent with the three iron-doped samples, an opposite trend was observed for $Sm_{0.5}Sr_{0.5}CoO_{3-\delta}$, showing a slight increase of C_{surf} with temperature. [15] This is not the case of SCN, which presents a notably higher capacitance than the Fe containing samples, and suggest that this effect may be associated with niobium dopant, which is present in all the samples.

	R ($\Omega \cdot cm^2$)	**E_a (eV)**	**Capacitance ($F \cdot cm^2$)**	**Proposed process**
High frequency process	0.02-2.5	0.7-1.5	0.0001-0.001	Charge transfer
Middle frequency process	0.015-12	1.3-1.8	0.02-0.1 (SCN) 0.005-0.02	Surface exchange
Low frequency process	0.01-0.025	/	3-7	Gas diffusion

Table 7.3: Resistance range, activation energy, associated capacitance and proposed process for every semicircle obtained in the EIS spectra.

Table 7.3 gives an overview on the chemical processes and associated resistances, activation energies and capacitances. The observed values are consistent with reported literature, however, despite showing similar capacitance values (0.005-0.2 $F \cdot cm^2$), the resistance associated with surface exchange process is larger than in most of the reported materials. It is well known that the electrodes microstructure plays an important role in determining the final properties of material and it has been observed several times that the electrode deposition procedure, the electrode layering structure, the use of pore formers and the chosen thermal treatment can deeply influence the electrochemical

properties of the material. [53,64,65] For this reason, the microstructure of the cell's electrodes has been investigated with SEM.

7.3.7 SEM after testing

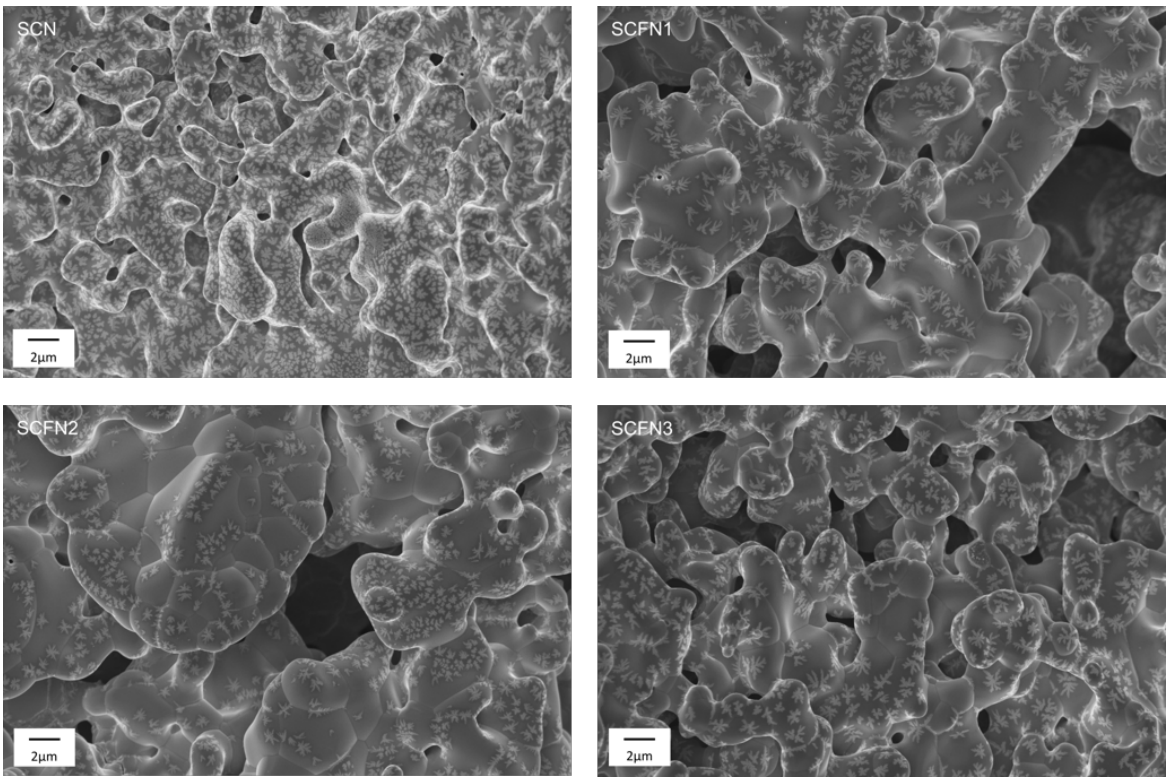

Fig 7.12: Scanning electron microscopy micrograph of the electrode surface of $SrCo_{0.95}Nb_{0.05}O_{3-\delta}$ (SCN), $SrCo_{0.85}Fe_{0.1}Nb_{0.05}O_{3-\delta}$ (SCNF1), $SrCo_{0.75}Fe_{0.2}Nb_{0.05}O_{3-\delta}$ (SCNF2), $SrCo_{0.65}Fe_{0.3}Nb_{0.05}O_{3-\delta}$ (SCNF3) deposited on CGO electrolyte and treated at 1100°C for 6 hours.

Figure 7.12 shows the electrode surface for all the samples. From a comparison with the starting powders morphology it is possible to observe that the grain dimensions are increased and the starting porosity of the powders is shrinked with the thermal treatments, with the result that a lower electrode surface is exposed. This could be a reason why a prominent contribution from surface exchange to the total resistance has been observed. In fact, oxygen vacancies are known to be the reaction sites for gaseous oxygen to adsorb, dissociate and be consequently reduced and smaller electrode surface results in fewer available sites for oxygen adsorption, dramatically reducing the activity of the electrode. Since all samples showed an increase in grain size and connection between

grains after the thermal treatment, it is reasonable to think that all the samples are affected by this phenomenon in a similar extent. However, in presence of a higher content of iron, the microstructure displays a smaller particle size associated with a higher porosity and less compact structure. This is not unexpected, since cobalt is known to be used as sintering addictive to enhance the densification of ceramics and has been exploited even with electrolyte materials. [68] Replacing cobalt for iron reduces the sinterability and thus results in smaller particle size, similar trends have been detected in other Co, Fe-containing perovskites and brownmillerites. [69,70] This observed trend is suggesting that the sintering behavior of a cobalt and iron containing material could be tuned with composition, in order to further improve the final electrodes microstructure.

7.4 Conclusions

In this chapter $SrCo_{0.95}Nb_{0.05}O_{3-\delta}$ (SCN), $SrCo_{0.85}Fe_{0.1}Nb_{0.05}O_{3-\delta}$ (SCNF1), $SrCo_{0.75}Fe_{0.2}Nb_{0.05}O_{3-\delta}$ (SCNF2), $SrCo_{0.65}Fe_{0.3}Nb_{0.05}O_{3-\delta}$ (SCNF3) were successfully synthesized by means of citrate route and their properties were characterized. Cubic perovskitic structure was observed in all the samples, showing the beneficial effects of niobium and iron doping on the stabilization of $SrCoO_{3-\delta}$ structure.

The oxygen nonstoichiometry (δ) at room temperature was determined by iodometric titration (IT) and showed a decrease in the value of δ and higher average B-site cations valence (n) with iron content, consistent with the formation of more Fe^{4+} and Co^{4+} p-type carriers. The decrease in oxygen nonstoichiometry is not linear with the amount of iron dopant, in fact SCFN2 showed the lowest value of δ (0.225) and the highest average B-site oxidation state (3.30). The evolution of δ and n with temperature in air was investigated with thermogravimetric analysis (TGA) and two different temperature windows were identified: in the low temperature region (T<400°C) a weight increase consistent with the incorporation of oxygen up to a maximum is observed, then in the high temperature region (T>400°C) a progressive release of oxygen occurs. Even though all the samples showed a similar behavior during the TGA, a smaller weight increase for SCFN2 was found, consistently with the higher value of δ determined by IT. The trend observed in TGA was consistent with the observed values in the four probes conductivity measurement: all the samples have a semiconductor to metal transition around 400°C which is consistent with the oxygen loss and consequent reduction of p-type carriers available for conduction. As a general trend Fe-doping was found to increase the activation energy for the polaron hopping conduction and decrease the samples conductivity from 500 (for SCN) to 300 $S \cdot cm^{-1}$. Surprisingly SCFN2 showed a conductivity value slightly higher than SCN which can be related to the higher amount of available carriers determined by TGA.

Symmetrical cells depositing porous electrodes on a dense GDC pellet were prepared and tested with electrochemical impedance spectroscopy in air, in order to evaluate the materials activity as cathodes. With a fitting procedure using an equivalent circuit, in all samples three contributions to the area specific resistance (ASR) were identified and separated: a high frequency semicircle, an intermediate frequency semicircle and a low

frequency semicircle which were assigned to charge transfer resistance, surface exchange resistance and gas diffusion resistance. While the first is detectable only at the lower temperatures, gas diffusion contribution has a major relevance at high temperature. The characteristic resistance, activation energies and capacitances of surface exchange were determined and, once again, iron doping was found to have an influence on them. Despite increasing the resistance and activation energy for ORR, the surface specific capacitances of Fe-doped samples are lower than the ones determined for SCN. At all temperatures the ASR of the samples increased with the following trend: SCN<SCFN2<SCFN1<SCFN3, in agreement with the electronic conduction properties observed with four probes measurement. As a general trend, the observed ASR values were larger than in other similar materials and only in the case of SCN and SCFN2 the ASR values fulfill the target value below 0.15 $\Omega \cdot cm^2$ identified by literature at a temperature 700°C, showing promising performance. For this reason scanning electron microscopy was performed on the powders and the final electrode microstructure, showing that the small starting particles with a high porosity increased in dimensions with thermal treatment and displayed a lower porosity. The final area of the electrode was observed to be lower than in the case of the starting powders. Since surface exchange was observed to be the prominent contribution to ASR, the decrease in surface area was related to a decrease in the number of active sites for oxygen adsorption and reduction exposed by the electrode. This suggests that a different electrode deposition procedure should be adopted in order to emphasize the electrocatalytic properties of the materials.

7.5 Bibliography

1. Lin, Y., Zhan, Z., Liu, J. & Barnett, S. A. Direct operation of solid oxide fuel cells with methane fuel. *Solid State Ionics* **176,** 1827–1835 (2005).
2. Park, S., Vohs, J. M. & Gorte, R. J. Direct oxidation of hydrocarbons in a solid-oxide fuel cell. *Nature* **404,** 265–267 (2000).
3. Jiang, Y. & Virkar, A. V. A High Performance, Anode-Supported Solid Oxide Fuel Cell Operating on Direct Alcohol. *J. Electrochem. Soc.* **148,** A706 (2001).
4. Kawada, T., Sakai, N., Yokokawa, H., Dokiya, M. & Anzai, I. Reaction Between Solid Oxide Fuel-Cell Materials. *Solid State Ionics* **50,** 189–196 (1992).
5. Van Roosmalen, J. A. M. & Cordfunke, E. H. P. Chemical reactivity and interdiffusion of (La, Sr) MnO3 and (Zr, Y)O2, solid oxide fuel cell cathode and electolyte materials. *Solid State Ionics* **52,** 303–312 (1992).
6. Yokokawa, H., Tu, H., Iwanschitz, B. & Mai, A. Fundamental mechanisms limiting solid oxide fuel cell durability. *J. Power Sources* **182,** 400–412 (2008).
7. Simner, S. P., Anderson, M. D., Engelhard, M. H. & Stevenson, J. W. Degradation Mechanisms of La–Sr–Co–Fe–O[sub 3] SOFC Cathodes. *Electrochem. Solid-State Lett.* **9,** A478 (2006).
8. Simwonis, D., Tietz, F. & Stover, D. Nickel coarsening in annealed Ni / 8YSZ anode substrates for solid oxide fuel cells. *Solid State Ionics* **132,** 241–251 (2000).
9. Wachsman, E. D. & Lee, K. T. Lowering the Temperature of Solid Oxide Fuel Cells. *Science (80-.).* **334,** 935–939 (2011).
10. Steele, B. Appraisal of Ce1−yGdyO2−y/2 electrolytes for IT-SOFC operation at 500°C. *Solid State Ionics* **129,** 95–110 (2000).
11. Steele, B. C. H. Material science and engineering: The enabling technology for the commercialisation of fuel cell systems. *J. Mater. Sci.* **36,** 1053–1068 (2001).
12. Liu, M. Significance of interfaces in solid-state cells with porous electrodes of mixed ionic–electronic conductors. *Solid State Ionics* **107,** 105–110 (1998).
13. Adler, S. B. Electrode Kinetics of Porous Mixed-Conducting Oxygen Electrodes. *J. Electrochem. Soc.* **143,** 3554 (1996).
14. Fleig, J. Solid Oxide Fuel Cell Cathodes: Polarization Mechanisms and Modeling of the Electrochemical Performance. *Annu. Rev. Mater. Res.* **33,** 361–382 (2003).
15. Baumann, F. S. *et al.* Quantitative Comparison of Mixed Conducting SOFC Cathode Materials by Means of Thin Film Model Electrodes. *J. Electrochem. Soc.* **154,** B931 (2007).
16. Atkinson, A. *et al.* Advanced anodes for high-temperature fuel cells. *Nat. Mater.* **3,** 213–223 (2004).
17. Hibino, T. *et al.* High Performance Anodes for SOFCs Operating in Methane-Air Mixture at Reduced Temperatures. *J. Electrochem. Soc.* **149,** A133 (2002).
18. de Souza, S. Reduced-Temperature Solid Oxide Fuel Cell Based on YSZ Thin-Film

Electrolyte. *J. Electrochem. Soc.* **144,** L35 (1997).

19. Cho, S., Kim, Y., Kim, J. H., Manthiram, A. & Wang, H. High power density thin film SOFCs with YSZ/GDC bilayer electrolyte. *Electrochim. Acta* **56,** 5472–5477 (2011).
20. Adler, S. B. Factors Governing Oxygen Reduction in Solid Oxide Fuel Cell Cathodes †. (2004). doi:10.1021/cr020724o
21. Dusastre, V. & Kilner, J. A. Optimisation of Composite Cathodes for Intermediate Temperature Soild Oxide Fuel Cell Applications. *Solid State Ionics* **126,** 163–174 (1999).
22. Perry Murray, E. (La,Sr)MnO3–(Ce,Gd)O2−x composite cathodes for solid oxide fuel cells. *Solid State Ionics* **143,** 265–273 (2001).
23. Jørgensen, M. J., Primdahl, S. & Mogensen, M. Characterisation of composite SOFC cathodes using electrochemical impedance spectroscopy. *Electrochim. Acta* **44,** 4195–4201 (1999).
24. Jørgensen, M. J. & Mogensen, M. Impedance of Solid Oxide Fuel Cell LSM/YSZ Composite Cathodes. *J. Electrochem. Soc.* **148,** A433 (2001).
25. Skinner, S. J. Recent advances in Perovskite-type materials for solid oxide fuel cell cathodes. *Int. J. Inorg. Mater.* **3,** 113–121 (2001).
26. Peña, M. A. & Fierro, J. L. G. Chemical structures and performance of perovskite oxides. *Chem. Rev.* **101,** 1981–2017 (2001).
27. Perry Murray, E., Sever, M. J. & Barnett, S. A. Electrochemical performance of (La,Sr)(Co,Fe)O3-(Ce,Gd)O3 composite cathodes. *Solid State Ionics* **148,** 27–34 (2002).
28. Xiao, G. *et al.* Synthesis and characterization of Mo-doped SrFeO3-δas cathode materials for solid oxide fuel cells. *J. Power Sources* **202,** 63–69 (2012).
29. Gao, L. *et al.* A novel family of Nb-doped Bi0.5Sr0.5FeO3-Δperovskite as cathode material for intermediate-temperature solid oxide fuel cells. *J. Power Sources* **371,** 86–95 (2017).
30. Jiang, S. *et al.* Cobalt-free SrNb<inf>x</inf>Fe<inf>1-x</inf>O<inf>3-δ</inf> (x = 0.05, 0.1 and 0.2) perovskite cathodes for intermediate temperature solid oxide fuel cells. *J. Power Sources* **298,** 209–216 (2015).
31. Zhao, H. *et al.* New cathode materials for ITSOFC: Phase stability, oxygen exchange and cathode properties of La2 - xNiO4 + ?? *Solid State Ionics* **179,** 2000–2005 (2008).
32. Chauveau, F., Mougin, J., Mauvy, F., Bassat, J.-M. & Grenier, J.-C. Development and operation of alternative oxygen electrode materials for hydrogen production by high temperature steam electrolysis. *Int. J. Hydrogen Energy* **36,** 7785–7790 (2011).
33. Natile, M. M., Eger, G., Batocchi, P., Mauvy, F. & Glisenti, A. Strontium and copper doped LaCoO3: New cathode materials for solid oxide fuel cells? *Int. J. Hydrogen Energy* **42,** 1724–1735 (2017).

34. Hildenbrand, N., Nammensma, P., Blank, D. H. A., Bouwmeester, H. J. M. & Boukamp, B. A. Influence of configuration and microstructure on performance of La 2NiO4+?? intermediate-temperature solid oxide fuel cells cathodes. *J. Power Sources* **238,** 442–453 (2013).
35. Huang, K., Wan, J. & Goodenough, J. B. Oxide-ion conducting ceramics for solid oxide fuel cells. *J. Mater. Sci.* **36,** 1093–1098 (2001).
36. Wang, Z. *et al.* Electrical conductivity and structural stability of SrCo 1-xFexO3-δ. *J. Phys. Chem. Solids* **72,** 50–55 (2011).
37. Y. Teraoka, H.M. Zhang, S. Furukawa, N. Y. Oxygen permeation through pervoskite-type oxides. *Chem. Lett.* 1743–1746 (1985). doi:10.1246/cl.1985.1743
38. Takeda, Y., Kanno, R., Takada, T. & Yamamoto, O. Phase Relation and Oxygen-non-stoichiometry of Perovskite- like Compound SrCoOx (2.29<x<2.80). *Z. anorg. allg. Chem.* **541,** 259–270 (1986).
39. Kruidhof, H., Bouwmeester, H. J. M., v. Doorn, R. H. E. & Burggraaf, A. J. Influence of order-disorder transitions on oxygen permeability through selected nonstoichiometric perovskite-type oxides. *Solid State Ionics* **63–65,** 816–822 (1993).
40. Yi, J., Feng, S., Zeng, Q. & Chen, C. Structure, Electrical and Oxygen Transport Properties of Fe-Doped SrCoO3—δ Perovskites. *Chinese J. Chem. Phys.* **28,** 189–192 (2015).
41. Lee, D. *et al.* Durable high-performance Sm0.5Sr0.5CoO3-Sm0.2Ce0.8O1.9core-shell type composite cathodes for low temperature solid oxide fuel cells. *Int. J. Hydrogen Energy* **36,** 6875–6881 (2011).
42. Zhou, W., Shao, Z., Ran, R. & Cai, R. Novel SrSc0.2Co0.8O3-δas a cathode material for low temperature solid-oxide fuel cell. *Electrochem. commun.* **10,** 1647–1651 (2008).
43. Wan, J.-H., Yan, J.-Q. & Goodenough, J. B. LSGM-Based Solid Oxide Fuel Cell with 1.4 W/cm2 Power Density and 30 Day Long-Term Stability. *J. Electrochem. Soc.* **152,** A1511 (2005).
44. Esquirol, A., Brandon, N. P., Kilner, J. A. & Mogensen, M. Electrochemical Characterization of La[sub 0.6]Sr[sub 0.4]Co[sub 0.2]Fe[sub 0.8]O[sub 3] Cathodes for Intermediate-Temperature SOFCs. *J. Electrochem. Soc.* **151,** A1847 (2004).
45. Yan, A., Yang, M., Hou, Z., Dong, Y. & Cheng, M. Investigation of Ba1-xSrxCo0.8Fe0.2O3-δas cathodes for low-temperature solid oxide fuel cells both in the absence and presence of CO2. *J. Power Sources* **185,** 76–84 (2008).
46. Nagai, T., Ito, W. & Sakon, T. Relationship between cation substitution and stability of perovskite structure in SrCoO3-??-based mixed conductors. *Solid State Ionics* **177,** 3433–3444 (2007).
47. Aguadero, A. *et al.* Structural and Electrical Characterization of the Novel $SrCo_{0.9}Sb_{0.1}O_{3-\delta}$ Perovskite: Evaluation as a Solid Oxide Fuel Cell Cathode Material.

Chem. Mater. **19,** 6437–6444 (2007).

48. Qu, B., Long, W., Jin, F., Wang, S. & He, T. SrCo0.7Fe0.2Ta0.1O3-δperovskite as a cathode material for intermediate-temperature solid oxide fuel cells. *Int. J. Hydrogen Energy* **39,** 12074–12082 (2014).
49. Aguadero, A., Pérez-Coll, D., Alonso, J. A., Skinner, S. J. & Kilner, J. A new family of mo-doped srcoo 3-delta; Perovskites for application in reversible solid state electrochemical cells. *Chem. Mater.* **24,** 2655–2663 (2012).
50. Cascos, V., Martínez-Coronado, R. & Alonso, J. A. New Nb-doped SrCo1-xNbxO3-δ perovskites performing as cathodes in solid-oxide fuel cells. *Int. J. Hydrogen Energy* **39,** 14349–14354 (2014).
51. Shen, Y., Wang, F., Ma, X. & He, T. SrCo1-yTiyO3-δas potential cathode materials for intermediate-temperature solid oxide fuel cells. *J. Power Sources* **196,** 7420–7425 (2011).
52. Porras-Vazquez, J. M. & Slater, P. R. Synthesis and characterization of oxyanion-doped cobalt containing perovskites. *Fuel Cells* **12,** 1056–1063 (2012).
53. Chen, D. *et al.* Compositional engineering of perovskite oxides for highly efficient oxygen reduction reactions. *ACS Appl. Mater. Interfaces* **7,** 8562–8571 (2015).
54. Cascos, V., Alonso, J. & Fernández-Díaz, M. Nb5+-Doped SrCoO3−δ Perovskites as Potential Cathodes for Solid-Oxide Fuel Cells. *Materials (Basel).* **9,** 579 (2016).
55. Aguadero, A. *et al.* SrCo1-xSbxO3-δperovskite oxides as cathode materials in solid oxide fuel cells. *J. Power Sources* **192,** 132–137 (2009).
56. Shannon, R. D. Revised Effective Ionic Radii and Systematic Studies of Interatomie Distances in Halides and Chaleogenides. *Acta Cryst.* 751–767 (1976).
57. Haas, O., Ludwig, C. & Wokaun, A. Determination of the Bulk Cobalt Valence State of Co-Perovskites Containing Surface-Adsorbed Impurities. *Anal. Chem.* **78,** 7273–7277 (2006).
58. Conder, K., Pomjakushina, E., Soldatov, A. & Mitberg, E. Oxygen content determination in perovskite-type cobaltates. *Mater. Res. Bull.* **40,** 257–263 (2005).
59. Kim, Y. N., Kim, J. H. & Manthiram, A. Effect of Fe substitution on the structure and properties of LnBaCo2-xFexO5+δ(Ln = Nd and Gd) cathodes. *J. Power Sources* **195,** 6411–6419 (2010).
60. Tai, L. W., Nasrallah, M. M., Anderson, H. U., Sparlin, D. M. & Sehlin, S. R. Structure and electrical properties of La1-xSrxCo1-yFeyO3. Part 1. The system La0.8Sr0.2Co1-yFeyO3. *Solid State Ionics* **76,** 259–271 (1995).
61. Tai, L. W., Nasrallah, M. M., Anderson, H. U., Sparlin, D. M. & Sehlin, S. R. Structure and electrical properties of La1 - xSrxCo1 - yFeyO3. Part 2. The system La1 - xSrxCo0.2Fe0.8O3. *Solid State Ionics* **76,** 273–283 (1995).
62. Steele, B. C. H., Hori, K. M. & Uchino, S. Kinetic parameters influencing the performance of IT-SOFC composite electrodes. *Solid State Ionics* **135,** 445–450 (2000).

63. Zhou, W., Jin, W., Zhu, Z. & Shao, Z. Structural , electrical and electrochemical characterizations of SrNb 0 . 1 Co 0 . 9 O 3 L d as a cathode of solid oxide fuel cells operating below 600 8 C. *Int. J. Hydrogen Energy* **35,** 1356–1366 (2010).
64. Nielsen, J., Jacobsen, T. & Wandel, M. Impedance of porous IT-SOFC LSCF : CGO composite cathodes. *Electrochim. Acta* **56,** 7963–7974 (2011).
65. Setevich, C., Prado, F. & Caneiro, A. Electrochemical response of several cathode configurations prepared with Ba0.5Sr0.5Co0.8Fe0.2O3-δ and Ce0.9Gd0.1O1.95 for IT-SOFC. *J. Solid State Electrochem.* **20,** 1633–1643 (2016).
66. Transactions, E. C. S. & Society, T. E. (BaxSr1-x)(CoyFe1-y)O3-δ Perovskites as SOFC Cathode Material: Electrode-Electrolyte Reactions and Electrochemical Characterisation Lei Wang. *Society* **7,** 1015–1024 (2007).
67. Steele, B. C. H. Survey of materials selection for ceramic fuel cells: II. Cathodes and anodes. *Solid State Ionics* **86–88,** 1223–1234 (1996).
68. Ni, D. W. & Esposito, V. Densification of Ce0.9Gd0.1O1.95barrier layer by in-situ solid state reaction. *J. Power Sources* **266,** 393–400 (2014).
69. Choi, S., Shin, J. & Kim, G. The electrochemical and thermodynamic characterization of PrBaCo 2-xFe xO 5+δ (x = 0, 0.5, 1) infiltrated into yttria-stabilized zirconia scaffold as cathodes for solid oxide fuel cells. *J. Power Sources* **201,** 10–17 (2012).
70. Mori, M. Effect of B-site doing on thermal cycle shrinkage for La 0.8Sr0.2Mn1-xMxO 3+δ perovskites (M=Mg, Al, Ti, Mn, Fe, Co, Ni; 0≤x≤0.1). *Solid State Ionics* **174,** 1–8 (2004).

Chapter 8

Conclusions and outlook

The objective of this thesis was elaborating new ceramic materials for the application in a sustainable energy conversion and storage context. This goal was pursued taking in account that, beside the research for new functional materials to deploy in developing technologies, the existing large scale facilities for energy production can still be improved. For this purpose the project has focused onto developing materials suitable for the application in the field of fuel cells, with particular attention to the electrolyte and the cathode, and oxygen permeation membranes, aiming to use them in oxy-fuel combustion plants. As an additional benefit, fuel cells cathodes and oxygen permeation membranes are characterized by similar requirements, and the investigation of the same materials in two different fields provided complementary information about their properties.

A first study involved an ink-jet printed thin film electrolyte based on a Gadolinium Doped Ceria (GDC) and Yttrium Stabilized Zirconia (YSZ). This was based on a hybrid ink consisting of pre-formed GDC nanoparticles dispersed into a liquid sol-gel matrix as a precursor of YSZ. In order to prevent reactivity of the zirconium precursor before printing, a chelating agent was used.

The crystal structure of the resulting material was investigated in relation to the thermal treatment temperature and atmosphere, to check the stability of the composite and observe when the formation of the solid solution between GDC and YSZ occurred.

The resulting ink was suitable for inkjet printing, showing low viscosity and a particle size dispersion falling into the optimal range for ink-jet printing even after the dispersion into the YSZ sol-gel matrix. With respect to the pure YSZ sol-gel ink, the characterization of the parameters influencing printability (density, surface tension, viscosity) showed that these were not significantly affected by the addition of GDC nanoparticles.

The observed ionic conductivity of the printed thin film was $5 \cdot 10^{-3}$ S·cm^{-1} at 600 °C, being higher than YSZ and making this composite promising for at low temperature application. When the sample was tested in reducing environment, no significant changes in the total conductivity were observed, showing that GDC nanoparticles are not sufficiently connected to allow percolation.

Another part of the work involved the development of mixed ionic and electronic conductors (MIECs) and for this purpose four cubic perovskites based on $SrCoO_3$ structure were investigated. These were obtained after an initial and accurate selection of donor dopants elements, which highlighted the positive effect of niobium on the stabilization of the cubic perovskite $SrCo_{0.95}Nb_{0.05}O_{3-\delta}$. In order to further enhance the material stability and its tolerance to CO_2, iron was chosen as additional dopant in the amount of 0, 10, 20 and 30 %, obtaining $SrCo_{0.95}Nb_{0.05}O_{3-\delta}$ (SCN), $SrCo_{0.85}Fe_{0.1}Nb_{0.05}O_{3-\delta}$ (SCFN1), $SrCo_{0.75}Fe_{0.2}Nb_{0.05}O_{3-\delta}$ (SCFN2) and $SrCo_{0.65}Fe_{0.3}Nb_{0.05}O_{3-\delta}$ (SCFN3). The effect of iron substitution for cobalt was investigated in terms of crystal structure, oxygen nonstoichiometry, mobility and desorption. Average oxidation state of B-site cations, surface composition and total conductivity were characterized as a function of iron content, too.

Iron doped compounds retained a cubic structure, however the presence of iron seemed to favor the formation of a small amount of brownmillerite impurities at lower calcination temperature, which decreased with a high temperature treatment. Besides that, iron doping proved to reduce the oxygen nonstoichiometry at room temperature, probably due to a an easier tolerance of iron to the 4+ oxidation state compared to cobalt, as observed from the average oxidation state of B-site cations. The oxygen nonstoichiometry showed a non-linear change with increasing iron content, with a minimum observed for SCFN2, suggesting a possible interaction effect between the dopants.

The evolution of oxygen nonstoichiometry and average B-site cations, investigated by thermogravimetric analysis, showed that in air an oxygen incorporation occurs around 400°C, forming a higher amount of Co^{4+} and Fe^{4+}. After this maximum an oxygen release is observed, which is slightly higher in iron containing samples. An opposite trend was

observed for the thermogravimetric analysis run in nitrogen, with iron doping hindering the release of oxygen at high temperature, due to a lower reducibility.

Not only the resistance in reducing atmosphere was enhanced with iron doping, but the surface analysis composition obtained by XPS showed a beneficial effect of iron in reducing the surface segregation of strontium.

The in-plane conductivity characterization showed a p-type conductivity having a maximum around 400 °C, consistently with the behavior observed by thermogravimetric analysis, and the highest conductivity values of 490 and 525 $S \cdot cm^{-1}$ were observed for SCN and SCFN2, respectively. Iron doping produced an increase in the activation energy for conduction.

Dense pellets were sintered and oxygen permeability using N_2 as sweep gas was tested. SCFN1 and SCFN2 were the only sample displaying stable and reliable performances, with a permeation flow of 1.21 and 1.00 $ml_N \cdot min^{-1} \cdot cm^{-2}$ at 750 °C, respectively, and a maximum permeation flux of 1.88 (at 850 °C) and 1.95 (at 950 °C) $ml_N \cdot min^{-1} \cdot cm^{-2}$, respectively.

Since SCFN2 showed the most stable performances it was tested in oxy-fuel conditions, using CO_2 as sweeping gas. Besides an initial decrease in performance at low temperature, probably due to CO_2 adsorption on the membrane, the performance was restored and a flow of 1.34 $ml_N \cdot min^{-1} \cdot cm^{-2}$ was obtained at 950 °C.

The oxygen permeation measurements allowed calculating the ionic conductivity and 0.34 and 0.26 $S \cdot cm^{-1}$ were observed at 750°C, being among the highest in literature for MIECs.

After test microstructural characterization showed the formation of pinholes in the samples with a lower iron doping, while larger cracks were observed for SCFN3 sample.

$SrCo_{0.95}Nb_{0.05}O_{3-\delta}$ (SCN), $SrCo_{0.85}Fe_{0.1}Nb_{0.05}O_{3-\delta}$ (SCFN1), $SrCo_{0.75}Fe_{0.2}Nb_{0.05}O_{3-\delta}$ (SCFN2) and $SrCo_{0.65}Fe_{0.3}Nb_{0.05}O_{3-\delta}$ (SCFN3) were deposited on symmetric cell and tested as cathodes in air and promising performances were observed, in particular SCN and SCFN2 had 0.097 and 0.148 $\Omega \cdot cm^2$ area specific resistance (ASR) at 700°C, respectively. In all the samples, the main contribution to the resistance was coming from the surface exchange reaction, suggesting that the high conductivity values observed allow a fast charge

transfer process. Once again, doping with iron was found to increase the activation energy for oxygen reduction reaction, with this effect being less pronounced in the case of SCFN2. After test microstructural characterization showed a compact microstructure with reduced porosity compared to the starting powders, suggesting that a decrease in the surface area of the electrode occurred during the consolidation process.

The results reported above are promising, but further improvements are still needed to make these materials appealing for a large scale application.

Concerning the GDC/YSZ composite electrolyte, further investigation on the maximum amount of GDC nanoparticles that can be dispersed in the ink is required. This could provide an estimation of an upper limit for both avoiding electronic percolation and not precluding printability, since the increase in solid loading is expected to affect them both. Additionally, a more detailed investigation on the thermal treatment is required in order to improve the deposition of the electrolyte on an anode substrate since the attempts (not reported here) to print the electrolyte on a tape-casted anode resulted in cracked films.

In the case of the $SrCo_{0.95-x}Fe_xNb_{0.05}O_{3-\delta}$ (x=0, 0.1, 0.2, 0.3) perovskites, since they displayed a change properties which is not linear in relation to the amount of inserted iron, a modellistic investigation of the effect of niobium and iron doping could provide a better understanding of the promising properties displayed by SCFN2.

In the context of permeation membranes, structural investigation of the materials with thermal XRD in different atmospheres (air, N_2, CO_2) could provide an insight on an eventual phase transition occurring in the membrane under testing conditions and clarify if the mechanism of CO_2 interaction with the surface of the membrane involves the occupation of vacancy sites or the formation of stable carbonates.

Finally, the permeation performances could be further enhanced by the deposition of an activation layer having the same composition of the membrane but treated at a lower temperature than the sintered samples, so to have a larger area available for the reaction.

Concerning the application of the same materials as cathodes, the formation of a more open electrode microstructure should be pursued, in order to prevent gas diffusion limitations and provide a larger surface area available for oxygen to react.

The investigation of the limiting step of the oxygen reduction reaction could provide an insight in the mechanism of oxygen reduction at the electrode, allowing to improve the reactivity. Finally, long term stability in atmospheric air should be checked to exclude a possible deactivation of the surface by CO_2 poisoning.

As a general remark, the sintering process and microstructure evolution of cobalt based compounds has demonstrated to be complicated and definitely requires a more detailed investigation, since it has been observed to play a major role in determining the final properties of the material. It is not excluded that an interaction between iron and niobium (often used as grain growth suppressor) may play a role in the final microstructure of the calcined material.

Acknowledgements

Firstly, I would like to express my gratitude to my supervisor, Professor Antonella Glisenti, for her guidance along this rollercoaster journey called PhD, in which I experienced the most extreme inner struggles and joys, feeling challenged both as scientist and person. Thank you from the scientific and the human side, for putting your trust in me once again and helping me in my development.

My deepest gratitude goes to Professor Vincenzo Esposito for his supervision during my stays at DTU, for having always a critical perspective and a clear view in our discussions and for his challenging approach which led me to growth. Thank you for inducing in me the desire to go deeper.

Many thanks to Dr. Christophe Gadea for introducing to me the fantastic world of inkjet printing and the cutting-edge field of self-writing papers, for our trip to Sion and for having always a lot of humor to share.

I owe a huge thank to Massimo Rosa for sharing the joys of PixDro printer and giving me many nice tips on how to obtain better inks. Thank you for the concerts and the DHL run we enjoyed together.

Thanks to Dr. Simone Sanna for giving me an insight on the world of thin films and introducing me to the Brouwer diagram and to an unmentionable and flawless tool for impedance measurements.

Thanks to Dr. Stéven Pirou and Lev Martinez Aguilera for providing me an insight and their invaluable help in the oxygen permeation measurements.

Thanks to Nicola Tiso for his help with iodometric titration measurements, carbon coating for SEM samples and for being always available and nice. Thanks to Roberta Saini for her help with TGA/DTA measurements.

Thanks to Stefano Mercanzin for the technical and moral support, which fortunately have never being missing along these years.

Mange tak til Dr. Simon Pitscheider for being always open and available when I had doubts, for the time spent at the gym training together and for being a friend even before meeting in person.

Thanks to Dr. Marta Maria Natile, Dr. Alberto Garbujo and Giovanni Carollo for their irreplaceable help with XRDs.

Thanks to all my group mates in Padova and Denmark.

A big thank to all the people I met at Risø, especially Tuk, Roberto, Ilaria, Daniel, Martina, Megha and Simone and everyone who has contributed to making fantastic my stay in Denmark. My thought goes especially to the Friday Bar, which I had the pleasure to run a few times.

Thanks to my flatmates Matteo, Laura, Lorenzo and Carolina who I shared a home with in via Colonnello de Cristoforis for three years, many cirullas, some really heavy pizzas and much more.

Thanks to all my friends, in particular to Massimo, Michela, Niccolò, Alessandro, Isabel and Pierpaolo for always being available and present during joyful and dark moments, sharing endless and stimulating conversations and rejuvenating the spirit through shared experiences.

Nonetheless I'd like to thank my bandmates and family in Crafter of Gods for having shared a plenty of evenings pursuing something more than a dream through the music we created together, playing live and enjoying Morgana's Castle.

My deepest gratitude goes to my family for their constant support along these years, to my father Patrizio for his skepticism and transport, to my mother Paola for her unconditioned support and to my sister Elettra for the many adventures, which still go on since 27 years. Special thanks go to my cousin Davide for teaching me a lot of pragmatic stuff which gave me an invaluable help during practice.

Finally I would like to thank Maria for her limitless love, support and comprehension in the last year and a half, for being always interested in what I'm doing and being able to give me strength and motivation. Thank you for being always by my side and sharing this wonderful journey together.